AD NUMBER

AD828705

NEW LIMITATION CHANGE

TO

Approved for public release, distribution unlimited

FROM

Distribution authorized to U.S. Gov't. agencies and their contractors; Administrative/Operational Use; MAR 1968. Other requests shall be referred to Air Force Rocket Propulsion Lab., Edwards AFB, OH 45433.

AUTHORITY

AFPRL ltr, 27 Oct 1971

AD828705

SYSTEM COUPLED DYNAMIC INSTABILITY
AMPLITUDE LIMITING ANALYSIS
AND EVALUATION
FINAL REPORT

PART I

Fred E. Bikle, Martin Marietta Corporation
Larry E. Fidler, Martin Marietta Corporation
Tom C. Hendricks, Martin Marietta Corporation
et al.

TECHNICAL REPORT AFRPL-TR-68-41

March 1968

SPECIAL NOTICES

When Government drawings, specifications, or other data are
used for any purpose other than in connection with a definitely
related government procurement operation, the United States
Government thereby incurs no responsibility nor any obligation
whatever; and the fact that the Government may have formulated,
furnished, or in any way supplied the said drawings, specifica-
tions, or other data is not to be regarded by implication or
otherwise as in any manner licensing the holder or any other
person or corporation, or conveying any right or permission to
manufacture, use or sell any patented invention that may in
any way be related thereto.

This document is subject to special export controls and each
transmittal to foreign governments or foreign nationals may be
made only with prior approval of AFRPL (RPEI/STINFO), Edwards
California.
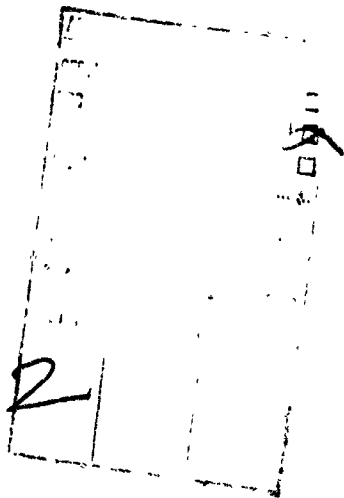
SYSTEM COUPLED DYNAMIC INSTABILITY

AMPLITUDE LIMITING ANALYSIS AND EVALUATION

FINAL REPORT

PART I

March 1968

Fred E. Bikle
Larry E. Fidler
Tom C. Hendricks
et al.

FOREWORD

The research described in this report was performed for the Air Force Rocket Propulsion Laboratory. Air Force Flight Test Center, Edwards Air Force Base, California, BPSN 623058, Project 3058 of AF04611-67-C0031, by Martin Marietta Corporation, Denver, Colorado. The Air Force program monitor assigned to this project was Charles Richard/ RPRPP. The report covers research performed between November, 1966, and December, 1967. This report, submitted in accordance with Exhibit B, Contract Data Requirements List Line Item B005. The preliminary issue of this report was identified as MCR-68-20.

In addition to the authors named on the title page, persons contributing to this document were:

> Milt A. Hetrick
>
> Mike P. Lorett
>
> John B. Rohrs

This technical report has been reviewed and is approved.

<div align="right">

Charles H. Richard
Project Officer

</div>

ABSTRACT

This report is concerned with the study of instabilities, generally referred to as POGO, resulting from coupling between liquid-fueled propulsion systems and structural dynamics. The report deals specifically with analysis of active and passive methods of stability compensation, methods of predicting POGO limit cycle amplitudes, and statistical methods of evaluating POGO stability margins. In addition, experimental studies were conducted to evaluate certain passive compensation methods. Specifically, sealed bag accumulator, gas injection, and cavitating venturi concepts were studied.

(The reverse of this page is blank.)

TABLE OF CONTENTS

Document Control Data - R & D (DD Form 1473)

LIST OF ILLUSTRATIONS

LIST OF TABLES

LIST OF ABBREVIATIONS AND SYMBOLS

Active Control Valve

A_{sf}	Cross section of fuel suction line
A_{so}	Cross section of oxidizer suction line
A_{Go}	Oxidizer control loop gain
A_{Gf}	Fuel control loop gain
C_p	Pump structural damping
C_o	Constant in valve resistance function accounting for different fluid specific gravities
C_v	Steady state valve flow coefficient
C_{ve}	Oscillatory valve flow coefficient
G_A	First mode structural gain
G_B	Second mode structural gain
g_c	Gravitational constant
h_{oA}	First mode oxidizer modal ratio
h_{oB}	Second mode oxidizer modal ratio
h_{fA}	First mode fuel modal ratio
h_{fB}	Second mode fuel modal ratio
I_p	Effective pump moment of inertia

I_{do}	Oxidizer discharge line inertance
I_{df}	Fuel discharge line inertance
I_{so}	Oxidizer suction line inertance
I_{sf}	Fuel suction line inertance
K_{co}	Oxidizer flowrate to chamber combustion coefficient
K_{cf}	Fuel flowrate to chamber combustion coefficient
K_{p}	Spring constant for pump structure
L_{so}	Oxidizer suction line length
L_{sf}	Fuel suction line length
L_{To}	Oxidizer fluid height in tank
L_{Tf}	Fuel fluid height in tank
l_{cg}	Pump radius of gyration relative to engine gimbal point
M_{v}	Dynamic mass of control valve
M_{p}	Effective rotational mass of pump
P_{1}	Pressure upstream of control valve
P_{2}	Pressure downstream of control valve
P_{do}	Oxidizer pump discharge pressure
P_{df}	Fuel pump discharge pressure

P_{so} Oxidizer pump suction pressure

P_{sf} Fuel pump suction pressure

P_{dGo} Oxidizer pump discharge pressure due to gain alone

P_{dGf} Fuel pump discharge pressure due to gain alone

P_{c} Chamber pressure

P_{co} Oxidizer component of chamber pressure

P_{cf} Fuel component of chamber pressure

$\ddot{Q}_{A}$ First mode gimbal acceleration

$\ddot{Q}_{B}$ Second mode gimbal acceleration

$\ddot{X}_{p}$ Pump acceleration relative to gimbal point

R Valve resistance

R_{po} Oxidizer pump resistance

R_{pf} Fuel pump resistance

R_{do} Oxidizer discharge line resistance

$\dot{R}_{df}$ Fuel discharge line resistance

$\dot{W}_{do}$ Oxidizer discharge flowrate

$\dot{W}_{df}$ Fuel discharge flowrate

$\dot{W}_{so}$ Oxidizer suction flowrate

$\dot{W}_{sf}$ Fuel suction flowrate

ω_{so}	Oxidizer suction line frequency
ω_{sf}	Fuel suction line frequency
ω_A	First mode structural frequency
ω_B	Second mode structural frequency
ω_v	Control valve natural frequency
ω_{so}	Oxidizer suction line damping ratio
ω_{sf}	Fuel suction line damping ratio
ζ_A	First mode structural damping ratio
ζ_B	Second mode structural damping ratio
ζ_v	Control valve damping ratio
τ_o	Oxidizer control valve time lag
τ_f	Fuel control valve time lag
τ_c	Combustion time lag
Θ'	Control valve blade deflection angle

Turbine Speed Control

C^*	Characteristic velocity (ft/sec)
G	Time dependent function
k	Specific heat ratio
K	Time independent, constant
N	Rotational speed (rad/sec)

P	Pressure (psia)
S	Laplace operator (d/dt)
μ τ	Torque (ft-lb)
V_1	Turbine spouting velocity (ft/sec)
$\dot{W}$	Flow rate (lb/sec)
γ ρ	Fluid density

Subscripts

c	Thrust chamber
f	Fuel
fa	Fuel upstream of bootstrap line
fb	Fuel bootstrap line
fe	Fuel inlet to controller
fd	Fuel pump discharge
fj	Fuel bootstrap line inlet
fs	Fuel pump suction
fsv	Fuel vapor
o	Oxidizer
oa	Oxidizer line upstream of bootstrap line
ob	Oxidizer bootstrap line
oc	Oxidizer inlet to cavitating venturi
od	Oxidizer pump discharge
oj	Oxidizer bootstrap line inlet
os	Oxidizer pump suction

osv   Oxidizer vapor

ss   . Steady state

ti   Turbine inlet

te   Turbine exhaust

Fluidic Amplifier Compensation

A   Effective cross sectional flow area (in^2)

P   Pressure (psi)

Q   Flow rate (lbs/sec)

U   Velocity of flow (in/sec)

ζ Resistance coefficient

Subscripts

C_1 Fluid amplifier control jet (left)

C_2 Fluid amplifier control jet (right)

d   Discharge line

LO   Fluid amplifier left output leg

RO   Fluid amplifier right output leg

P   Fluid amplifier power jet

S   Suction line

Turbopump Model Development

A   Area or slope of saturation curve for pump fluid

B   Constant in equation for pump fluid saturation curve

b   Thickness of streamtube of revolution

D   Thermal diffusivity or diameter

E	Abscissa of E, F plane
F	Ordinate of E, F plane
g	Gravitational acceleration
H	Height of gas or liquid column for gas POGO simulator
h	Static enthalpy
H_o	Total enthalpy
k	Thermal conductivity of pump fluid
L	Latent heat of vaporization
M	Meridional streamline
m	Mass
N	Normal to meridional streamlines
P	Pressure
Q	Rate of heat transfer
R	Bubble radius or radius of elbows in gas POGO simulator
r	Radius coordinate
r_c	Radius of curvature
S	Entropy
T	Temperature
T_p	Saturation temperature corresponding to pressure P
t	Time
U_1	E velocity component for hypothetical flow in E, F plane
V_1	F velocity component for hypothetical flow in E, F plane

V	Velocity relative to impeller
V'	Absolute velocity
$\dot{W}$	Flow rate
W	Work
W	Weight of fluid in a specified volume
Y	Translation of time axis associated with Laplace transformation
Z	Coordinate in r, Θ, Z space
α	Angle between meridional streamline and impeller axis
β	Angle between stream sheet and plane containing impeller axis
Γ	Circulation
γ	Ratio of specific heats for vapor
ζ	Abscissa in n, plane and velocity potential for hypothetical flow in E, F plane
η	Ordinate in n, plane and streamfunction for hypothetical flow in E, F plane
θ	Coordinate in r, Θ, Z space
λ	Turbopump prewhirl
ρ	Density
σ	Surface tension constant
τ	Shear force per unit area
φ	Velocity potential for compressible flow in an impeller streamtube of revolution
ψ	Streamfunction for compressible flow in an impeller streamtube of revolution

ω	Impeller angular velocity

Statistical Gain Margin Studies

A	System matrix
A_o	Suction line area at pump inlet
G_l	Structural response characteristic
G_s	Suction line response characteristic
G_d	Discharge line response characteristic
g_A	Mode A structural gain
j	$\sqrt{-1}$
K_p	Pump Gain
NPSHO	Net positive suction head of oxidizer
NPSHF	Net positive suction head of fuel
v_i	System eigenvector (left)
x_i	System eigenvector (right)
x	System state vector
ZPG	Zero phase gain
ζ_A	Mode A structural damping ratio
λ_i	System eigenvalue
μ	Mean
σ^2	Variance
σ	Standard deviation

| ω_A | Mode A structural resonant frequency |
| ω_s | Suction line resonant frequency |

Amplitude Limiting

A_{sf}	Cross sectional area of fuel suction line
A_{so}	Cross sectional area of oxidizer suction line
C_{fA}	Thrust coefficient
C_p	Pump structural damping
g	Structural acceleration
g_c	Gravitational constant
g_p	Pump acceleration
G_A	First mode structural gain
G_B	Second mode structural gain
G_f	Fuel pump gain (linearized)
G_o	Oxidizer pump gain (linearized)
I_{df}	Fuel discharge line inertance
I_{do}	Oxidizer suction line inertance
I_p	Turbopump effective moment of inertia
I_{sf}	Fuel suction line inertance
I_{so}	Oxidizer suction line inertance

K	Constant relating p_{mix} and p_s
K_c	Generalized chamber resistance
K_p	Spring constant for pump truss
K_t	Generalized thrust coefficient
K_{eo}	Oxidizer flowrate to chamber coefficient
K_{cf}	Fuel flowrate to chamber coefficient
L	Fluid head in propellant feedline
L_{sf}	Fuel suction line length
L_{so}	Oxidizer suction line length
L_{Tf}	Fuel height in tank
L_{To}	Oxidizer height in tank
m_{mix}	Mass of liquid-vapor mixture
$(M+1)$	Linearized pump gain
M_p	Effective rotational mass of pump
P_c	Combustion chamber pressure
P_{cf}	Fuel component of chamber pressure
P_{co}	Oxidizer component of chamber pressure
P_d	Discharge pressure (including resistance term)
P_{dG}	Discharge pressure (steady-state head rise data)

K	Constant relating p_{mix} and p_s
K_c	Generalized chamber resistance
K_p	Spring constant for pump truss
K_t	Generalized thrust coefficient
K_{so}	Oxidizer flowrate to chamber coefficient
K_{cf}	Fuel flowrate to chamber coefficient
L	Fluid head in propellant feedline
L_{sf}	Fuel suction line length
L_{so}	Oxidizer suction line length
L_{Tf}	Fuel height in tank
L_{To}	Oxidizer height in tank
m_{mix}	Mass of liquid-vapor mixture
$(M+1)$	Linearized pump gain
M_p	Effective rotational mass of pump
P_c	Combustion chamber pressure
P_{cf}	Fuel component of chamber pressure
P_{co}	Oxidizer component of chamber pressure
P_d	Discharge pressure (including resistance term)
P_{dG}	Discharge pressure (steady-state head rise data)

P_{dGf}	Fuel pump steady-state discharge pressure
P_{dGo}	Oxidizer pump steady-state discharge pressure
P_{df}	Fuel pump oscillatory discharge pressure
P_{do}	Oxidizer pump oscillatory discharge pressure
P_o	Reference pressure
P_{ref}	Reference pressure
P_s	Suction pressure
P_{sf}	Fuel suction pressure
P_{so}	Oxidizer suction pressure
P_{Tf}	Fuel tank top pressure
P_{To}	Oxidizer tank top pressure
q_p	Turbopump coordinate
$\dot{q}_p$	Turbopump velocity
$\ddot{q}_p$	Turbopump acceleration
$\ddot{Q}_A$	First mode gimbal acceleration
$\ddot{Q}_B$	Second mode gimbal acceleration
R_{df}	Fuel discharge line resistance
R_{do}	Oxidizer discharge line resistance
R_p	Pump resistance

R_{pf}	Fuel pump resistance
R_{po}	Oxidizer pump resistance
s	Laplace operator
T	Thrust
T_{in}	Thrust
V_{liq}	Specific volume of liquid phase
V_{mix}	Specific volume of liquid-vapor mixture
V_{vap}	Specific volume of vapor phase
$\dot{W}_d$	Discharge flowrate
$\dot{W}_{df}$	Fuel discharge flowrate
$\dot{W}_{do}$	Oxidizer discharge flowrate
ΔW_f	Difference between fuel suction and discharge flow
ΔW_o	Difference between oxidizer suction and discharge flow
x	Quality of liquid-vapor mixture
Z_d	Discharge system impedance
γ	Ratio of specific heats
ζ_A	First mode structural damping ratio
ζ_B	Second mode structural damping ratio
ζ_{sf}	Fuel suction line damping ratio

ω_{so} Oxidizer suction line damping ratio

ρ Propellant density

ρ_f Fuel density

ρ_o Oxidizer density

τ Combustion time constant

ω Frequency

ω_A First mode structural frequency

ω_B Second mode structural frequency

ω_{sf} Fuel suction line frequency

ω_{so} Oxidizer suction line frequency

Sealed Bag Accumulator Analysis

C_a Compliance of accumulator

C_p Pump compliance

C_s Compliance of the suction line

I_a Accumulator inertance

I_{ap} Inertance, line from accumulator to pump

I_d Discharge line inertance

I_s Inertance of the suction line

K_p Pump gain

R_a	Resistance, accumulator
R_d	Resistance, discharge line
S	Laplace variable
ΔV	Pulser volumetric displacement
ω_r	Resonant frequency

Sealed Bag Accumulator Tests

C	Compliance
E	Voltage analog of P_s
f	Break frequency
L_1	Accumulator inductance
L_2	Unidentifiable inductance of test fixture
M	Slope of the volume change - pressure curve
P_s	Oscillatory suction pressure at accumulator
P_{ss}	Steady state suction pressure
Q	Electrical analog of ΔV
R_1	Accumulator resistance
R_2	Unidentifiable resistance of test fixture
ΔV	Volumetric displacement of pulser

ρ	Fluid density
ω	Frequency

Cavitating Venturi Analysis

AI	Inlet area
AT	Throat area
CD	Venturi flow coefficient
D	Tube diameter
f	Friction factor
g_c	Gravitational constant
L_e	Tube length
P_t	Throat pressure
PI	Inlet pressure
PT	Throat pressure
PR_{ov}	Pressure recovery ratio
Re	Reynolds number
W_c	Flowrate through cavitating section
W_{DOT}	Total flowrate
W_{DT}	By-pass flowrate

ρ	Fluid density	
μ	Fluid viscosity	
η	Recovery coefficient	

Gas Injection Analysis

A_E	Entrance area of cavitating venturi	(ft^2)
A_t	Throat area of cavitating venturi	(ft^2)
C	Compliance, empircal correction factor	
C_p	Compliance of pulsing unit	(in^2)
D_i	Inside diameter of feedline	(in)
D_o	Outer diameter of line	(in)
E	Elasticity of wall material	(lb_f/in^2)
f	Friction factor, single phase flow	(1)
f'	Two phase friction factor	(1)
g	Gravitational constant	(ft/sec^2)
I	Inertance	(sec^2/in^2)
I_{MAX}	Amplitude of current generator	(amps)
I_P	Inertance associated with pulser	(sec^2/in^2)
K_C	Loss coefficient (Ref. 11)	(1)

L	Inductance or length	
$\dot{m}_{G,g}$	Mass flow rate of injected gas	(lb_m/sec)
$\dot{m}_{L,l}$	Mass flow rate of liquid	(lb_m/sec)
$\dot{m}_v$	Mass flow rate of vapor	(lb_m/sec)
$M_{G,g}$	Molecular weight of injected gas	$(lb_m/lb_m\text{-mole})$
M_v	Molecular weight of vapor	$(lb_m/lb_m\text{-mole})$
P_s	Oscillatory static pressure	(lb_f/in^2)
P_m	Local static pressure of mixture	(lb_f/in^2)
P_E	Static pressure at venturi entrance	(lb_f/in^2)
P_i	Local static pressure at injector	(lb_f/in^2)
P_t	Pressure at throat of cavitating venturi (vapor pressure)	(lb_f/in^2)
P_v	Vapor pressure	(lb_f/in^2)
$\dot{Q}$	Volumetric flow rate	(ft^3/sec)
r	Bubble radius	(in)
R	Resistance	(sec/in^2)
R_d	Venturi resistance	(sec/in^2)
R_G	Gas constant	$(lb_f\ in/lb_m\text{-mole R})$
R_p	Pulser resistance	(sec/in^2)

Re	Reynolds number for single phase flow	(1)
Re'	Two phase Reynolds number	(1)
$T_{L,l}$	Liquid temperature	(°R)
$T_{G,g}$	Gas temperature	(°R)
T_m	Temperature of gas/vapor mixture	(°R)
V	Volume or velocity	
V_{gv}	Gas/vapor volume	(in^3)
V_i	Volume of bubble at point of injection	(in^3)
ΔV_{NET}	Net change in volume resulting from evaporation and increase in head pressure	(in^3)
$\dot{W}$	Weight flow rate	(lb_f/sec)
X_P	Pulser displacement	(in)
$\beta_{E,a}$	Effective bulk modulus of segment including pipe elasticity	(lb_f/in^2)
β_G	Bulk modulus of gaseous phase = γR ($\gamma = 1.4$ adiabatic process)	(lb_f/in^2)
β_{GV}	Bulk modulus of liquid/vapor mixture	(lb_f/in^2)
$\rho_{G,g}$	Density of injected gas	(lb_m/ft^3)
$\rho_{L,l}$	Liquid density	(lb_m/ft^3)
ρ_m	Density of gas-vapor/liquid mixture	(lb_m/ft^3)

ρ_v	Vapor density	(lb_m/ft^3)
ω	Circular frequency	(radians/sec)
$\mu_{G,g}$	Absolute viscosity of gas	$(lb_m in/sec)$
$\mu_{L,l}$	Viscosity of liquid	$(lb_m in/sec)$
σ	Surface tension	(lb_f/in)

SECTION 1

SUMMARY

1. PROGRAM DESCRIPTION

The research work effort concentrated on analyzing and
evaluating hitherto untried methods of POGO stability compen-
sation, developing a unique method for predicting POGO stabil-
ity, and developing a model for explaining the existence of
stable limit cycles observed on all linearly unstable config-
urations. In addition, analysis was performed on three con-
cepts of POGO compensation (sealed bag accumulator, gas injec-
tion, and cavitating venturi) to establish the relationship of
dynamic characteristics to specific design parameters. Two of
these concepts were further studied experimentally to evaluate
the analytical conclusions. Results of the analyses and exper-
imentation are briefly summarized below.

2. CONTROL VALVE COMPENSATION

Stability compensation was achieved using a valve to mod-
ulate suction line flow rates in direct response to suction
pressure perturbations.

The study revealed that suitable choice of control gains
required rather precise knowledge of both suction line and
structural frequencies. The method would be least effective
on configurations where compensation would be required most;
namely, under conditions where suction line and structural
frequencies were equal. This limitation could be avoided if
the control valve were placed in the discharge lines where
phase between flow rate and pressure is not affected by system
frequencies.

3. TURBINE SPEED CONTROL

Studies revealed that pump discharge flow rate could be
modulated by controlling fuel flow to the turbine gas genera-
tor. The gas generator/turbine system acts as an amplifier
whose output varies the main pump flow rate in response to sig-
nals introduced in the turbine bootstrap system. Results of
the analysis showed that the method of control was effective
when suction line frequencies and structural frequencies were
sufficiently separated. However, if suction line frequencies

were equal or nearly equal to structural frequencies, this method of control produces equal but offsetting effects in suction and discharge systems. Thus, under the conditions of equal suction line and structural frequencies when the system stability is most critical, the method of compensation is least effective.

4. AMPLITUDE LIMITING STUDIES

Analysis showed that stable limit cycles in the amplitude range observed during Titan II flights could be simulated by a mathematical model in which the only non-linearity present arose from thermodynamic processes in the pump cavitation region. The non-linearity was, however, too weak to make limit cycle amplitudes independent of other system parameters. In fact, the study showed that limit cycle amplitude was extremely sensitive to uncertainties in pump gain, structural frequency, and suction line frequency. Normal but uncontrollable variation in these quantities from one vehicle to another could produce an order of magnitude uncertainty in limit cycle amplitude prediction.

5. STATISTICAL STABILITY STUDIES

A method was developed for relating system gain margin to probability of system stability. Statistical distributions of critical system parameters treated as random or functionally related variables were combined by Monte Carlo analysis technique which simulated any specified number of flights. Results from analysis of a representative Titan III MOL configuration indicate that the customary method of root sum squaring tolerance response variations results in gain margin requirements that can be too large by a factor of 3 or 4.

6. FLUIDIC AMPLIFIER CONTROL

Only preliminary analysis was required to demonstrate that fluidic amplifiers were not practical devices for modulating main stream flow in response to pressure or acceleration signals. The principle disadvantage of the fluidic amplifier results from the pressure loss that must occur by virtue of requiring a rather large part of the total flow for use as a control jet. Also pressure noise resulting from mixing the control jet with main flow can mask the signal present in the main flow. Because of the pressure losses, the method would impose intolerable performance losses. The noise problem would make the control insensitive to pressure

7. SEALED BAG ACCUMULATOR

The sealed bag accumulator POGO fix was evaluated to determine the effects of accumulator design parameters (geometry and system static pressure) on its dynamic characteristics (inertance, compliance, and resistance). One series of tests determined that accumulator compliance was independent of geometry for the designs tested and primarily a function of pressure. As system static pressure was increased accumulator compliance decreased. Through dynamic testing the mathematical model synthesis for the accumulator was found to be in error. This result inhibited data analysis and only qualitative results were attainable.

8. SUCTION SYSTEM GAS INJECTION

The gas injection program consisted of both analytical and experimental phases. Analysis resulted in a math model for predicting suction system response with gas injection. The experimental effort consisted of five test sequences utilizing water, aerozine 50 and nitrogen tetroxide as propellants. The experimental results indicate that a correlation between analysis and experiment is in general difficult to obtain with a horizontal test section. Vertical testing yields the best results. Additional conclusions are that certain gases - CO_2 in water and N_2 in nitrogen tetroxide are dissolved quite rapidly and produce no significant shift in suction system frequencies. Furthermore, it was found that gas injection does affect pump performance. An evaluation of the extent to which altered performance is undesirable must be considered in terms of the particular turbopump application.

9. CAVITATING VENTURI

The cavitating venturi which through previous analyses was found to induce unacceptable pressure losses in the suction system was re-examined with a modification which it was felt would reduce losses. The modification provided for a low loss bypass tube for most of the flow. Through analysis it was found that even with a bypass the venturi losses were still sufficient to make the device unacceptable as a POGO fix.

SECTION II

INTRODUCTION

1. OBJECTIVES

All program objectives sought to extend and improve the basic understanding of the system coupled POGO instability problem. In particular, analysis was directed toward the following ends:

a. Further refinement of methods for evaluating and determining system stability.

b. Evaluation and comparison of relative effectiveness of passive and active POGO compensation methods.

c. Refinement of models for critical system elements such as the pump and suction line.

The experimental efforts were designed to complement certain facets of the analytical studies and provide means of substantiating analysis conclusions. The studies and analysis that were made are briefly described as follows:

1) Turbine Speed Control - feasibility studies were conducted of modulating pump flow by using suction pressure or acceleration signals to control fuel delivered to the gas generator.

2) Active Valve Control - studies were made to determine whether POGO stability could be improved by controlling suction line and discharge flow rate in response to suction pressure or acceleration signals.

3) Fluidic Amplifier - the fluidic amplifier was investigated to determine whether suction line or discharge line flow could be modulated without the use of mechanica valves.

4) Amplitude Limiting Studies - analysis was performed to identify the non-linearity responsible for stable limit cycling on basically unstable configurations.

5) Statistical Stability Analysis - a method was developed for basing the probability of system stability on various critical system parameters treated as random or functionally related statistical variables.

6) Sealed Bag Accumulator - the purpose of examining this device was to 1) determine the relationship of accumulator compliance to system static pressure, 2) devise an analytical model which would relate accumulator dynamic characteristics to specific design parameters, and 3) verify the results of the analytical effort with experimental data.

7) Gas Injection POGO Compensation - this method of correcting POGO was studied in order to 1) develop an analytical model describing the suction system performance with gas injection, 2) verify the model through experiment, 3) establish the differences between horizontal and vertical testing techniques, 4) evaluate the effects of gas injection n pump performance, and 5) establish the effectiveness of certain gases for POGO compensation.

8) Cavitating Venturi - the cavitating venturi concept was re-examined to determine if a bypass tube would reduce pressure losses to the extent that this method of POGO compensation would become feasible.

SECTION III

ACTIVE CONTROL VALVE ANALYSIS

1. **SYSTEM DESCRIPTION AND ANALYSIS APPROACH**

    The introduction of Section I contained a discussion of
the potential advantages associated with an active POGO Control
Device. The active control valve concept was one of the com-
pensation methods examined during the Phase I Program. Choice
of the active valve as a method of compensation originated
from recognizing that it would be desirable to control directly
the flow of propellant to the combustion chamber. All analysis
was conducted on typical Titan III vehicle configurations in
order to use readily available parameter values and to assure
that results would not be subject to too many idealizing
assumptions required of a more general analysis. A wide
enough range of actual parameter valves for structure and
propulsion system were considered to assure that conclusions
drawn were not based on a special situation peculiar to any
particular set of parameter values.

    a. Analysis Methods - The first part of the analysis
was conducted on the analog computer with a complete simulation
of the Titan III B Structure and Propulsion Systems. The pur-
pose of this effort was to evaluate the feasibility of con-
trolling POGO with active butterfly control valves located in
the fuel and oxidizer suction lines. In addition to the analog
study a digital analysis was performed which consisted of both
frequency response and root-locus studies of the decoupled fuel
and oxidizer systems.

    For both phases of investigation, valve actuation
was coupled to sensed suction pressure through a mechanical
linkage characterized by a second order system representative
of dynamics, a gain, and a time lag. For a detailed description
of the control valve, the reader is referred to Appendix I.
Figure 1 shows the essential blocks of the oxidizer side of
the system along with the coupling networks. The fuel side is
similar except for values of characterizing parameters. The
control valve loop is indicated by the heavy lines in the
Figure. The following paragraphs contain a discussion of the
math model development along with the details and results of
the two phases of analysis.
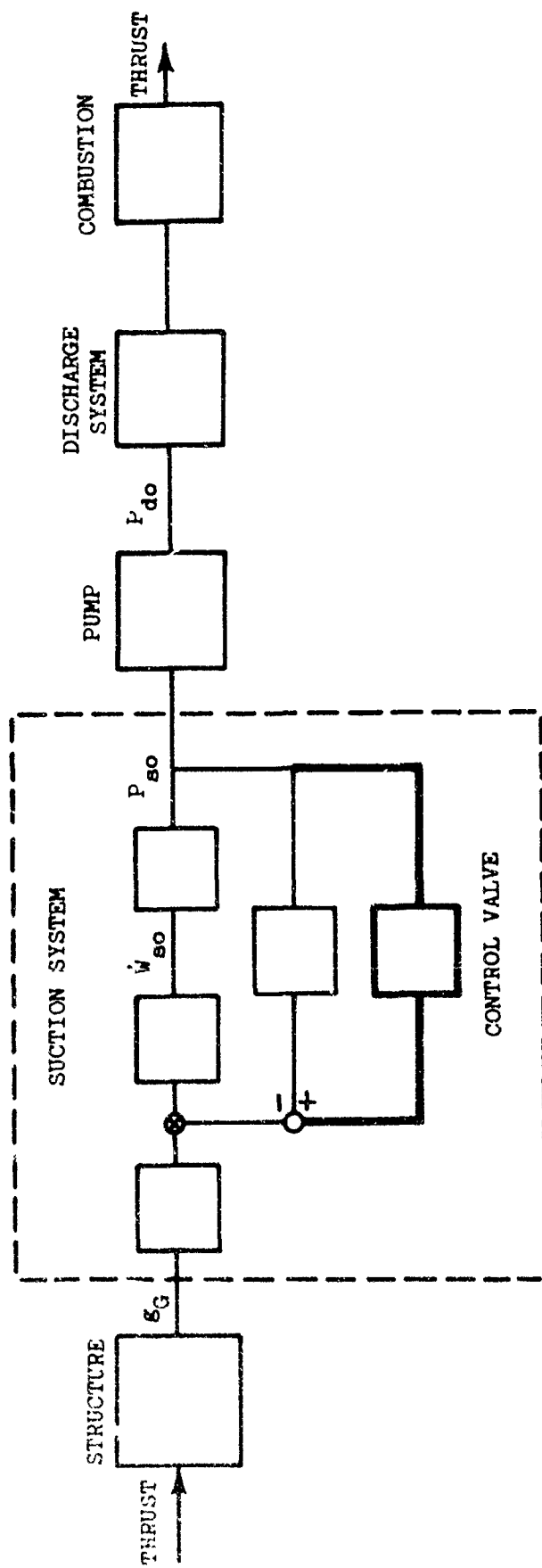
Figure 1 Oxidizer System Block Diagram

2.   MATHEMATICAL DEVELOPMENT

The equations describing the dynamic operation of a butterfly valve were derived and initially combined with the discharge line equation for discharge flow modulation.

a.   Discharge System - From the development presented in Appendix II, the pressure upstream of a valve (P_{10}) is related to the downstream pressure (P_{20}), steady state flow rate $(\dot{W}_v)$, steady state flow coefficient (C_v), oscillatory flow rate $(\dot{W}_{vo})$, and oscillatory flow coefficient (C_{vo}) by:

$$P_{10} - P_{20} = 2\dot{W}_v \left(\frac{C_o}{C_v}\right)^2 \left[\dot{W}_{vo} - \dot{W}_v\left(\frac{C_{vo}}{C_v}\right)\right] \tag{1}$$

where C_o is a constant allowing for different fluid specific gravities. From Appendix I the equation relating oxidizer discharge pressure, flow rate, and impedance is:

$$P_{do} - P_c = I_d \ddot{W}_{do} + R_d \dot{W}_{do} \tag{2}$$

Where: P_{do} is the oscillatory discharge pressure

P_c is the oscillatory combustion chamber pressure

I_d is the discharge line inertance

R_d is the discharge system resistance

$\dot{W}_{do}$ is the oscillatory discharge flow rate

Upon adding the valve pressure drop (Equation 1) to the inertive and resistive pressure drops of the discharge system, Equation 2 becomes:

$$P_{do} - P_c = 1_d \ddot{W}_{do} + R_d \dot{W}_{do} + 2\dot{W}_v \left(\frac{C_o}{C_v}\right)^2 \dot{W}_{do} - 2\dot{W}_v^{\ 2} \left(\frac{C_o}{C_v}\right)^2 \frac{C_{vo}}{C_v} \qquad (3)$$

The above relationship then describes the behavior of the oxidizer discharge system containing an active valve element. A similar relationship exists for the fuel discharge system.

    b.   Suction System - Equation 1 was subsequently combined with the suction system equation as described in Appendix II. Repeated here the resulting functional relationship is:

$$I_{so} \ddot{W}_{so} + 2 \zeta_{so} \omega_{so} I_{so} \dot{W}_{so} + 2\dot{W}_v \left(\frac{C_o}{C_v}\right)^2 \dot{W}_{so} = (L_{so} g_{so} + L_{To} g_{To})$$

$$- P_{so} + \left[2 \zeta_{so} W_{so} \rho_o L_{so} \frac{1}{gc} + 2\dot{W}_v \left(\frac{C_o}{C_v}\right)^{2-} \rho_o A_{so} \right]$$

$$\left[\dot{q}_p + g_c (1 + h_{tf}) \cdot (\dot{Q}_A + \dot{Q}_B) \right] + 2\dot{W}_v^{\ 2} \left(\frac{C_o}{C_v}\right)^2 \frac{C_{ov}}{C_v} \qquad (4)$$

Where: I_{so} is the suction line inertance

          ζ_{so} is the suction line damping ratio

          ω_{so} is the suction line natural frequency

          $\dot{W}_v$ is the steady state suction flow rate

          C_v is the steady state valve flow coefficient

          L_{so} is the suction line length

          g_{so} is the absolute acceleration of the suction line

          L_{To} is the height of propellant in oxidizer tank

g_{To} is the absolute acceleration of the propellant in the oxidizer tank

P_{so} is the oscillatory suction pressure

ρ_o is the oxidizer density

A_{so} is the cross sectional area of the suction line

$\dot{g}_p$ is the pump velocity relative to the gimbal point

h_{tf} is the tank bottom modal amplitude ratio

$\dot{Q}_A$ and $\dot{Q}_B$ are respectively the first and second mode gimbal velocity.

C_{ov} is the oscillatory valve flow coefficient which is a function of blade angle.

    c.   Valve and Suction System Characteristics - As discussed in Appendix II the steady state valve flow coefficient (C_v) and the oscillatory flow coefficient (C_{vo}) will be a function of the steady state butterfly position. Figure 2 shows the variation of both steady state and oscillatory flow coefficients as a function of blade angle for a typical butterfly valve used in this investigation. The steady state blade angle was chosen as 60 degrees. When Equation (4) is combined with equations of Appendix I and valve control loop added, the suction system equation upon taking the Laplace transform becomes:

$$P_{so}\left[\frac{1}{I_{so}\omega_{so}} + \frac{M_o + 1}{(Z_{do} + K_{co} + R_{po})S}\right]\left(I_{so}S^2 + 2\zeta_{so}\omega_{so}S + C_{10}S\right)$$

$$+ P_{so} - C_{10}\dot{W}_{vo}C_\theta\left(\frac{10}{S^2 + 2\zeta_v\omega_v S + \omega_v^2}\right)\left(\frac{A_{GO}}{M_v(1 + \tau_o S)}\right) = \quad (5)$$

$$\rho_o g_G (L_{so} + L_{To}) + \frac{1}{S}\left(2\zeta_{so}\omega_{so}\rho_o L_{so} \cdot \frac{1}{g_c} + C_{10} \, o^\wedge_{so}\right)g_G \cdot 2g_c$$
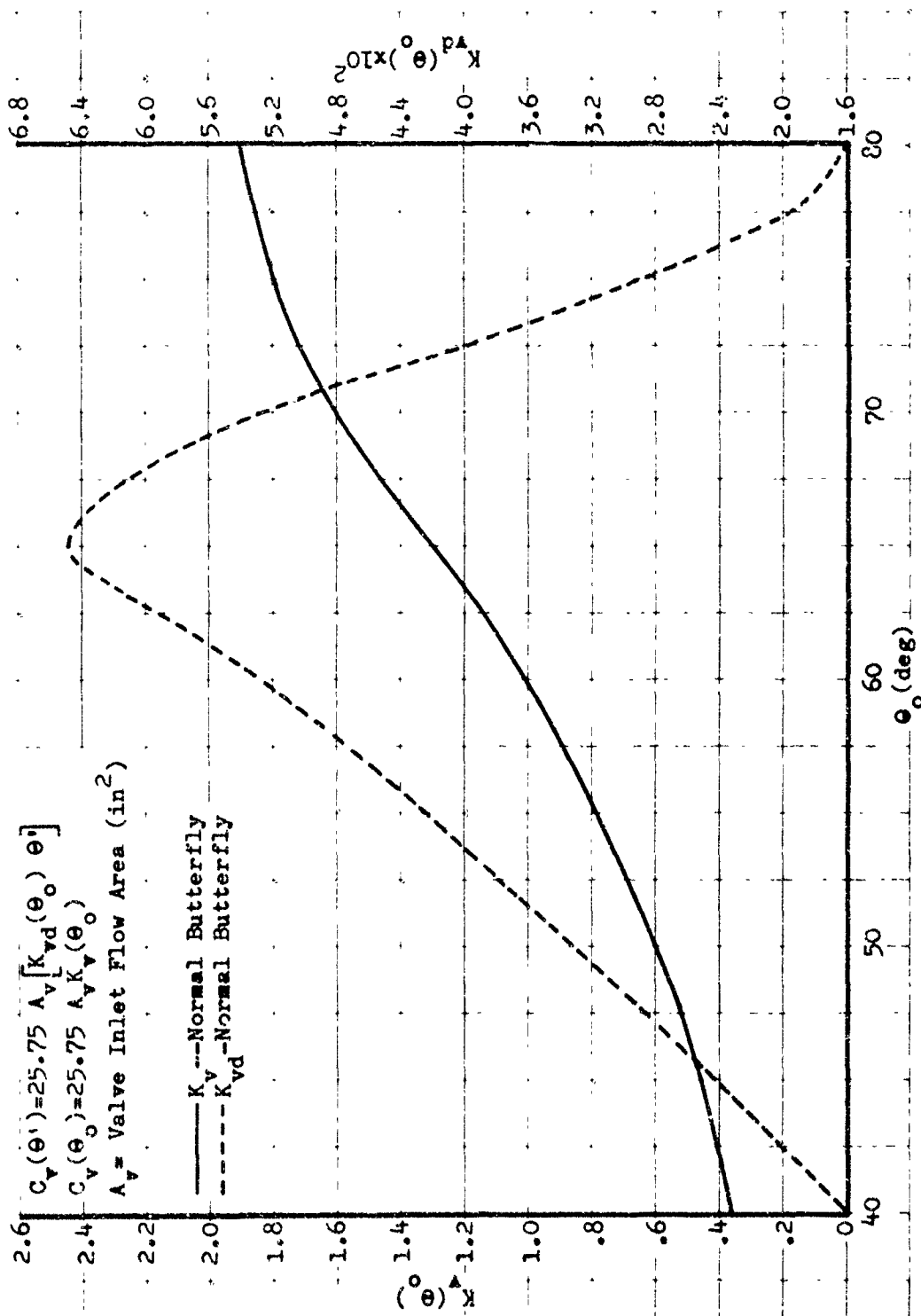
Figure 2   Mason-Neilan Butterfly Valve Flow Characteristics Cat. No.307 1/64

11

Where: C_{10} is the steady state flow coefficient.

$\dot{W}_{vo}$ is the steady state flow rate

C_Θ is the oscillatory flow coefficient $= 2\dot{W}_v^2 \dfrac{C_o}{C_v}^2$

ω_v is the natural frequency of the control system

ζ_v is the damping ratio for the control system

M_v is the effective control system mass

A_{Go} is the control loop gain

τ_o is the control loop time constant

The fuel suction system equation corresponding to Equation (5) is:

$$P_{sf}\left[\frac{1}{I_{sf}\omega_{sf}} + \frac{M_f + 1}{(Z_{df} + K_{cf} + R_{pf})S}\right](I_{sf}S^2 + 2\zeta_{sf}\omega_{sf}I_{sf}S + C_{1f}S)$$

$$+ P_{sf} - C_{1f}\dot{W}_{vf}C_\Theta\left(\frac{10}{S^2 + 2\zeta_v\omega_v S + \omega_v^2}\right)\left(\frac{A_{Gf}}{M_v(1 + \tau_f S)}\right) \quad (6)$$

$$= \rho_f g_G(L_{sf} + L_{Tf}) + \frac{1}{S}(2\zeta_{sf}\omega_{sf}\rho_f L_{sf} \cdot \frac{1}{g_c} + C_{1f}\tau_f A_{sf})g_G \cdot 2g_c$$

The fuel and oxidizer equation defines the complete relationship between pump suction pressure, P_{so}, P_{sf}, valve flow rate, $\dot{W}_{vo}, \dot{W}_{vf}$, discharge system parameters, Z_d, K_c, R_p, and parameters affecting the control dynamics, $A_{Go}, M_v, \zeta_v, \omega_v, \tau_f$. The equations were incorporated in the complete POGO system mathematical model and programmed for stability analysis on an analog computer.

3. ANALOG COMPUTER ANALYSIS

As a first step of the analog investigation, it was necessary to evaluate the behavior of the system without the active control valves. This provided data which would serve as a basis for evaluating control system behavior.

a. Basic No-Fix System - Appendix I presents the basic uncompensated system equations which were programmed. Figure 3 displays the network coupling the various subsystems together. For evaluation of both the basic system and the active control valve, various TIII configurations were chosen corresponding to flight times of 80, 120, and 148 seconds. Figures 4, 5, and 6 illustrate for the above times the characteristics of the basic uncompensated system in terms of Nyquist plots. The system loop has been opened at thrust T, and the Nyquist plots are for the gain and phase of the quantity T_{out}/T_{in} (Reference Figure 3). Although the three figures show the uncompensated system to be stable (encirclement of the +1 zero Phase gain indicates an unstable condition) the overall system gains are sufficient to demonstrate any stabilizing effects produced with the control valves.

b. System with Control Loop - The system equations used for the control valve simulation were those given in Appendix I with the exception of the suction line equations. The suction line equations were replaced with Equations (5) and (6) above. Before proceeding with evaluation of the compensation devices, it was necessary to determine values for the control loop gains, A_{Go} and A_{Gf}, which would produce stabilization. To accomplish this task, the oxidizer and fuel systems were considered separately without the influence of pump dynamics. Referring to Appendix I, the fuel and oxidizer systems are decoupled by replacing P_c with P_{co} in the oxidizer equations and P_c with P_{cf} in the fuel equations. Upon taking the Laplace transform of the system of equations, the following transfer functions can be written.

13
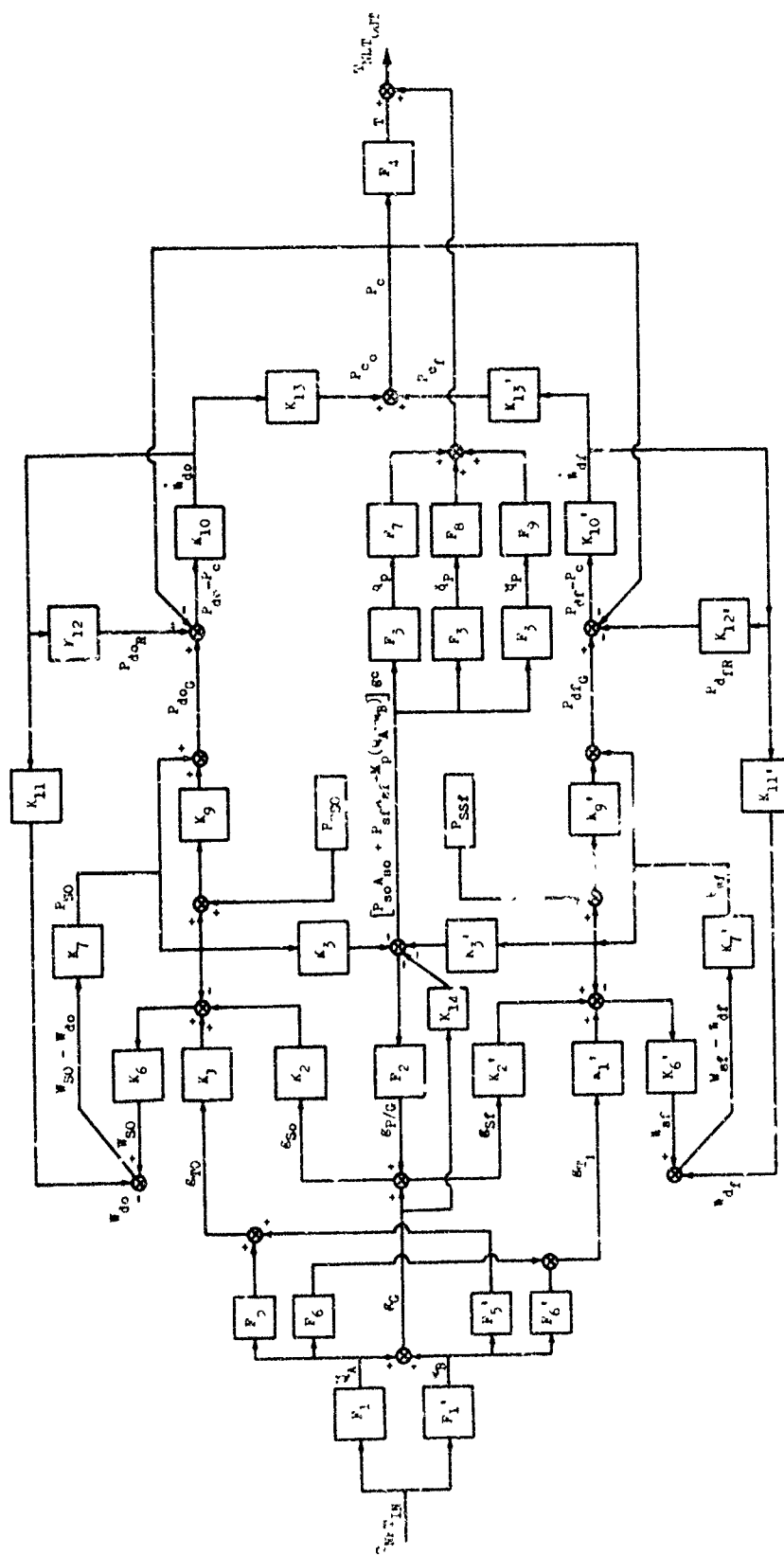
Figure 3 Basic No-Fix Schematic Diagram

14

Figure 4 Active Control Valve Study 80 Sec Analog Data

Nyquist Stability Plots - Mode 1
No Fix

Nyquist Stability Plot – Mode 1
No Fix

Active Control Valve Study 120 Sec Analog Data

Figure 5

Nyquist Stability Plot - Mode 1
Nc Fix

Figure 6 Active Control Valve Study 146 Sec Analog Data
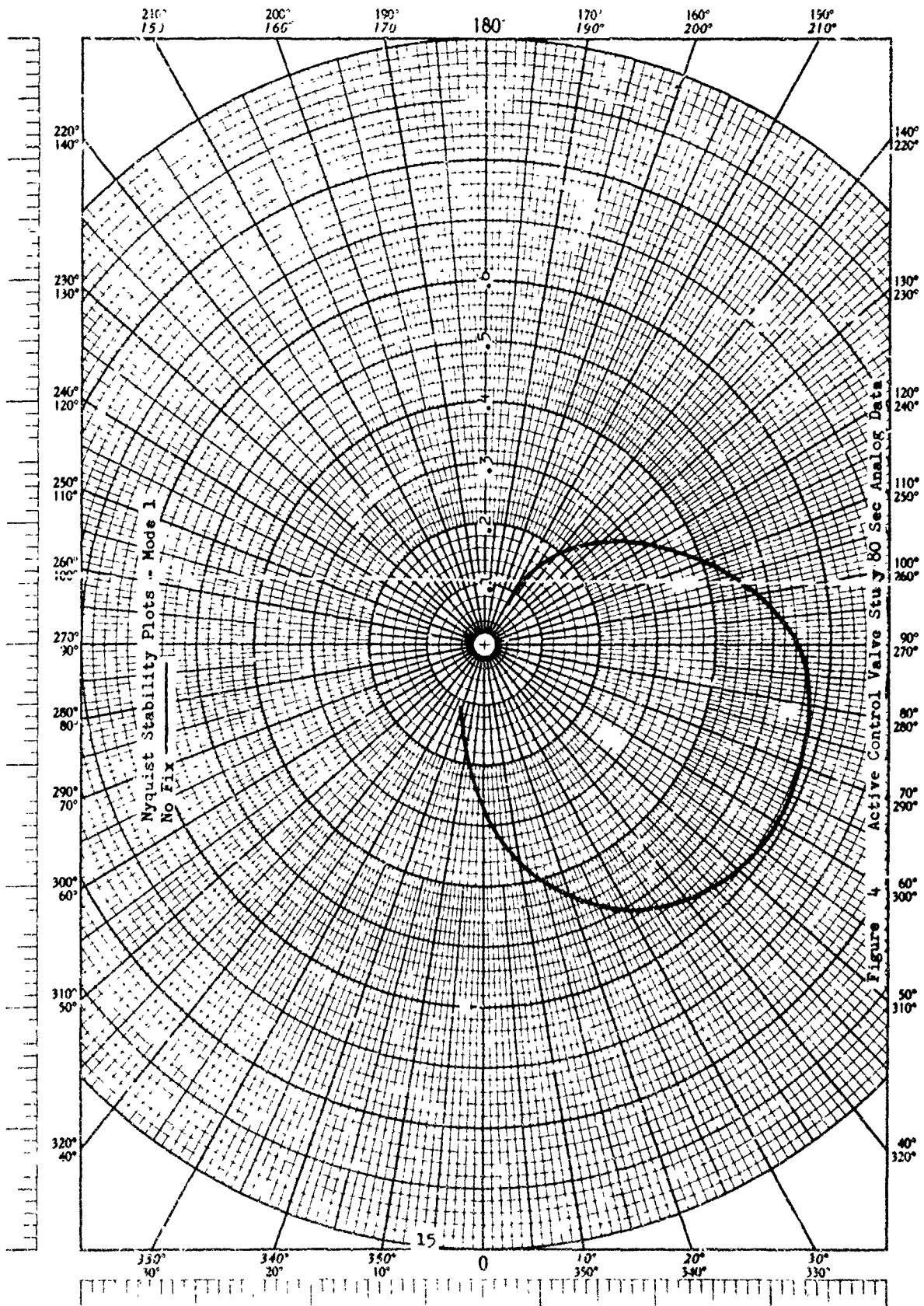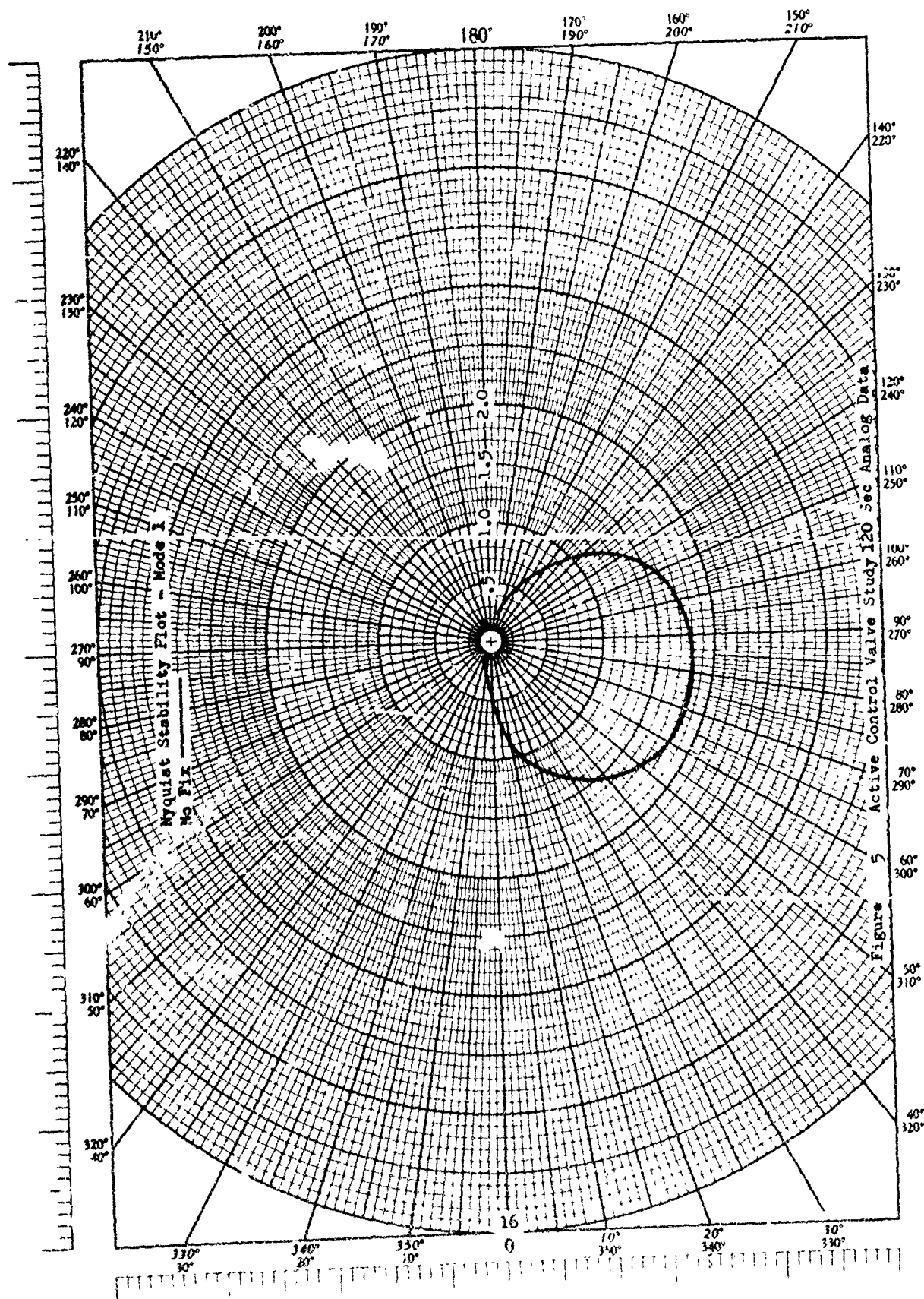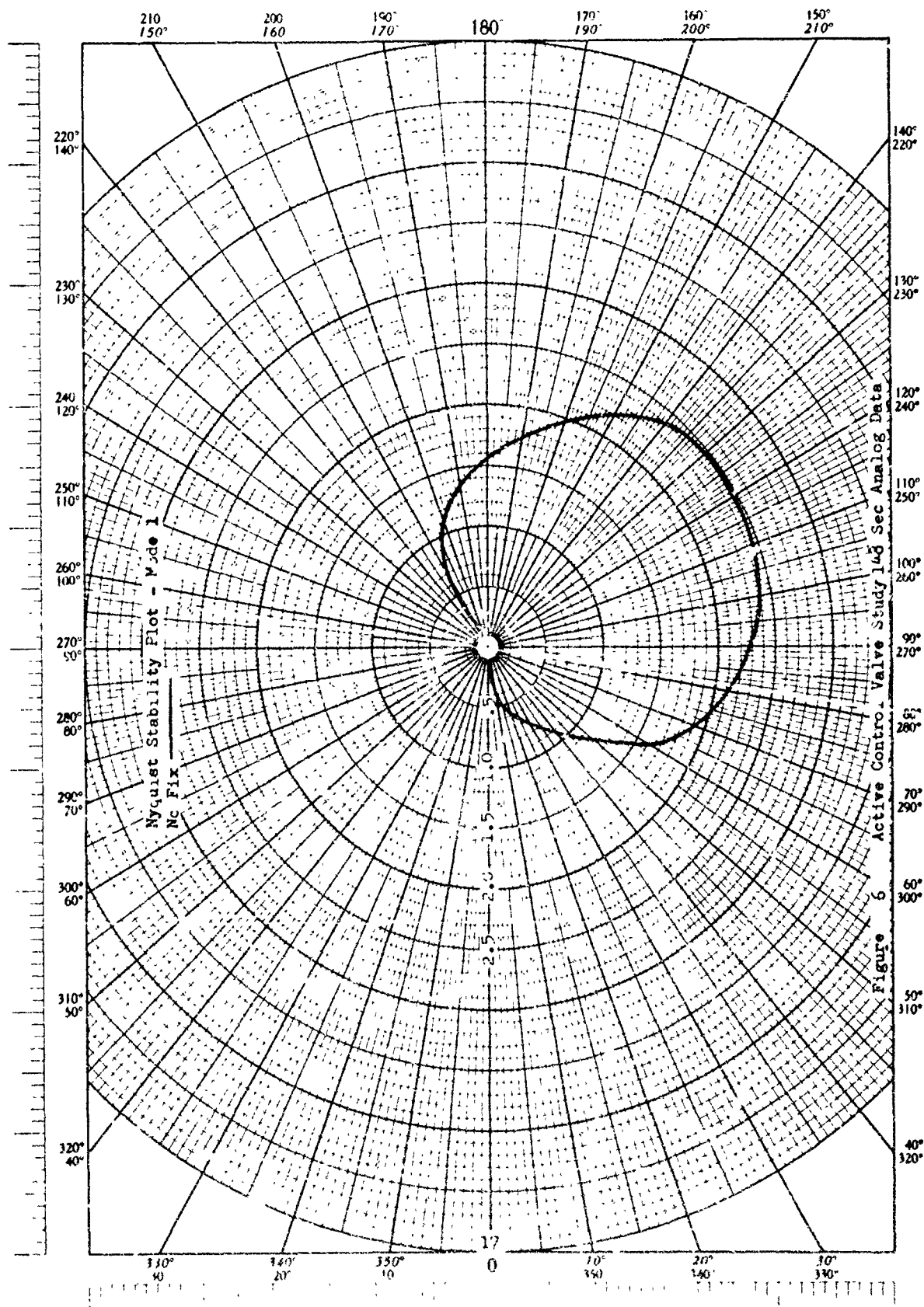
OXIDIZER		FUEL	
$(\ddot{Q}_A + \ddot{Q}_B)/T_{in}$		$(\ddot{Q}_A + \ddot{Q}_B)/T_{ir}$	(7a, b)
$P_{so}/(\ddot{Q}_A + \ddot{Q}_B)$		$P_{sf}/(\ddot{Q}_A + \ddot{Q}_B)$	(8a, b)
$\dot{W}_{do}/P_{so}$		$\dot{W}_{df}/P_{sf}$	(9a, b)
$P_{co}/\dot{W}_{do}$		$P_{cf}/\dot{W}_{df}$	(10a, b)
T_{out}/P_{co}		T_{out}/P_{cf}	(11a, b)

Combining expressions (7) through (11) will yield the open loop
transfer functions.

$$(T_{out}/T_{in})_{ox} \qquad\qquad (T_{out}/T_{in})_{fuel} \qquad (12a, b)$$

Substitution of the appropriate flight time parameters produces
the following forms:

OXIDIZER SYSTEM

80 Seconds: $\omega = 69$ Radians/Second

$$\frac{T_{out}}{T_{in}} = \frac{(6580. + j860.)}{14170. - 10800. + \dfrac{281.5A_{Go} + j43.6A_{Go}}{1 + j69\tau_o}} \qquad (13)$$

120 Seconds: $\omega = 81$ Radians/Second

$$\frac{T_{out}}{T_{in}} = \frac{15950. - j6315.}{20970. - j16910. + \dfrac{395A_{Go} + j72.2A_{Go}}{1 + j81\tau_o}} \qquad (14)$$

18

148 Seconds: $\omega = 104$ Radians/Second

$$\frac{T_{out}}{T_{in}} = \frac{14150. - j4300.}{6600. - j15350. + \dfrac{690A_{Go} + j162A_{Go}}{1 + j104\tau_o}} \tag{15}$$

FUEL SYSTEM

80 Seconds: $\omega =$ Radians/Second

$$\frac{T_{out}}{T_{in}} = \frac{-1760. + j1365}{-20800. - j17650. + \dfrac{389.A_{Gf} + j257A_{Gf}}{1 + j69\tau_f}} \tag{16}$$

120 Seconds: $\omega = 81$ Radians/Second

$$\frac{T_{out}}{T_{in}} = \frac{2800 - j1485}{-1950 - j20680 + \dfrac{560A_{Gf} + j425A_{Gf}}{1 + j81\tau_f}} \tag{17}$$

148 Seconds: $\omega = 104$ Radians/Second

$$\frac{T_{out}}{T_{in}} = \frac{2280 - j1165}{7500 - j20660 + \dfrac{980A_{Gf} + j960A_{Gf}}{1 + j104\tau_f}} \tag{18}$$

An examination of Equations (13) through (15) indicates that certain values of both positive and negative control gains will reduce the oxidizer T_{out}/T_{in} functions. Smaller positive control gains for A_{Go} however will accomplish a greater total system gain reduction than will negative control gains. Based on these results oxidizer control loop gains (A_{Go}) of +50 and +100 were selected for the initial analog analysis.

Considering the fuel system, Equations (16) through

19

(18) again indicate overall system gain reductions can be accomplished with either positive or negative control gains. In this case, however, negative values are more desirable than positive. Hence, fuel control gains of -50 and -100 were selected for initial examination.

At this point, the question should be raised as to what system characteristics necessitate gains of opposite sign in the fuel and oxidizer control loops. The answer is found through an examination of the suction system pressure-flow rate relationships. At a frequency corresponding to the resonant frequency of the first structural mode, the oxidizer pressure and flow rate are in phase. Thus, with a positive control gain, an increasing pressure drives the valve closed, which in turn reduces the amplitude of the flow rate. The fuel suction pressure and flow rate, however, are approximately 180 degrees out of phase at the structural first mode frequency. Thus, if the flow rate amplitude is to be reduced, a negative gain is required.

The dependence of control gain on ratio of suction line to structural frequency represents an undesirable characteristic of the control system. If either the fuel or oxidizer suction line frequencies crossed over the structural frequency during flight, a change in sign on the control gain would be required. Several solutions to this problem exist and will be discussed in later paragraphs.

4.   ANALOG ANALYSIS RESULTS

The analog data was reduced to the form of Nyquist plots which are shown in Figures 7 through 12.

a.   Oxidizer Fix with no Time Lags - Figures 7, 8, and 9 show the effect of an oxidizer valve alone on system response for flight times of 80, 120, and 148 seconds respectively. The control loop in these cases is characterized by a gain (A_{Go}) of +50 and zero time lag. Compared with the no-fix Nyquist plots, it is observed that the oxidizer valve produces significant changes in gain for both the 80 second and 120 second cases. Specifically at 80 seconds, the zero phase gain is reduced from .27 to .12; and at 120 seconds, the gain is reduced from .55 to .40. At 148 seconds, the oxidizer valve produces little effect on system response. This weak influence can be explained in terms of the reduced coupling between the oxidizer

Nyquist Stability Plot - Mode 1
No Fix —————
With Oxidizer Valve ($A_{go} = +50$, $Tau_o = 0$) ——————
With Oxidizer Valve and Fuel Valve
($A_{go} = +50$, $Tau_o = 0$, $A_{gf} = -50$, $Tau_f = 0$) ——————

Figure 7   Active Control Valve Study 80 Sec Analog Data

Nyquist Stability Plot

No Fix —— • × —
With Oxidizer Valve ($\lambda_{go} = +50$, $Tau_o = 0$) ————
With Oxidizer Valve and Fuel Valve
($\lambda_{go} = +50$, $Tau_o = 0$, $\lambda_{gf} = -50$, $Tau_f = 0$) —·—·—

Figure 8   Active Control Valve Study 120 Sec Analog Data

Nyquist Stability Plot – Mode 1
No Fix
with Oxidizer Valve (A_{go} = +5C, Tau_o = 0)

Figure 9   Active Control Valve Study 1.3 Sec Analog Data

Nyquist Stability Plot — Mode 1

No Fix ─────────
With Oxidizer Valve ($A_{go} = +50$, $Tau_o = 0$) ─────
With Oxidizer Valve ($A_{go} = +50$, $Tau_o = .0179$)
With Oxidizer Valve ($A_{go} = +50$, $Tau_o = .0358$)

Figure 10   Active Control Valve Study   80 Sec Analog Data
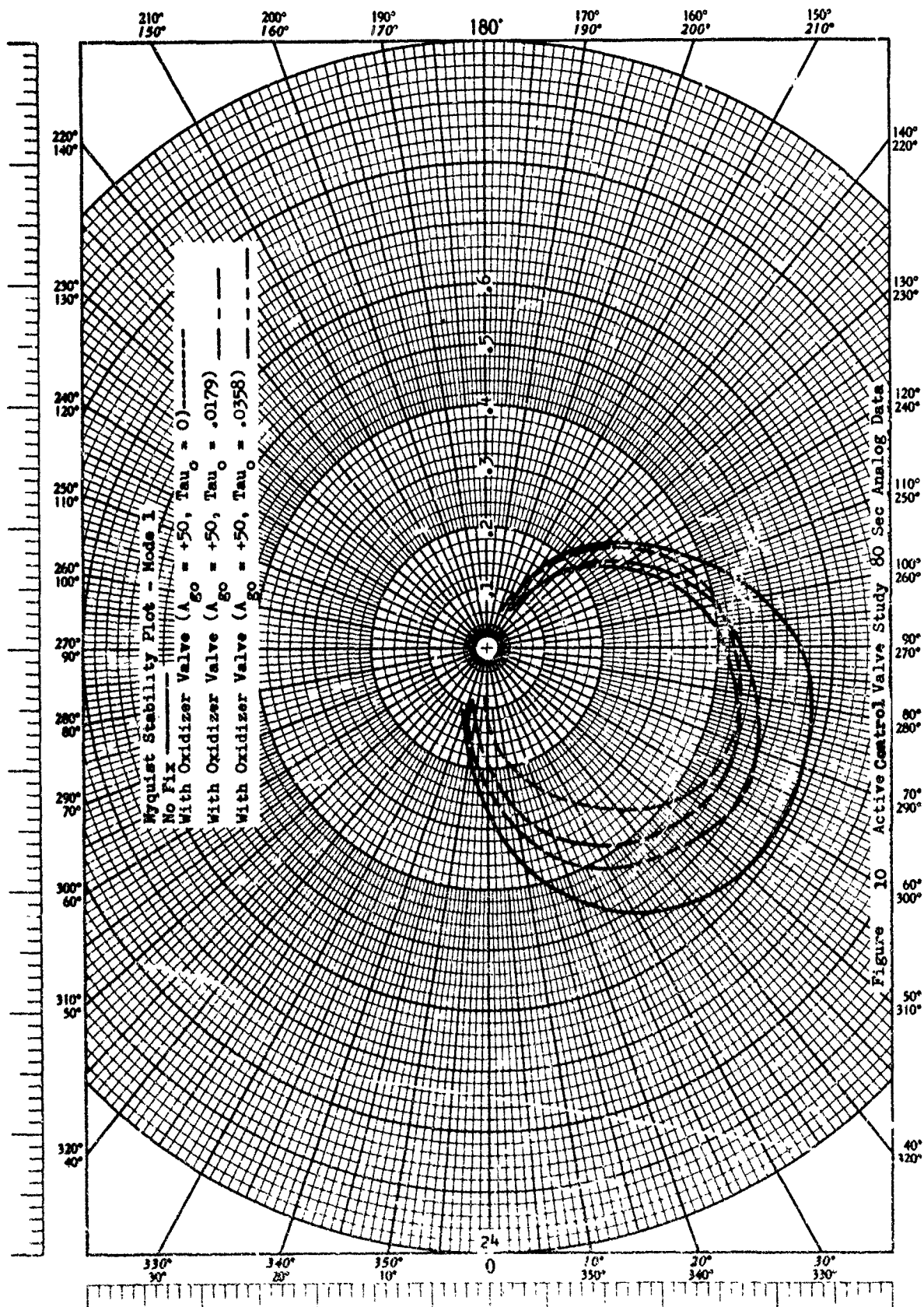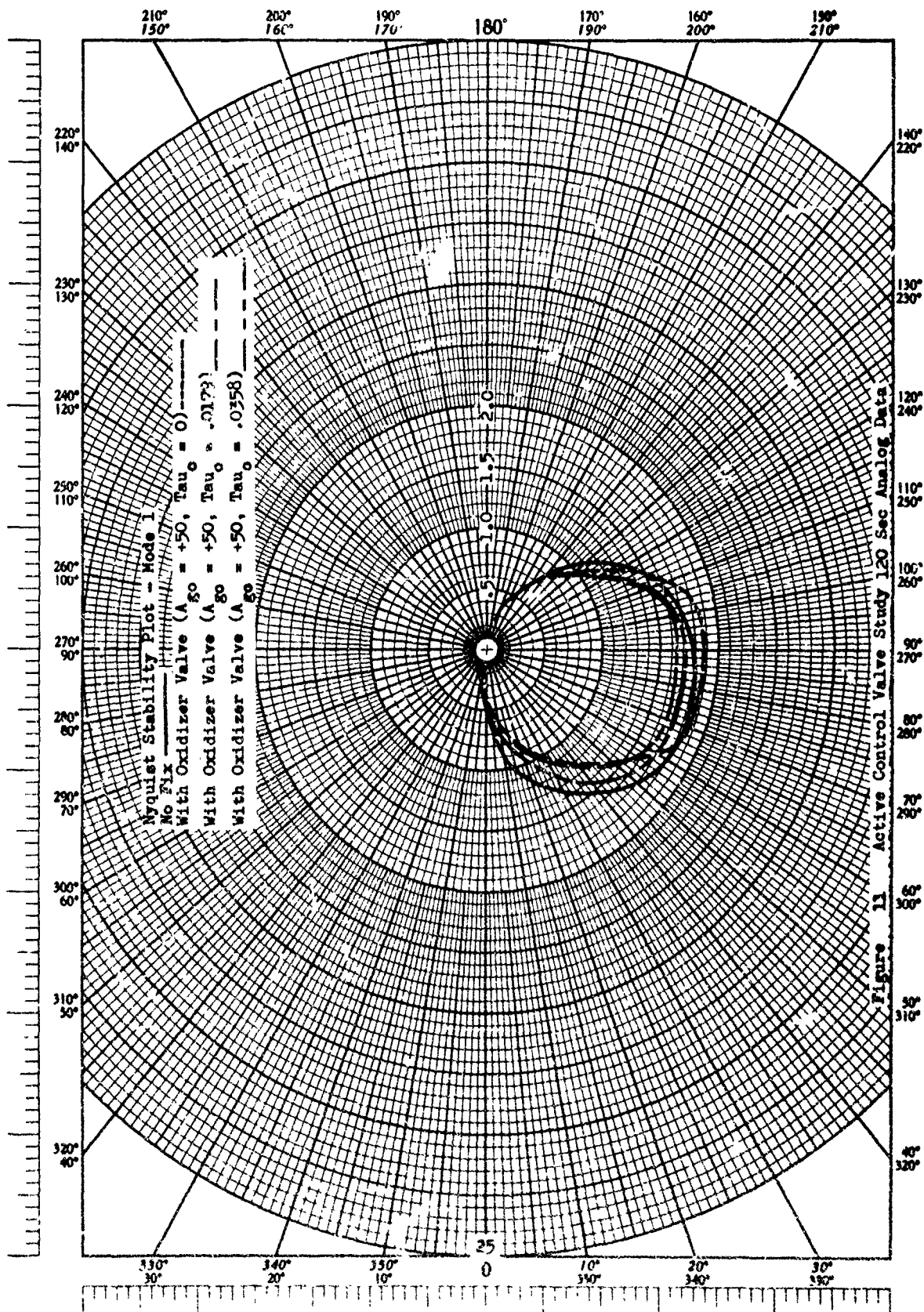
Figure 11. Active Control Valve Study 120 Sec Analog Data

Nyquist Stability Plot — Mode 1

No Fix ——————
With Oxidizer Valve (A_{go} = +50, Tau$_o$ = 0) ——————
With Oxidizer Valve (A_{go} = +50, Tau$_o$ = .0179) ——————
With Oxidizer Valve (A_{go} = +50, Tau$_o$ = .0358) ——————

Nyquist Stability Plot - Mode 1
No Fix
With Oxidizer Valve (A_{go} = +50, Tau_o = 0) ————
With Oxidizer Valve And Fuel Valve
(A_{go} = +50, Tau_o =0, A_{gf} =-50, Tau_f =0) ————

Figure 12   Active Control Valve Study 148 Sec Analog Data
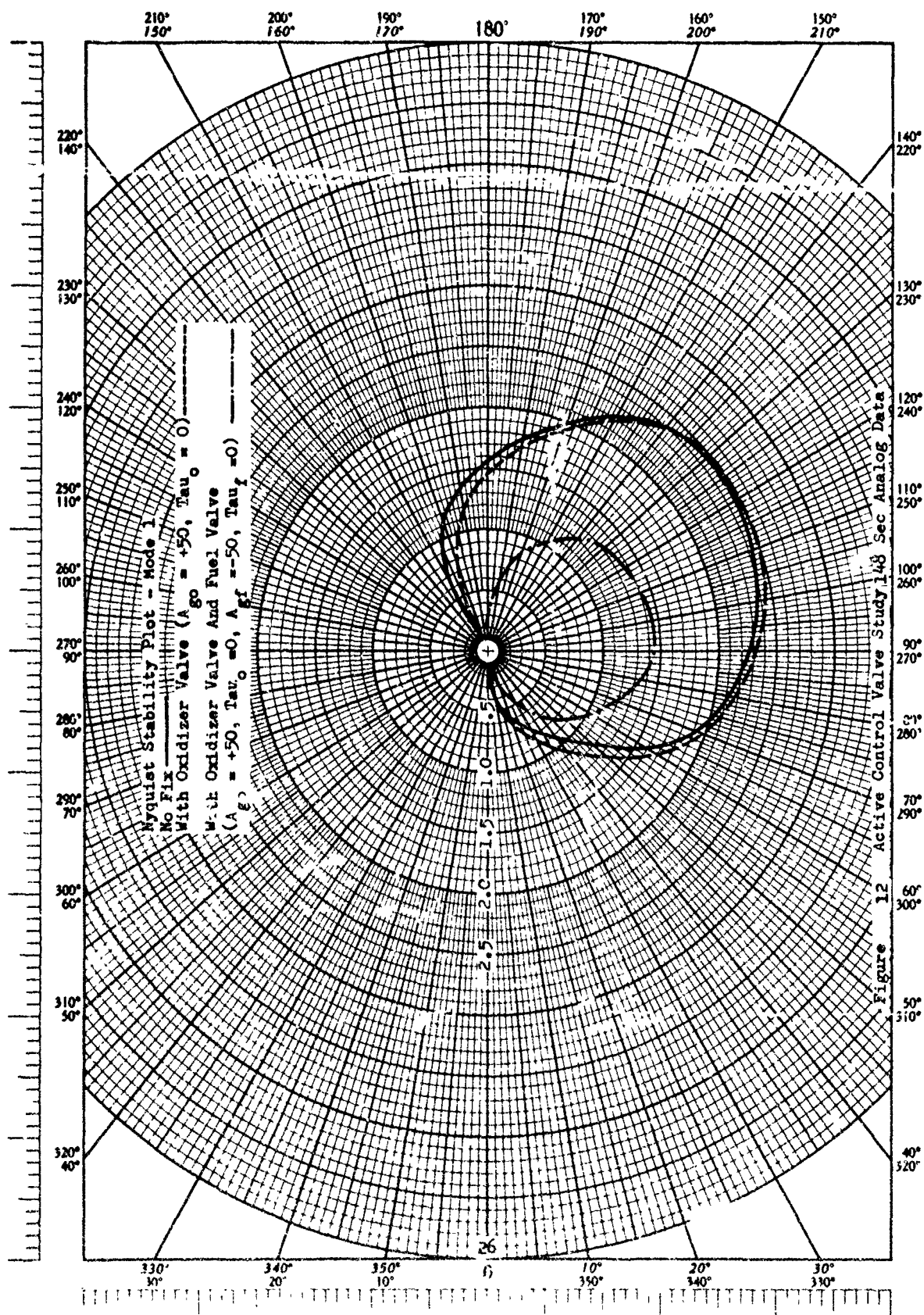
system and structure. The strongest coupling at 148 seconds
exists between the fuel suction system and structure.

b. Oxidizer Fix with Time Lags - Time lags added to the
oxidizer control loop alter the Nyquist plots to those shown
in Figures 10 and 11 from 80 to 120 seconds respectively.
In all cases the time lags tend to reduce the gain margin im-
provements achieved with the active valve. For a flight time of
148 seconds, time lags produced little effect on the Nyquist
plots; again, due to the weak coupling of oxidizer and structure
systems.

c. Oxidizer and Fuel Fix - Addition of the fuel control
valve to the system produced the most significant changes at
120 and 148 seconds. At 80 seconds, the coupling between the
fuel system and structure is quite weak; hence, as in the case
of the oxidizer system at 148 seconds, the fuel control loop
is relatively ineffective. The performance of the fuel fix
can be assessed from the Nyquist plots of Figures 7, 8 and 12.

d. System Instabilities - During the analog analysis, a
number of unexpected results were encountered. For example,
divergence of the open loop system response occurred when an
oxidizer control loop gain of +100 was used. The second
problem arose while attempting to evaluate the effect of time
lags in the fuel control loop. In this case, a diverging
oscillation appeared in the system. Both of these instabili-
ties can generally be associated with an unstable internal
system loop. The only candidates in this case were the control
loops themselves. In order to determine the particular elements
in the control system which led to the observed instabilities
a root locus analysis was initiated utilizing an existing
digital computer program. The details and results of this
analysis are presented in the following section:

5. DIGITAL COMPUTER ANALYSIS

The analysis of the observed control loop instabilities
was performed using the Martin Marietta Corporation's Root
Locus Program QD 030. The decoupled fuel and oxidizer P_s/g_G
transfer functions provide all the functional relationships
necessary for the investigation.

a. Digital Equations - Referring to Figure 13 below
the decoupled P_s/g_G transfer function describing the suction

system containing an active control valve is expressed as:

$$P_s/g_G = \frac{G_1}{\frac{1}{G_2 G_3} - G_4} \tag{19}$$

where: $G_1 = \rho h$

$$G_2 = 1/\left(I_s S^2 + 2 \zeta_s \omega_s I_s S + C_{1x} S \right)$$

$$G_3 = 1/\left[\frac{1}{I_s \omega_s^2} + \frac{M+1}{(Z_d + R_p + K_c) S} \right]$$

$$G_4 = C_{1x} \dot{W}_v C_\Theta \left(\frac{A_O/M_v}{S^2 + 2 \zeta_v \omega_v S + \omega_v^2} \right) \left(\frac{10}{1 + \tau S} \right) - 1$$

In the above expressions, the parameters have been written in a general form such that the P_s/g_G function applies to both the fuel and oxidizer systems.
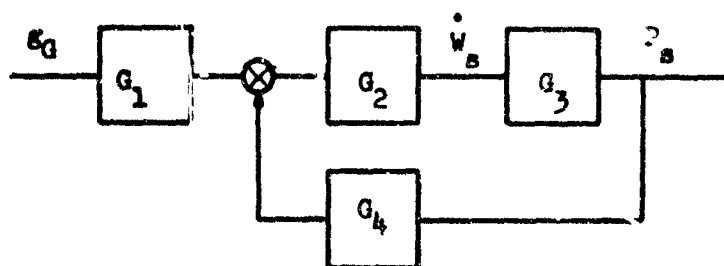
Figure 13   Suction Block Diagram

Substitution of the above expressions in Equation 19 yields a P_s/ε_G transfer function containing a sixth degree "S" polynomial in the denominator. The stability of the control valve-suction system can be established from an examination of the roots associated with the denominator polynomial. If the real parts of the roots all lie in the negative half of the "S" plane, the system will be stable. Roots lying in the positive half of the "S" plane will produce either a pure system divergence or an oscillatory instability depending on whether or not the roots contain imaginary components. A root at zero produces a metastable system.

b. Root Locus Results - Figures 14, 15, 16 and 17 present the results of the digital analysis in terms of root loci with variations in control parameters. Figure 14 demonstrates the behavior of the oxidizer side as the control gain, A_{GO}, varies from 0 to +100 ($\tau = 0$). It is observed that the system is stable up to a gain of 60.5, metastable at 60.5, and unstable for A_{GO} between 60.5 and 100 Also it will be noted that the roots for control gains of 60.5 and greater have no imaginary component. Hence, the instability will produce a pure divergence as observed during the analog analysis.

The characteristics of the oxidizer control loop are shown in Figure 15 for variations in control loop time lag τ_o. The curves indicate the system is stable for variations in τ from 0 to .050 ($A_{GO} = +50$); however, an unstable condition is approached as τ is increased beyond .050.

Figure 16 which demonstrates the behavior of the fuel system to variations in A_{Gf}, is very similar to Figure 14. For the fuel valve an A_{Gf} equal to 84.3 defines the boundary between a stable and an unstable system. Finally, the stability of the fuel side for variations in time lag is observed in Figure 17. The system is stable for $\tau = 0$; however, as τ increases up to about .035, the system is unstable. In this case, due to the imaginary components of the roots, the system will experience an oscillatory instability. Again this result is confirmed by the analog analysis. The data also shows that stability is regained for time lags between .035 and .050.

c. Valve Effects on Suction System - In addition to defining regions of stability for the system, the root locus
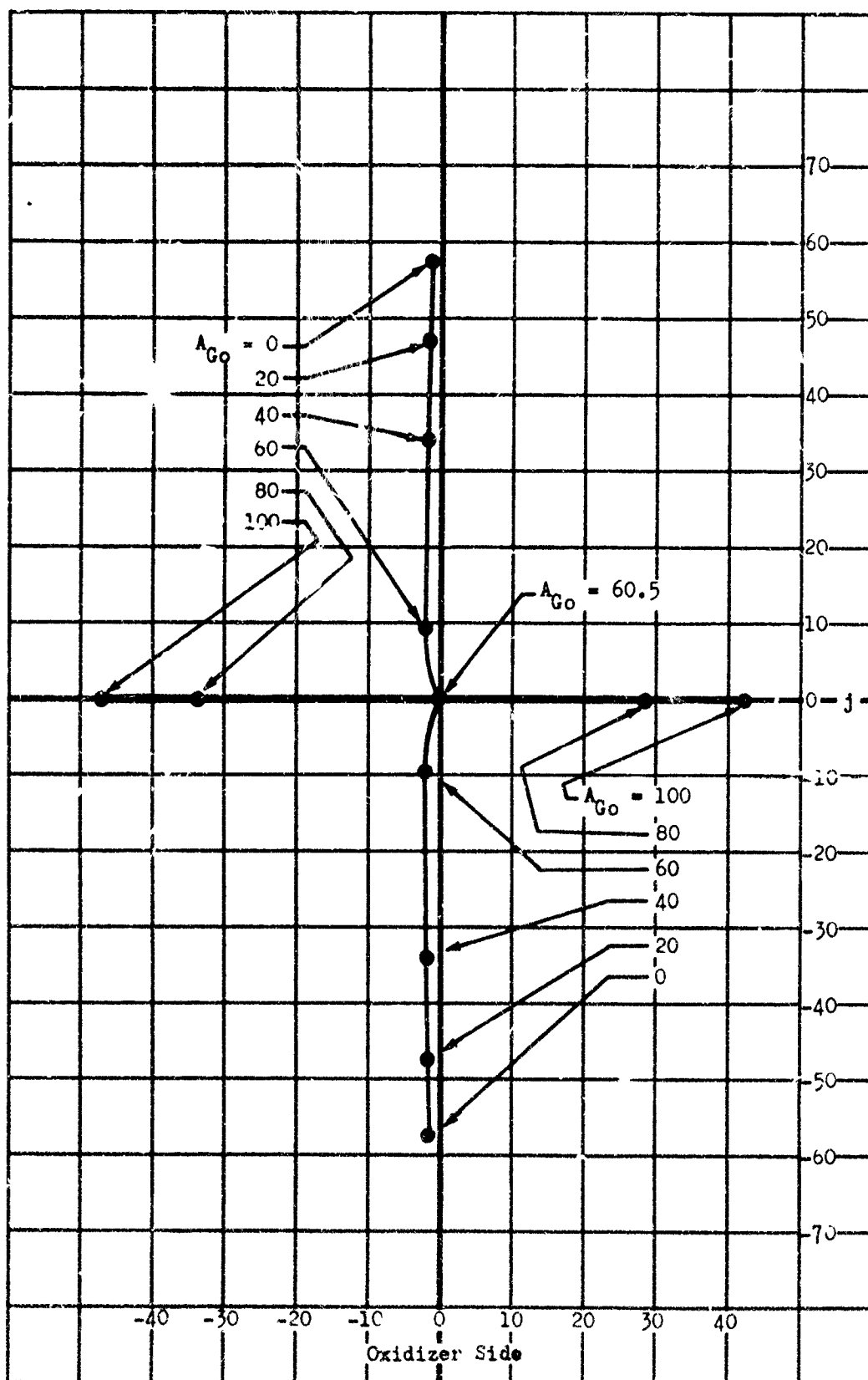
Figure 14 P_g/g_a Poles in S" Plane - $\tau = 0$
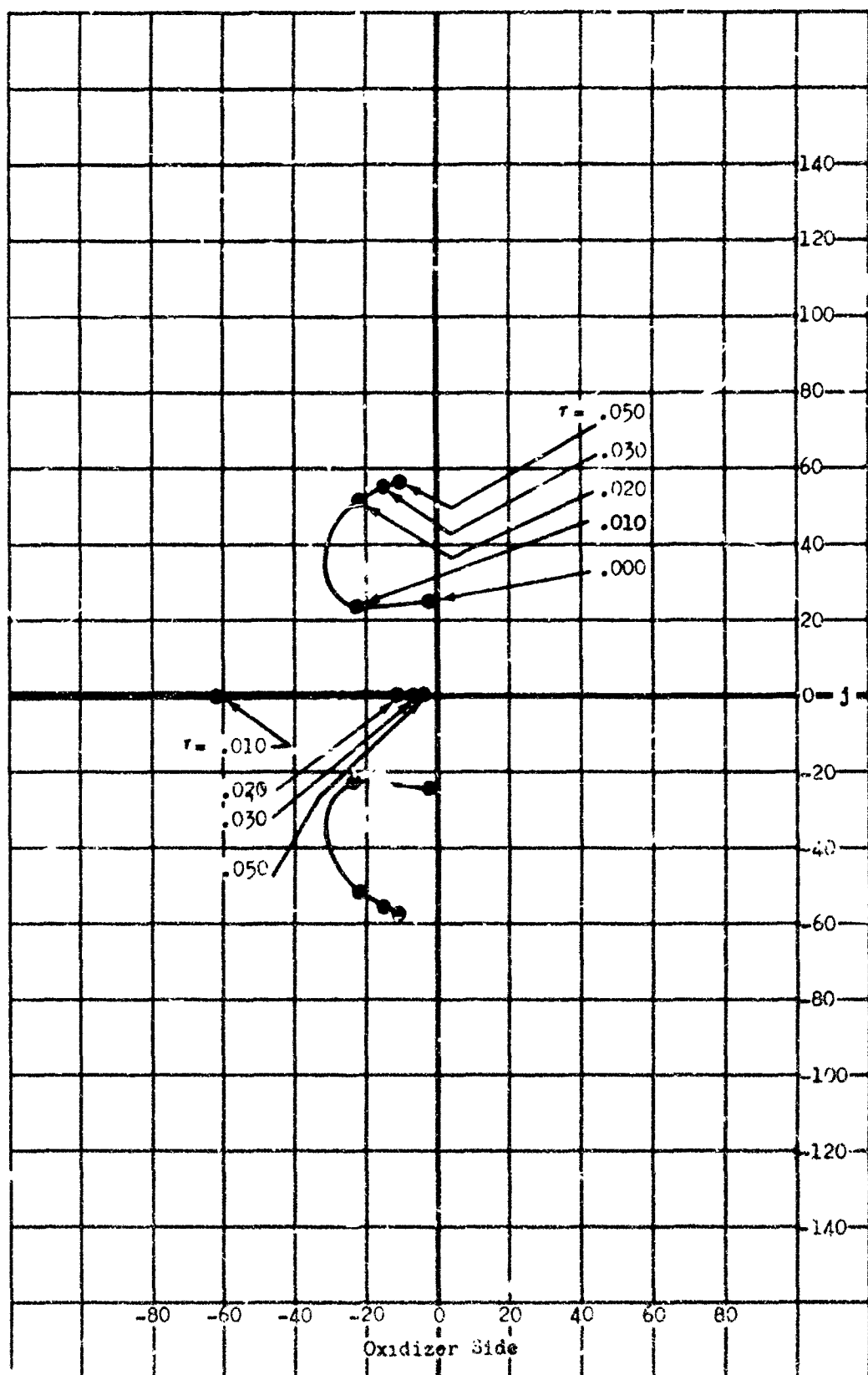
Figure 15 P_s/g_a Poles in S" Plane - A_{GO} = 50

31

Figure 16 P_g/g_G Poles in "S" Plane $- \tau = 0$

32
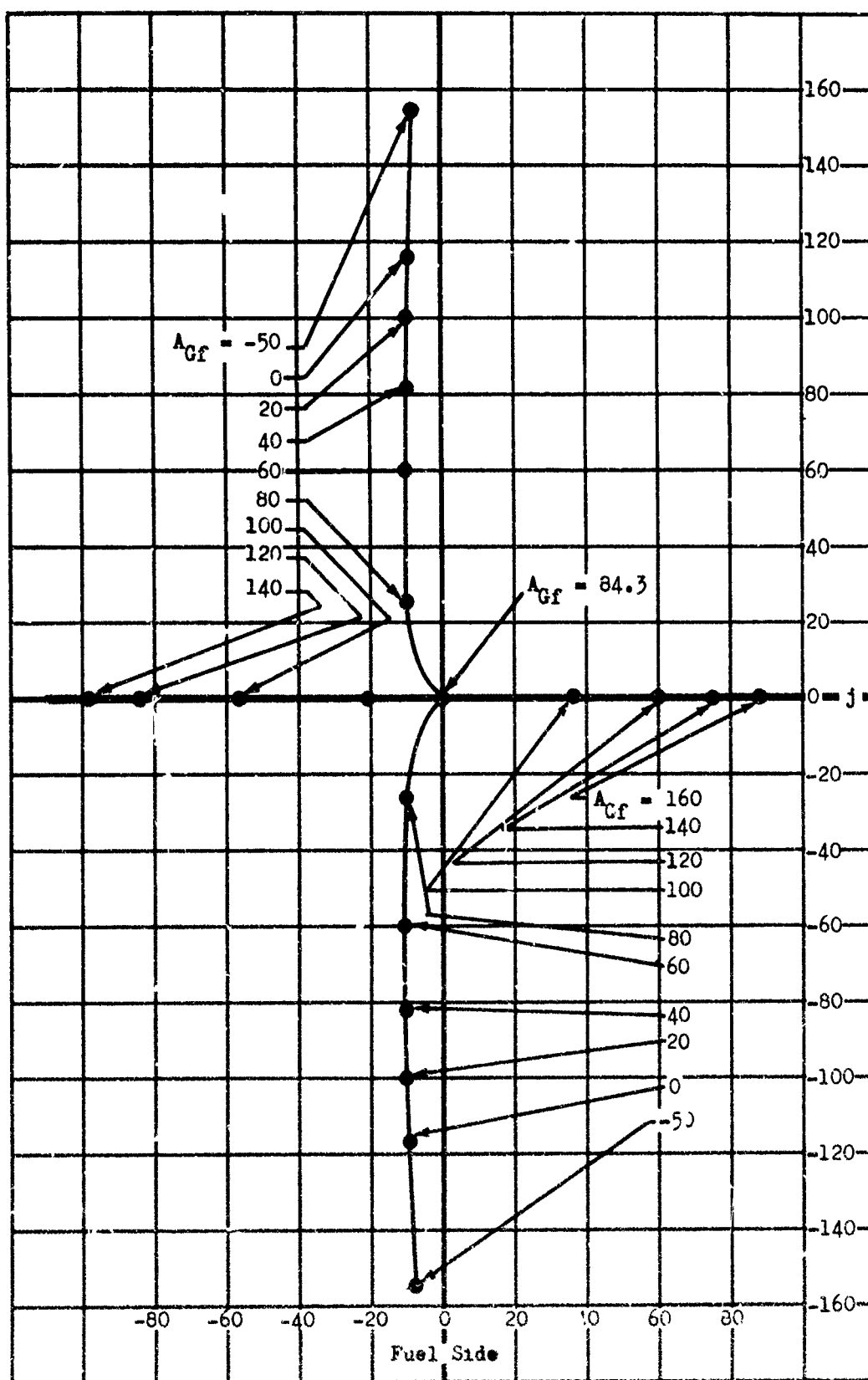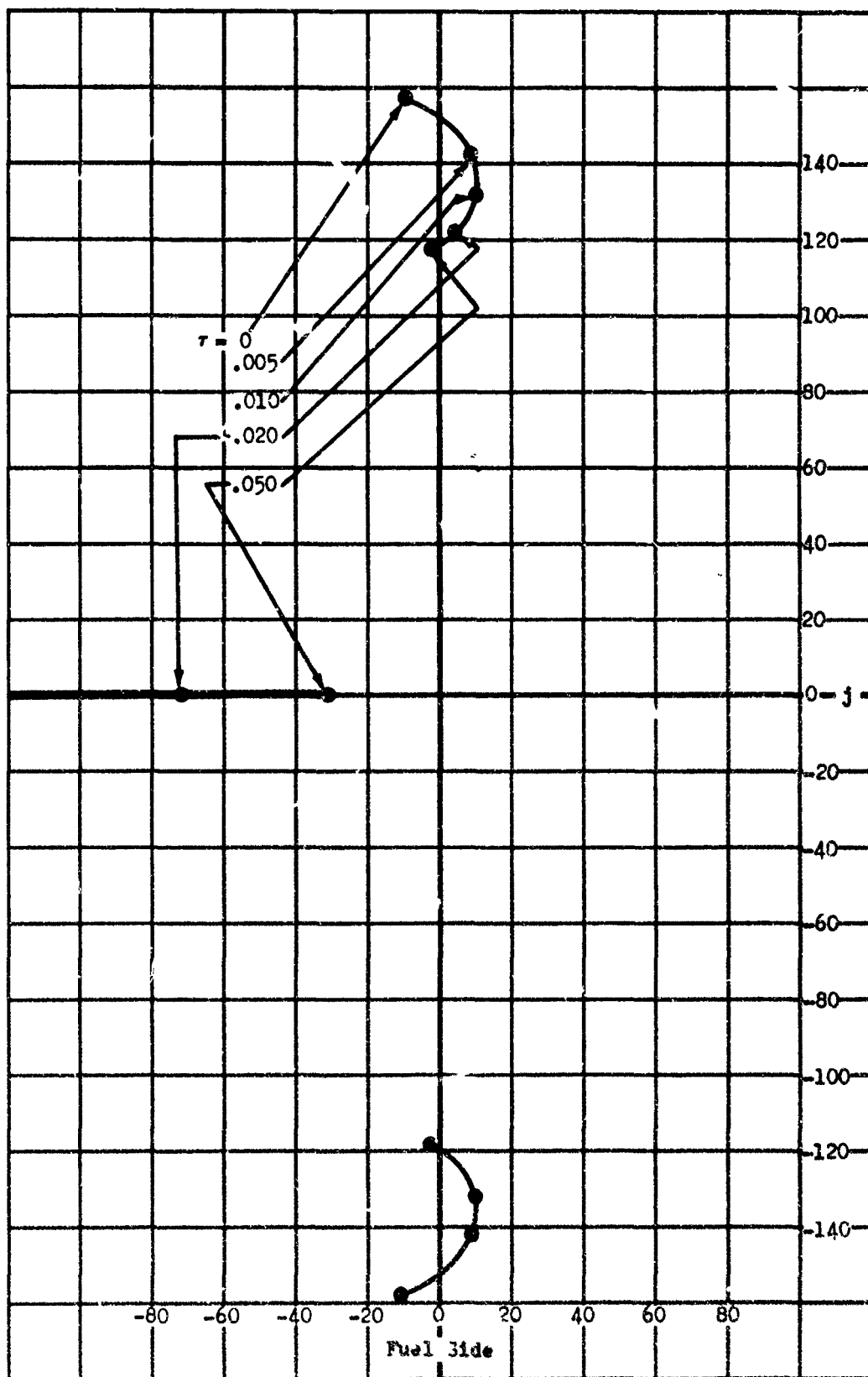
Figure 17 P_s/g_G Poles in "S" Plane – $\dot{A}_{Gf} = -50$

33

analysis demonstrates the manner in which the control valve changes the suction system response. In Figure 14, the magnitude of the imaginary root components in the negative half plane is a direct indication of suction system frequency. Thus, it is observed that increasing the oxidizer gain from zero to 60.5 degrees the suction system frequency from 9.3 to 0.0 cps. A further increase in A_{GO} introduces a negative frequency and the pure divergence which is indicated. Also apparent is the fact that suction system frequency is quite sensitive to A_{GO} for A_{GO} in the vicinity of 60. On the fuel system, the frequency decreases from 18.65 cps for $A_{Gf} = 0$ to 0.0 cps for $A_{Gf} = 84.3$. Again the sensitivity of frequency to A_{Gf} increases as the frequency approaches zero. The final observation is that increasing the control loop gain results in an increase in the suction system damping as indicated by the increasing angle between the j axis and the root vector.

It may be concluded, therefore, that gain in the control valve loop produces a change in the suction system frequency. In terms of the total system, increased stability is achieved by separation of the suction system and the structural frequencies.

The effects of time lag (τ) are indicated in Figures 15 and 17. Time lag is seen to affect P_s/g_G gain in both the fuel and oxidizer systems. In the oxidizer side, increasing τ initially increases the system stability up to $\tau = .015$; however, additional increases tend to reduce the stability margin. The opposite effects are observed on the fuel system. As τ is increased from zero, the fuel side becomes more unstable. At $\tau = .007$ a maximum in instability is indicated. For τ greater than .007, the roots move toward the region of stability and the suction system control loop ultimately becomes stable for τ greater than .035.

6.   CONCLUSIONS

The purpose of this investigation was to determine if POGO Longitudinal Oscillations could be controlled with active valve elements in the vehicle propulsion system.

a. Control Feasibility - Based on the analyses conducted, it appears that this method of control is in fact feasible. The control valve affects longitudinal stability by changing the suction system natural frequency. The frequency shift is accomplished with changes in the control loop gain; however, there are restrictions imposed on the gain levels. If the control gains are too large, a divergence in the system characterized by the control valve going to either a full open or full closed position will result. The same situation will develop in the fuel system if control gains are too large. In addition, the fuel system appears to be susceptible to oscillatory instabilities for small-time lags in the control loop.

b. Control Disadvantages - One of the disadvantages encountered in this particular control system is the sensitivity of stability to control valve gains. In the system studied, it was necessary under some conditions to use control gains of opposite sign on the fuel and oxidizer control loops. This requirement was incurred because structural first mode frequency are higher than the oxidizer suction system frequency and lower than the fuel system frequency. A positive gain in the oxidizer control loop lowered the suction frequency thereby separating it from the structural frequency while negative gains in the fuel system achieved frequency separation by raising the fuel suction frequency. For later flight times, the structural frequency may cross-over the fuel suction frequency thereby requiring a change in sign on the control loop gain. Furthermore, it appears that the control valve will have little or no influence in the system when suction line and structural frequencies are equal. There are at least two ways of avoiding the above difficulties. If a parameter which maintained the same phase relationship with flow rate were used to actuate the valve, the sign change could be avoided. Such a relationship exists between the suction pressure and pump discharge flow. The phase difference between the two remains at approximately 180 degrees throughout flight. The active valve, in this case, would use suction pressure for actuation; however, it would be located in the discharge system and would modulate discharge flow rate. The disadvantages of locating the valve in the discharge system as presently viewed would be:

(1) The limited physical location envelope in which the valve could be placed.

(2) The possible necessity of an engine modification with the required requalification test program.

(3) The higher pressure losses across the valve.

The other possible solution is to use control loop gain to lower both fuel and oxidizer suction system frequencies below the structural first mode frequency for all flight times. One problem which would be encountered here is the extreme sensitivity the control loop frequency displays as function of gain for low frequencies. Precise knowledge of all propulsion system parameters would be required in order to establish the proper control gain. Unfortunately, examination of the latter POGO control concepts was not within the scope of the present program. If the active control valve concept is to be pursued further, it is recommended that the above considerations be evaluated in order to establish an optimum control valve configuration.

f.   Summary - In conclusion, the active valve appears to be a feasible method for controlling POGO. There are a number of features, however, which would be undesirable for certain vehicle configurations. It is felt that additional investigations would provide practical methods of avoiding these disadvantages.

SECTION IV

TURBINE SPEED CONTROL

1. GENERAL THEORETICAL CONSIDERATIONS

a. Introduction: Control of POGO via modulation of propellant flow to the turbine gas generator represents a unique change from conventional passive methods of eliminating coupled propulsion system flow and pressure oscillations. Control is achieved using components and subsystems already present in a pump/engine assembly and adds less hardware to the system than most of the other passive or active POGO compensation techniques. In addition to providing a means for stabilizing POGO, turbine speed control offers the possibility of using the same hardware components to vary thrust in response to signals generated by trajectory optimization guidance commands.

Control of the system is achieved by using the turbine/gas generator as an amplifier to modulate the flow to the main engine combustion chamber. By controlling flow to the turbine gas generator, turbine speed can be varied which in turn directly changes pump power output and subsequently pump flow rate. The basic cause and effect relationships follow directly from the block diagram below.
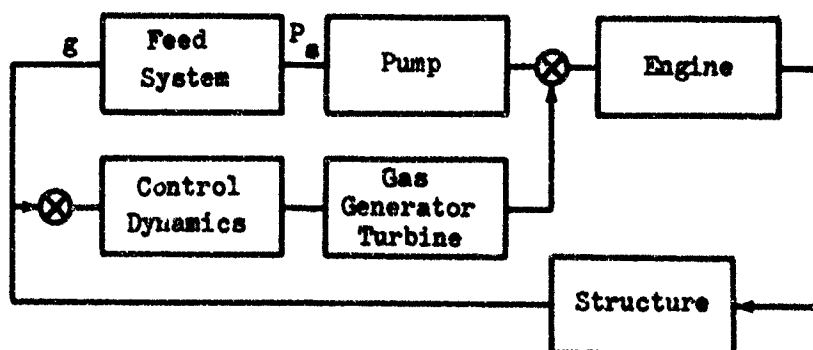
Figure 18   Basic System With Turbine

As shown, the control elements, including the gas generator
supply lines (bootstrap lines) are in parallel with the feed
system and pump. Control is obtained by driving a valve in the
bootstrap lines with a signal, g, obtained from an accelerometer.
Control can also be achieved by driving the gas generator valve
with a suction pressure signal, Ps. Both types, acceleration
and suction pressure control, will be discussed subsequently.
The effectivity of either method depends largely upon how much
gain attenuation and or advantageous phase shift can be obtained
by replacing the natural feed system and pump dynamic elements
by the parallel combination of those elements with the control
dynamics and gas generator/turbine systems.

     b. System Model Without Compensation. The standard
POGO mathematical model does not ordinarily contain the gas
generator/turbine dynamics. The impedance of the bootstrap
system compares with the main discharge system impedance is too
high to allow POGO induced discharge pressure variations to
significantly affect the bootstrap system flow rates. That is,
referring to the sketch below, the gain around the loop contain-
ing the bootstrap system is very much less than the gain around
the primary loop; hence the bootstrap system is usually omitted
from POGO analysis. However, if the gain around the bootstrap
system loop can be increased, i.e., by use of a valve that
decreases the bootstrap line resistance, then that feedback
path becomes available as a means of control.
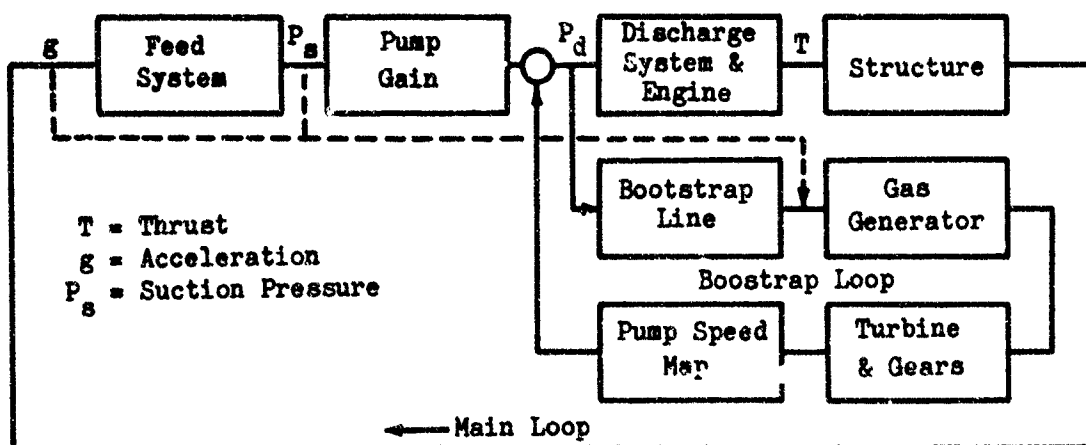
Figure 19   Basic System With Control

c. Analysis with Gas Generator/Turbine Loop Compensator. The complete set of equations for the compensated system are developed in Appendix III . The discussion that appears below is presented with the aid of simplified equations and block diagrams that retain the important elements of the system and control method.

(1) Control via acceleration feedback - Since it is intended to stabilize a system for which the prime consideration is limiting oscillatory acceleration, acceleration feedback will first be attempted as the primary control mode. The block diagram shows the pricipal fuel and oxidizer system elements including the control loop through the gas generator, turbine, and pumps. As shown, control is achieved by direct modulation of the gas generator fuel flow by the acceleration control signal, g. Fuel flow only is modulated because of extremely rich mixture ratio in the gas generator. The transfer function from g through the gas generator, turbine, and pump is given by:

$$\frac{\delta P_{df,o}}{g} = \frac{K_c \, G_{6F} \, G_7 \, G_{4F,o}}{1 + G_7 \, (G_{4F} \, G_{3F} \, G_{8F} + G_{40} \, G_{30} \, G_{80})} = \bar{G}_c \quad (20)$$

Where the elements are as defined on the block diagram with g and $\delta P_{df,o}$ the incremental change in fuel or oxidizer pump discharge pressure per unit of acceleration input. When the transfer function, $\frac{\delta P_d}{g}$, is reduced to essentials in terms of Laplace variable S, one can easily observe the effect of control. Reduction of the $\frac{\delta P_d}{g}$ function thus produces the following:

$$\frac{\delta P_d}{g} = \frac{K_c \, G_g}{1 + \tau_g S} \quad (21)$$

Where $K_c \, G_g$ is the total control path gain and is the time constant. Such a simple relationship results from the fact that τ_g is much larger than any of the other system time constants so that they can be neglected for purposes of illustrating the control method. The time constant, τ_g, is associated with the relatively large turbine and pump rotary inertias incorporated in the system element G_7. Effects of the control can be evaluated by observing the effect of the $\frac{\delta P_d}{g}$ functions
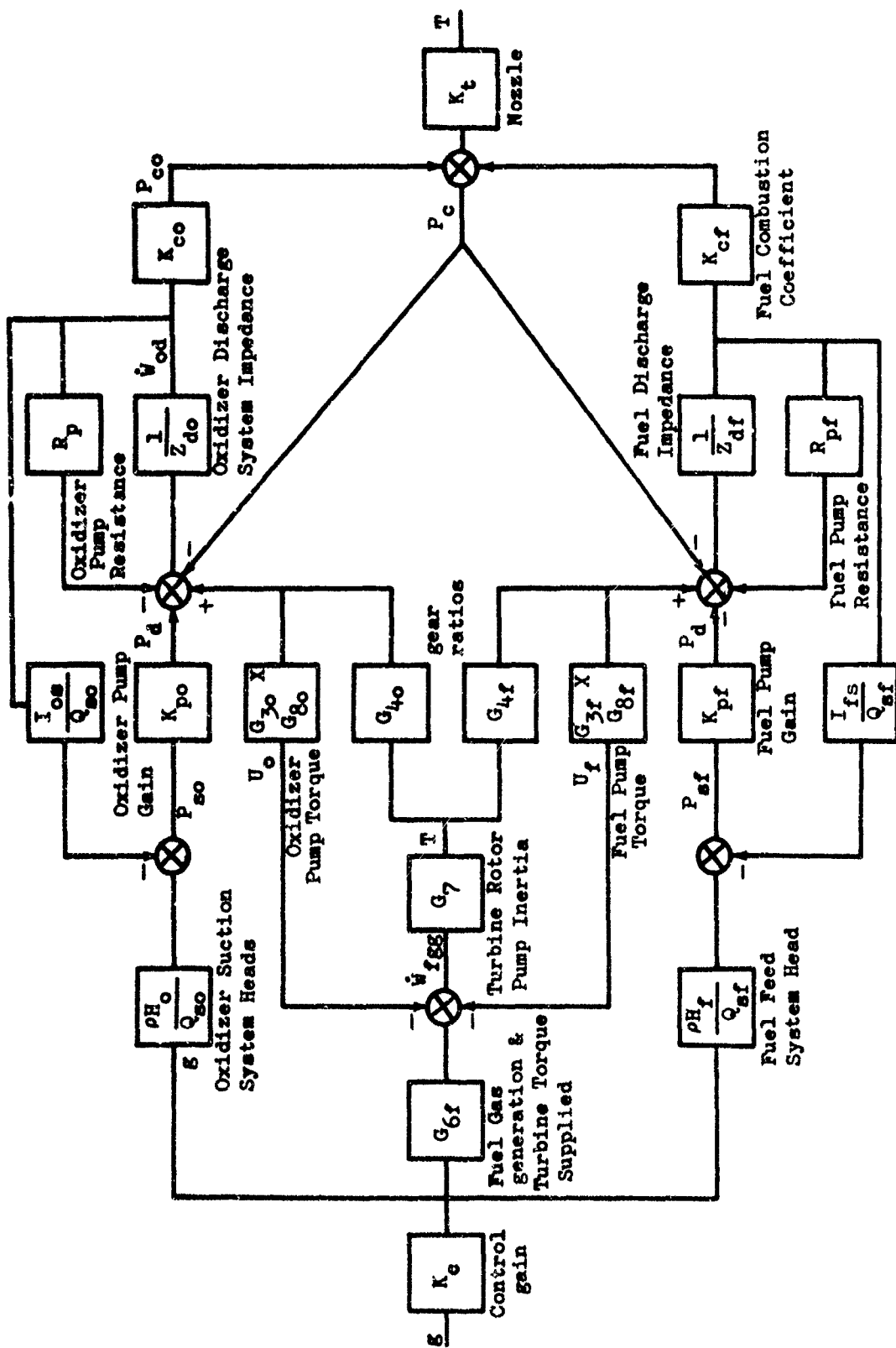
Figure 20 Turbine Speed System Complete Block Diagram

in the main system functions $\dfrac{P_s}{\mathcal{E}}$ and $\dfrac{P_c}{\mathcal{E}}$ for both fuel and oxidizer. The two main system functions can be simply expressed if the main fuel and oxidizer systems are decoupled at P_c to permit only the oxidizer component of P_c to feed back into the oxidizer system and only the fuel component of P_c to feed back into the fuel system. The suction system response with control present is then expressed as:

$$\frac{P_s}{\mathcal{E}} = \frac{\rho H - \left(\dfrac{SIG_c}{Zd}\right)}{Q_s + S\left(\dfrac{IK_p}{Z_d}\right)} = \frac{\rho H - \left(\dfrac{K_c G_s}{Z_{d(1 + \tau_g S)}}\right)}{Q_s + S\left(\dfrac{IK_p}{Z_d}\right)} \quad (22)$$

Where $\bar{G}_c$ is the total control function

The feed system response, $\dfrac{P_s}{\mathcal{E}}$, without control

differs from the response with control only by the presence of the control term in the numerator of the transfer function. The control term also affects the discharge system response so that the total propulsion system transfer function reflects the presence of the control function. Results of determining the effect of control on the combustion chamber pressure response expresses the total impact of the control function as follows:

$$\frac{P_c}{\mathcal{E}} = \frac{P_s}{\mathcal{E}} \frac{P_c}{P_s} = \left[K_p\left(1 + \frac{R_p}{Z_d + K_c}\right)\left(\frac{\rho H - \dfrac{SIG_c}{Z_a}}{Q_s + \dfrac{SIK_p}{Z_a}}\right) \right.$$

$$\left. + \frac{G_c}{1 + \dfrac{R_p}{Z_d + K_c}} \right]\left(\frac{R_c}{Z_d}\right)\left(1 + \frac{R_c}{Z_d}\right) \quad (23)$$

The $1 + \dfrac{R_p}{Z_d + K_c}$ term and $1 + \dfrac{K_c}{Z_d}$ term can be dropped

without much loss of generality so that,

$$\frac{P_c}{S} = \left[\frac{K_p \left(\rho H - \frac{\overline{SIG_c}}{Z_d} \right) + \overline{G}_c}{Q_s + \frac{SIK_p}{Z_d}} \right] \frac{R_c}{Z_d} \qquad (24)$$

From the transfer function, it follows that the control term, G_c, cancels under the condition where $Q_s = 0$. This condition pertains when the complex frequency, S, is equal in magnitude to the suction line natural frequency since $Q_s = \frac{S^2}{\omega_s^2} + 1$.

Since the POGO system instability manifests itself at some frequency close to the natural frequency of the structure, we can say the $Q_s = 0$ when the natural frequency of the suction system is equal to the natural frequency of the structure. When this occurs, the G_c terms in the P_c transfer functions cancel. This is equivalent to $\frac{P_c}{S}$ saying that the control would not be effective for systems where the structural and suction system material frequencies were equal or nearly equal.

(2) Compensation for Various Configurations Dependent on Ratio of Feed System Frequency to Structural Frequency. Although the acceleration control method is not effective when the structure and suction line natural frequencies are equal, system stability can be considerably improved for structural modes with frequencies different from the suction line modes.

The responses will be discussed in terms of Nyquist diagrams or frequency response plots of system gain and phase with frequency as a parameter. A typical plot for both a stable and unstable system are shown in Figure 21.

The maximum response vector corresponds to a frequency that is very nearly equal to the frequency at the structural mode one is attempting to stabilize.
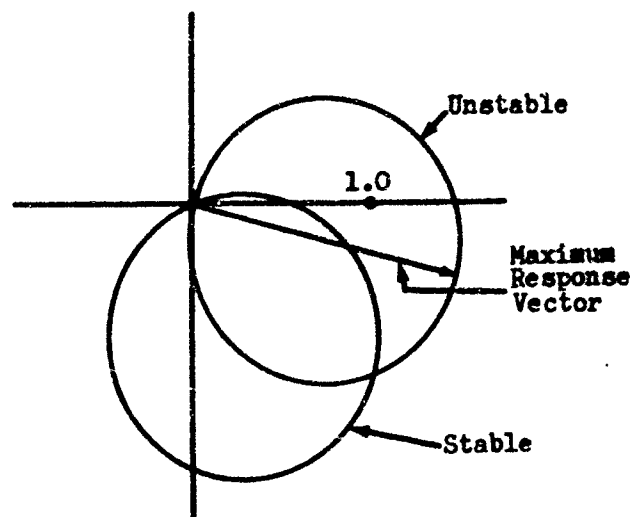
Figure 21 Typical System Response

(3) Structural Frequency Greater than Suction Line Frequency. The response function of concern is -

$$\frac{P_e}{\mathcal{E}_{in}} \frac{\mathcal{E}_{out}}{P_c} = \frac{K_s \omega^2}{2\zeta_s} \cdot \frac{R_c}{Z_d} \left[K_p \frac{\left(\rho H - j\omega I \frac{K_c}{1 + j\tau_g} \frac{1}{Z_d} \right)}{1 - \left(\frac{\omega}{\omega_s}\right)^2 + j\omega I \frac{K_p}{Z_d}} + \bar{G}_e \right] \qquad (25)$$

For purposes of discussion the total open loop system response is broken into five parts designated a - e, where -

$$a = \frac{- K_s \omega^2}{2jz_s} \frac{K_c}{Z_d}$$

$$c = K_p \rho H$$

$$b = \frac{1}{1 - \left(\frac{\omega}{\omega_s}\right)^2 + j\omega \frac{IK_p}{Z_d}}$$

$$d = - j\omega K_p I \frac{K_c}{1 + \tau_g} \frac{1}{Z_d}$$

$$e = \frac{K_c}{1 + j\omega \tau_g}$$

The response is then given by:

$$\frac{\mathcal{E}_{out}}{\mathcal{E}_{in}} = a\left[b(c + d) + e \right] \qquad (26)$$
$$= abc + abd + ae$$

43

Typical responses for the abc, abd, and ae components are shown in vector diagram form from which the total response vector is constructed. Typical response for the case where $\omega > \omega_s$ is shown in the sketch below for control gain, K_c, positive and K_c negative.

abc

ac

1.0 Stability Point

$a\left[b(c+d)+e\right]$
K_c Positive

β

α

γ

Compensated Response K_c
Positive

abc

Uncompensated Response

Compensated Response, K_c Negative

$a\left[b(c+d)+e\right]$
K_c Negative
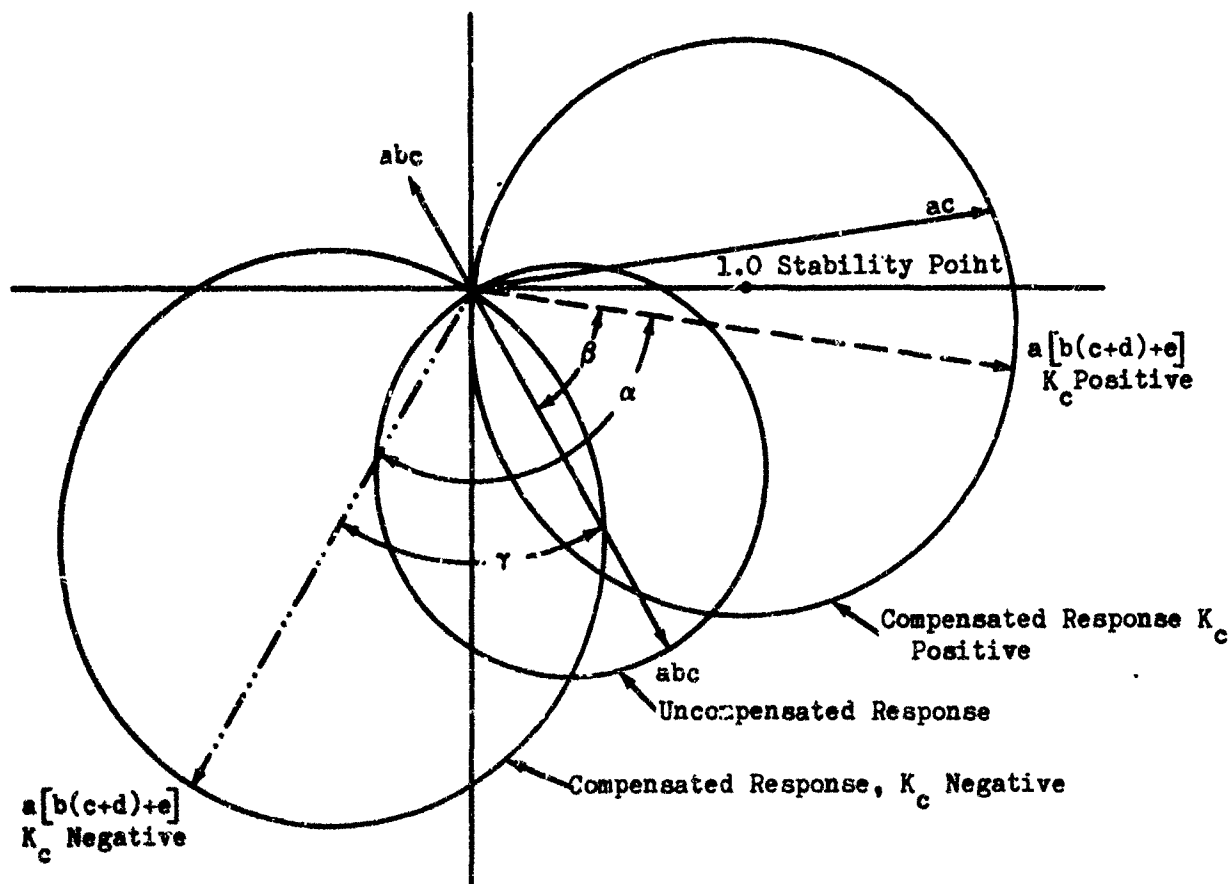
Figure 22   System Response Control Added

The figure shows that addition of compensation produces a system response whose gain and phase are significantly different from the uncompensated response. Regardless of whether K_c is positive or negative, the maximum gain (vector length) increases. For K_c positive, the originally stable system (vector abc) is made unstable because of increased gain and additional positive phase of β . For K_c negative, the marginally stable system is made more stable despite increased gain because of the

negative phase shift. The stabilizing effect of negative K_c agrees with the intuitive conclusion that a decrease in turbine speed in required to offset the effects of an increase in flow, $_d$, that accompanies increasing suction pressure, P_s.

(4) Structural Frequency Less than Suction Line Frequency. The stability diagram for the case where the structural frequency is less than the suction line frequency differs considerably from the previous case.
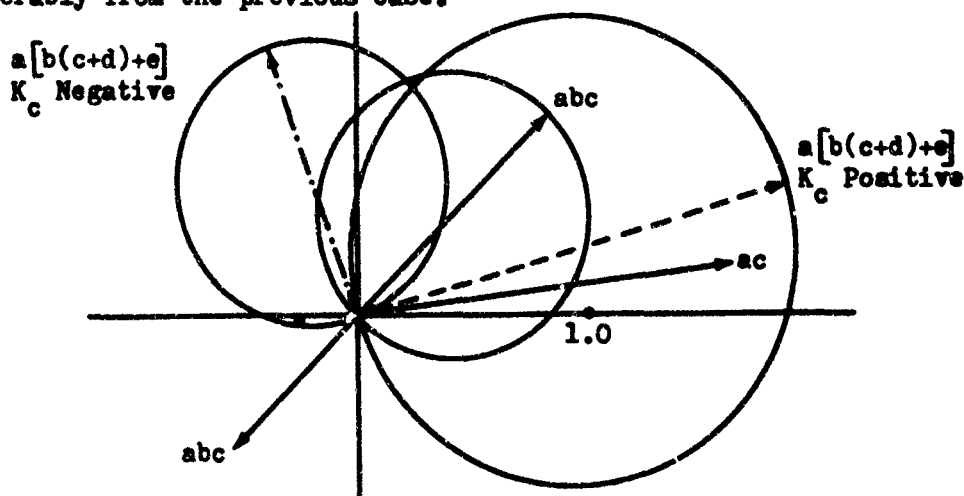
Figure 23   Response When Structural Frequency ÷ Suction Line Frequency $<$ 1.0

In this case, compensation increases the maximum gain for K_c is again destabilizing because of gain increase and unfavorable phase shift. Negative K_c decreases gain slightly and shifts the phase of the response into a more stable condition.

It is interesting to note that the case where structual frequency and suction line frequency are equal corresponds to conditions for which the ae vector and the abd vector are equal in magnitude but opposite in sign and hence cancel. The response diagram then reduces to the abc vector which is exactly equal to the uncompensated case. It is also important to note that the magnitude of the abc response is greatest and the phase most unfavorable for the condition where structure and suction line frequency are equal. Thv under conditions which lead to the least stable configuration, the compensation does little or nothing to improve stability.

d. Control with Suction Pressure Feedback. If suction pressure instead of acceleration is used as the control variable,

stability can be improved in some cases by an effect that : equiv-
alent to separating the suction line frequency from the stiuctural
frequency. With P_s feedback through the gas generator/turbine loop,
the P_s/g transfer function assumes the form shown below:

$$\frac{P_c}{g} = \frac{\rho H}{Q_s + \frac{SI}{Z_d} (K_p + \frac{K_c}{1 + \tau_s})} \qquad (27)$$

and P_e is given by -
$$\frac{}{g}$$

$$\frac{P_e}{g} = \frac{\rho H}{Q_s + \frac{SI}{Z_a} (K_p + \frac{K_c}{1 + \tau_s})} \ X \qquad (28)$$

$$(K_p + \frac{K_c}{1 + \tau_s})\frac{R_c}{Z_d}$$

We note here again that when $Q_s = 0$ (when structural
frequency and suction line frequency are equal) that the $K_p + K_c/1$
$+ \tau_s$ terms in numerator and denominator cancel indicating that the
compensation resulting from the control function has been nullified.
Thus, as in the case of acceleration feedback, the least stable
case is not improved by presence of the control compensation.
If the control gain, K_c, is made much larger than K_p, and if $\tau_s >>$
1, which it usually is for the frequency range of interest, the
system function can be approximated by -

$$\frac{P_c}{g} = \frac{\rho H}{Q_s + \frac{I K_c}{Z_d \ \tau}} \cdot \frac{K_c}{\tau_s} \cdot \frac{R_c}{Z_d} \qquad (29)$$

The resonant frequency of this function is given by the
equation:

$$Q_s + \frac{\frac{K_c}{I}}{Z_d \tau} = 0 \qquad (30)$$

or

$$\omega_{res} = \omega_{\substack{suction \\ line}} \sqrt{1 + \frac{\frac{K_c I}{Z_d \tau_c}}{}} \qquad (31)$$

The resonant frequency is lowered if K_c is negative and $1 > \frac{K_c I}{Z_d \tau_c}$. Thus, theoretically, at least, it appears possible to shift the resonant frequency of the propulsion system response function below any structural frequency that may be troublesome.

In the numerator of the response function, the effect of the pump gain is almost completely nullified by the control function. The total system maximum response including structure is shifted to a relatively stable phase condition as shown in the figure below:
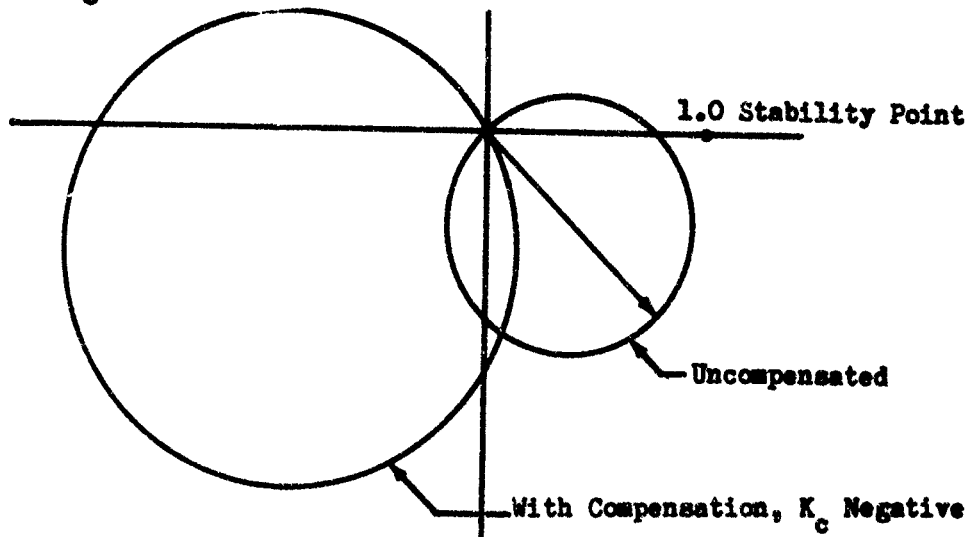
Figure 24   Use of P_s Feedback as Control Variable

In order to test the feasibility of setting K_c to nullify the pump gain and shift the effective feed line frequency, the percent change in gas generator flow required must be computed. Parameter values corresponding to a Titan III engine system were put in the model to determine that about 5% modulation of fuel flow to the gas generator was required to reduce a typical suction line frequency by a factor of 4.

47

The large gain magnifies the effects of uncertainties resulting
from parameter tolerances. Thus, if this method of control were
used, it would be necessary to conduct extensive analysis to de-
termine whether adequate phase margin could be held for realistic
tolerances placed on parameters that strongly affect system phase.

2. SPECIFIC APPLICATION

a. Introduction. The application of turbine speed control
to eliminate POGO is based on the use of the propellant pump as
an amplifier in which a 180 degree phase lag is maintained between
the discharge line flow and the suction pressure. The net result
is a smooth propellant flow to the main engines and the associated
absence of any thrust perturbation.

A simulation of pump turbine speed modulation which was
conducted on the analog computer was based on a model of the Titan
II Stage I booster engine configuration. The basic system for this
configuration is shown in block diagram form in Figure 25. The oxi-
dizer and fuel systems as shown begin with the suction line followed
by the pump, discharge line, and injectors which supply propellants
to the combustion chamber. The pumps are driven mechanically by
the turbine through reduction gears with energy for the turbine
supplied by a fuel-rich gas generator. The propellants for the gas
generators are tapped from the pump discharge lines, fed through
the footstrap lines and metered through a fixed area cavitating
venturi. Thrust is controlled primarily by proper sizing of the
cavitating venturi. The nominal fuel flow rate to the gas generator
is about 11.0 lbs/sec with an oxidizer flow rate of approximately
1.0 lbs/sec. Since a large part of the propellant flow to the gas
generators is fuel, thrust can be controlled by varying the fuel
flow to the gas generator and replacing the presently used fixed
area cavitating venturi with a variable area cavitating venturi
used as the control valve illustrated in Figure 25.

Theoretical considerations indicate that gas generator
temperatures and mixture ratios over a $\pm$ 6% thrust range are well
within design limits for the particular system under consideration.

b. Propulsion System Equations, Pump Through Injector. The
system equations which were used to develop the mathematical model
for the analog simulation were derived for a system that includes
propellant pumps, discharge lines, and main engine injectors.
(See appendix IIIa for these equations). The complete model includes,
analytical descriptions of the pump, turbine, gas generators and
discharge as well as bootstrap feedlines.

48
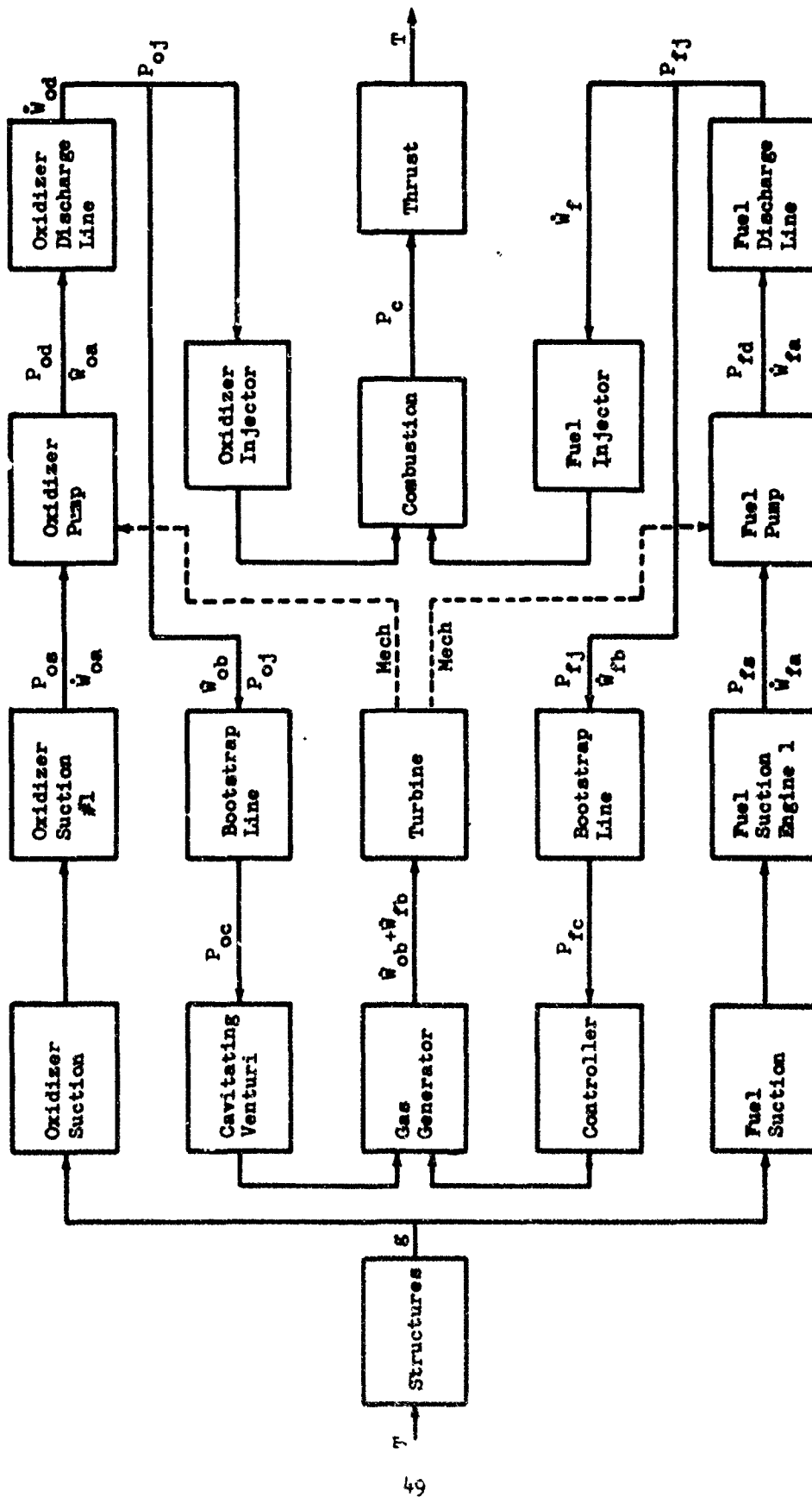
Figure 25   Turbine Speed Control Schematic

c. Model Development, Linearized Equations. A linearization of the system equations for programming on the analog computer was performed for two reasons. First, the simulation was based on small variations about nominal or steady-state operating conditions.

Thus, the original equation non-linearities arising from complex coordinate coupling in the bootstrap and turbine system as well as flow non-linearities were transformed by the well-known differential method expressed in general as:

$$dY_i = \sum_{i=1}^{n} \frac{\partial Y_i}{\partial x_i} dx_i \tag{32}$$

The linearization made it possible to study stability of the system by conventional frequency response methods. The method used in linearizing the functions describing the basic propulsion system can best be shown with an example using the oxidizer pump equation (89). The effect of small changes of P_{os}, N_o, and $\dot{W}_{os}$ on $(P_{od} - P_{os})$ can be functionally written as:

$$d(P_{od} - P_{os}) = \frac{\partial(P_{od} - P_{os})}{\partial P_{os}} dP_{os} + \frac{\partial(P_{od} - P_{os})}{\partial N_o} d N_o + \tag{33}$$
$$\frac{\partial(P_{od} - P_{os})}{\partial \dot{W}_{os}} d\dot{W}_{os}$$

or, $$(P_{od} - P_{os}) = K_{o8} P_{os} + K_{o9} N_o + K_{o10} \dot{W}_{os} \tag{34}$$

Where: $$K_{o8} = \frac{\partial(P_{od} - P_{os})}{\partial P_{os}} \tag{35}$$

All variables in eq. (34) now represent small changes about a nominal set of conditions. These conditions or steady-state values are used to determine the constants or coefficients in the perturbation equations. This procedure was used to derive the set of linearized equations which appear in Appendix IIIb.

d. Analog Model of Complete Simulation. The combined equations of appendixes IIIb and IIIc comprised the complete system for the analog simulation.

Interdependence of these equations as combined is demonstrated by the block diagram of Figure 26. The propulsion sub-systems are outlined in the flow diagram according to their basic functions. The remainder of the system including the structure and pump dynamics couple with the propulsion system and are given in detail in appendix IIIc.

(1) Gas Generators, Turbine Dynamics. The response of the gas generator, turbine, and pump pressure and flow to variations in bootstrap system is dominated by a first-order time lag associated with the turbine and pump rotary inertia. The lag in this part of the system accounts for approximately 80° phase lag at "POGO" frequencies of about 11.0 cps. This, of course, assumes no time lag in the gas generator combustion which although small remains as one of the uncertainties in the analysis.

(2) Fuel and Oxidizer Pump Dynamics. Both the fuel and oxidizer pump are represented by gains and resistances as shown in the equations and the blocks of Figure 26. This representation is consistant with flight data which shows discharge and suction pressures that are consistant with the linear representation.

(3) Oxidizer Discharge Dynamics. The oxidizer discharge system is characterized by short discharge lines from the pump to the injectors. The bootstrap line for the gas generator branches off from the discharge line and presents a very high impedance to pressure oscillations in the discharge system. This impedance is in the form of a large resistance caused by the relatively small diameter bootstrap line and cavitating venturi represented by (K_{o22}) in Figure 26. Consequently, any pressure disturbance in the oxidizer discharge line is greatly attenuated before reaching the gas generator injector. The high impedance of the gas generator bootstrap lines relative to the main pump discharge lines make it possible to use the gas generator loop for control without fear of causing instability because of the inherently large time lag.

(4) Fuel Discharge Dynamics. The main fuel pump discharge system contains regenerative cooling tubes whose inertance produces a significant time lag at POGO frequencies. The presence of the time lag is first evident from a comparison of coefficients G_7 and G_{10} (See appendix IIIb) in the system equations. The remainder of this fuel system is much like the oxidizer system since the fuel
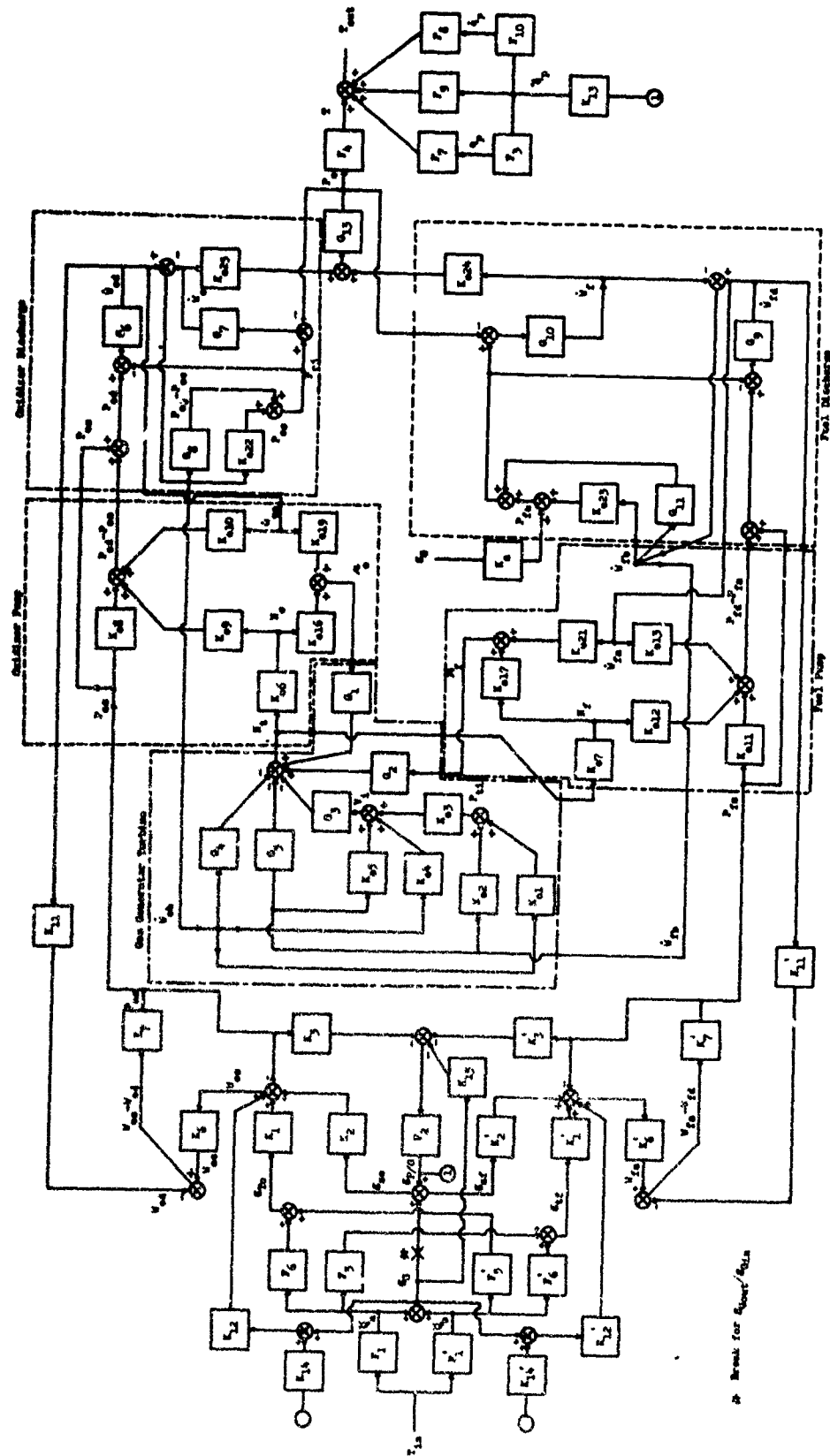
Figure 26   Analog Flow Diagram for Pump Turbine Speed Modulation Complete System

52

bootstrap line presents a high impedance to the fuel pump discharge pressure.

(5) Fuel Controller and Gas Generator. System control as previously stated was accomplished by replacing the cavitating venturi in the fuel footstrap line with a servo operated control valve. The resulting analytical expression which describes the behavior of the controlled fuel flow to the gas generator is then written as:

$$P_{fc} = K_{023} \, \dot{W}_{fb} + K_c \left(\frac{1 + \tau_1 S}{1 + \tau_2 S} \right) g_{Gin} \qquad (36)$$

where the primary feedback for control is acceleration at the engine gimbal point. The gain of the system, K_c, and the leads or lags τ_1 and τ_2 respectively are design parameters which are optimized for the desired control. With P_{fc} remaining relatively constant due to high impedance of the bootstrap line, the flow rate to the gas generator, $\dot{W}_{fb}$, is essentially proportioned to the accelerations, g_{Gin} with a lead or lag as dictated by τ_1 or τ_2. Use of acceleration as the feedback variable rather than another parameter such as suction pressure is preferred because control of acceleration itself is the final requirement.

e. Results of Simulation. The bootstrap control system was studied by an open loop stability analysis using an analog computer. With the loop opened at acceleration, g, frequency responses were computed and compared with an uncompensated configuration. The uncompensated or no-fix case shows marginal stability of about 20° phase margin, Figure 27.

When the compensation was introduced by changing the control gain, K_c, greater stability is achieved. Although the absolute value of the gain at resonance has increased, the additional lag in the system increases the phase margin to a value of about 98° for the case of $K_c = 160$.

It becomes apparent that as K_c is increased beyond a value of 160, the Nyquist swings back into a region of less stability at the higher frequencies. The particular numerical value of $K_c = 160$ is not in itself very significant. However, for the example chosen, it shows that control gain cannot be increased indefinitely without adversely affecting stability. The effect of introducing a lead or lag by way of τ_1 and τ_2 is shown by part (d) of Figure 27 in
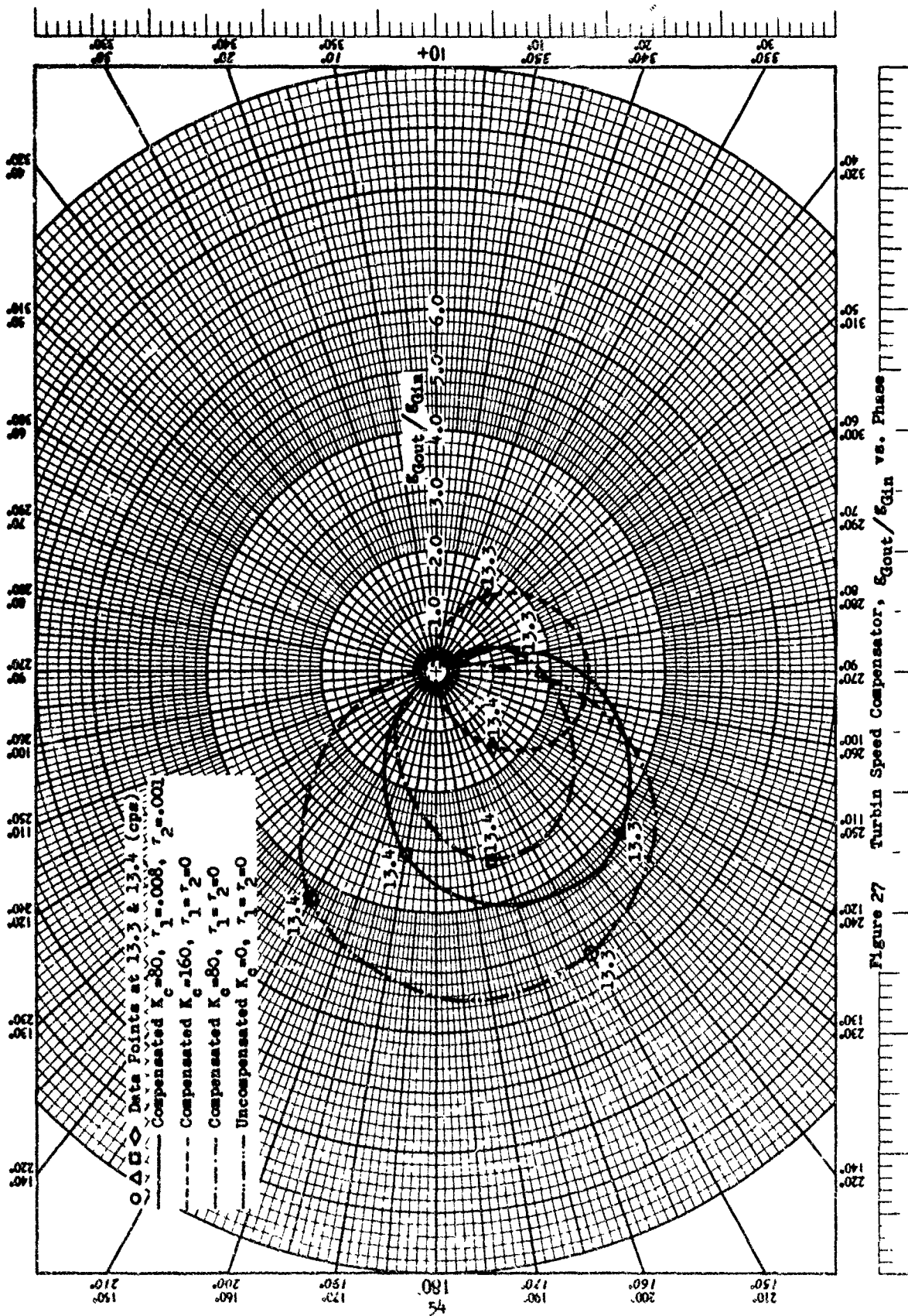
Figure 27   Turbin Speed Compensator, $\varepsilon_{Gout}/\varepsilon_{Gin}$ vs. Phase

54

which a lead of about 30° at 13 cps has been introduced. A corresponding loss of phase margin is the result. Likewise, if a lag is applied to the system, a shift toward a more stable region will occur provided the gain is not so large that stability of higher system modes is diminished.

f. Other Analysis Considerations.

(1) Oxidizer vs Fuel Control. Two modes of control are possible using modulation of either fuel or oxidizer bootstrap flows. Fuel control as studied in the preceding analysis can be replaced by control of the oxidizer flow. However, since the steady-state oxidizer flow rate is approximately 10% of the fuel flow rate, the oxidizer control gains would be much more critical. From a practical viewpoint the parameter tolerances on the oxidizer valve system would require closer control assuming the same percent change in main engine thrust as can be achieved in the fuel control system.

(2) Gas Generator Mixture Ratio Insensitivity. The analysis revealed that the system is dynamically quite insensitive to gas generator mixtures ratio because mixture ratio effects are overshadowed by the sensitivity of the turbine spouting velocity, V_i, to changes in $\dot{W}_{ob}$ and $\dot{W}_{fb}$. This can be seen by a comparison of K_{o4} and K_{o5} with K_{o1} and K_{o2} in the equation of appendix IIIb. However, this assumes that the mixture ratio of $\dfrac{\dot{W}_{ob}}{\dot{W}_{fb}}$ must remain between fairly narrow limits on the very fuel-rich mixture ratio, as seen in Figure 86 of appendix IIIa. If the mixture ratio falls below a value of 0.067, the C^* falls off rapidly. The total effect is to make turbine inlet pressure very sensitive in this region which would cause sudden changes or non-linear response of the gas generator combustion process. The POGO simulation placed a lower limit on $\dot{W}_{ob}/\dot{W}_{fb}$ of .067 so that this non-linear region need not be considered. An upper limit on the mixture ratio was set at limit temperatures, below values at which the gas generator would burn up.

(3) Mechanical replacement of the venturi in the gas generators feedline with a control valve could be done with little difficulty. There appears to be ample access to the engine assembly on most liquid fuel engines operating with a bootstrap system. The valve to be considered might be of a variable venturi type but would need lean and rich stops to maintain the proper mixture ratio range for stable gas generator performance.

FLUIDIC AMPLIFIER COMPENSATION

1. INTRODUCTION

The use of a fluidic device or amplifier for control of
POGO is similar in application to a valve modulating flow in
the propulsion system.

A fluidic device was studied because it seemed possible to
modulate flow without having to drive some mechanical component
with a sensed variable such as suction pressure or acceleration.

The attractive features of a fluidic device in this capac-
ity is the absence of moving parts. The reliability, therefore,
should be greater.

2. PROPORTIONAL FLUID AMPLIFIER

The operation of a proportional fluid amplifier can best be
described with the aid of the schematic diagram shown below
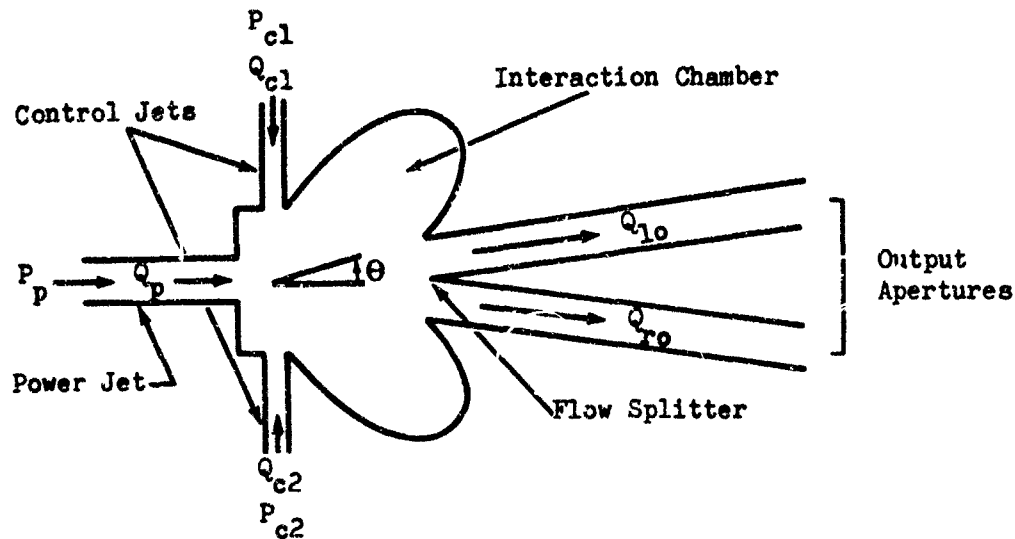
Figure 28   Fluid Amplifier Schematic

The input power to the amplifier is applied through a
pressure to the power jet, P_p, which in turn results in a flow
Q_p. The control jets flows, Q_{c1} and Q_{c2} combine with the power

jet flow in the interaction region to effect a momentum exchange which deflects the output flow Q_o through an angle θ. The angle of deflection is proportional to the ratio of the momentums of the control stream and the power stream as given in the formula.

$$\tan \theta = \frac{A_c \left(U_{c_2}^2 - U_{c_1}^2 \right)}{A_p \left(U_p^2 \right)} \tag{37}$$

Where: U = fluid velocity

A = nozzle area

After stream interaction, the velocity profile of the output stream is approximately gaussian. The profile broadens and decreases in centerline velocity as it moves downstream from the interaction region. The flow splitter divides the stream which is then collected in the two output apertures. For small angles of deflection, the changes in output flows are approximately proportional to the changes in control flows. Essential to the operation of the proportional amplifier is an interaction chamber as shown which prevents the fluid stream from attaching itself to the wall in the output region causing bistable operation of the amplifier. The flows gains, $\dfrac{\Delta Q_o}{\Delta Q_c}$, for this type of amplifier may be as high as 10.0 while pressure gains may reach 16.0. However, the amplifiers are extremely sensitive to loading which can drastically reduce their gain as well as affect their operating stability.

3. METHODS OF CONTROL WITH FLUID AMPLIFIER

a. Fluid Amplifier/Variable Resistance - Initial considerations involved the use of a fluid amplifier with its output legs attached to a converging Y joint as seen in the schematic below:
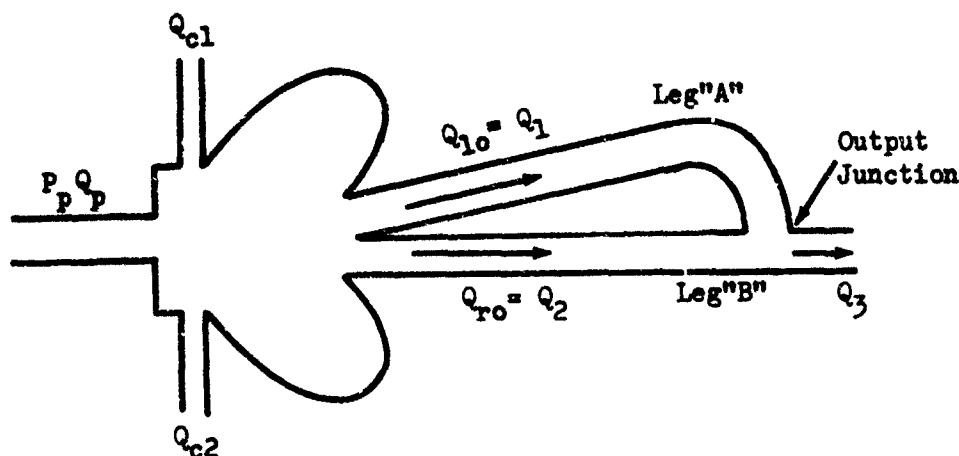
Figure 29   Amplifier/Resistance

Basically this system acts as a variable resistance when placed in series with another system such as a propellant line. The amplifier can route flow to either leg, as shown. As more of the flow is routed through leg A, a greater amount of fluid interaction occurs at the output function which results in a greater pressure drop at this point. A resistance coefficient for this function is defined as follows:

$$\zeta = \frac{Q_1}{Q_3}\left[\ 1\ +\left(\frac{U_1}{U_3}\right)^2\ \right] + \frac{Q_2}{Q_3}\left[\ 1\ -\ \frac{U_2}{U_3}\right]^2 \tag{38}$$

Where: U = fluid velocity

   Q = fluid flow rate

This assumes an angle of 90° for leg A with respect to leg B and the output Q_3. The pressure drop is then defined as

$$\Delta P = \frac{\zeta \rho U_3^2}{2} \tag{39}$$

for the output function with respect to flow past the junction. Theoretical values of ζ vary with flow in A and range from 0.0 to 2.0 with experimental observations indicating the maximum value to be somewhat nearer 1.7 to 1.8.

1) Series Suction Line Configuration Method

a) One method of using the variable resistance configuration, inserts the amplifier in the suction line as a series component. The accompanying schematic of the system shows the major components.
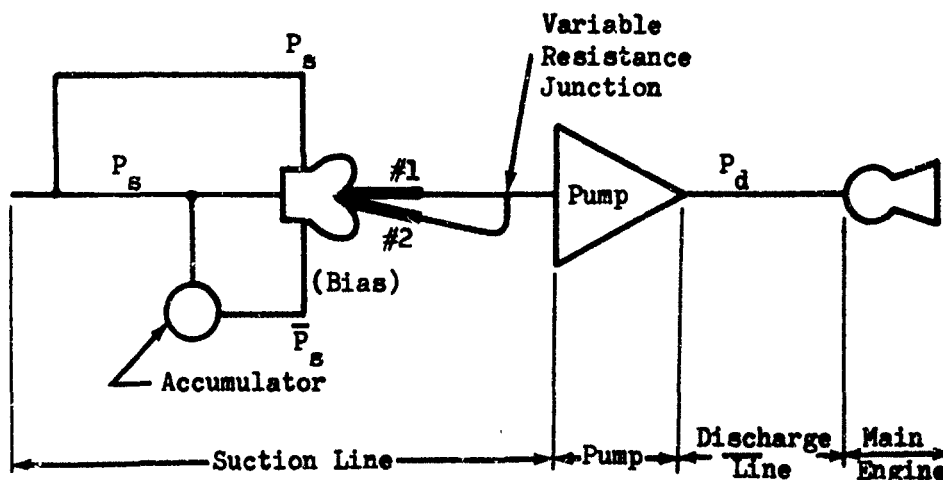
Figure 30   Series Suction Line Compensation

This configuration shows one of the control jets operating as a bias so that the main stream flow is not deflected at steady state pressures. As suction pressure, P_s , begins to increase, the output flow swings into leg #2. Since the resistance of leg #2 is higher than leg #1, the flow rate decreases thereby tending to counteract the effect of increased pressure. Ideally the fluidic amplifier can maintain pressure at the pump inlet at a constant level for small disturbances in the suction line.

b) Practical Considerations and Results. Two basic problems arise with the fluidic amplifier used as a variable resistance configuration. First, operation of the power jet and control jet at the same pressure is not practical or in most cases even possible. An alternative method controls flow in the discharge line where the operating pressures are sufficiently high. The discharge line of a typical system has pressures of 1200 ± 20 psia (steady state ± oscillatory) as compared to suction line pressures of 45 ± 20 psia (steady state ± oscillatory). However, the control jet generates enough pressure noise to obscure the signal present in the discharge line. The second

59

reason for discarding the series suction line configuration stems
from the fact that a 20% pressure drop developes across the fluid
amplifier even under the most ideal conditions. A steady state
pressure drop of this magnitude degrades performance to such an
extent ' at it cannot be tolerated in the suction line of pre-
sent-day propulsion systems. Therefore, this particular method
of compensation was abandoned.

2) Modified Amplifier - Suction Line Compensation

a) Method. This method was conceived as a possible
way of introducing a variable resistance into the suction line
without adding a steady-state pressure drop. A diagram of basic
elements of this system follows:
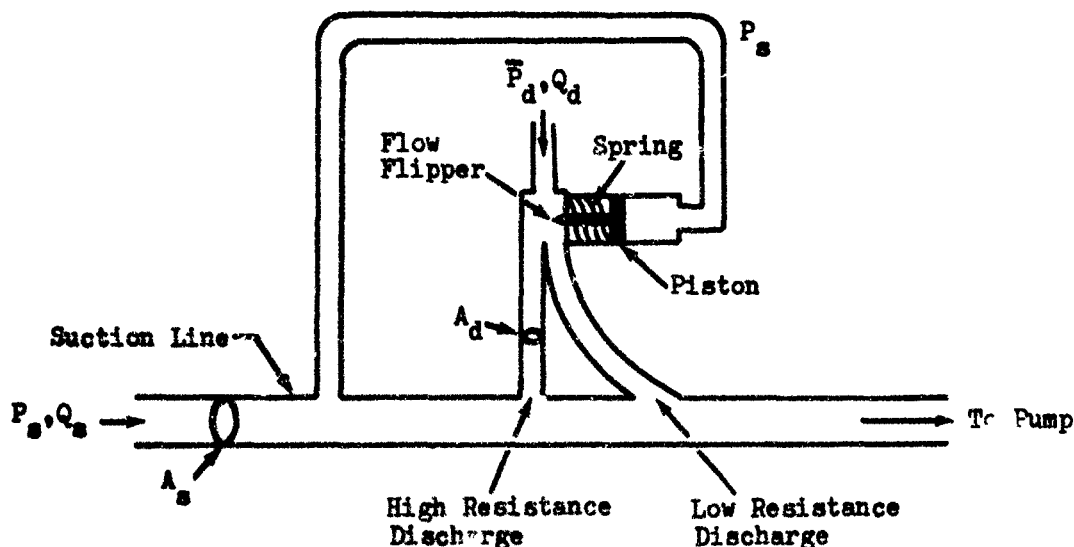
Figure 31   Modified Amplifier Compensation

The actuator shown has replaced the true fluid amplifier although
its action produces similar results by means of the flow-flipper
vane used to deflect the fluid flow into either of two paths.
The high-resistance path again creates a virtual resistance to
fluid flowing in the suction line while the other path is ef-
fectively a zero resistance in the suction line. The actuator
as shown has as its fluid power source the steady-state pressure
from the discharge system, P_d. The maximum tolerable flow that
can be fed back without significant loss of performance is about
5% of steady state - for a typical system this is about 27.0
lbs/sec. As suction pressure increases, the spring loaded piston
drives a flipper vane forward resulting in more fluid flowing into
the high-resistance leg of the compensator discharge system.

The higher resistance that the suction line now sees because of fluid interaction, under ideal conditions, will compensate for the increased pressure in the suction line to give zero net flow past the interaction region.

b) Results. If all of the flow from the compensator is directed through the low resistance discharge path at steady-state suction pressure, a half wave rectified flow variation accompanies the positive pressure pulses. Typical values from an analysis in which idealized conditions were assumed and the following system parameters used, indicate a compensation in the amount indicated in the following figure:

$$P_s = 45 \pm 20 \text{ psia}$$

$$P_d = 900.0 \text{ psia (steady state)}$$

$$\zeta = 2.0$$

$$A_s = 36.3 \text{ in}^2 \text{ (suction line area)}$$

$$A_d = 0.22 \text{ in}^2$$

$$Q_s = 540.0 \text{ lbs/sec}$$

$$Q_d = 27.0 \text{ lbs/sec}$$
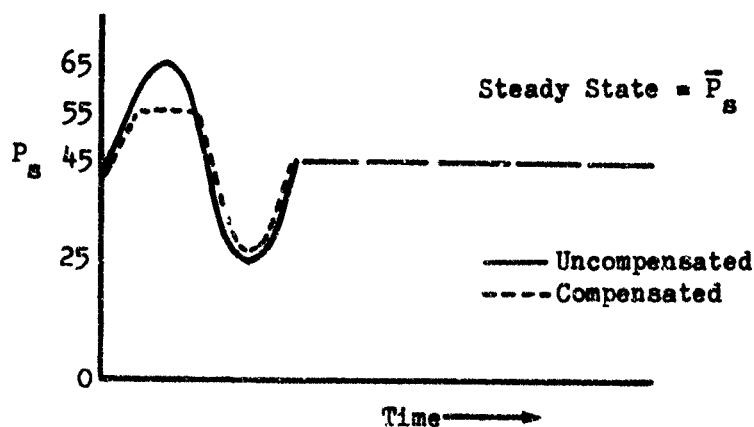
Figure 32   Modified Compensation Response

This indicates a maximum pressure compensation of about 10 psia on the positive half cycle or a reduction in the POGO content of the suction pressure response of about 25%. Any compensation by this method which would work on the negative half of the cycle would be implemented by a shift in biasing or operating point of the compensator. This would also necessitate an additional steady state suction line resistance which as before is intolerable. In either case, the total pressure compensation cannot exceed 10 psia.

c) Fluid Amplifier Compensation and the Discharge System. As was previously mentioned, it is necessary for pressures to the control jets of a fluid amplifier to be greater than the pressure to the power jet for proper performance. This precludes the use of the discharge system pressures for any control purposes of an amplifier operating on flow in a discharge system As we have seen, the signal would indeed be small when compared to the noise generated at the control jet orifices and, therefore, made such a system ineffective.

4. CONCLUSIONS AND RECOMMENDATIONS

Fluid amplifiers although attractive as simple control devices are generally impractical for POGO stability compensation because of the wide range of operating parameters which exist in a modern rocket propulsion system. Noise levels, internal stability and effects of loading on performance could be defined only after full-scale tests under intended operating conditions. If further investigations are carried out, it would be advisable to consider testing to determine performance characteristics with control jet pressures of about the same order of magnitude as those of the power jet.

SECTION VI
CAVITATION COMPLIANCE MODEL DEVELOPMENT

1. INTRODUCTION AND MODEL DESCRIPTION

In the analysis of structure - propulsion system coupled instabilities, turbopump cavitation compliance has long been subject to uncertainty that has limited the accuracy of stability prediction. In order to obtain a better understanding of how the cavitation process affects the cavitation compliance, a mathematical model development study was initiated to provide a description of turbopump operation. This effort has been carried over into the present program and is continuing at this time. A summary description of the development and results which have been achieved to date is contained in the following sections.

a. Model Requirements. The objective of the cavitation compliance analysis was to derive mathematical descriptions that could be related directly to the thermodynamic and fluid-mechanic conditions in a turbopump. Semiempirical approaches were discarded because of their demonstrated deficiencies when dealing with the problem of pump head rise under conditions of cavitation.

The following sequence of steps, therefore, were considered to constitute a logical analysis approach:

1) Development of the basic turbopump flow equations into which two-phase flow phenomena could be incorporated and that could later be expanded to include more complex flow situations.

2) Development of a two phase thermodynamic model that was independent of time and conditions of nucleation and that could be combined with the flow equations to give a description of turbopump cavitation compliance.

3) Development of a two phase thermodynamic model that included time effects and dependence on nuclei and that, when combined with the flow equations, would also yield an improved description of cavitation compliance.

63

b. Turbopump Flow Equations, General Description. The
development of the turbopump flow equations began with the as-
sumptions that 1) tip clearance flow was not present 2) There were
no vapor filled separation cavities within the impeller, and
viscous effects were negligible. Furthermore, the three-dimen-
sional flow equations were found to be too complex for solutions
consistent with the scope of the program; and in their place,
a quasi-three-dimensional potential flow approach was taken.
Many of the techniques used in the development were modifications
of similar techniques used for analysis of centrifugal compres-
sors (Ref. 1).

The quasi-three-dimensional analysis proceeds first
with the solution of the flow problem in the meridional plane.
It is assumed that channel flow exists between the impeller blades;
and, therefore, a stream surface the same shape as the blade plane
is located midway between blades (Fig. 33). The relationship
between the stream surface and the meridional plane is illustrated
in Figure 34. The flow equations are written for the stream sur-
face and then referenced to the meridional plane. Solution of
the equations yields a description of the flow field in the meri-
dional plane as shown in Figure 34 . A detailed derivation of
the meridional plane flow equations is given in Appendix I of
reference 2 .

The second phase of solution involves rotating one of
the meridional plane streamlines and its associated streamtube
around the impeller axis to form another stream surface and a
streamtube of revolution. The flow equations are written for
the stream tube of revolution, and their solution yields a blade-
to-blade description of the flow.

One further simplification of the flow equations for
the streamtube of revolution was derived that allowed additional
reduction of problem time. The simplification is accomplished
by applying a number of conformal transformations to the flow
equations. The advantage of performing the transformations is
realized when several different flow conditions in a pump re-
quire fluid-dynamic description. Once the coordinate trans-
formation is performed, all pump operating conditions are analyzed
in the simplified coordinate system. Derivations of the stream
tube of revolution flow equations and the accompanying coordinate
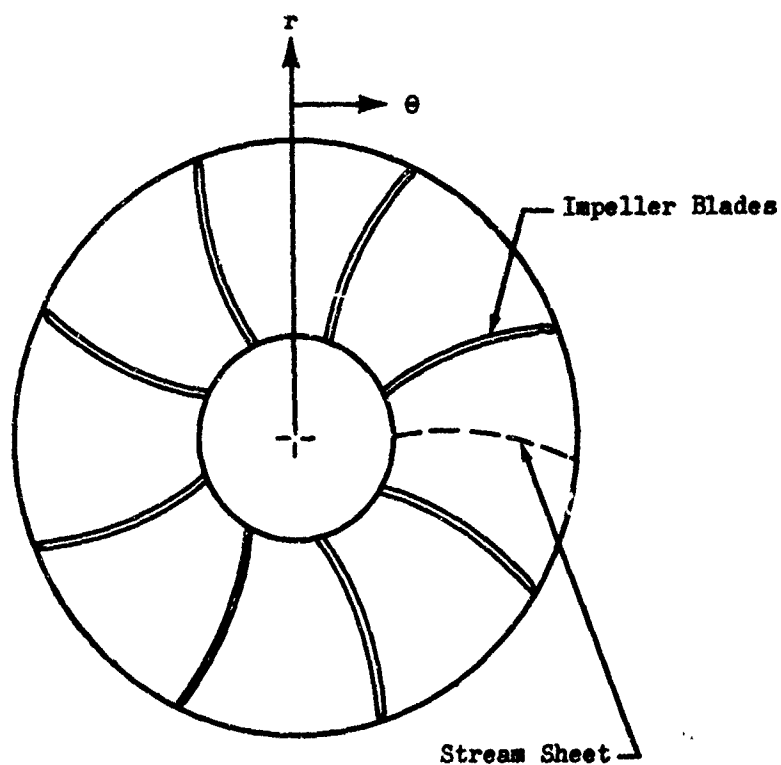transformations are given in reference 1 .

Figure 33   Axial View of Impeller
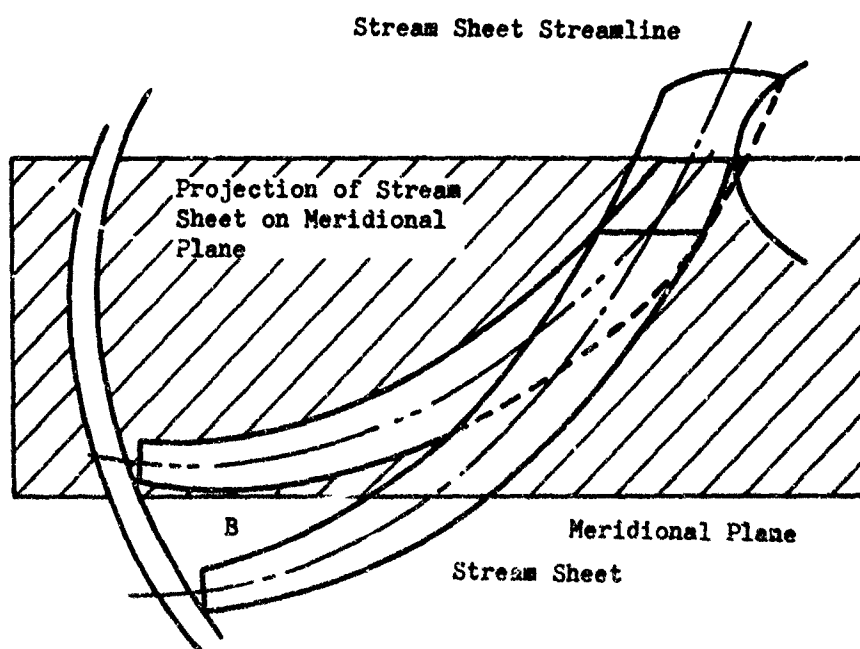
Figure 34   Projection of Stream Sheet on Meridional Plane

Solution to the flow equations for both the meridional plane and the streamtube of revolution is accomplished by numerical procedures. Due to the potentially large number of flow conditions that might require examination for a given pump and the large number of calculations required for a single solution, the problems were programed for the digital computer using Fortran IV language. For this investigation, two programs were written. The first program performs the coordinate transformations mentioned above. The second program combines the streamtube of revolution flow equations with a thermal equilibrium cavitation model to give a blade-toblade description of the compressible flow problem.

c . Cavitation Compliance Problem Solution. Using the equation and computer program development described above the turbopump nonseparated flow, thermal eauilibrium cavitation compliance is evaluated as follows:

The meridional plane flow equations are used along with the impeller geometry and pump inlet conditions to obtain a description of the flow streamlines in the meridional plane. The succeeding step of the analysis involves selection of a particular streamline in the meridional plane and defining as a function of radius the width of its associated stream tube (distance between streamlines adjacent to the chosen streamline) and angle α the streamline makes with the impeller axis. These quantities are tabulated along with coordinates of the impeller blades and constitute input data for the coordinate transformation program. The coordinate transformation program transforms the input data from the R, Θ, Z coordinates to the E, F plane and subsequently to the ζ, η plane. An example of the transformations is shown in Figures 35 thru 38 .

Figure 35 shows the pump blades in the r, Θ plane. Figure 37 shows the blades transformed to the E, F plane. Also shown are the ζ, η coordinates. Figure 38 shows the blades in the ζ, η plane where it is seen that they are parallel, flat, and of zero thickness.

Following the coordinate transformation, the two phase flow problem is solved in the ζ, η plane, utilizing the compressible flow program described in appendix I of reference 2 The two equations that yield the ζ, η plane solution are:

66

Figure 35 Pump Blades - r, θ Plane
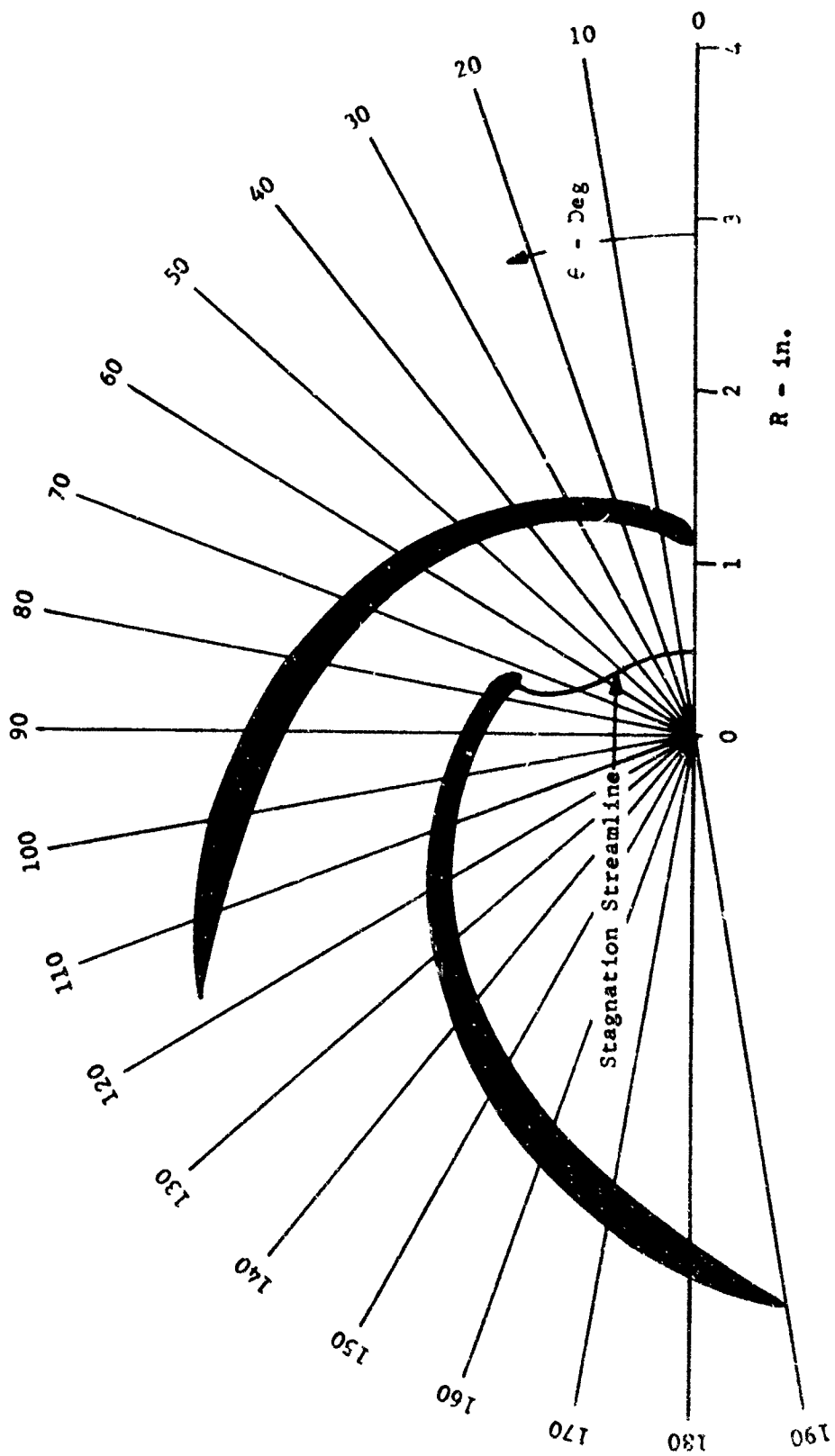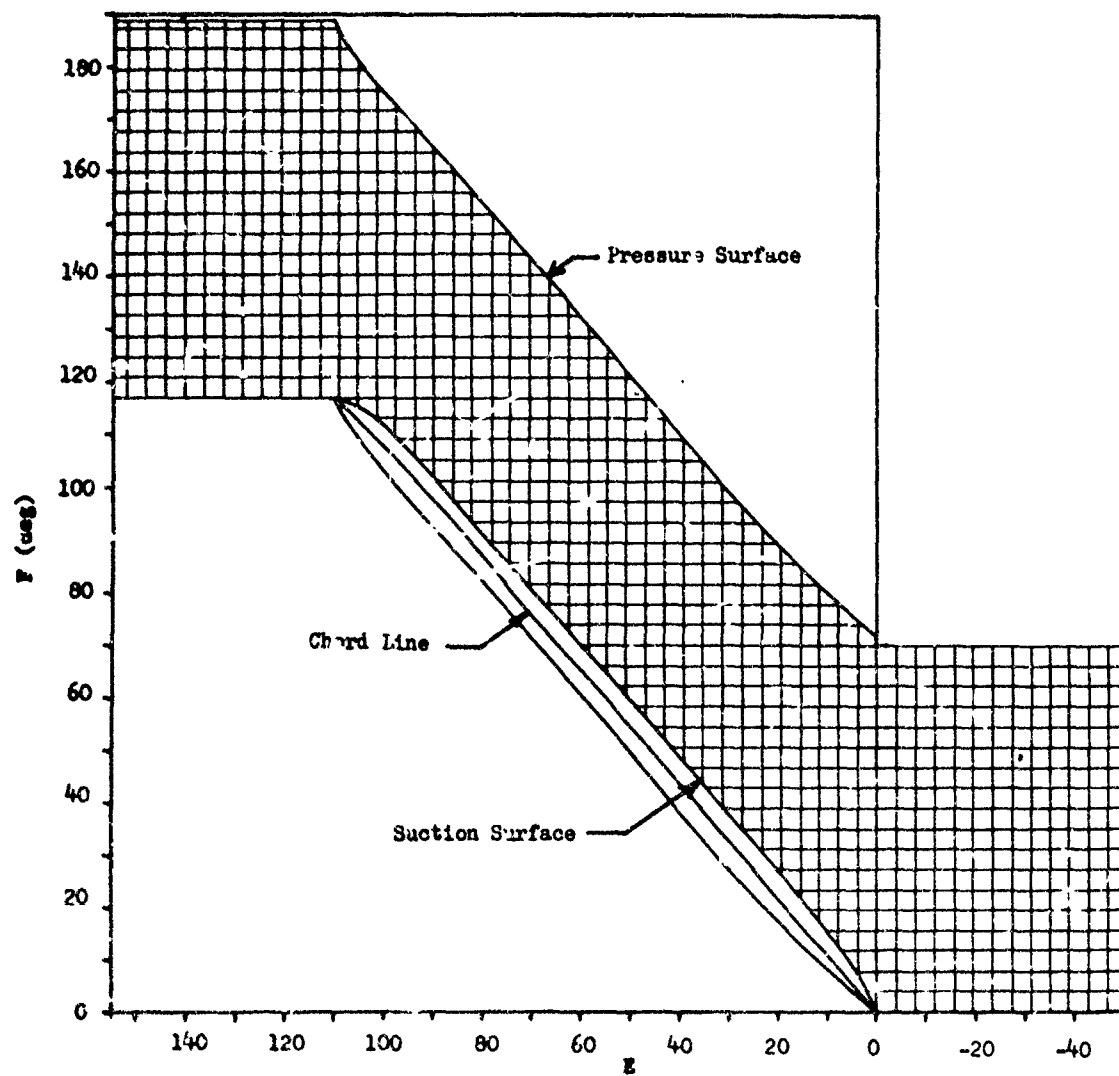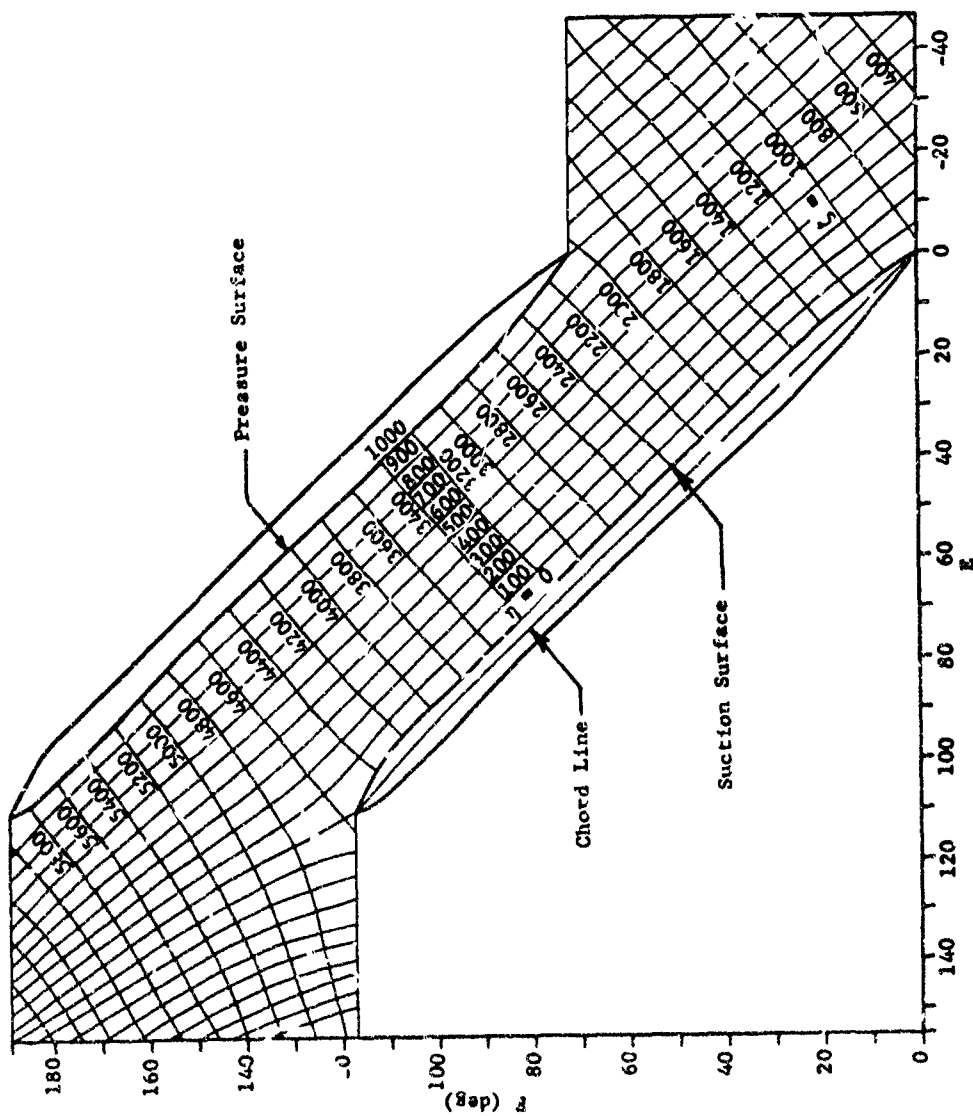
Figure 36 Relaxation Gridwork

Figure 37 Pump Blades - E, F Plane

69
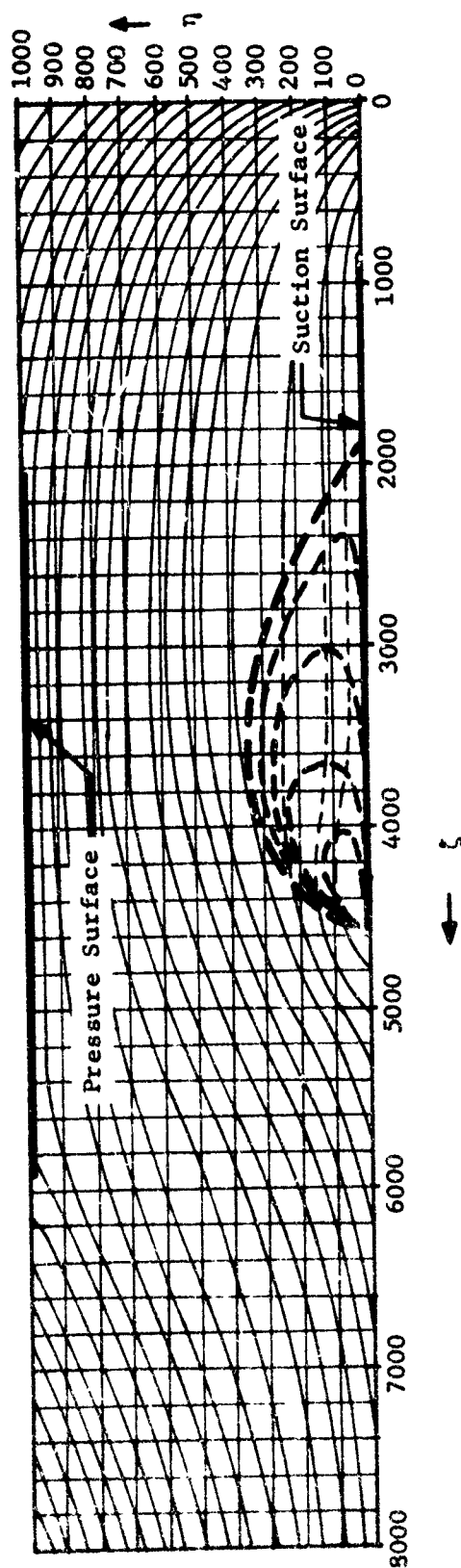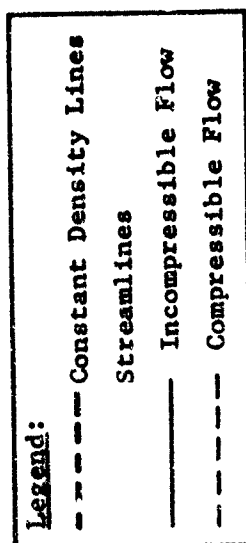
Figure 38   Pump Blades — η, ζ Plane

$$\frac{\partial^2 \psi}{\partial \zeta^2} + \frac{\partial^2 \psi}{\partial \eta^2} - \frac{\left(V_i \frac{\partial \psi}{\partial \zeta} - U_i \frac{\partial \psi}{\partial \eta}\right)}{U_i^2 + V_i^2}\left[V_i \frac{\partial}{\partial \zeta}\left(\ell n\ b\right) - \dot{U}_i \frac{\partial}{\partial \eta}\left(\ell n\ b\right)\right]$$

$$-\left[\frac{\partial \psi}{\partial \zeta} \cdot \frac{\partial}{\partial \zeta}\left(\ell n\ \rho\right) + \frac{\partial \psi}{\partial \eta} \cdot \frac{\partial}{\partial \eta}\left(\ell n\ \rho\right)\right] = \frac{2r^2 \cdot \omega \cdot b \cdot \rho \cdot \sin\alpha}{U_i^2 + V_i^2} \quad (40)$$

$$h(\rho) - \frac{(\omega r)^2}{2\zeta} + \frac{1}{8\zeta}\left(\frac{1}{\rho br}\right)^2\left(U_i^2 + V_i^2\right)\left[\left(\frac{\partial \psi}{\partial \zeta}\right)^2 + \left(\frac{\partial \psi}{\partial \eta}\right)^2\right]$$

$$= H_{0_u} + \frac{\omega \lambda}{g} \quad (41)$$

where the quantities U_i, V_i, b, r, and $\sin\alpha$ are defined in the reference and are generated by the coordinate transformation program. The relationship between density and enthalpy in Equation 41 is obtained from the thermodynamic properties of the working fluid. For pressures below the saturation pressure (corresponding to the fluid bulk temperature) a relationship similar to that shown in Figure 39 can be obtained. For pressures above the saturation pressure, the flow is considered imcompressible.

Completion of the solution requires transforming the streamlines and density lines from the ζ, η plane to the E, F plane and finally to the R, Θ, Z coordinates where the relative volumes of vapor and liquid can be assessed along with pump discharge conditions.

2. STATUS OF ANALYSIS

The pump modeling phase of the program is currently involved with debugging of the compressible flow program and generation of density pressure relationships for various pump fluids.

Following the debugging operation it will be necessary to checkout both the coordinate transformation program and the compressible flow program. Part of the phase I effort has been devoted to compiling fluid properties from which pressure-density relations could be formulated. These functions will be necessary input to the compressible flow program. Figures 39 and 40 present the variation of density with pressure for water and $N_2 O_4$ respectively.
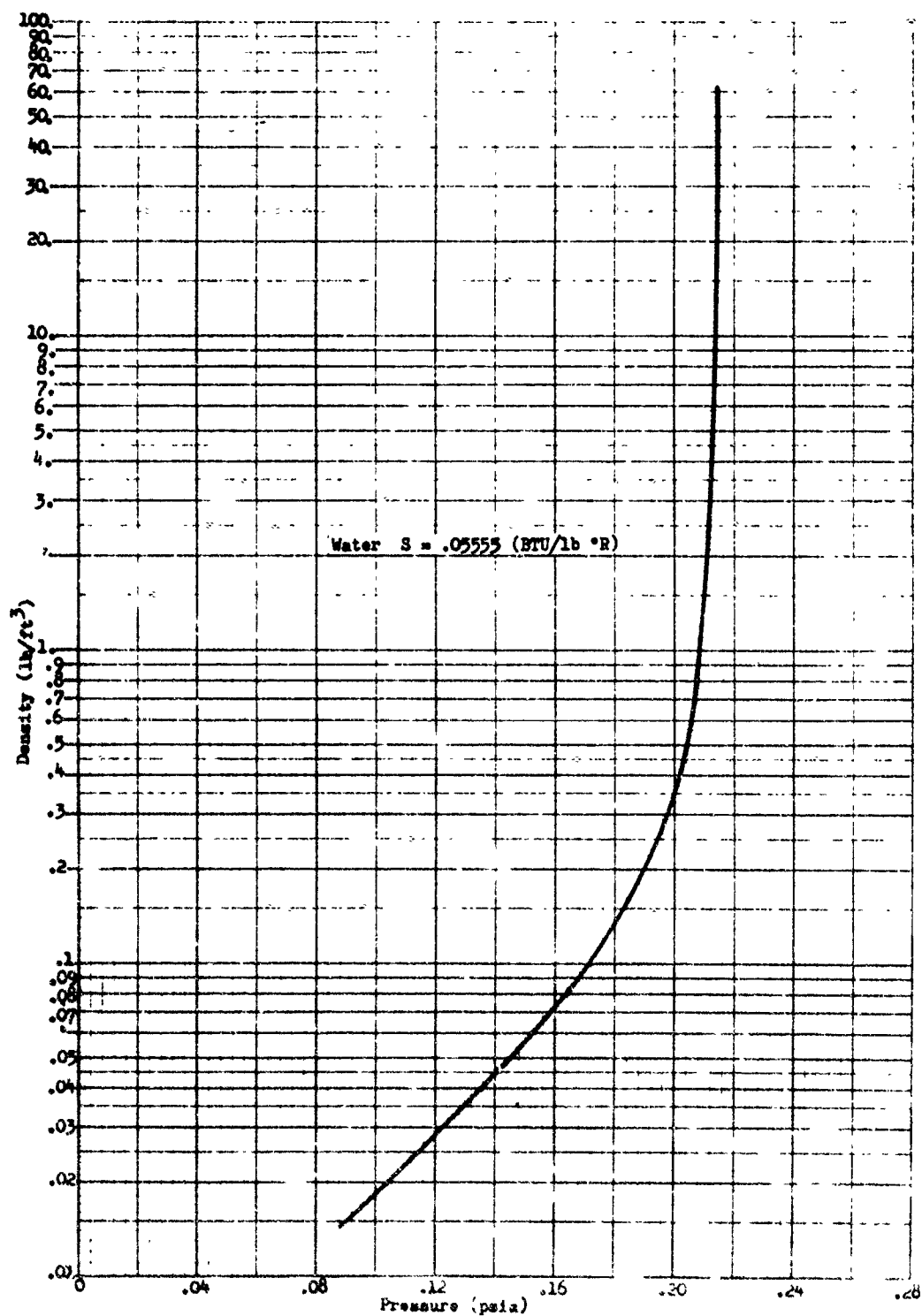
Figure 39   Density-Pressure Variations for Isentropic Expansion Process
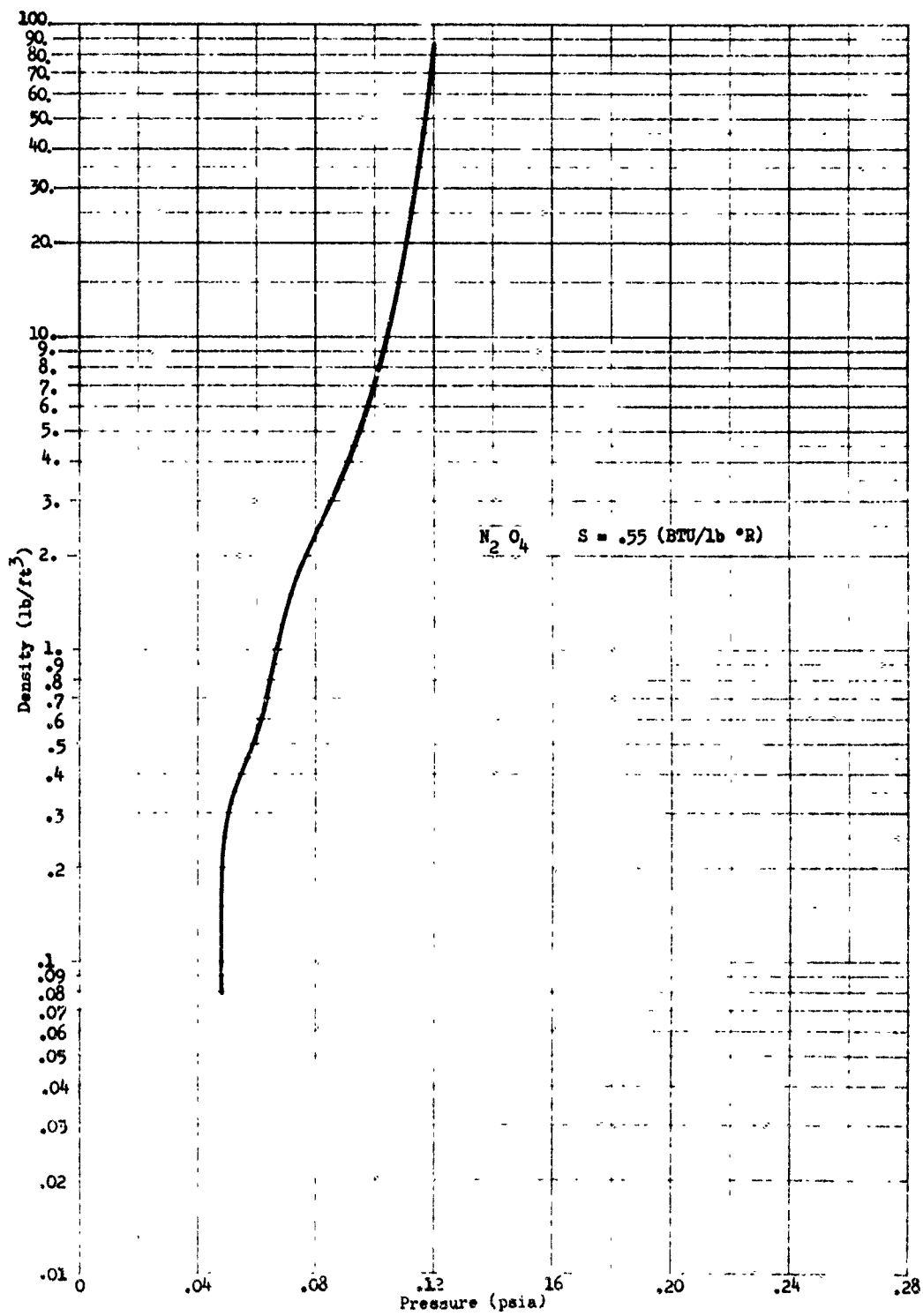
Figure 40 Density-Pressure Variations for Isentropic Expansion Process

Both functional relationships are bases on isentropic processes below the saturation curve.

Additional work has been done during the phase I program to try and locate a pump impeller geometry and sufficient cavitation test data which can be used for program checkout. This work is continuing at present.

3. CONCLUSIONS

In order to obtain additional understanding of turbopump operation under cavitation conditions and at the same time provide means of assessing the quantity of vapor participating in the cavitation process, the development of a two-phase flow turbopump model is essential. The model should relate as closely as possible the thermodynamic and fluidmechanic processes occurring in the pump so that the more sensitive parameters in the system and their effect on the POGO Problem can be recognized. The model described herein is a start in this direction; however, due to the broad range of flow conditions possible, the model will apply only to certain pump operating conditions. Additional improvements will be necessary to describe some of the dynamic pump performance characteristics and their relation to the suction system continuity functions. The amplitude limiting analysis performed in this program has adequately demonstrated the difference in dynamic and steady state pump operation along with the need for a realistic continuity relationship for the suction system.

If the gas injection concept of POGO control is pursued to any depth, it will become necessary to evaluate the effects of injected gas in the suction line and pump on reducing suction line natural frequency as wel as assessing its influence on pump performance. Here again a two-phase flow model will become necessary.

Based on the many potential uses and needs for a turbopump cavitation flow model, it is recommended that the development described in the preceding paragraphs be continued in the phase II effort culminating with the mapping of a turbopump and correlation of test and analysis results.

SECTION VII

STATISTICAL GAIN MARGIN STUDIES

1. DESCRIPTION

The primary result of this study is the development of a
method which relates a mean gain margin to a probability of
stability particularly as applied to the POGO model. In the
mathematical description of any physical system, there are
parameters which are inaccurately known, or are known only
within broad limits. Parameter uncertainties make it diffi-
cult to determine system stability when a "worst case" stabili-
ty analysis indicates instability and the system is stable
using mean parameter values. For systems of this kind, a
qualitative measure of stability is needed. Gain margin is
a qualitative measure of stability, but is of little use when
mean parameter values produce marginally stable results. It
seems reasonable to assume a more natural approach is to com-
pute an actual probability of stability. Then knowing this
number, it is easy to predict from N flights, the number
expected to be stable. For simple systems it is possible to
compute a probability analytically; however, for complex
systems, an analytic computation of a probability of stability
becomes impossible. Hence the analytical approach must be
abandoned in favor of a computer oriented Monte Carlo technique
if an answer is to be obtained. The Monte Carlo approach for
computing the probability of stability is conceptually equiva-
lent to flying a large number of missiles; tabulating those
which are stable; and computing the probability of stability,
i.e., the ratio of the stable missiles to the total number
flown. Specifically, each system parameter which is identified
as being uncertain is assumed to be either uniformly or normally
distributed with mean equal to the design or nominal value and
variance determined either from statistical considerations, e.g.,

$$\sigma^2 = \frac{1}{N-1} \sum_{i=1}^{N} (X_i - \text{mean})^2$$ or empirically. Parameters which are

related functionally to statistical parameters are assumed to
be totally dependent, i.e., once the statistical parameter has
been chosen from a distribution, its value completely determines
the value of the functionally related parameter. During each
iteration of a Monte Carlo run, all statistical parameters are
drawn from their respective distributions and are inputed along

75

with the deterministic parameters into the mathematical model.
The gain margin is then computed, and the system stability is
determined and tabulated. After a suitable number of itera-
tions, (typically about 200) the probability of stability,
mean gain margin and variance are computed and printed. In
addition, a histogram of the gain margin is plotted. The gain
margin histogram, properly normalized, is a probability density
function of the gain margin.

a. Objection to conventional gain margin

A possible objection to the above approach is that
the computed gain margin histogram depends on where the feed-
back loop is opened. In multiloop feedback systems, the gain
margin does indeed depend on where the loop is opened and is
not a unique indication of stability. However, it is true
that a stable or unstable system is accurately determined
regardless of where the measurement is taken, i.e., where the
loop is opened. Therefore, as the feedback loop is opened at
various places, the resulting gain margin histogram will be
different but the resulting probabilities of stability remain
constant. In other words, the probability of stability
remains an invariant function of where the loop is opened,
whereas the gain margin histogram is not.

2. MATHEMATICAL MODEL

Previous analyses concerning POGO were performed using
the system equations in second order form. For instance, to
compute the gain margin, the system equations are written as

$$Ay = f \qquad (42)$$

where y and f are column matrices and A is an $n \times n$ matrix with
typical elements of the form $A_{ij}s^2 + B_{ij}s + C_{ij}$. By setting
$s = j\omega$, the elements of A become complex constants. A complex
matrix inversion followed by a complex multiplication yields
the solution

$$y = A^{-1}f \qquad (43)$$

76

A frequency sweep for the open loop transfer function $P_{c_{out}}/P_{c_{in}}$ is terminated when the phase of this expression approaches zero. The resulting number is the zero phase gain (ZPG), from which gain margin follows directly.

a. Gain Sensitivity

To study the variation of the gain margin with respect to certain critical system parameters, it is first necessary to determine what system parameters are critical. One possible approach is to increment each parameter individually and compute the change in gain margin. Those parameters which result in a large change in the gain margin are the critical parameters. A better and computationally more efficient approach is to compute the eigenvalue sensitivities, i.e., the change in the system eigenvalues divided by the change in a system parameter. Such an approach, however, requires the system to be represented in first order differential form; that is the system represented by Equation 42 must be rewritten in closed loop form as

$$\dot{x} = Ax \tag{44}$$

Then to compute the sensitivities of Equation 44 requires solving Equation 45 .

$$\frac{\partial \lambda_i}{\partial a} = \frac{\langle \frac{\partial A}{\partial a} x_i , v_i \rangle}{\langle x_i , v_i \rangle} \tag{45}$$

where λ_i = system eigenvalue

x_i = right hand eigenvector

v_i = left hand eigenvector

and x, y represents the conventional scalar or inner product of two vectors. The derivation of Equation 45 is given in Appendix IV.

Table I   Typical Eigenvalue Sensitivities for Simplified Model

Eigenvalue	Sensitivity with respect to	Eigenvalue Sensitivity
$-403.8 + j0$	ω_A	$1.2 \times 10^{-10} - j9.2 \times 10^{-8}$
$-403.8 + j0$	ω_{so}	$1.31 + j6 \times 10^{-6}$
$-403.8 + j0$	ω_{sf}	$0 + j0$
$-443.9 + j0$	ω_A	$-2.9 \times 10^{-8} - j5.28$
$-443.9 + j0$	ω_{so}	$1.8 + j1.6 \times 10^{-3}$
$-443.9 + j0$	ω_{sf}	$0 + j0$
$-2.3 \pm j119.2$	ω_A	$-9.5 \times 10^{-4} - j3.2 \times 10^{-4}$
$-2.3 \pm j119.2$	ω_{so}	$-5.2 \times 10^{-3} - j4.29 \times 10^{-3}$
$-2.3 \pm j119.2$	ω_{sf}	$1.43 \times 10^{-2} + j1.81$
$.54 \pm j63.1$	ω_A	$.18 - j2.51$
$.54 \pm j63.1$	ω_{sf}	$.18 - j1.3 \times 10^{-2}$
$.54 \pm j63.1$	ω_{so}	$-1.0 \times 10^{-2} + j2.07$
$-21.2 \pm j58.0$	ω_A	$-.83 - j1.04$
$-21.2 \pm j58.0$	ω_{sf}	$31.4 + j2.01$
$-21.2 \pm j58.0$	ω_{so}	$-1.4 \times 10^{-1} + j.65$
$-103.6 + j0$	ω_A	$-4.0 \times 10^{-12} + j5.4 \times 10^{-12}$
$-103.6 + j0$	ω_{sf}	$-2.42 \times 10^{-6} + j3.4 \times 10^{-6}$
$-103.6 + j0$	ω_{so}	$6.36 \times 10^{-2} + j1.6 \times 10^{-3}$
$-106.7 + j0$	ω_A	$3.4 \times 10^{-10} - j6.38 \times 10^{-10}$
$-106.7 + j0$	ω_{sf}	$2.02 \times 10^{-4} - j4.12 \times 10^{-4}$
$-106.7 + j0$	ω_{so}	$2.75 \times 10^{-3} - j3.68 \times 10^{-4}$

In theory it is always possible to transform Equation 42 into Equation 44 at least via a computer program. This, however, is unacceptable for in the execution of Equation 45 , matrix A is required to be in analytical form so that the expression $\partial A / \partial a$ can be evaluated. It was possible to analytically transform from Equation 42 to Equation 44 for a simplified POGO model (see Appendix V) but not for the more complicated model. The sensitivity analysis was performed with the model described in Figure 41 and the results are described below. Three system parameters were identified as being most sensitive. The selection process was arrived at by computing the eigenvalue sensitivities of all system parameters appearing in the simplified POGO model and choosing the three most sensitive, which in this case were identified as the mode A structural frequency ω_A, fuel suction line frequency ω_{sf} and the oxidizer suction line frequency ω_{so}. The simplified POGO model is described in ten first order differential equation; hence, the sensitivity analysis relates to the ten associated eigenvalues. The results are shown in Table I. Only seven eigenvalues are shown in Table I since three of the eigenvalues are complex and the sensitivity of the two complex conjugate poles are identical. Of the ten POGO system eigenvalues, two are apt to be unstable depending on the configuration being studied. The roots located at $+.542 \pm j63.1$ are unstable and have sensitivities of $+.18 - j2.5$, $+.18 - j0.013$, and $-0.01 + j2.07$ with respect to the parameters, ω_A, ω_{so} and ω_{sf} respectively.

This indicates the magnitude and direction of the change in the eigenvalue divided by the change in a system parameter. The most critical parameter then, for the unstable eigenvalue, is ω_A.

3. RANDOM NUMBER GENERATOR

The random number generator used in the Monte Carlo gain margin study is based on a recurrence relationship involving integers. Two uniform distributions are generated on the interval 0 to 1. A change of variables is then made which transforms these two uniform distributions into a normal distribution with specified mean and variance. The generation of the uniform distributions is discussed in Appendix VI.

4. RESULTS OF ANALYSIS

The dynamical model used for the Monte Carlo statistical
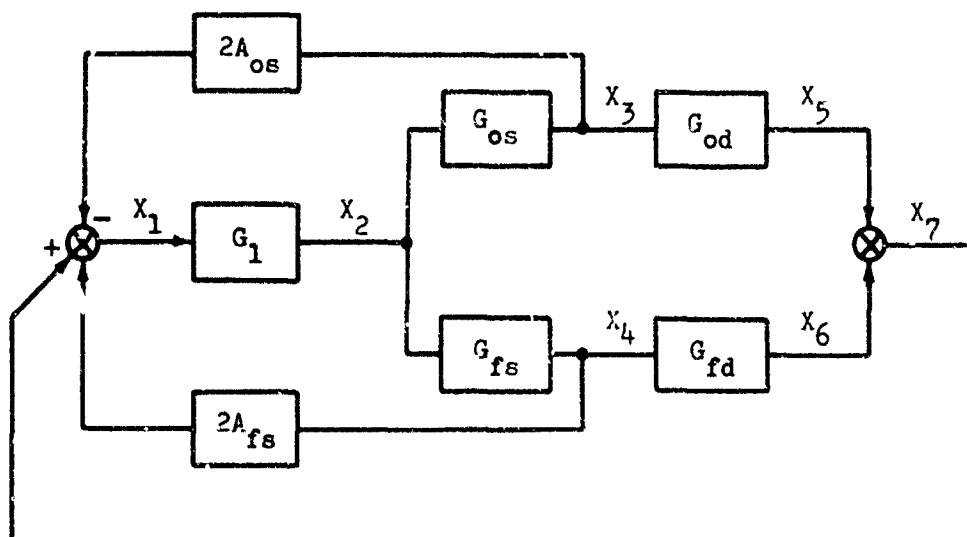
Figure 41 Simplified POGO Model

where:

G_1 = Structural response characteristic

G_s = Suction line response characteristic

G_d = Discharge line response characteristic

A_o = Suction line area at pump inlet

80

gain margin studies was developed during analysis of the Titan II and III POGO problems. A T-III MOL configuration was chosen to illustrate the statistical stability analysis for the following reasons;

1) all necessary parameter values were readily available from previous studies;

2) the results of the study are useful for the MOL program;

3) much of the data taken from Titan II flights is applicable for determining the means and variances for Titan III parameters.

The Titan III POGO math model is written in the form of Equation 44 with the dimension of the A matrix, in the uncompensated configuration, equal to 13. The uncertain quantities which may be inputed into the A matrix at each iteration of a Monte Carlo run are: g_A, g_B, g_C, g_D (mode A, B, C, D structural gain), ω_A, ω_B, ω_C, ω_D (mode A, B, C, D, structural frequency), ζ_A, ζ_B, ζ_C, ζ_D, (mode A, B, C, D damping ratio), NPSHO (net positive suction head of oxidizer, and NPSHF (net positive suction head of fuel). The model developed for the present study treats pump gain (K_p) and suction line frequency (ω_s) as functions of NPSH.

For typical values of the means and variances imputed into a Monte Carlo run, see Table II . Variables with zero deviations are set equal to their mean value. Since, in most cases, flight data is not available for structural gains, frequencies, and damping ratios, a heuristic approach was used in determining their statitistical properties. Mean values are taken as the design value and variances were determined by using estimates of prediction accuracy for structural parameters such as frequency and gain. All statitistical variables used in this study were assumed to be gaussian or normally distributed. The option is available however to use uniform distributions if desired. The mean and variance for the NPSH fuel and oxidizer variables are determined from the equations

81

Table II Independent Input Variables

		Titan III @ 100 sec	
Symbol	Symbol Definition	Mean	Deviation
GAINA	Mode A Structural Gain x 10^6	3.14	1.05
GAINB	Mode B Structural Gain x 10^6	8.20	0
GAINC	Mode C Structural Gain x 10^6	1.04	0
GAIND	Mode D Structural Gain x 10^6	.0084	0
OMEGA	Mode A Frequency hz	9.4	.31
OMEGB	Mode B Frequency hz	16.41	0
OMEGC	Mode C Frequency hz	14.30	0
OMEGD	Mode D Frequency hz	26.87	0
ζ_A	Mode A Damping Ratio	0.01	.0033
ζ_B	Mode B Damping Ratio		
ζ_C	Mode C Damping Ratio		
ζ_D	Mode D Damping Ratio		
NPSHO	Net Positive Suction Head (Oxidizer)	81.4	17.5
NPSHF	Net Positive Suction Head (Fuel)	32.5	4.18

$$\mu = \frac{1}{N} \sum_{i=1}^{N} NPSH_i \qquad\qquad (\text{o})$$

$$\sigma^2 = \frac{1}{N-1} \sum_{i=1}^{N} (NPSH_i - \mu)^2 \qquad\qquad (47)$$

and may be updated as more flight data becomes available.

   a.   Typical Analysis

   Typical POGO stability analyses are performed using "best estimates" for input quantities. When there is a large uncertainty for a particular input quantity it is chosen in a manner which minimizes the gain margin. This conservative approach is unsatisfactory except when trying to determine the least possible system stability. For example an analysis which predicts stability using average input values and instability using worst case input values leaves unsettled the fundamental question: "Will the vehicle oscillate?" A quantitative judgment of the significance of gain margin can be made by treating the input parameters as random variables with specified distributions. Then the gain margins computed from these input parameters are in turn random variables and their associated probabilities are the desired quantitative results. In most realistic problems, a closed form solution is impossible; and Monte Carlo technique must be used to obtain the probability of stability. The use of a Monte Carlo technique assumes that an infinite population can be adequately approximated by a finite population. This then gives a clue in determining when the number of samples are sufficient large. Determining an adequate number of samples is done by doubling the number of iterations and noting whether the answer changes significantly. After several tests it was determined that 200 iterations appeared to be sufficient to obtain reliable probability estimates.

   b.   Computer Time

   In any iterative scheme programmed on a digital computer a few seconds saved per iteration results in a large time saving per problem. Considerable effort was expended improving the convergence time required to obtain the

zero phase gain. The result was a reduction in convergence time from 2 sec to 0.2 sec per zero phase gain calculation. This is reflected in a computer time saving from 400 sec to 40 sec per Monte Carlo run. Of course, as computers are improved and the arithmetic processors become faster, the time per computation is also reduced; in fact five years ago the same problem would have taken more than 10 minutes compared with 40 sec today.

c.   Results of Typical Run

The main results obtained from a typical statistical gain margin Monte Carlo run are:

1)   a histogram of the zero phase gain; upon normalization the histogram becomes the zero phase gain density function;

2)   the probability of stability;

3)   the sample mean of the zero phase gain;

4)   the sample variance of the zero phase gain;

5)   a listing of the computed zero phase gains.

A histogram is a plot of the number of the zero phase gains contained in a specified interval. The abscissa of the plot is subdivided into N intervals and the number of zero phase gains contained in each interval is tabulated and plotted in the form of a bar graph. Figure 42 displays a typical zero istogram for the Titan III vehicle in the MOL uncompensated configuration at $t = 80$ sec. The interesting aspect of Figure 42 , which is true of all histograms computed (over a hundred), is that it is severely skewed with a long tail from the left and very little from the right. Obviously the zero phase gain density function is not normal even though all the input quantities are normal.

If the zero phase gain histogram were symmetric, the mean of the zero phase gains and the zero phase gain obtained by using the mean input value should coincide. Because the zero phase gain histogram is not symmetric, the mean zero phase gain and the zero phase gain of mean inputs are not identical. Skewing to the left will cause the mean zero phase gain to be less than the zero phase gains of mean inputs and hence reflects a more optimistic picture of vehicle stability than would otherwise be determined.
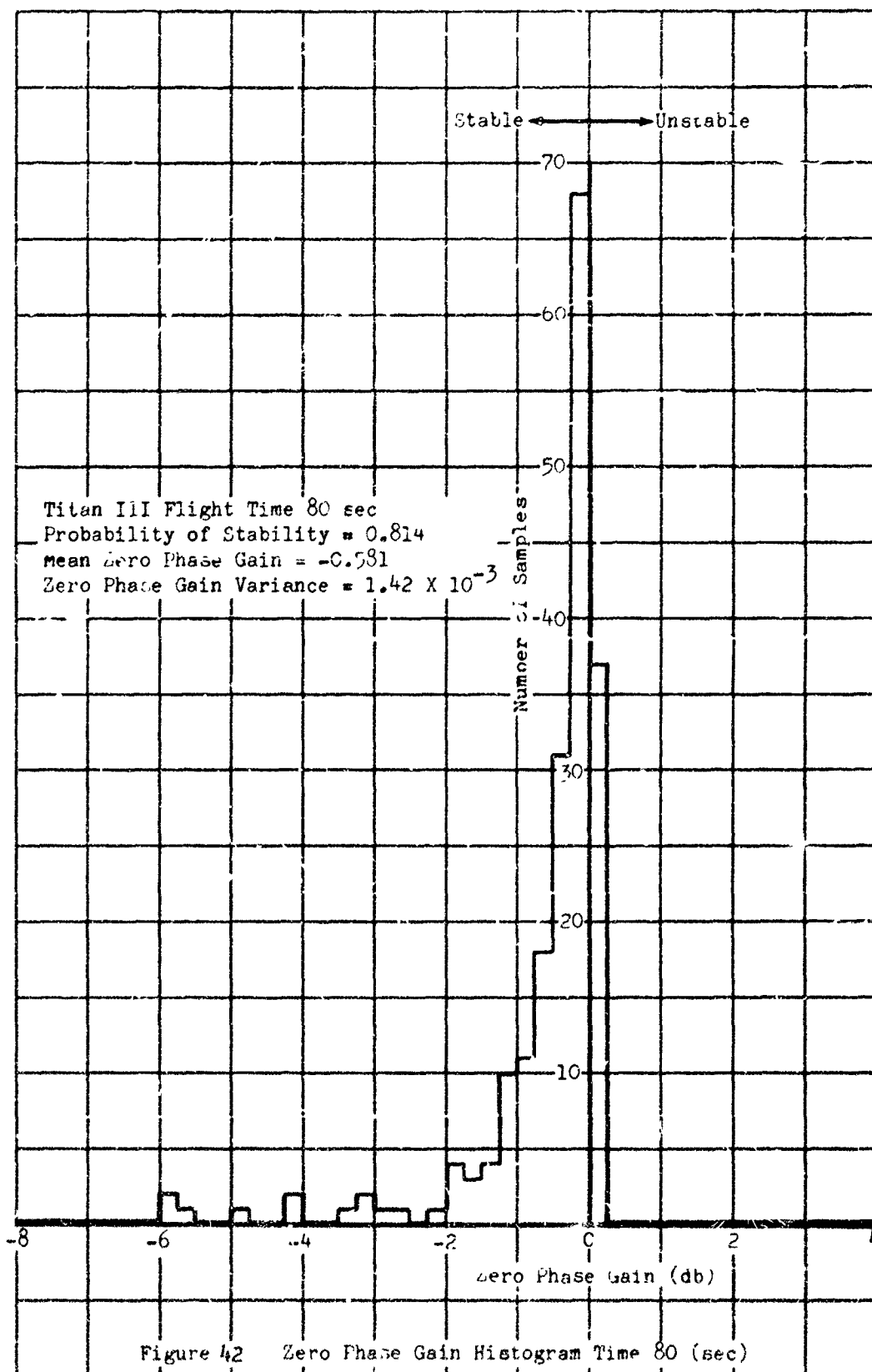
Figure 42   Zero Phase Gain Histogram Time 80 (sec)

85

The mean zero phase gain and the zero phase gain of mean inputs
are compared for several configurations corresponding to
flight time of 80-140 seconds.

Table III A Comparison of Zero Phase Gains

Time	Mean Zero Phase Gain (db)	Zero Phase Gains of Means (db)
80	- .58	0
90	1.13	1.8
100	2.44	3.2
110	3.9	4.4
120	4.49	6.0
130	6.12	6.8
140	6.62	7.2

Histograms corresponding to flight times 90 sec through 140 seconds
are shown in Figures 42, 43, 44, 45, 46 and 47. These figures
reveal that every zero phase gain histogram is skewed to the
left and each succeeding histogram is displaced farther to the
right, i.e., the vehicle tends to be less stable with increasing
flight time. It is noticed that the probability of instability
increases rapidly from t = 80 sec to t = 90 sec even though the
mean zero phase gain changed less than 0.6 of a db. The reason
is obvious upon examining Figures 42 and 43; since the density
function is skewed, a small shift to the right greatly increases
the area to the left of the 0 db line.

    d.   Effects of Shifts in Parameter Means

        The critical system parameters have been identified,
their distributions approximated and a Monte Carlo gain margin
analysis performed. A natural question remaining concerns
what effect the shift in the mean values of critical parameters
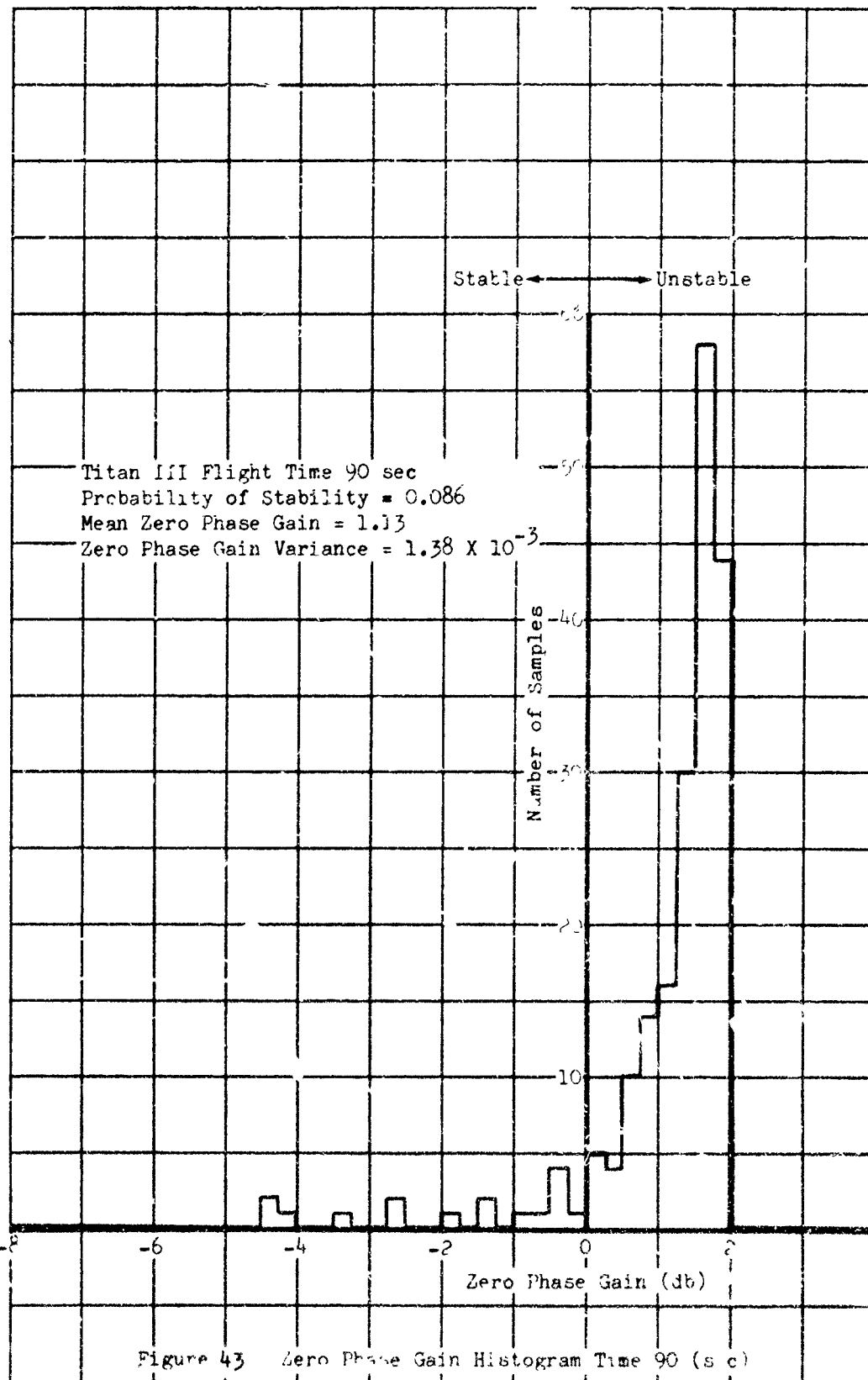has on the zero phase gain distribution shape and mean value.
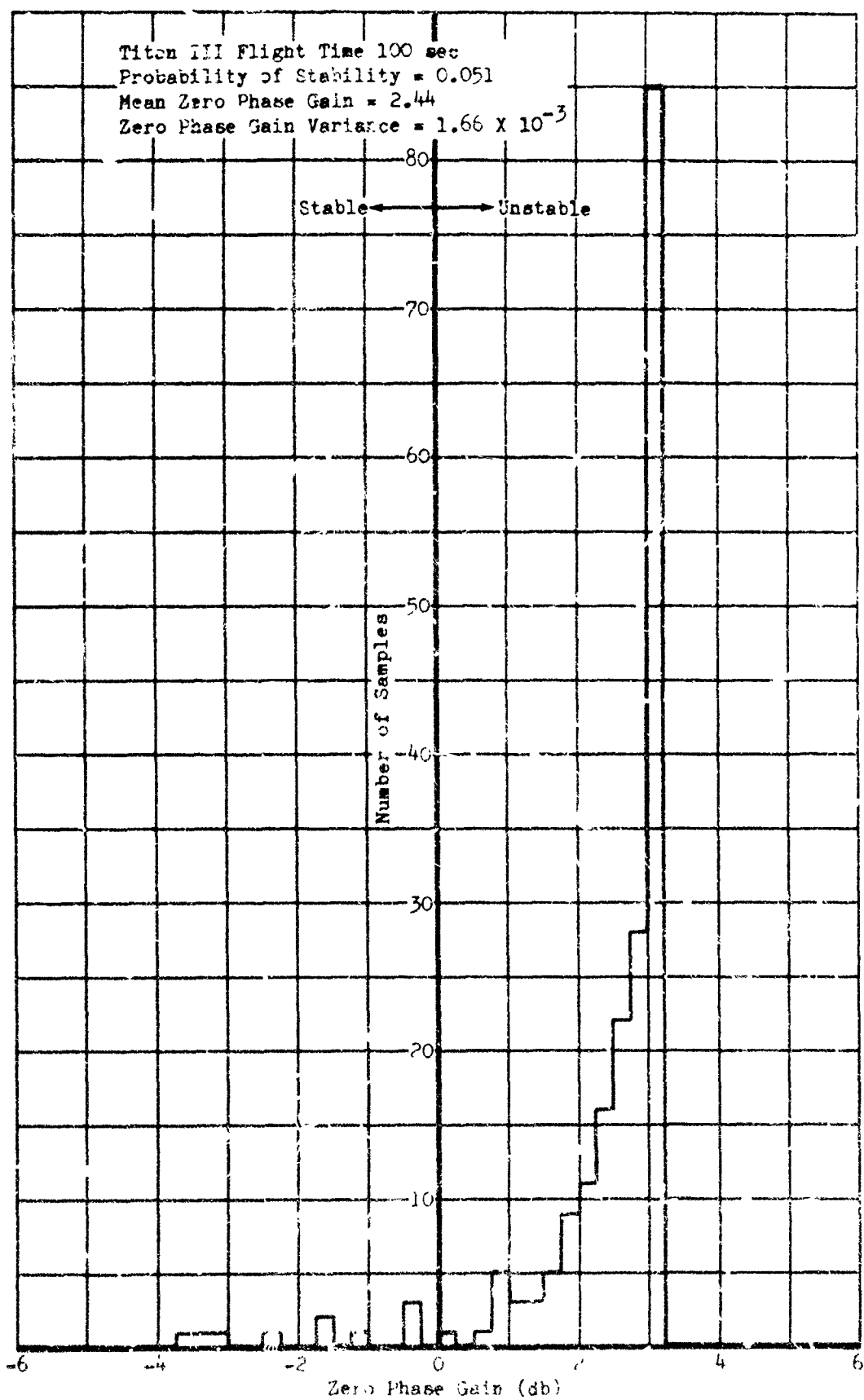
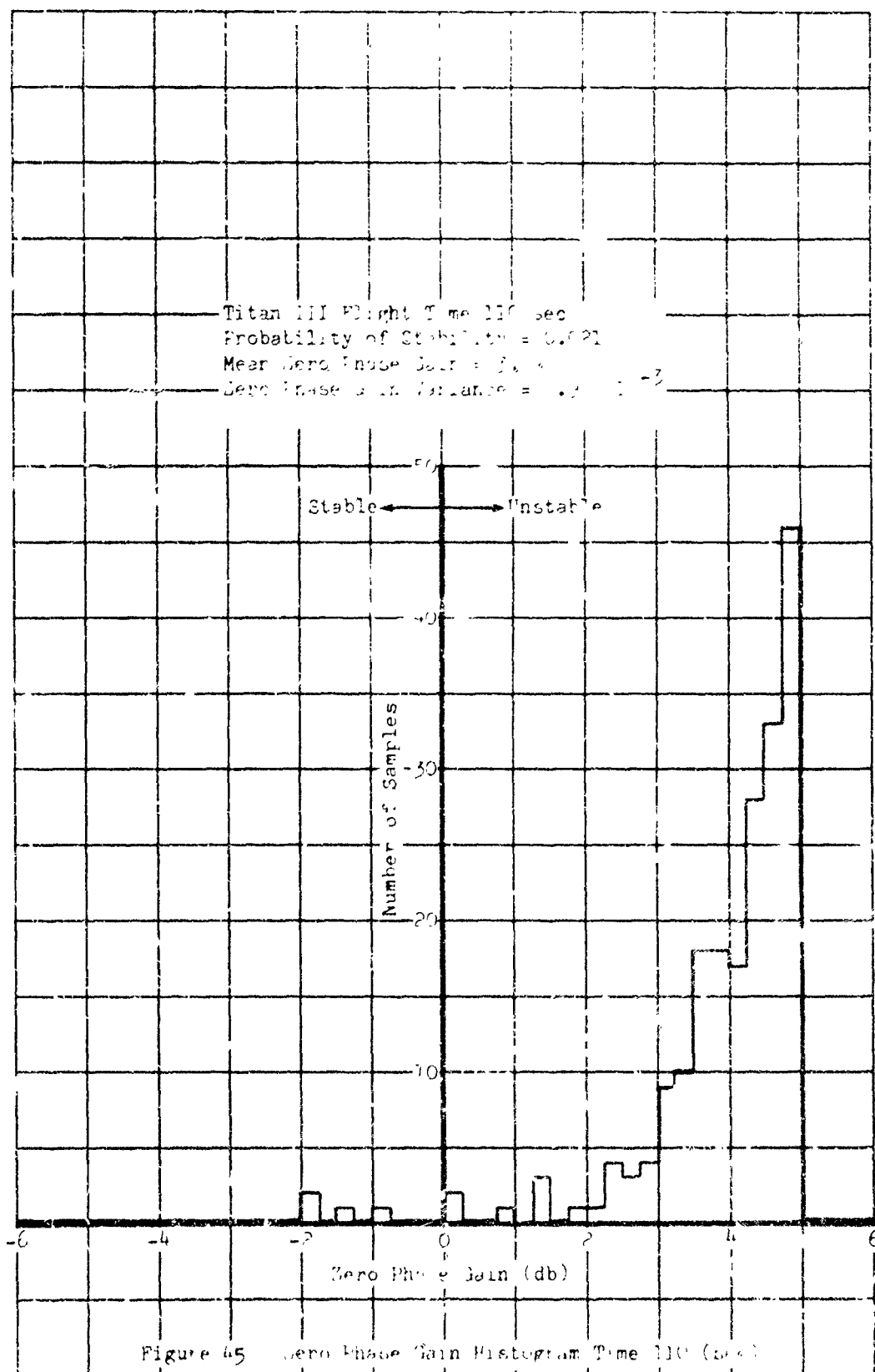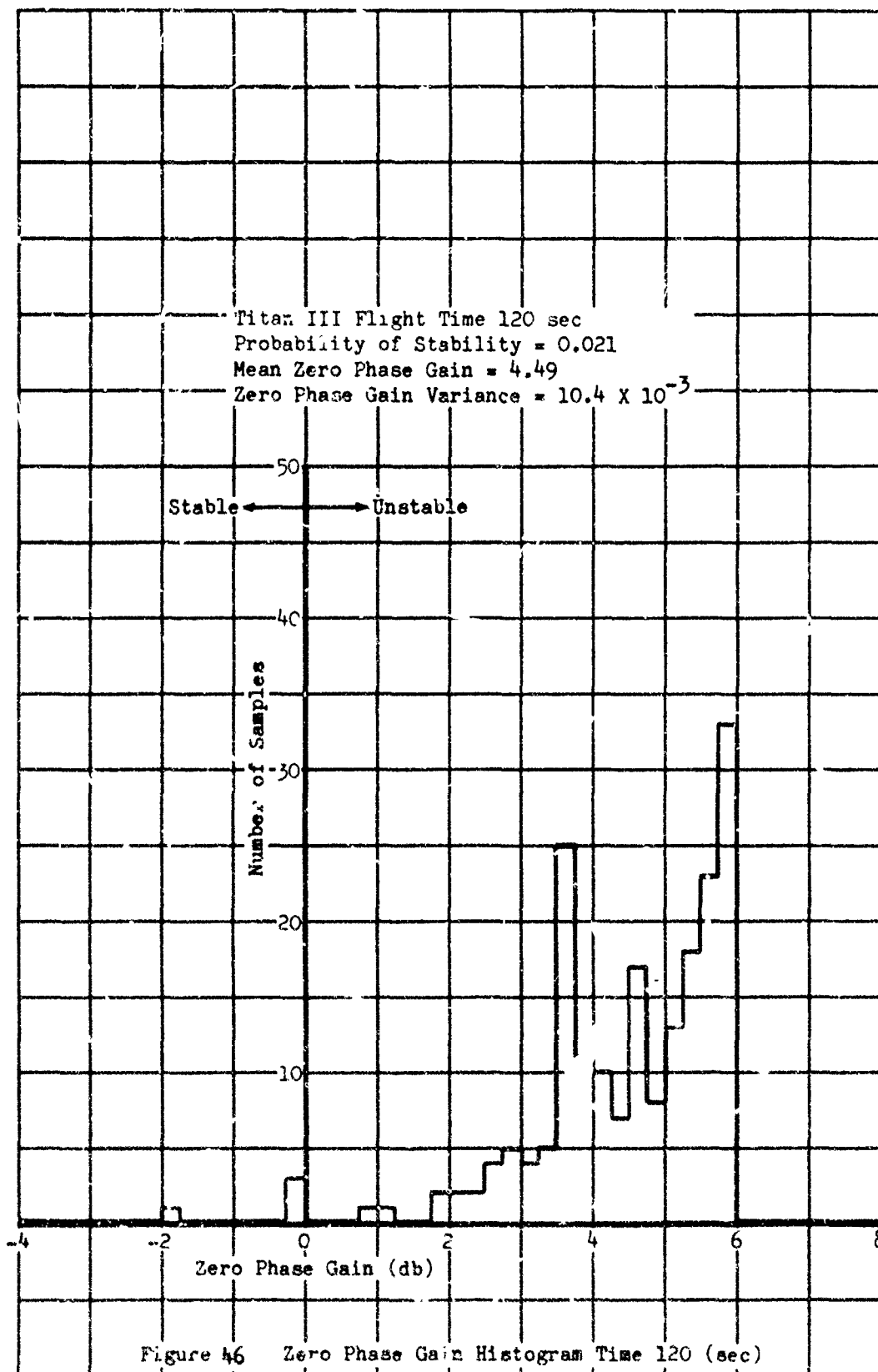Figure 43   Zero Phase Gain Histogram Time 90 (sec)

87

Figure 44   Zero Phase Gain Histogram Time 100 (sec)

Figure 45   Zero Phase Gain Histogram Time 110 (sec)

Figure 46   Zero Phase Gain Histogram Time 120 (sec)

Figure 47 Zero Phase Gain Histogram Time 130 (sec)
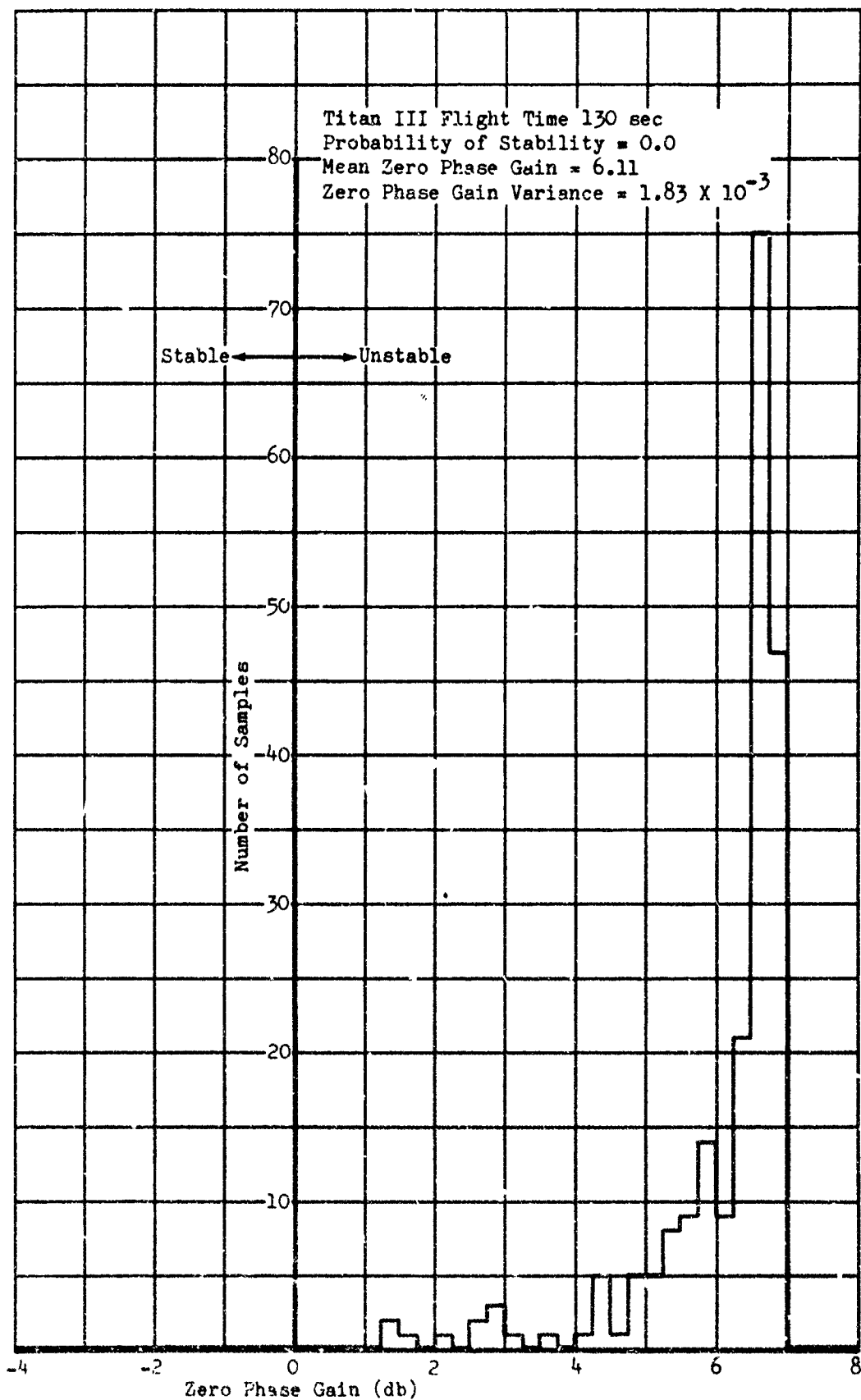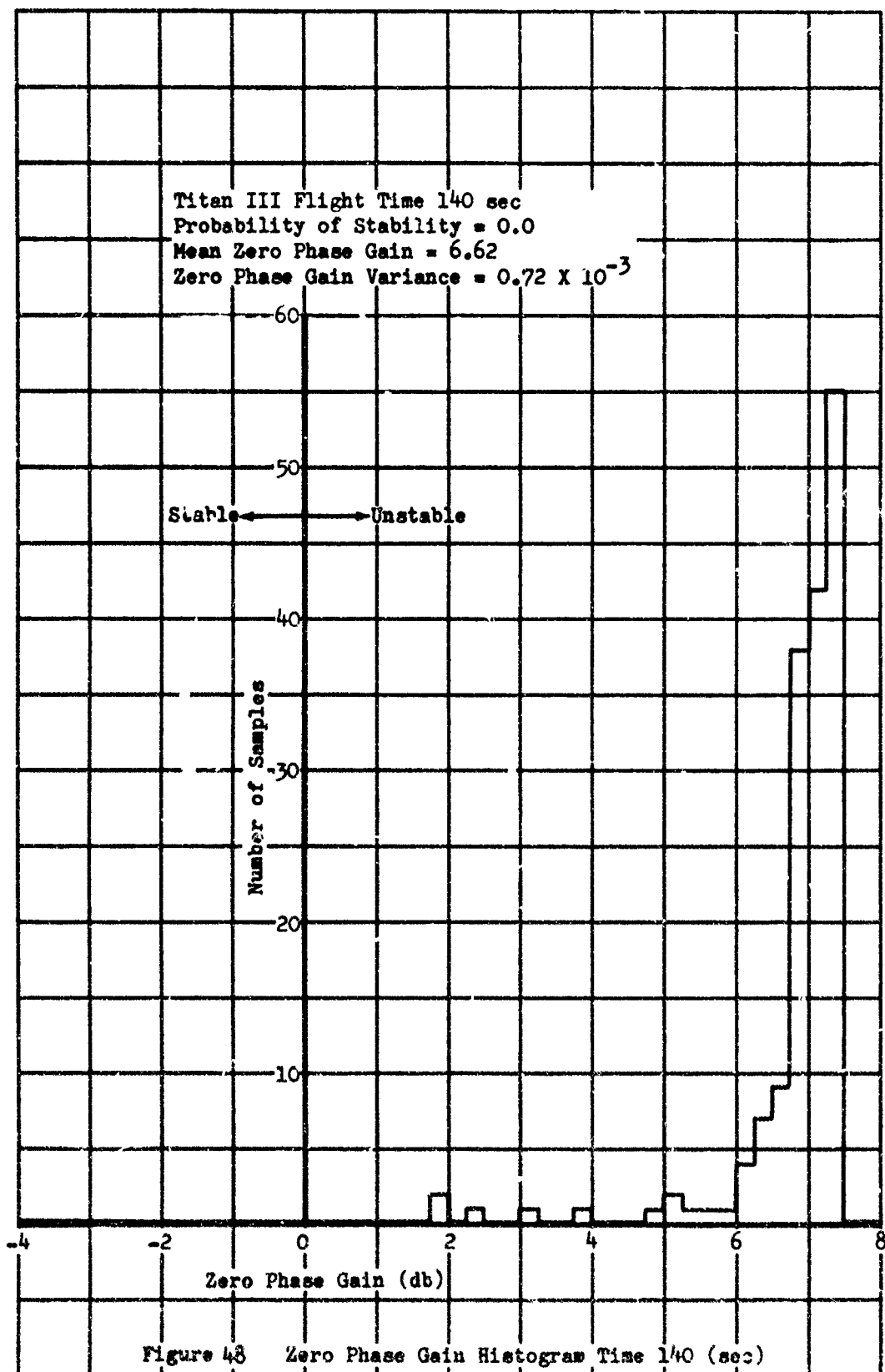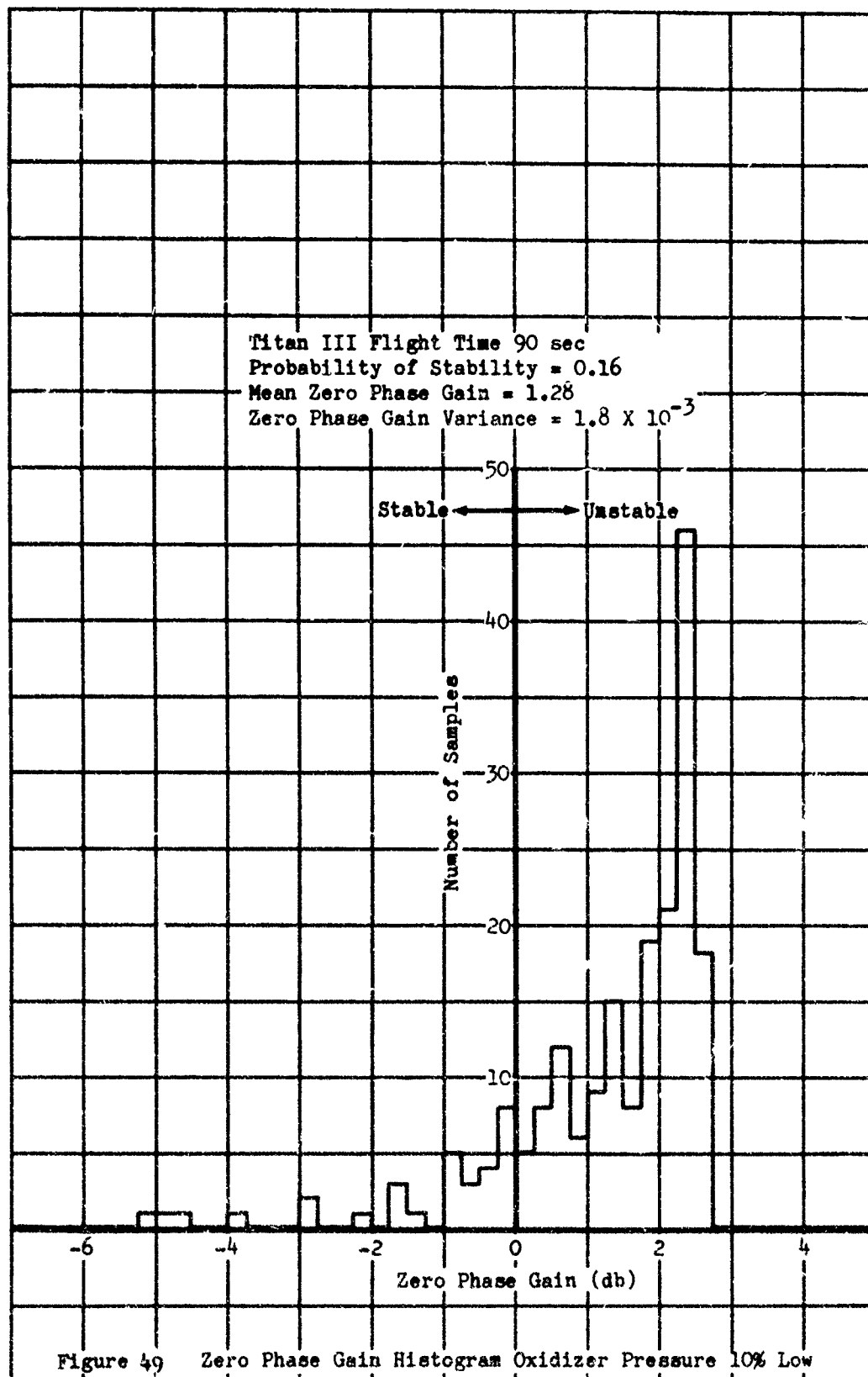
91

Figure 48   Zero Phase Gain Histogram Time 140 (sec)

Accordingly, a Monte Carlo analysis was run with the mean values of ω_A, NPSHO and NPSHF incremented. The results, for a change in the mean NPSHO, are shown in Figures 49 and 50 . Figure 49 shows the zero phase gain histogram with the mean NPSHO 10% low whereas in Figure 50 the mean NPSHO is 10% high. For a decrease in mean NPSHO the mean zero phase gain increased, i.e., the system becomes more unstable; as the mean NPSHO is increased the mean zero phase gain is decreased and the system stability is increased. Also the spread or variance of the zero phase gain density function increases with decreasing NPSHO. A possible explanation is that as the mean NPSHO increases, the separation betwee. structural and suction line frequencies also increases which results in an increased stability margin. Also the variability or the second moment of the zero phase gain density function seems to be highly dependent upon the separation of the structural and suction line frequencies. That is, as the suction line and structural frequencies tend to become equal, a small change in a system parameter results in a large change in the zero phase gain; whereas for the case where the structural and suction line frequencies are widely separated, a small change in a system parameter results in a small change in the zero phase gain. The significance of the above observation relates to the desirability of maintaining a separation between the structural and suction line frequencies when system predictability is concerned.
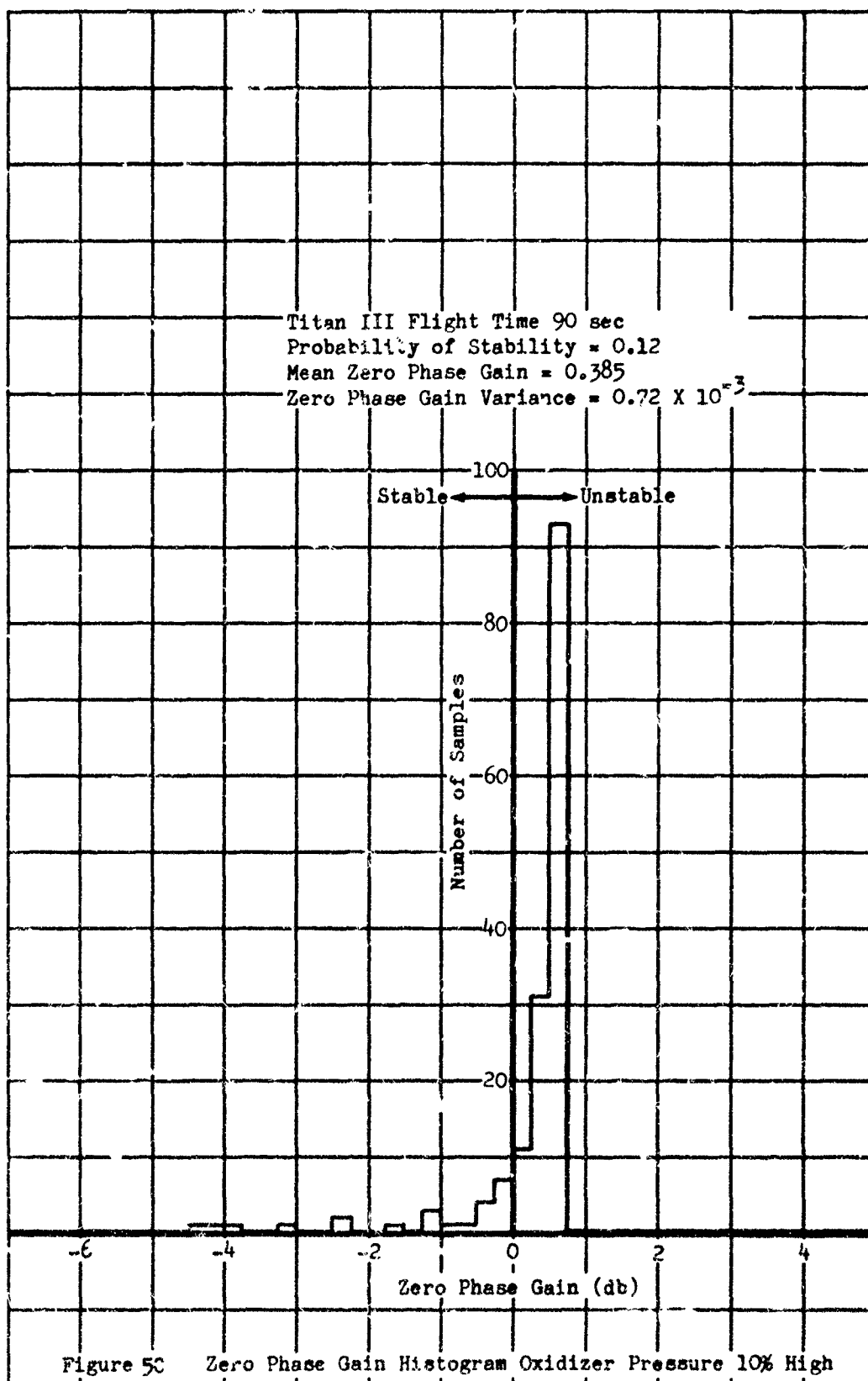
e.   Skewing of the ZPG Density Function

By viewing Figures 42 through 48 , the one consistent characteristic evident in all the curves is a skewing to the left. An explanation evolves from the functional relationship between the inputed random variables and the zero phase gain. Functionally we have;

$$\text{Zero Phase Gain} = f(\omega_A, \text{NPSHO}, \text{NPSHF}) \qquad (48)$$

Clearly, since ω_A, NPSHO and NPSHF are random variables, the zero phase gain is also a random variable. The problem which is solved by the Monte Carlo technique is the determination of the zero phase gain density function. If the functional relationship expressed by Equation 48 were a simple one, it would be possible to derive the distribution for the zero phase gain and the Monte Carlo simulation would not be necessary. This however is not the case. The question to answer next is:

Figure 49   Zero Phase Gain Histogram Oxidizer Pressure 10% Low

94

Figure 5C   Zero Phase Gain Histogram Oxidizer Pressure 10% High

What kind of functional relationship, expressed by Equation 48, is required to result in skewing of the zero phase gain density function? It can be shown that to obtain skewing, Equation 48 definitely must not be linear.

It is possible, but tedious to construct, by a graphical technique, the functional relationship described by Equation 48 when the form of the zero phase gain, ω_A, NPSHO and NPSHF density functions are known.

f.   Plotting Histogram vs Gain in db vs Plotting in Gain Units

There are two ways of plotting the zero phase gain histogram: the gain can be plotted as a simple ratio of input over output or the gain can be plotted in terms of db. The result is simply a mapping from one variable to another. For instance, suppose the zero phase gain density function were expressible as an analytic curve of gain units y, i.e.,

$$ZPG = f(y) \tag{49}$$

and since $db = 20 \log y$ the expression for the zero phase gain density function in terms of db is simply

$$ZPG = f(10^{db/20}) = g(db). \tag{50}$$

Hence, it is a simple matter to transform from the one coordinate system to another. Figure 42 which is the zero phase gain density function plotted as a function of db is replotted as a function of gain units in Figure 51. Some of the minor details are different, but the overall characteristics remain unchanged. Obviously the above change of variable does not change the probability of stability, but does change both the mean and variance.

g.   Probability Contours

Once the zero phase gain density function has been obtained it is possible to compute a probability of stability. Then as conditions change with flight time, a new zero phase gain density function can be computed and also a corresponding

Figure 51   Zero Phase Gain Histogram in Numerical Units
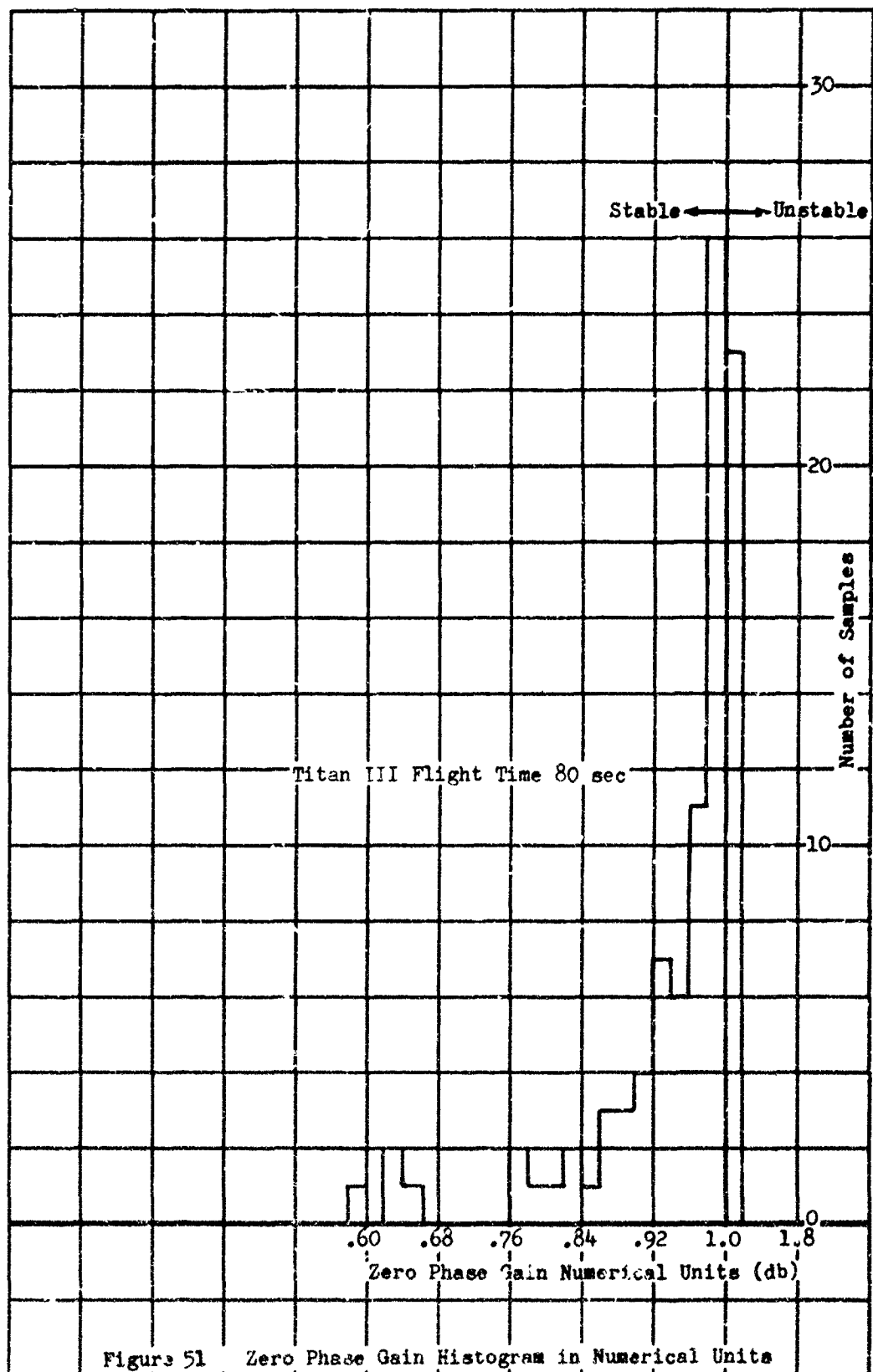
probability of stability. Such a procedure can result in a plot of probability of stability versus flight time; for various flight times there corresponds various probabilities. Once the zero phase gain density functions have been obtained it is possible to specify requirements of a compensator capable of maintaining a particular probability of stability over a specified flight time. For instance consider a zero phase gain density of the form shown below in Figure 52.
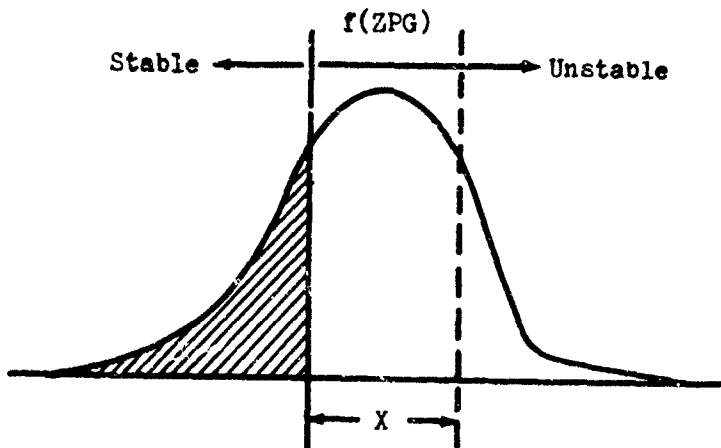

Figure 52 Typical ZPG Density Function

Assume for purposes of illustration that the probability of stability is 0.25. It is desired to compensate this system so that the probability of stability is increased to 0.75. By integration it is possible to determine the distance X so that 75% of the area of the curve is to the left of the dotted line. The value of X then is the amount of compensation required to maintain the probability of stability at the desired level. For such an approach to be valid we have implicitly made several assumptions. First, we have assumed that the compensator will not change the shape of the zero phase gain density function; and secondly, we have assumed that the compensator is in series with the rest of the systems where the loop is opened. Under these assumptions, the approach is valid.

Using the above approach, and the zero phase gain curves shown in Figures 42 through 48, plots of constant probability were obtained. The three curves shown in Figure 53 correspond to probabilities .95, .75 and 0.5. The ordinate of Figure 53 corresponds to the compensation, in db, required to maintain the associated probabilities. Because of the skewed nature
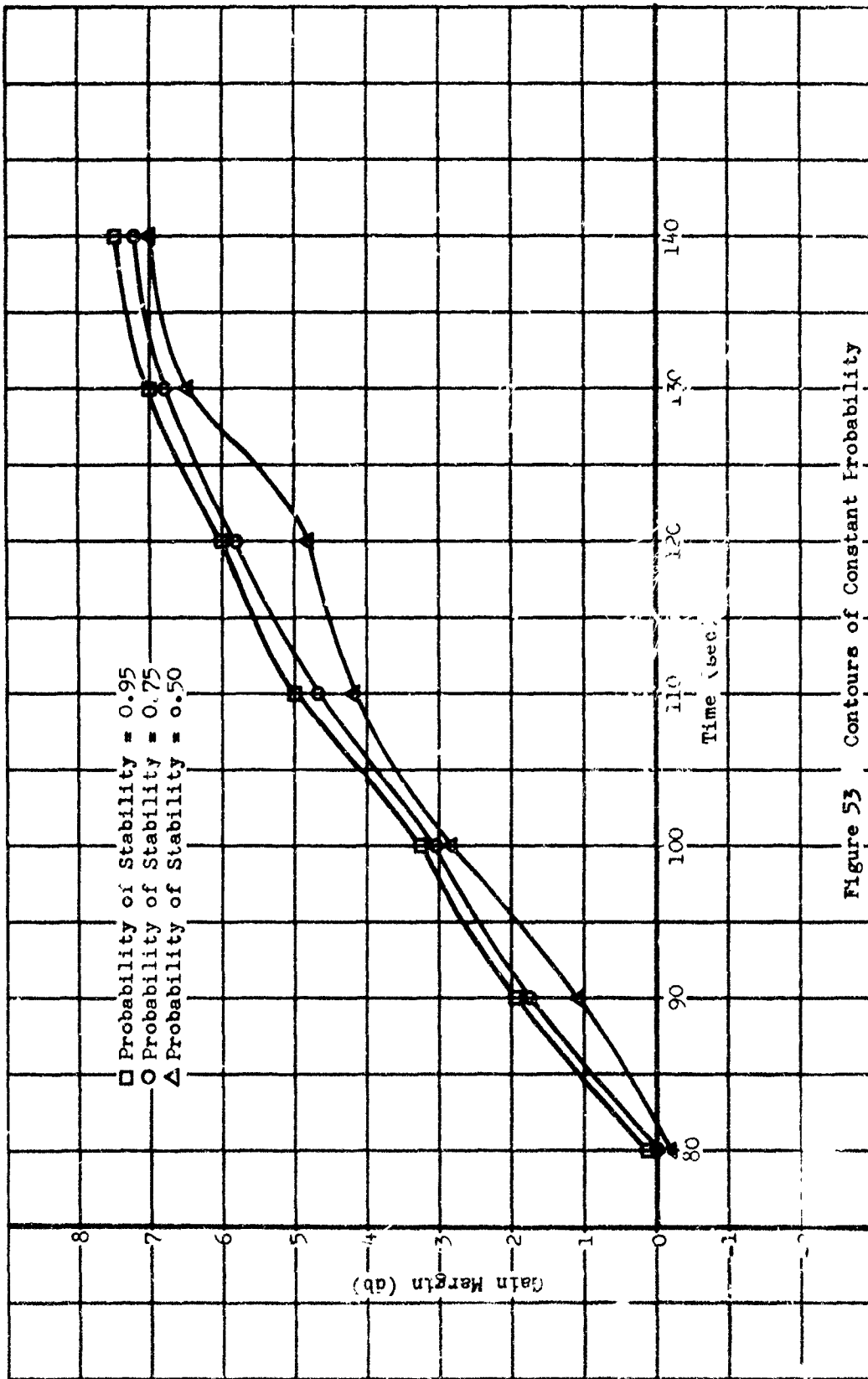
Figure 53   Contours of Constant Probability

□ Probability of Stability = 0.95
○ Probability of Stability = 0.75
△ Probability of Stability = 0.50

Gain Margin (db)

Time (sec)

of the density functions all three curves of Figure 53 tend to be grouped together.

5. A COMPARISON OF MONTE CARLO METHOD WITH RSS METHOD

a. RSS Background

When the components of any system are operating in cascade, each may be generating a random error. If the cause of the error in one component is unrelated to the cause of the error in some other component, they are said to be independent. Thus while the error in one component may be positive the error in another component can be negative, etc. However, when it is necessary to add up all the errors to determine the total error, straight addition of 1-sigma values would give a pessimistic description of the probable error. Thus the usual technique of combining 1-sigma errors when they are independent of one another is the root-sum-square technique. If $\sigma_1, \sigma_2, \ldots, \sigma_n$ represent several errors combining to cause an overall error, then the overall error is called the 1-sigma RSS (root-sum-square) and is obtained by:

$$\sigma_{RSS} = (\sigma_1)^2 + (\sigma_2)^2 + \ldots + (\sigma_n)^2 \tag{51}$$

In the gain margin version of the RSS technique the system parameters NPSHO, NPSHF, ω_A and g_A are sequentially varied. The difference between the nominal gain margin and

In the gain margin version of the RSS technique the system parameters NPSHO, NPSHF, ω_A and g_A are sequentially varied.

The difference between the nominal gain margin and the incremented gain margin is computed as each parameter is varied, and these are combined according to Equation 51 This number then is an estimate of the zero phase gain standard deviation. It is interesting to compare this estimate of the zero phase gain standard deviation with that obtained by the Monte Carlo technique. Using the RSS technique on the Titan III POGO model, the computed value of σ was

$$\sigma_{RSS} = 0.406 \tag{52}$$

Using the same mathematical model in a Monte Carlo simulation, the resultant value of σ was computed to be:

100

$$\sigma_{\text{Monte Carlo}} = 0.114 \qquad\qquad (53)$$

Since the Monte Carlo technique is a simulation of the statistical processes involved, it is reasonable to assume that the zero phase gain deviation ($\sigma_{\text{Monte Carlo}}$) so computed should be reasonably accurate. Hence the RSS estimate of the standard deviation is overly pessimistic in its approximation to the true parameter.

6. CONCLUSIONS

The primary result of this study has been the development of a computer program which relates a mean gain margin to a probability of stability. Any linear constant coefficient feedback system in which the parameters can be described as random variables with specified distributions is amenable to this approach. Using the Titan III POGO Model, several illustrative examples were worked. In particular the probability of stability was computed, a zero phase gain histogram constructed, and the sample mean and sample variance of the zero phase gain calculated. It was shown that the shape of the zero phase gain histogram is related to where the measurement is taken (i.e., where the loop is opened) whereas the probability of stability is not. The zero phase gain histogram when properly normalized becomes a probability density function. Every histogram, constructed from the Titan III POGO Model, displayed a skewing to the left. This was assumed to have been the result of the functional relationships between the statistical parameters and the deterministic parameters. As more flight data is obtained, it is always desirable to use this data to improve previous parameter estimates. This approach is amenable with the Monte Carlo simulation. With increased flight data, the statistical input parameters (mean and variance) can be updated using Equations 46 giving improved estimates of system stability.

a. Disadvantage of Method

A possible drawback of the Monte Carlo method, when extremely small or accurate estimates of the probability are desired, is that many iterations are required. If for instance a probability of stability of 0.959 is required, the number of

Monte Carlo iterations to obtain this accuracy would be approximately 5,000. With present computing speeds, 5000 iterations results in approximately 16 minutes of machine time. To obtain estimates of the extremes or tails of distributions without taking many iterations, it is possible to use special sampling techniques which accentuate these extremes. Special sampling techniques, however, were not used in this study. It seems that the association of a probability to quantitatively describe the degree of stability is both a natural and useful approach. The price one pays for this approach is that:

1) An analytical computation, in most cases, is impossible.

2) A large amount of computer time may be required.

The last objection, however, will considerably diminish as computational speeds are increased.

SECTION VIII

AMPLITUDE LIMITING

1.   INTRODUCTION - STATEMENT OF PROBLEM

In trying to augment the basic understanding of the POGO
phenomena, one has to contend with the observation that the longi-
tudinal oscillations on Titan II Vehicles increased to a limiting
value and then diminished to a much lower level or disappeared be-
fore first-stage burnout. In the first few flights on Titan II,
the duration of instability as shown in Figure 54 covered approximately
the same time in flight; however, the limiting amplitude and the ampli-
tude envelope did vary substantially over these flights which exhibited
POGO.
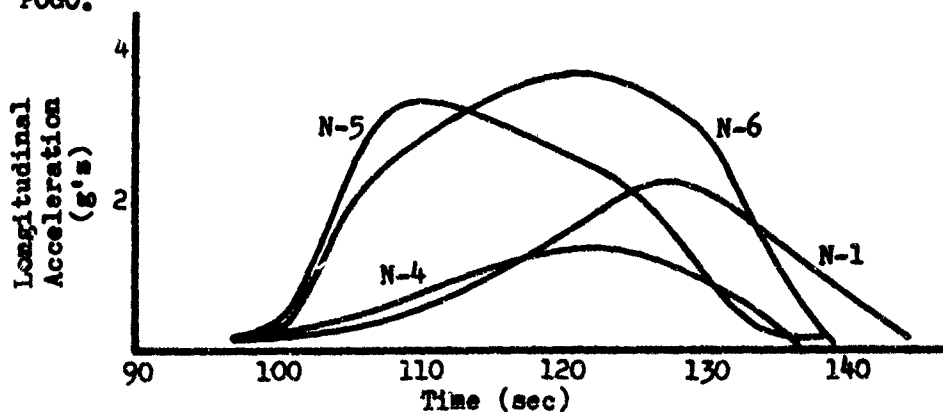
Figure 54   Titan II Structural Acceleration

a. Observed Variations. Those parameters which are considered
to be input variables for the math model and were observed to vary
from flight to flight are listed in the table below. The range
of variation of these parameters presents a formidable problem to
the investigator trying to model the POGO phenomena in a manner
capable of duplicating individual vehicle behavior.

TABLE IV INPUT PARAMETER VARIATIONS

| Missile | At 90 Sec Into Flight | | | |
| | Tank Top Pressure | | Steady State Suction Pressure | |
	P_{T_O}	P_{T_f}	P_{s_O}	P_{s_f}
N-1	20.0	21.5	66.0	27.8
N-4	16.7	23.5	65.5	30.0
N-5	17.2	19.0	70.0	25.9
N-6	17.5	19.5	71.0	26.0

b. Objectives. The objectives of the amplitude limit study were to identify and define the mathematical form of system non-linearities responsible for the salient features of the stable POGO limit cycle. To this end, flight data was used in conjuction with an existing linear model to derive a system whose critical system elements were determined by response magnitude.

2. PROPOSED APPROACH

Linear math models of the coupled propulsion system and structure have been successful in predicting the period of instability but cannot duplicate the amplitude limiting that has been observed from the Titan II flights. Although the depletion of propellant has an appreciable effect on both the vehicle's structural behavior and the feed system response (Fig. 91 & 92), the shift in natural frequencies of the various subsystems is not sufficient to confine the oscillations with the linear model alone. For this reason, it became necessary to assume the observed amplitude limiting was the result of a nonlinear phenomena somewhere within the vehicle.

a. Possible Nonlinearities. Upon examining the steady-state governing equations used in the linear POGO mode., it was possible to see a number of nonlinearities that could conceivably enter into the systems response for large amplitude oscillations. Nonlinearities could appear within the structural behavior of the vehicle making the second order differential equation used in the linear description inadequate for large amplitude oscillations. Reference 7, for example, points out that on Titan II vehicles having low ullage pressures the region of the stage I oxidizer and fuel tanks can be seen to exhibit buckling at certain times in the flight with consequent abrupt loss of stiffness. The inability of the propellants to sustain any appreciable tensile force causes a number of other nonlinear behavior patterns to evolve when the fluid is made to pulsate at sizeable amplitudes. In addition to the nonlinear fluid mechanic aspects, large perturbations in the propellant flow rates can alter the mixture ratio and result in nonlinear changes in combustion and thrust.

Some of the above nonlinearities were investigated by Goldman (Ref. 6) but only to determine their effect on open loop system gain. As pointed out earlier, the objective here was to determine possible non-linearities which could cause a closed loop system that is basically unstable to limit cycle.

b. Dominant Nonlinearities. It was found that the dominant nonlinearities are those associated with the propellant feed system,

the turbopump, and its related cavitation region. An earlier study (Ref. 2) investigated the importance of this cavitation region and how the presence of vapor in the feed system affected the system's response to perturbations. It was in this study that the relation of cavitation compliance to POGO amplitude limiting was discussed (Section IV, 6a).

3. NONLINEAR MATHEMATICAL MODEL

The equations used to describe the nonlinear POGO response are discussed in Appendix VIII.

a. Nonlinear Model. The linear math model used in earlier studies was revised by incorporating two nonlinear relationships. One dealt with the pressure amplification through the turbopump by relating the suction and discharge pressures; the other involved description of flow continutity between the suction and discharge flows. Although the two are inherently the result of the same cavitation phenomenon, they were considered independently. During the study, one relationship was held constant while the other was varied in an attempt to get some idea of their relative importance.

b. Cavitation Compliance. The mathematical models of the cavitation compliance are derived and discussed in detail in Appendix IX. In brief, the cavitation region was represented three different ways.

(1) Amount of Vapor Involved. Assume a fixed mass of vapor is present in the cavitation region at any time during the pressure oscillations.

(a) Adiabatic Process. Further assume the fixed mass of fluid undergoes expansion and compr ,sion without the addition or deletion of heat. With the above two restrictions the following continutity expression between $\dot{W}_{so}$ and $\dot{W}_{do}$ results:

$$P_{so} = P_{ref} \left[\frac{1}{\left[1 - \frac{\Delta V_o}{\rho V_o} \right]^{1.4}} - 1 \right] \quad (54)$$

where $\Delta V_o = \int (\dot{W}_{so} - \dot{W}_{do}) dt$

and in a similar manner for the fuel system

105

$$P_{sf} = P_{ref}\left[\cfrac{1}{\left[1 - \cfrac{\Delta W_f}{\rho V_0}\right]^{1.13}} - 1\right]$$ (55)

(b) Isothermal Process. The second representation which was examined assumed the expansion-compression process took place while maintaining a constant temperature.

$$P_{so} = P_{ref}\cfrac{\left[\cfrac{\Delta W_e}{\rho V_o}\right]}{\left[1 - \cfrac{\Delta W_e}{\rho V_o}\right]}$$ (56)

$$P_{sf} = P_{ref}\left[\cfrac{\Delta W_f}{1 - \Delta W_f}\right]$$ (57)

(2) Amount of Vapor-Liquid Involved. A third model of the cavitation region assumed a fixed mass of a liquid-vapor mixture to be involved in the pressure-volume changes. During oscillations in pressure within the propellant lines, the mixture was allowed to change quality. For example, during that part of the cycle where the pressure was increasing, vapor was allowed to condense into liquid. The heat of vaporization released during the phase change was stored within the fixed mass of mixture as random kinetic energy. This process was assumed to follow a constant enthalpy line under the saturation curve for the preliminary study because of the ready availability of temperature - enthalpy relationship for the oxidizer. (Ref. 8).

(3) Representative Curves. A typical plot of each of the three-proposed models is presented in Figure 55 . Each of the models had two points in common:

(a) The cavitation region is occupied by a fixed mass of fluid which undergoes this pressure-volume change.

(b) Thermodynamic equilibrium exists throughout the cycle; thus, vaporization and condensation are considered as instantaneous processes without any associated time lag.
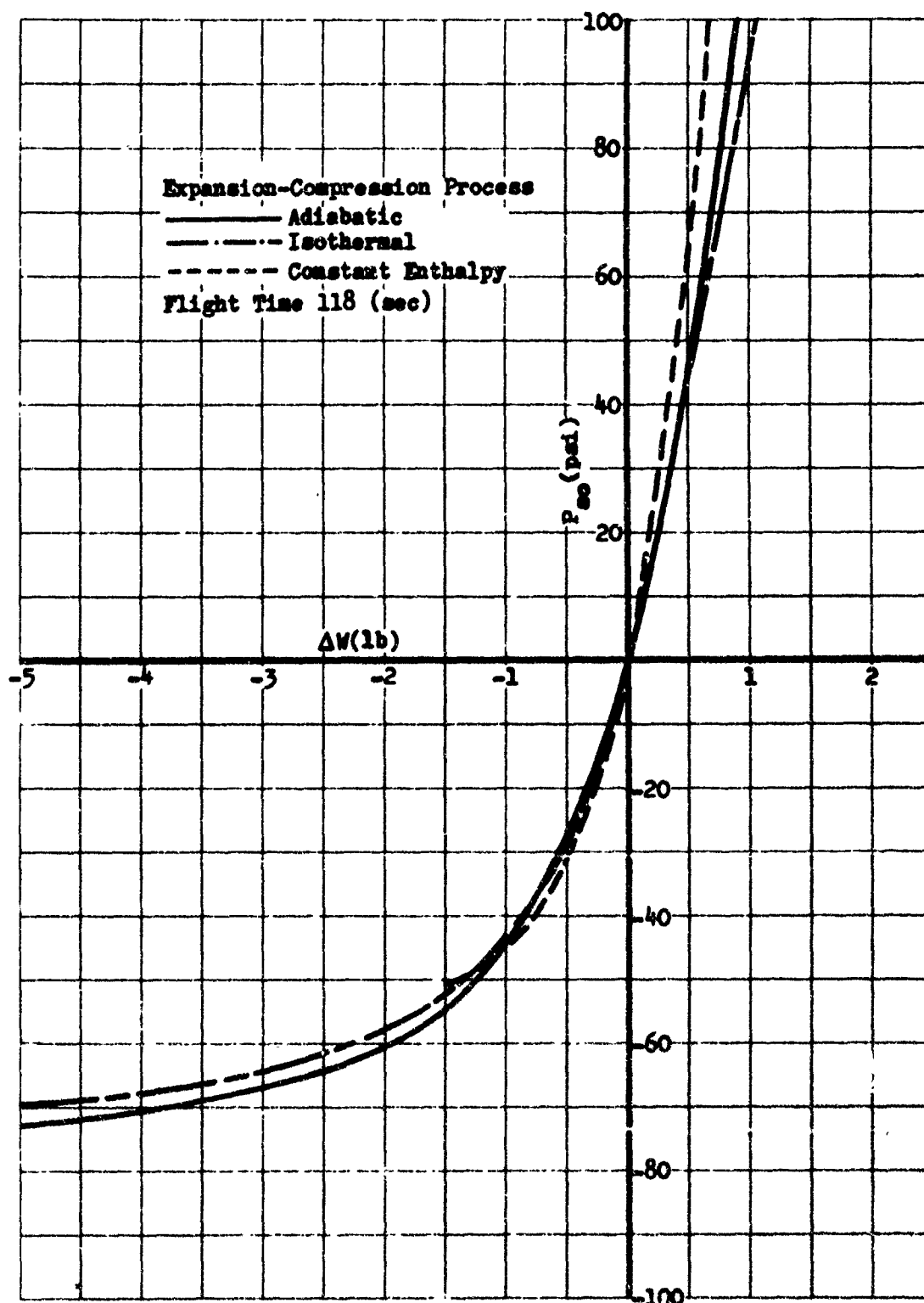
Figure 55 Comparison of Three Cavitation Compliance Models

Although different approaches were used in arriving at the three representations, there is surprisingly little difference in the resulting P_{so} vs ΔW relationships as shown in Figure 55.

e. Turbopump Characteristic Curve. The other nonlinearity which was used in conjuction with one of the above forms of the continuity equation was the turbopump characteristic curve. Test data derived from steady-state operation of the pumps were used to represent the dynamic behavior. Later in the program a more thorough examination of the pump model was undertaken and results show that dynamic pump operation departs significantly from the static characteristic.

(1) Governing Equation. The discharge pressure was expressed as a function of the suction pressure and flow rate through the pump.

$$P_d = P_{dG} (P_s) - R_p \dot{W}_d \tag{58}$$

where: R_p = pump's internal resistance

P_{dG} = discharge pressure from steady-state head-rise data

$\dot{W}_d$ = discharge flow rate.

(2) Linearized Pump Model. Two different pump models evolved from Equation 58. The first expressed P_{dG} as a linear function of the suction pressure.

$$P_d = (M + 1)P_s - R_p \dot{W}_d \tag{59}$$

where $(M + 1)$ = linearized pump gain.

A typical plot of P_{do} vs P_{so} for the linear model is shown in Figure 56. Inclusion of the internal resistance term introduces a phase shift between the suction and discharge pressure as shown by the envelope of operation. The amount of separation between the upswing path and the downswing path was found to depend on the amplitude of oscillation. If the same linear pump model were driven by a suction pressure resulting from a nonlinear cavitation compliance, the discharge pressure would behave as shown in Figure 57.

(3) Nonlinear Pump Model. The second way of expressing

108
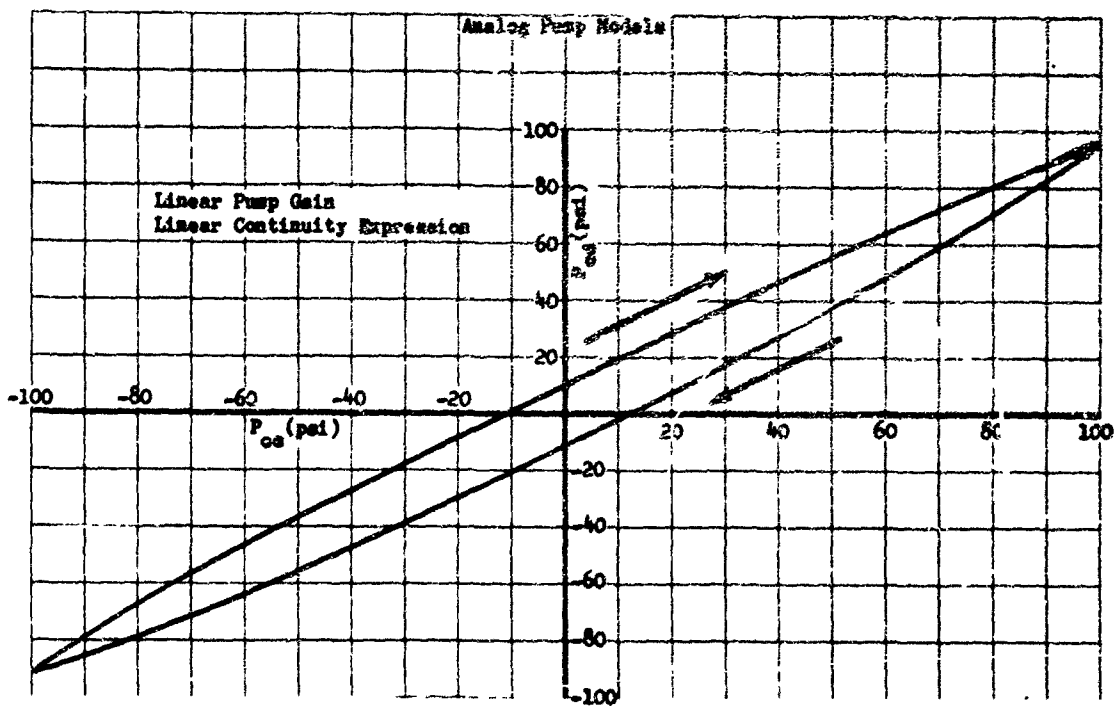
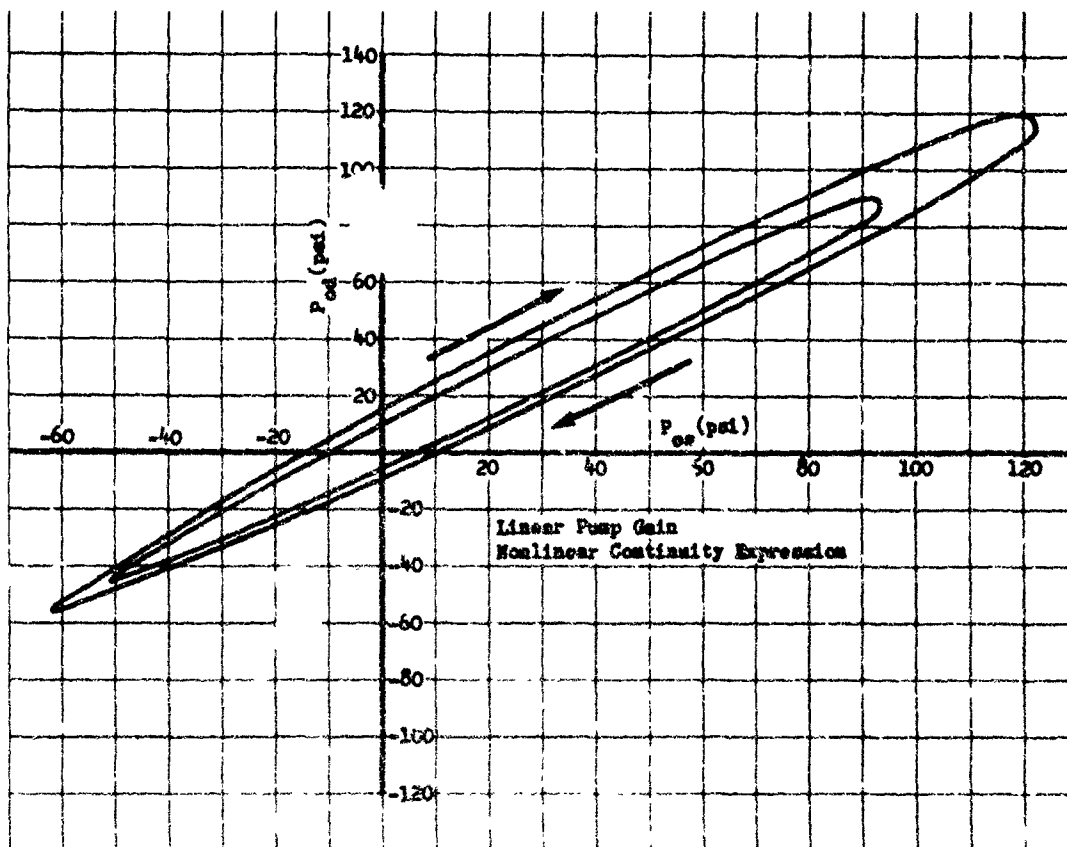Figure 56 Envelope of Operation for Analog Turbopump Model

Figure 57 Envelope of Operation for Analog Turbopump Model

pump head rise, P_{dG}, was as a nonlinear function of suction pressure. Data from the steady-state head rise curves were set into diode function generators for input into the analog program. This method of introducing nonlinear relationships into the electrical analog requires that such functions be approximated by a series of straight line (linear) segments. It was for this reason Figures 94 and 95 appear as segmented curves. The nonlinear pump model not only produced the double valued P_d vs P_s relationship, but it also furnished the sharp drop in discharge pressure normally associated with the appearance of cavitation within the pump. (Fig. 58).
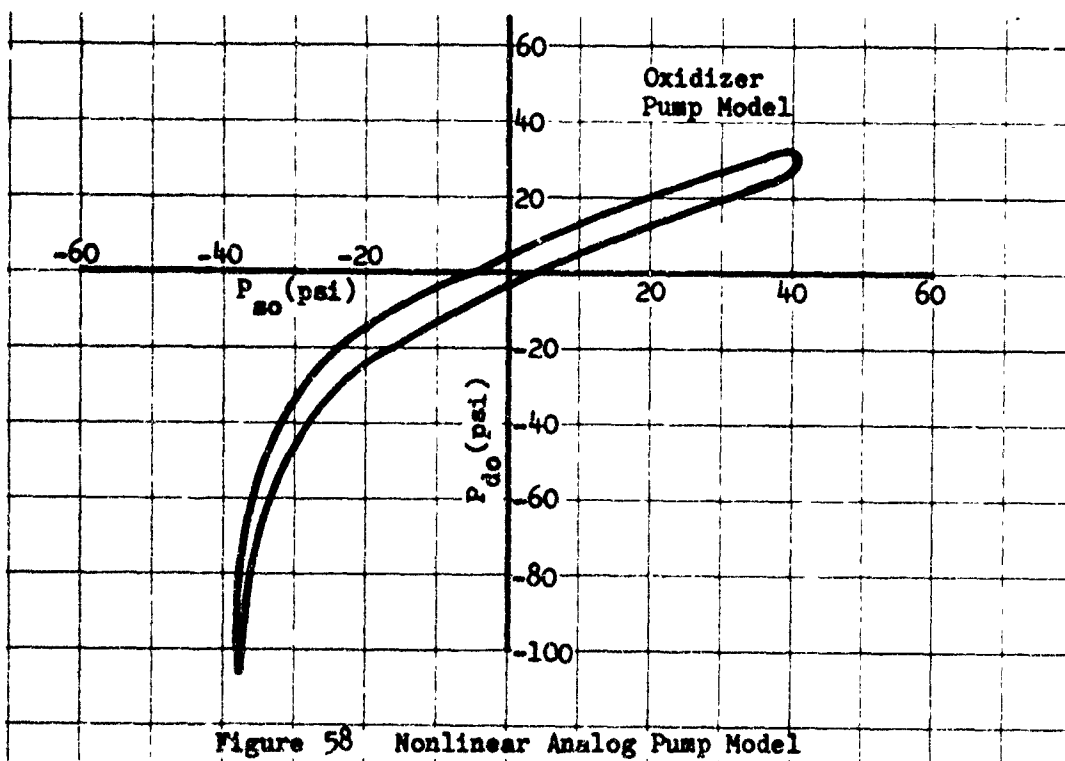
Figure 58   Nonlinear Analog Pump Model

(4) Flight Pump Data. In order to evaluate the above mathematical description of turbopump operation, suction and discharge pressures recorded during actual flights of Titan II vehicles were examined.

The telemetered PCM pressure transducer data were analyzed digitally and plotted for individual cycles of oscillation. Results of this comparison of P_d vs P_s, although clouded by noise, indicate the pump operation follows two different paths under oscillatory conditions as shown on Figure 59 .
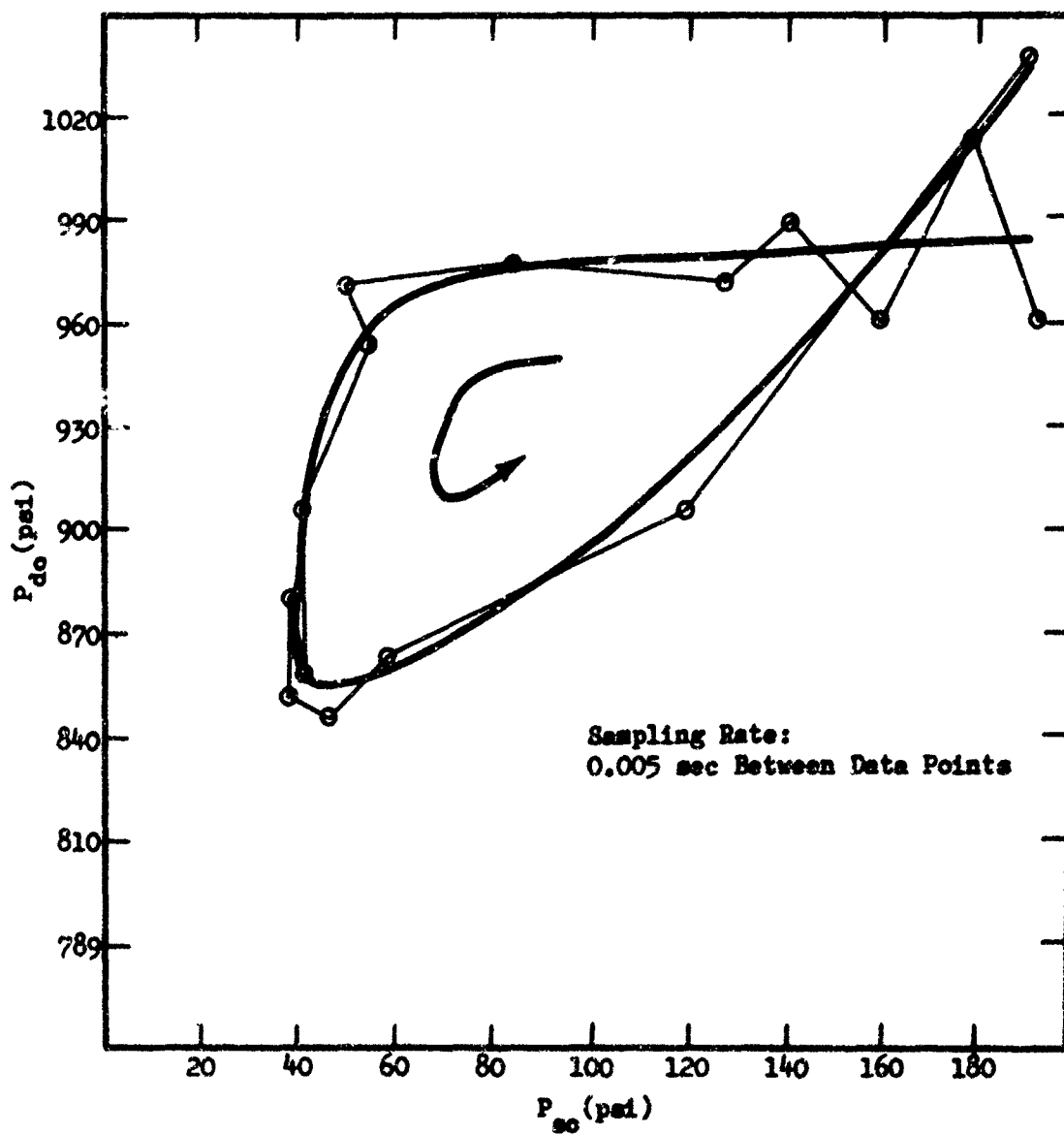
Figure 59 Titan II Flight N-5 Pressure Data 120.947 to 121.027 (sec)

Assuming the pressure transducers have accurately
monitored the physical situation, a number of observations can be
made:

(a) During the increasing pressure portion of the
cycle, the relationship between P_{do} and P_{so}
is nearly linear. Operation with decreasing
suction pressure appears to follow the steady-
state head rise curve.

(b) The time spent between given points along the
cycle varies appreciably. The upswing part
of the cycle occurs within $\sim.020$ sec whereas
the downswing requires $\sim.070$ sec.

(c) The flight data shows P_d to be lagging P_s in-
dicating an inherent time lag within the pump.
Since the analog model indicated that P_d leads
P_s by a small amount, it must be concluded that
either or both the vaporization and condensation
can not be considered as instantaneous processes.

4. NONLINEAR SYSTEM RESPONSE

The electrical analog study of the nonlinear POGO model was
conducted in two parts. The first phase involved a simplified model
and served as a preliminary evaluation of the proposed nonlinear-
ities - only the oxidizer feed system was allowed to influence the
vehicle response. The second phase of the study incorporated the
system into the model.

a. Response to Oxidizer System Alone. During the first
phase of the analog study, it was found that the nonlinear pump
characteristics in conjuction with the proposed nonlinear con-
tinuity expressions caused the system to oscillate far beyond the
amplitudes observed on the Titan II flights. For this reason it
was necessary to revert to the linear pump relationship for which
limiting was achieved within the observed range of amplitudes.

(1) Limiting Amplitude vs Resonant Frequen. ratio.
Figure 60 serves to point out the values at which the gimbal
acceleration limited as a function of W_A/W_{so}. The ratio of the
natural frequencies is a relative indication of the separation
in resonant frequencies. As shown in the figure, the system can
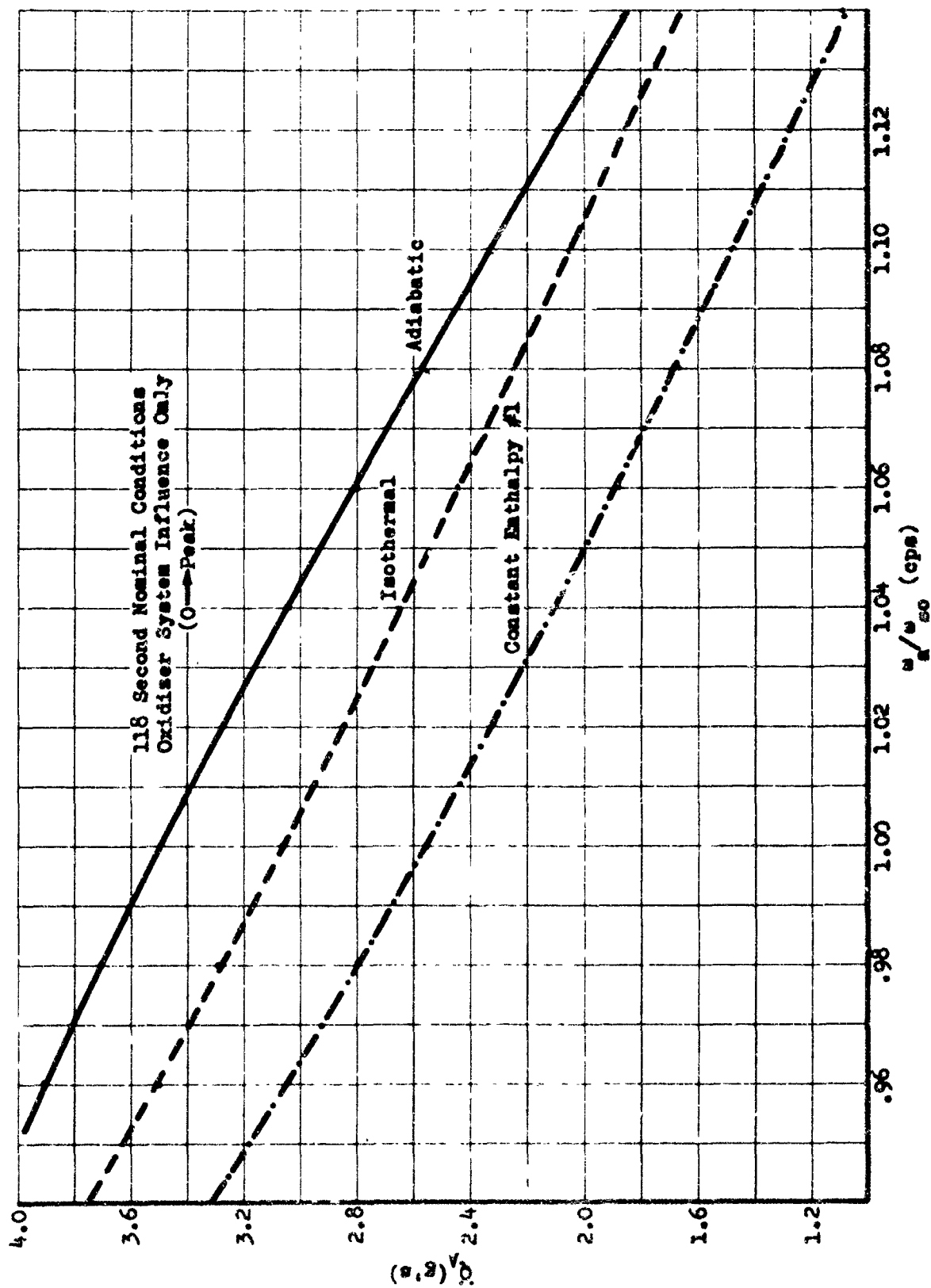be made to limit at any of a large range of values simply by·

112

Figure 60 Limiting Gimbal Acceleration for Various Forms of Continuity Equation

113

shifting the resonant frequencies of the structure or suction line.

(2) Suction Pressure Amplitude Envelope. The envelope within which the suction pressure oscillated at each limited condition is shown in Figure 61 .

(3) Limiting Amplitude vs Structural Gain. One of the system parameters which is difficult to evaluate is the structural gain. During this phase of the study, the structural gain was varied in an attempt to determine its influence on the total systems behavior at the limiting condition. The results are shown in Figure 62 .

(4) Pump Truss Flexibility. It was previously known that flexibility in the turbopump supports affected the stability of the system; here it was found that by allowing the pump to move relative to its structural support the limiting amplitude was decreased appreciably. Figure 63 illustrates the difference in response between the rigid pump truss and the flexible pump truss.

(5) Phase A Conclusions. The conclusions which were drawn at the end of the first phase of the analog study were the following:

(a) Proper limiting amplitudes could not be achieved with the nonlinear pump characteristics because the use of steady-state pump curves to predict dynamic response was inaccurate. An attempt should be made to define dynamic pump characteristics before making a final evaluation of the models of the cavitation region.

(b) The system could be made to limit within the proper range of observed Titan II amplitudes with each of the proposed forms of the continuity expression - each model furnished a different limiting envelope. The envelopes are compared in Figure 61 and indicate that the constant enthalpy process best achieves low amplitude limiting values.

b. Response to Coupled System. The second phase of the analog study of the POGO amplitude limiting problem incorporated the fuel feed system into the math model. The linear pump characteristics had to be employed to achieve the desired limiting amplitudes. Flight data was evaluated in order to arrive at a better dynamic pump representation.
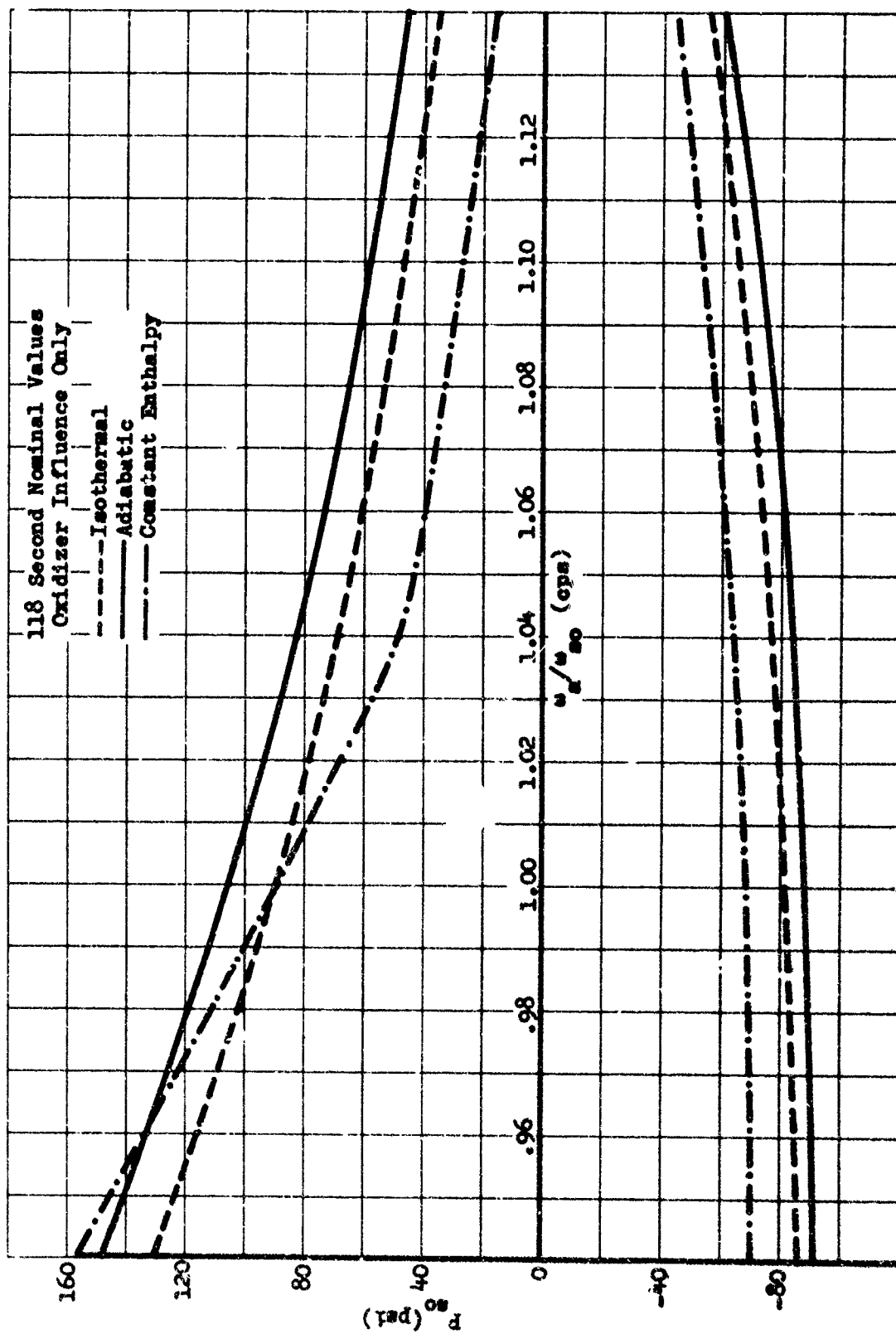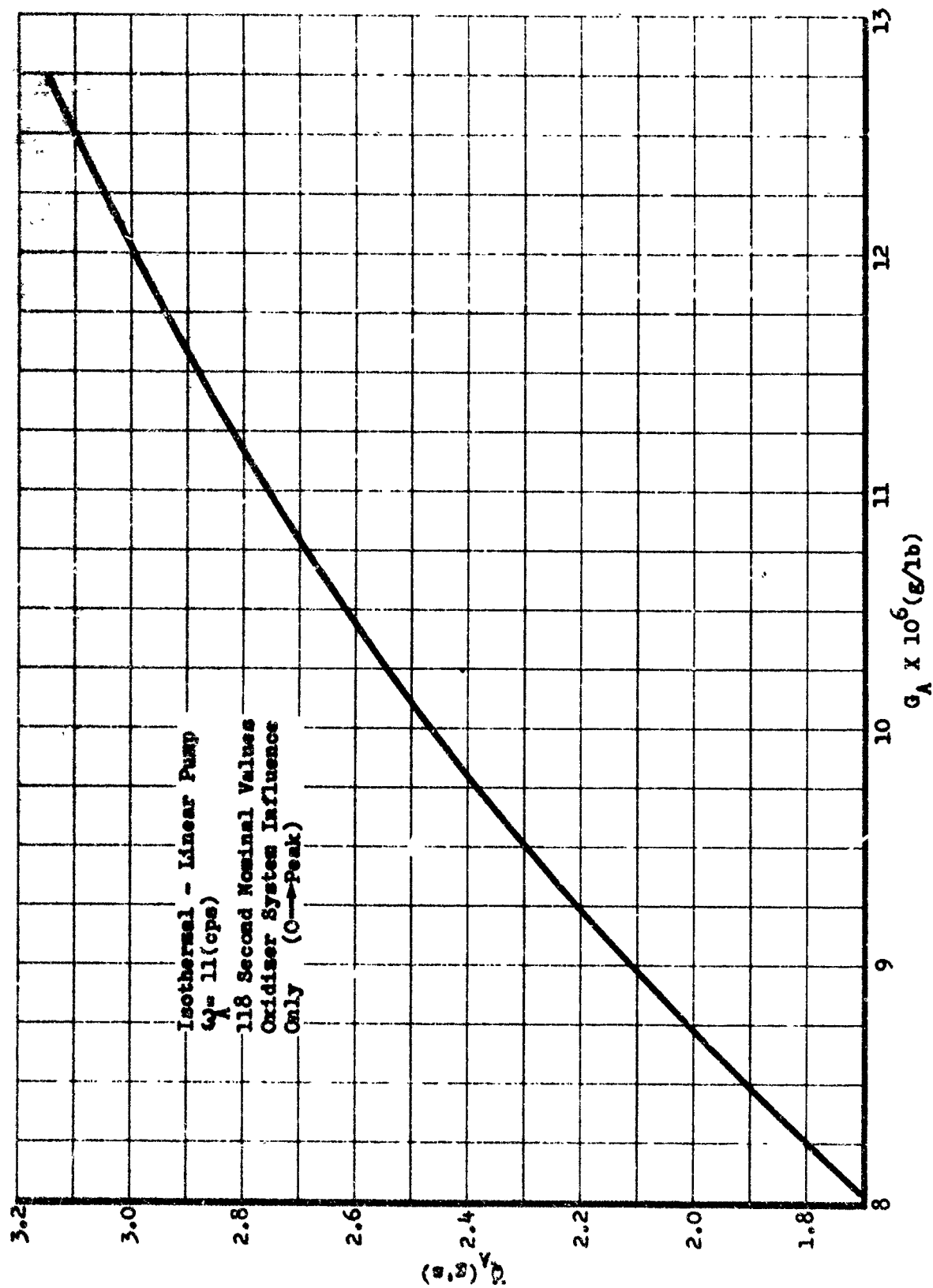
114

Figure 61 Limiting Envelope

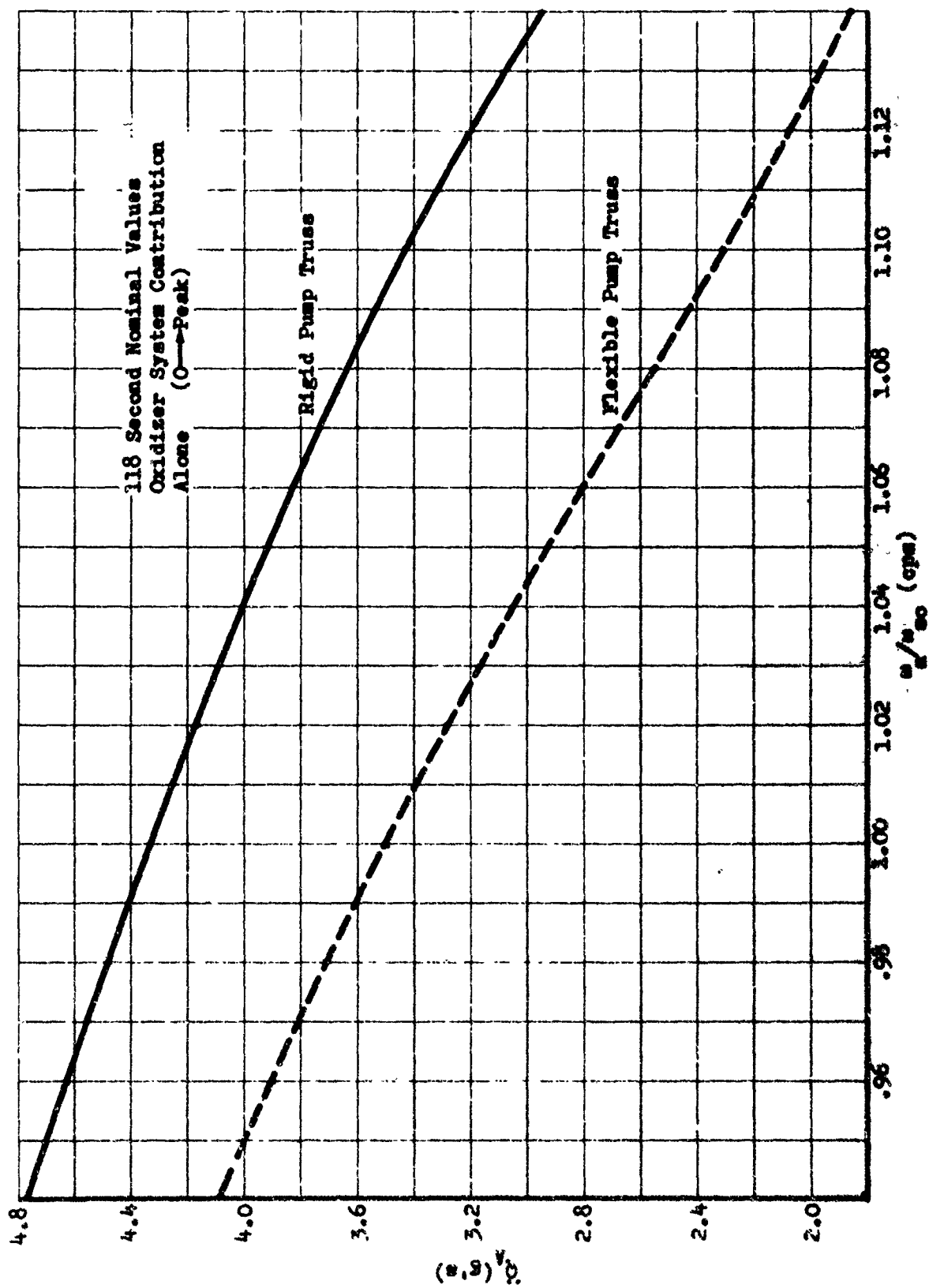Figure 62   Limiting Gimbal Acceleration vs Structural Gain

116

Figure 63 Limiting Gimbal Acceleration Rigid Pump Truss vs. Flexible Pump Truss

(1) Input Parameters. The systems response was again examined at conditions corresponding to various times after lift off. Specifically times of 100, 110, 120, 130, 135 and 140 seconds were investigated. Nominal ullage pressures and propellant consumption rates were used. Time dependent parameters are illustrated in Figures 91, 92, 93 and 96. During the study some question was raised over which set of fuel pump characteristics were appropriate, so pump gains were parameterized in the range 1.0 to 2.6.

(2) General Effects of Fuel System. The general patterns of behavior that were recorded during phase A were again observed with the fuel feed system included in the total systems response. Because minor revisions were made on the nonlinear elements for the second phase of the study, it is not possible to qualitatively compare the sole effects of adding the fuel system.

(3) Pump Gain Sensitivity. Because of lack of data describing dynamic pump characteristics, the sensitivity of limiting amplitude to this parameter was investigated. Earlier studies which delat with the stability of the linear POGO model found that pump gain had little effect on stability. This was illustrated by the two transfer functions:

$$\left(\frac{P_s}{s}\right)\left(\frac{T}{P_s}\right) = \left[\frac{\rho L}{\frac{s^2}{\omega_{so}^2} + \frac{(M+1) I_{so}}{Z_d + R_p} s + 1}\right]\left[\frac{(M+1) K_c K_t}{Z_d + R_p}\right] \tag{60}$$

The expression above shows a tendency for the pump gain, M + 1, to cancel and nullify its effects on the linear open loop gain.

(a) Limiting Amplitude. Figure 64 shows the effect of pump gain variation on the limiting amplitude under conditions where the fuel system response is strong. It appears from the analog data that for the vehicle configuration studied, small variations in the open-loop gain produce relatively large changes in limiting amplitude. The reason the limiting amplitude is so sensitive to pump gain or other system parameters has been attributed to the relatively weak nonlinearity that is limiting the oscillations. For example, the 135 sec configuration that limited at 4 g's (0 to peak) was oscillating over only a small portion of the continuity curve as shown in Figure 65 .
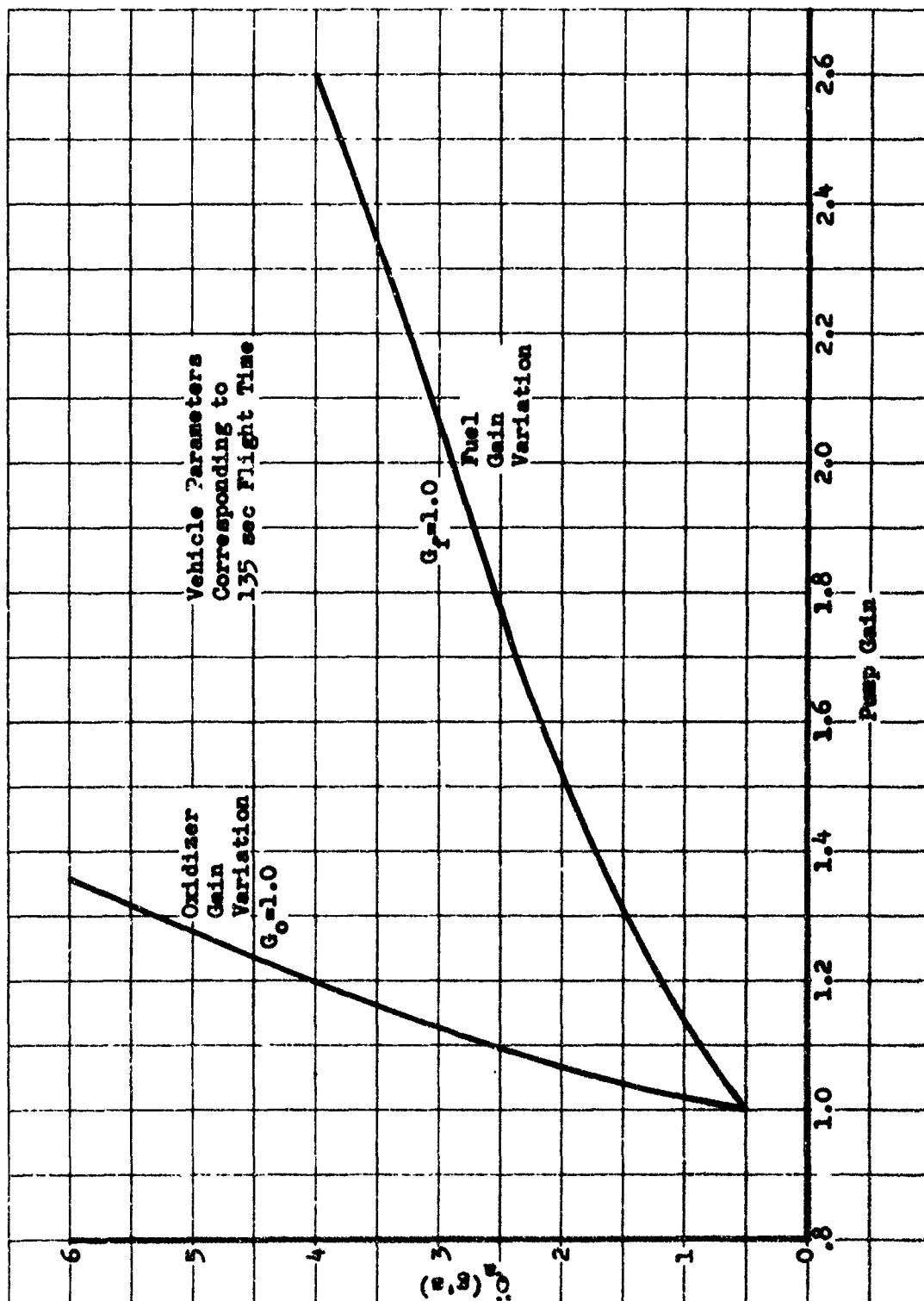
118

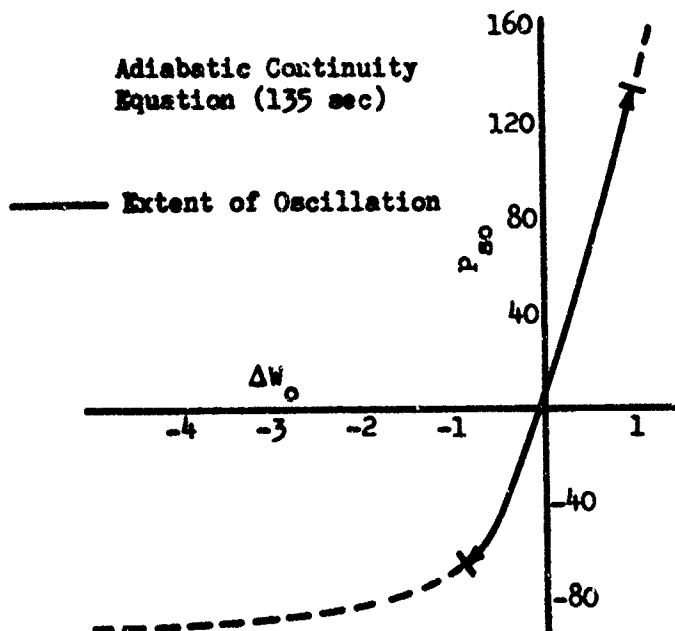Figure 64 System's Response to Pump Gain Variation

Figure 65 Extent of Nonlinearity - 135(sec) Limited Condition

Were the nonlinear continuity relationship more severe, the amplitude of oscillation would need to change less to acquire the same amount of nonlinearity. If the nonlinear continuity expression were more drastic, it may also have been able to offset the destabilizing turbopump nonlinearity.

　　　　(b) Fuel Pump Gain. Figure 66 shows the influence the fuel pump gain has on the amplitude at which the vehicle limits.

　　c. P_s/g Ratio. Another aspect of the nonlinear model which can be compared with flight data is the ratio of the suction pressure, P_s, to the structural acceleration, g. Duplicating this ratio with a mathematical model implies the coupling between the structure and feed system has been adequately described.

　　　　(1) Comparison of Results. Data from some of the earlier Titan II flights is presented in Figures 67 and 68 superimposed on the flight data are the results of the analog study.

　　　　(a) Oxidizer Side. Although the P_{so}/g from the

120
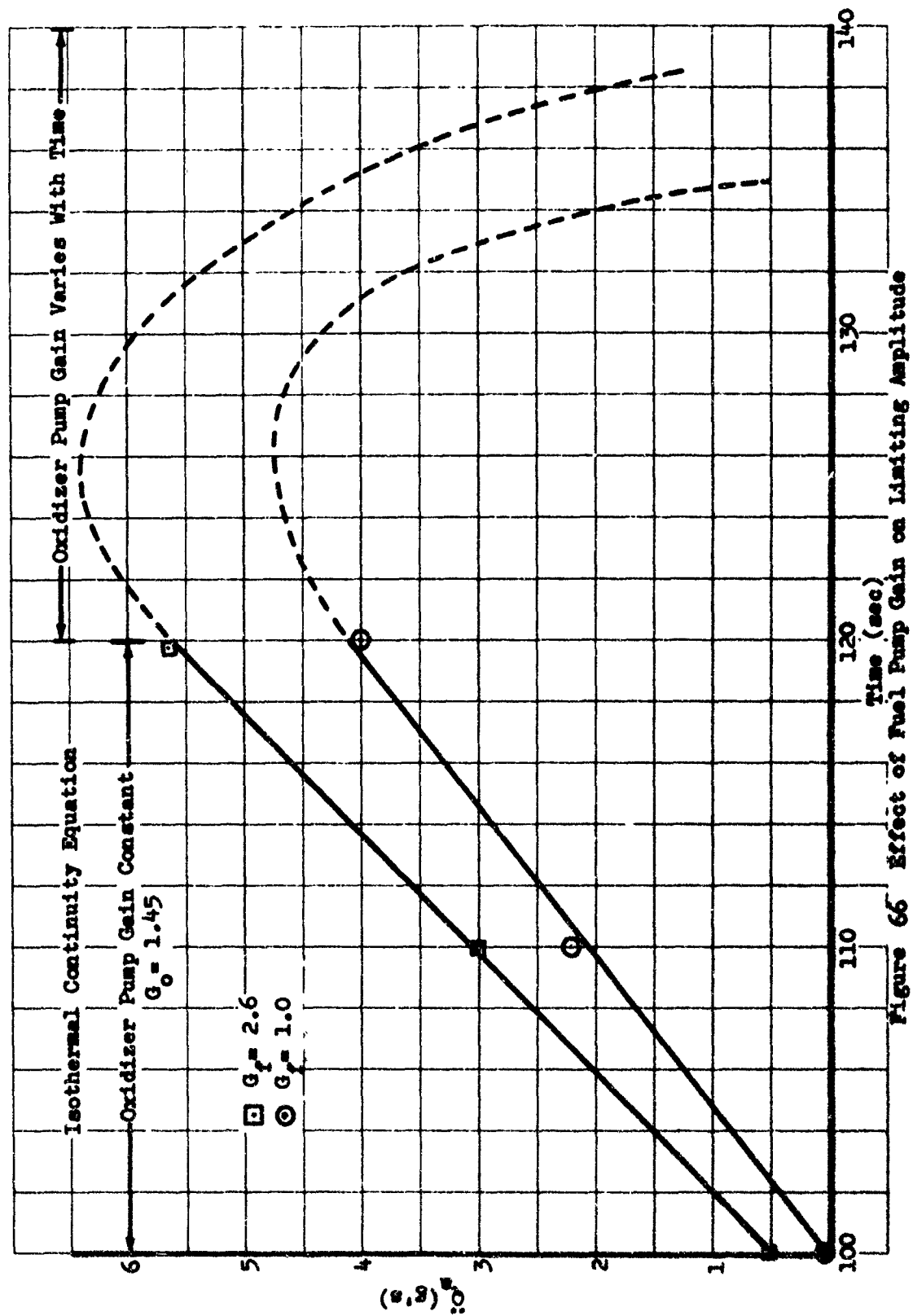
Figure 66 Effect of Fuel Pump Gain on Limiting Amplitude
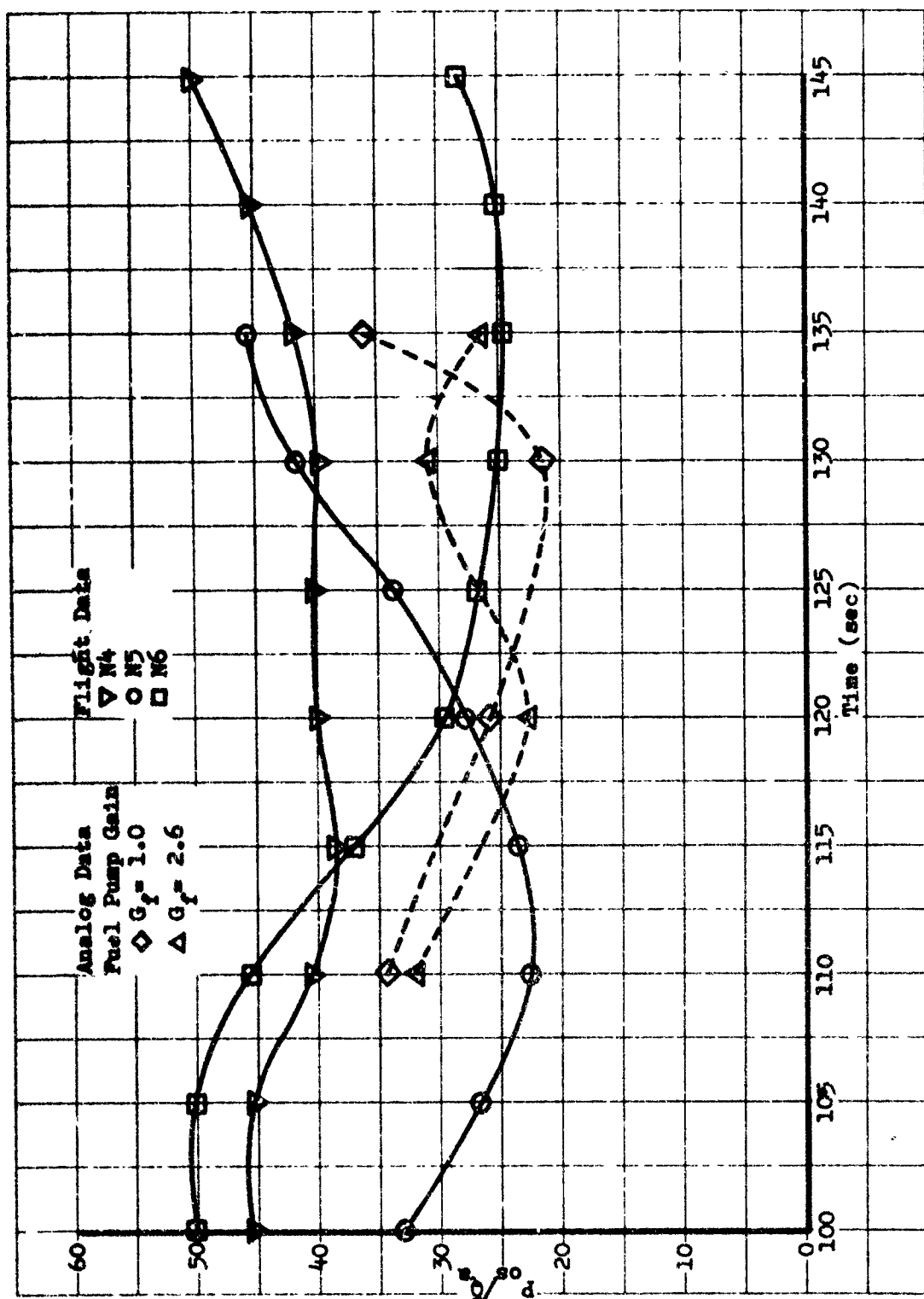
Figure 67   Comparison of Analog Data and Flight Data for P_g/g

122
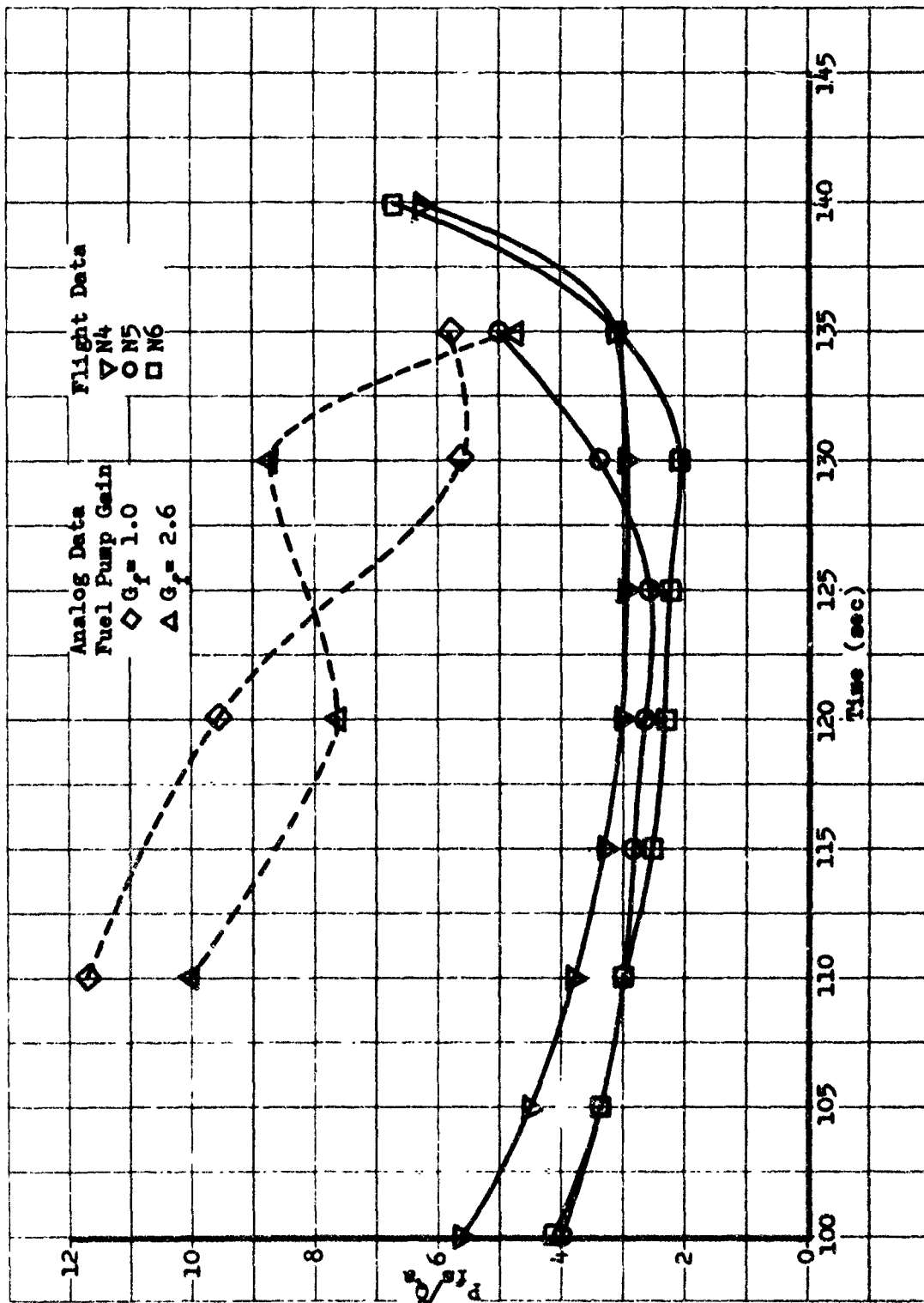
Figure 68   Comparison of Analog Data and Flight Data for P_s/s

analog study appeared to run somewhat lower than the flight data, the difference between the analog data and any particular flight is no more than variations between individual flights.

(b) Fuel Side. Figure 68 shows P_{sf}/g observed on the Titan II flights to be lower than that obtained from the analog study. Note that these ratios are based on conditions where limiting has occurred. A closer examination revealed that P_{sf}/g adhered closely to flight data when the model was oscillating at small amplitudes and was in the linear range. As the amplitudes increased, and the nonlinearity on the fuel side became of importance, P_{sf}/g rose from 5.0 to 8.0 at the limiting condition. This would indicate that the form of the nonlinearity may need to be modified on the fuel side in order to match this aspect of the nonlinear model with the actual vehicle.

d. Fuel Feed System Contribution. The effects of modifying the fuel feed system on the total systems response is illustrated in the table below. Six different fuel system representations were investigated with respect to the same structural and oxidizer system configuration.

TABLE V EFFECT OF FUEL SYSTEM PUMP GAIN AND CONTINUITY EQUATION ON LIMITING AMPLITUDE

Cavitation Compliance Model	Fuel Turbopump Model	Structural Acceleration Limiting Amplitude (0-peak) g's
Nonlinear	Nonlinear	2.0
	Linear Pump Gain = 1.0	1.8
	Linear Pump Gain = 2.6	2.7
Linear	Nonlinear	2.1
	Linear Pump Gain = 1.0	1.9
	Linear Pump Gain = 2.6	2.8

It can be observed from the table that use of a nonlinear head rise model on the fuel side is de-stabilizing; use of a linear cavitation compliance is de-stabilizing; the amplitude is not as sensitive to fuel-pump gain as it was to oxidizer pump gain.

5. CONCLUSIONS

Conclusions which were drawn after the second phase of the analog study are the following:

1) The nonlinear POGO model produced a system that had a response which limited at amplitudes within the range of values observed on Titan II flights. This indicates that nonlinear phenomena associated with cavitation in the feed system is the most important system non-linearity.

2) For the model investigated, the closed loop nonlinear system response was very sensitive to the manner in which the turbopump was modeled. Examination of individual cycles of turbopump behavior based on flight data indicate possible inadequacies with the analog dynamic pump model. Further investigation of the dynamic turbopump performance would be warranted.

3) Because the cavitation compliance nonlinearity was a weak nonlinearity, small variations in other system parameters produced significant changes in the limiting amplitude. Since small variations in system parameters are found to occur from flight-to-flight one naturally expects corresponding variation in POGO limit cycle amplitude from apparently identical vehicles. Thus it would not be possible to predict limit cycle amplitudes on a given unstable flight.

SECTION IX

SEALED BAG ACCUMULATOR ANALYSIS PROGRAM

1. INTRODUCTION

The sealed bag accumulator has been used with success on a number of Titan vehicle missions. The accumulators have been designed primarily from the standpoint of the amount of compliance they add to a suction system. The inertance, resistance, and compliance of the accumulator itself have been investigated only over a limited range of geometry and system static pressure conditions. As the amount of gain or phase margin provided by the present accumulator designs decreases the dynamic characteristics of the accumulator will become more important. Furthermore, if new designs become necessary additional design data will be required. It was the purpose of this program therefore to investigate the dependance of accumulator dynamic characteristics on specific design parameters.

The first step of this effort was the development of an analytical model of the accumulator and establishment of the proper experimental procedure to evaluate the model. The details of the analysis phase are described below.

2. SEALED BAG COMPENSATOR ANALYSIS

   a. Discharge Line Pulsing.

      (1) Test configuration. An analysis was made to determine the theoretical response of the sealed bag accumulator test configuration. The analysis was conducted on the electrical analog shown below:
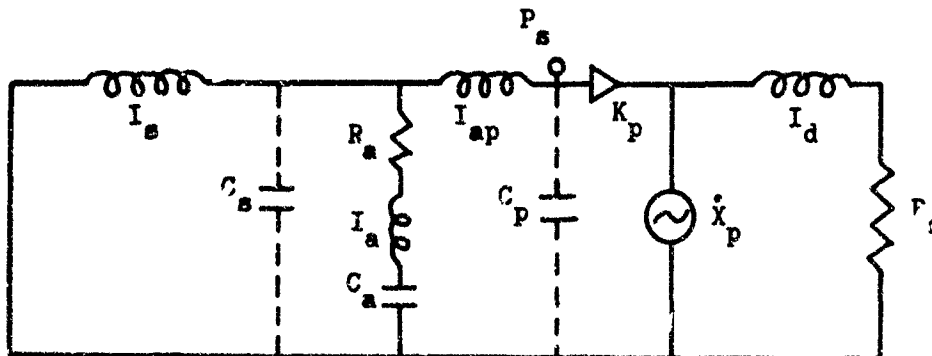
Figure 69   Sealed-bag Equivalent Circuit

126

where: K_p = pump gain

I_s = inertance, suction line

I_{ap} = inertance, line from accumulator to pump

I_a = inertance, accumulator

I_d = inertance, discharge line

C_s = compliance, suction line (neglected)

C_a = compliance, accumulator

C_p = compliance, cavitation of pump, (neglected, pump is not operated in cavitating region)

R_a = resistance, accumulator

R_d = resistance, discharge line

$\dot{X}_p$ = pulser instantaneous velocity

P_s = instantaneous suction line pressure

This configuration is characterized by the accumulator placed in the suction line and excited by a pulser located in the discharge line immediately downstream of the pump.

(2) Results. The response of the system expressed as suction pressure as a function of frequency follows the sketch shown in Figure 70 . The initial peak or resonance is a result of the interaction of the suction line inertance, I_s, with the accumulator compliance. This is followed by an antiresonance which is a function of the accumulator resistance R_a, and its inertance, I_a. One of the primary objectives of the test is to investigate the effect of accumulator geometry on its resistance and inertance. Obviously, since these parameters are associated with the antiresonance, the dynamic response will be too small to observe. Therefore, the configuration was changed so that the accumulator inertance could be interpreted in terms of effects on a measurable system resonance.
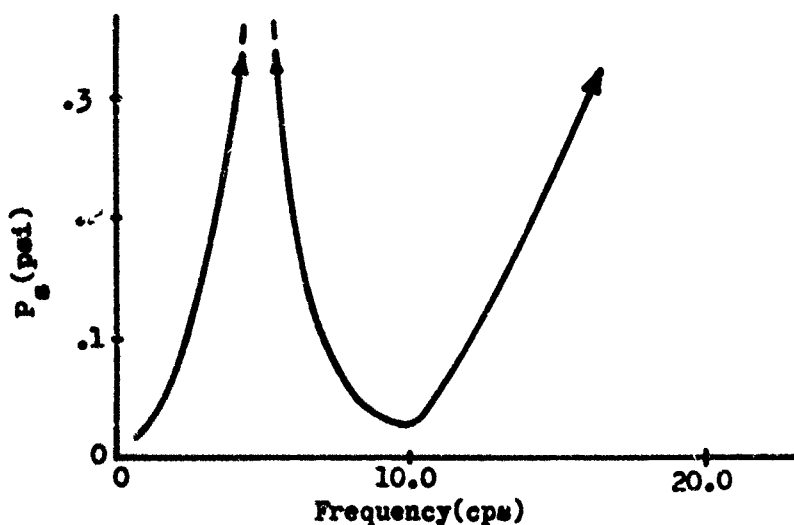
Figure 70. Typical Response

b. Sealed-Bag Compensator, Gas Pulsing

(1) Test Configuration. A change in the test configuration can be simply accomplished which will allow effects of accumulator inertance changes to be evaluated in terms of changes to a system resonant response. A typical response is shown in the following figure in which the resonant frequency, ω_r, is most sensitive to accumulator inertance and compliance.
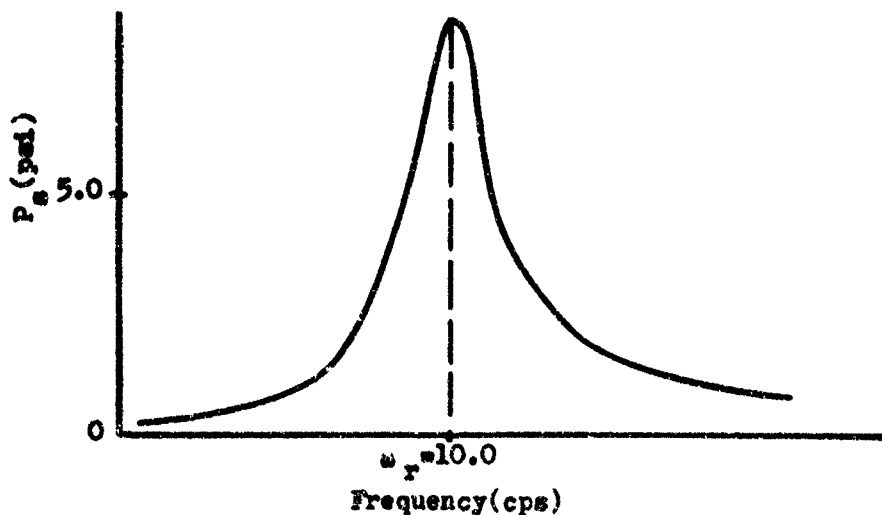

Figure 71 Typical Gas Pulsing-Sealed-bag Response

128

The configuration change requires direct pulsing of
the gas in the accumulator bags instead of the system fluid.
This method can best be understood by referring to the electri-
cal analog diagram below:
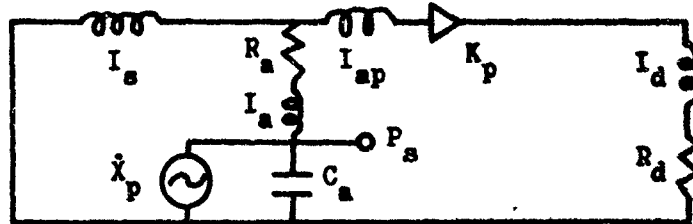
Figure 72   Sealed-bag-Gas Pulsing Analog

By making the suction line as short as possible,
or in other words, by attaching the accumulator to the supply
tank outlet, the impedance due to the inertance, I_s, can be
made very small compared to the downstream impedance which in-
cludes I_{ap}, I_d, R_d. With these impedances in parallel across
the accumulator, the net impedance is essentially that due to
I_s or on redrawing the schematic we have,
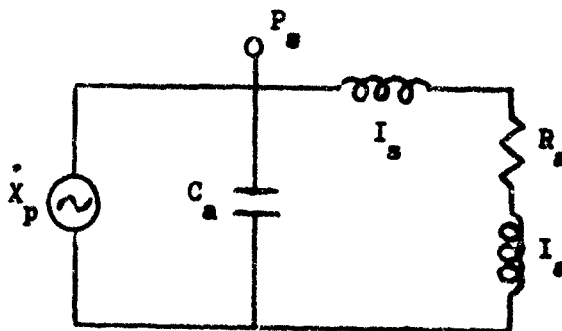
Figure 73   Simplified Electrical Model For Gas Pulsing

The final result is a parallel resonant circuit
which exhibits a high impedance at resonance. The $P_s/\Delta V$ trans-
fer function for this circuit is given by

$$P_s/\Delta V = \frac{S(I_a + I_s) + R_a \frac{1}{SC_a}}{S(I_a + I_s) + R_a + \frac{1}{SC_a}} \qquad (61)$$

where ΔV is the pulser volumetric displacement. By keeping I_a and I_a approximately equal, changes in I_a can readily be observed in the system performance.

(2) Results. Typical theoretical values for system parameters based on current designs give a response as shown in Figure 74. Of the curves shown, one represents an accumulator inertance of .001 sec^2/in^2 while the other is for a value which is 100% greater. These inertance values cover an expected range with respect to present design. Each family of three curves is for an accumulator resistance which reflects fluid damping ratios of 0.10, 0.30, and 0.50. Assuming that the accumulator compliance, C_a, will be determined through an accurate calibration, the compensator inertance, I_a, can be measured by the resonance while the resistance R_a, will be obtained from the peak response at resonance.
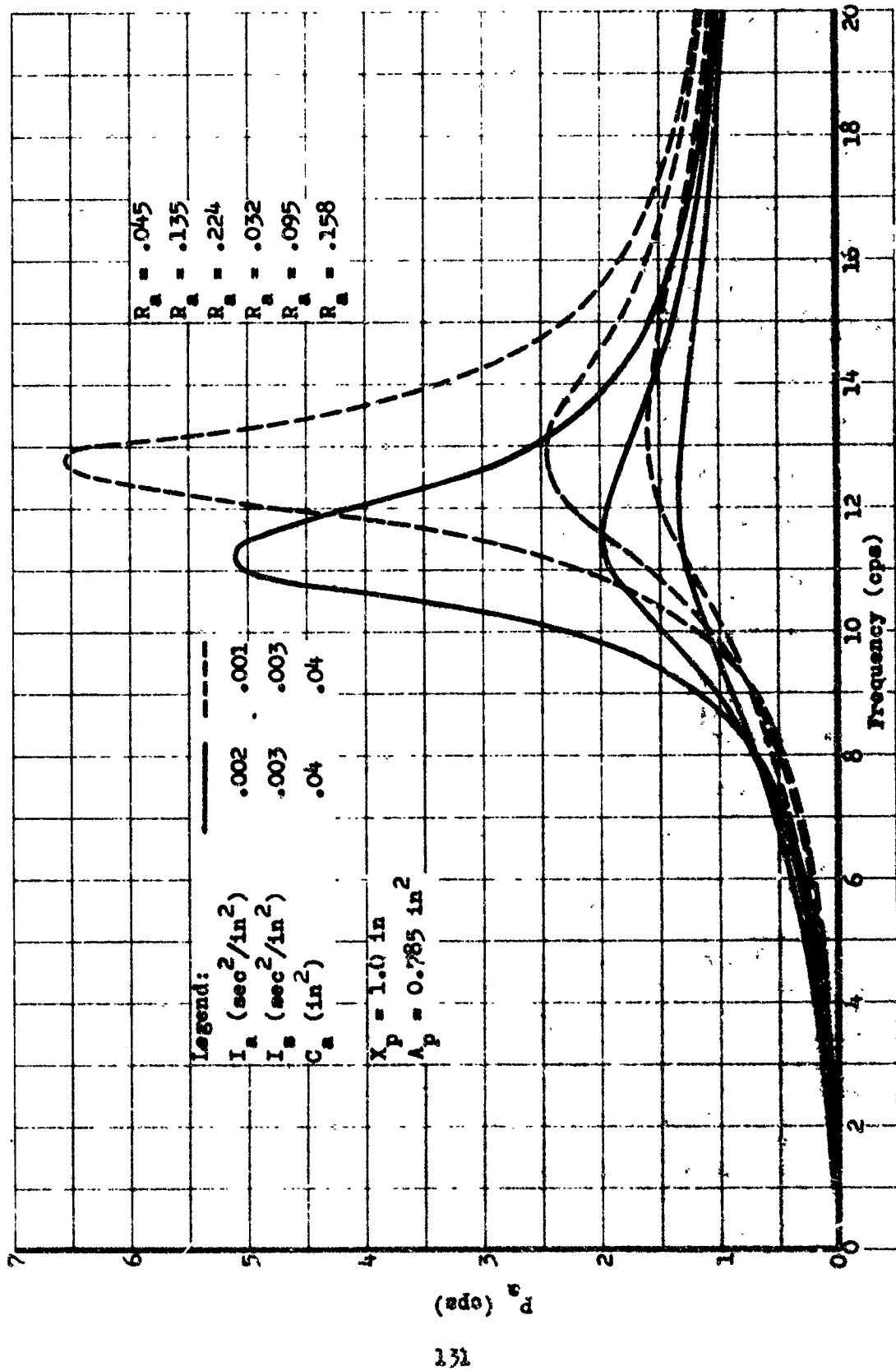
Figure 74   Sealed-Bag System Response Compensator Gas Pulsing

SECTION X

SEALED BAG ACCUMULATOR TESTS

1. INTRODUCTION

The sealed bag accumulator tests were performed to evaluate the analytical results of Section IX and the behavior of certain sealed bag accumulator dynamic characteristics as a function of pressure and accumulator geometry. Accomplishment of these objectives was attempted through a test program of two phases. The following paragraphs provide a description of the test fixture, test procedure and experimental measurements taken during each test run. The results of the experimental study are presented in Part 3 of this section.

2. TEST FIXTURE AND PROCEDURE

The basic experimental fixture was the same for both phases of testing. Figure 289 shows the complete configuration as an assembly of tanks, accumulator, suction line, pump, and return or discharge line. Figures 290 and 291 of Appendix XIV are detailed drawings of the accumulator itself and show how the compliant elements are located within the accumulator. Figures 78 through 81 are photographs of the disassembled accumulator, including bags and retainer sleeve. Detailed drawings of the remaining system elements are given in Figures 290 through 292 of Appendix XIV. Photographs of the fixture are given in Figures 82 and 83 .

a. Sealed Bag Accumulator. The accumulator is shown as an element short coupled to the supply tank. As discussed in Section IX above the short coupling minimizes the inertance upstream of the accumulator. The pulser is located close to the accumulator where it can effectively excite the system by pulsing the gas in the accumulator bags. Figure 293 (Appendix XIV) details the pulse drive assembly which includes the variable drive motor and a cam follower which actuates a bellows-type pulser illustrated in Figures 292 and 293, Appendix XIV. Figures 294 and 295 illustrate a valve which was devised to seal off the inlet side of the accumulator. Because of the necessity for short coupling the accumulator to the tank, an ordinary valve could not be used at this location. The inlet seal is used in conjunction with a ball valve at the accumulator outlet to isolate the accumulator from the remainder of the system. This is done after static pressures have been applied
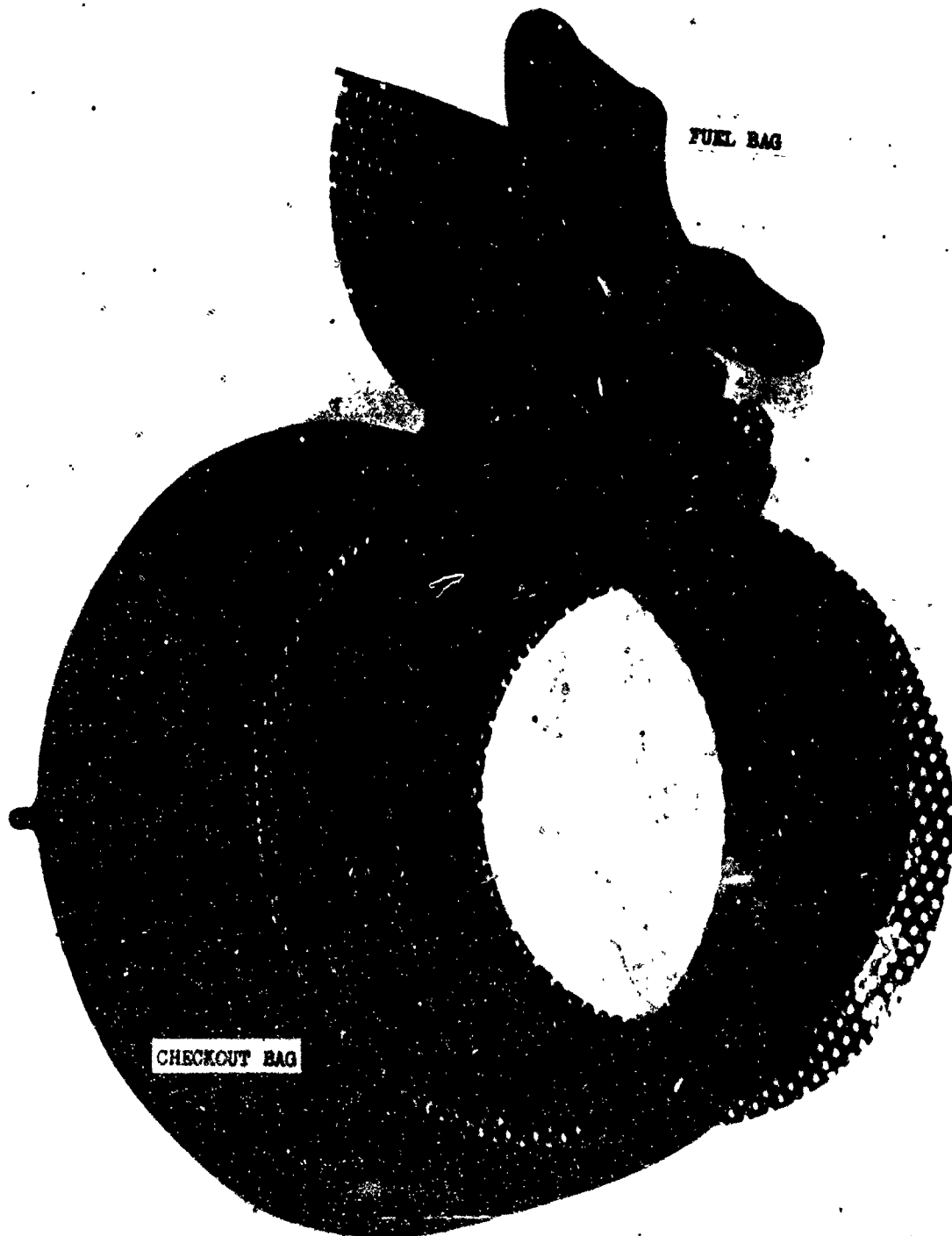
Figure 75 Sealed Bag Accumulator, Bags and Retainer

Figure 76 Sealed Bag Accumulator, Flex Sleeve Assembled

134

ACCUMULATOR

ACCUMULATOR HOUSING

Figure 77   Sealed Bag Accumulator, Flex Sleeve Disassembled
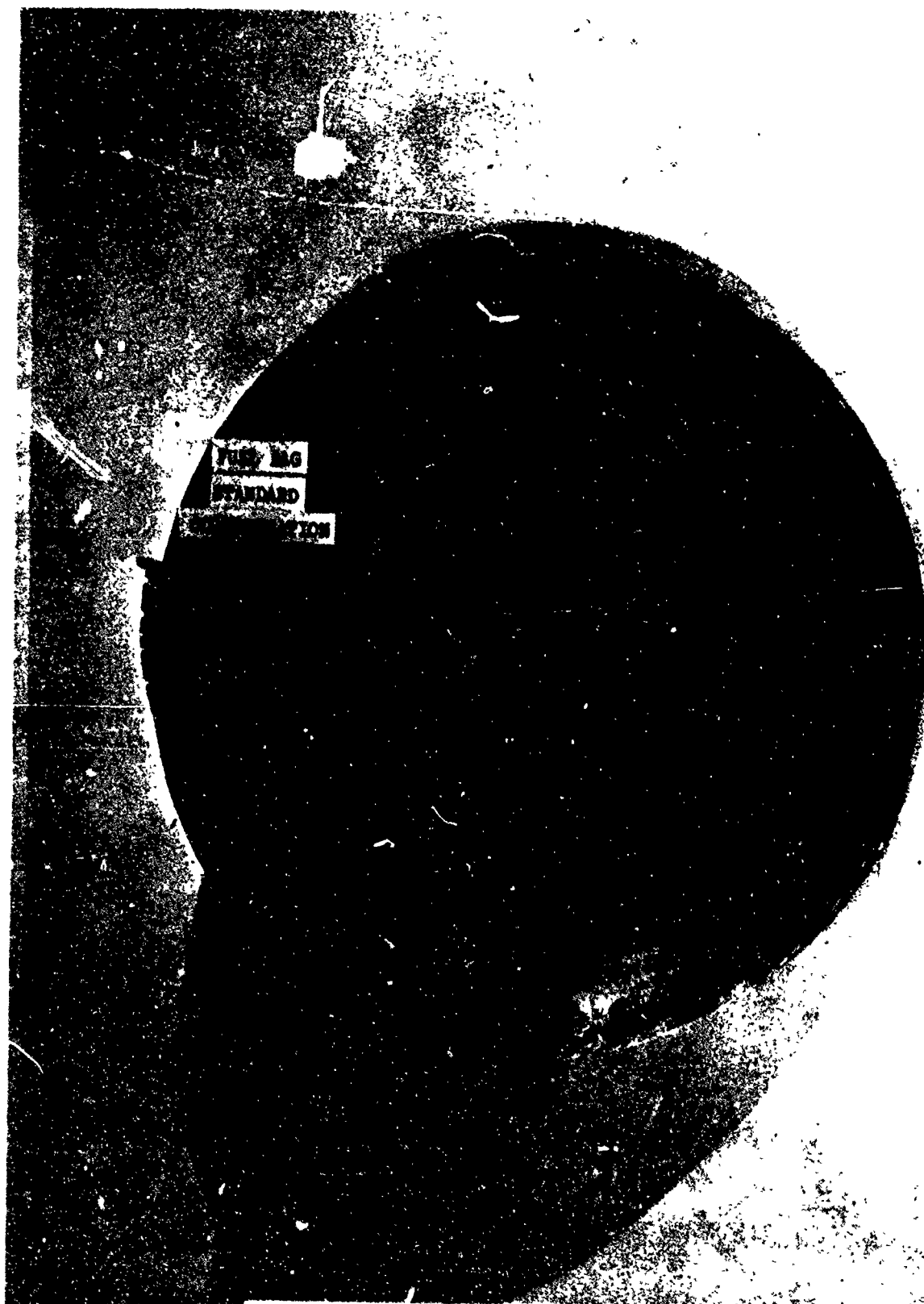
Figure 78   Sealed Bag Accumulator, Fuel Bag-Standard

136

FUEL BAG CLOSE CONFIGURATION

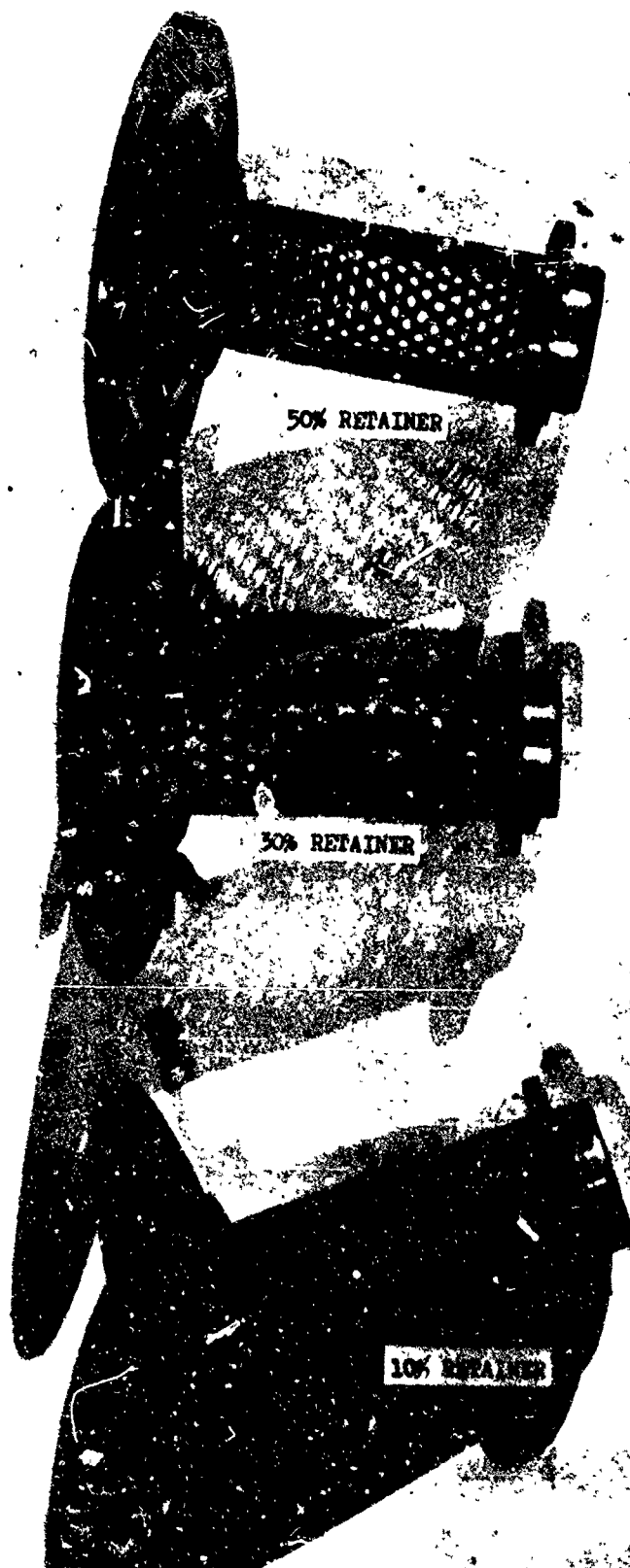Figure 79 Sealed Bag Accumulator, Fuel Bag-Cl

137

Figure 80 Sealed Bag Accumulator, Retainer Sleeves
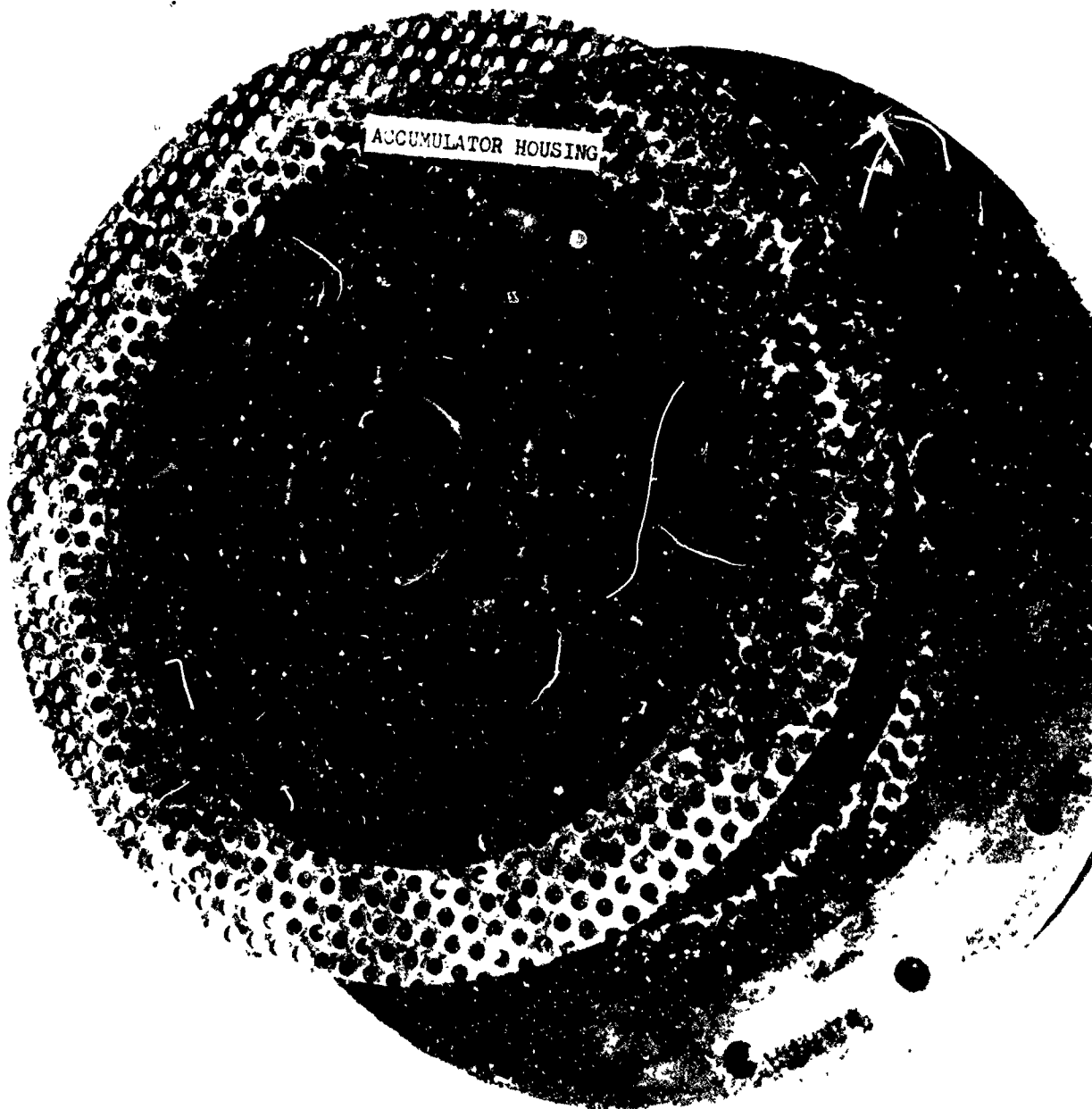
Figure 81 Sealed Bag Accumulator, Sleeve and Housing

139

Figure 82 Sealed Bag Accumulator Test Fixture
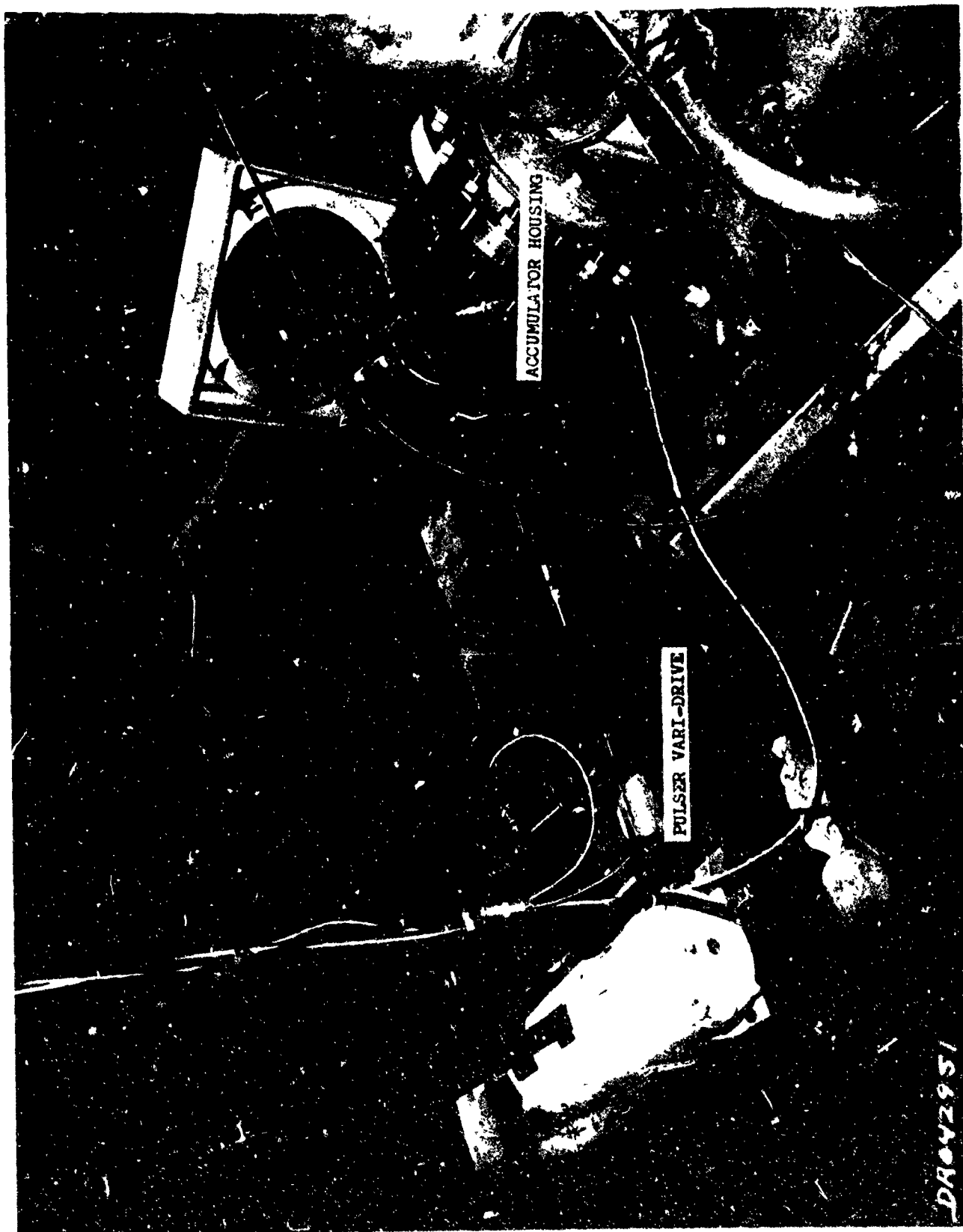
Figure 83 Sealed Bag Accumulator Pulser and Vari-Drive

141

to both the gas in the bag and the tank top or system liquid. The purpose of using the valves in this manner is to measure only the compliance of the accumulator under operating conditions and to be able to perform this operation immediately preceding a dynamic test.

b. Phase One. The two test phases were integrated in certain respects. The first phase which consisted of evaluating the variation in compliance as a function of pressure and geometry, involved measuring the change in volume of the sealed bag accumulator prior to each of the second phase runs. The method of measuring volume change was to first isolate the sealed bag accumulator by means of the valves described above. The second step involved pressurizing the bags to 15 PSIA and then sealing the bags. The pressure in the accumulator was then increased to 20 PSIA. From this starting point the pressure in the accumulator was further increased in 5.0 PSI increments to 40.0 PSIA and the volume of water added to the accumulator for each increment was measured.

c. Phase Two. The second phase of sealed bag accumulator testing provided frequency response data on the accumulator as a function of system static pressure, per cent hole area in the retainer sleeve and accumulator geometry. The test procedure employed was very similar to that described in Section XIII. Basically, upon establishing system steady flow and pressure conditions the pulser varidrive system was actuated to induce flow displacement oscillations in the system with a continuous variation in frequency from 2 to 30 cycles per second. The total time for the sweep of frequencies was about 70 seconds. In each test the flow displacement resulted from a pulser volumetric displacement of 20 cubic centimeters. Measurements for the Phase II tests were pulser displacement and frequency, flow rate, system static pressure and accumulator oscillatory pressure. Table VI contains a list of the test runs performed along with the pressure, retainer hole area, and configuration conditions. As indicated in the table, four basic accumulator designs were examined. In addition, the bag retainer hole area ratio (ratio of hole area to total area) was included as a geometric parameter.

The results of the sealed bag accumulator test program are given in the following paragraphs along with a discussion of the conclusions and recommendations.

TABLE VI

SEALED BAG ACCUMULATOR
TEST CONDITIONS

Bag Configuration	Fuel Bag Standard Configuration	Fuel Bag Close Configuration	Checkout Bladder	Flex Sleeve Accumulator
20 PSI 10%	Run 1	Run 10	Run 13	Run 22
20 PSI 30%	Run 4		Run 16	Run 25
20 PSI 50%	Run 7		Run 19	Run 28
30 PSI 10%	Run 2	Run 11	Run 14	Run 23
30 PSI 30%	Run 5		Run 17	Run 26
30 PSI 50%	Run 8		Run 20	Run 29
40 PSI 10%	Run 3	Run 12	Run 15	Run 24
40 PSI 30%	Run 6		Run 18	Run 27
40 PSI 50%	Run 9		Run 21	Run 30

3. SEALED BAG ACCUMULATOR TEST RESULTS

As described in previous paragraphs the sealed bag accumulator tests were performed in two phases. The Phase I data provided information regarding the effects of accumulator geometry and system static pressure on accumulator static compliance. The results of the Phase II test along with the math model were to be utilized in establishing relationships between accumulator dynamic parameters such as inertance, resistance, and compliance and the accumulator design parameters of geometry, and system pressure. The results of this effort are considered in the following paragraphs along with conclusions derived from post test analysis.

4. PHASE I RESULTS

In order to examine the influence of accumulator geometry on compliance four basic designs were studied. Three of the designs - fuel bag standard configuration, checkout bag configuration, and flex sleeve accumulator were tested with three variations in the retainer sleeve hole area ratio. In each, retainer sleeves having hole area to total area ratios of 10%, 20%, and 50% were examined. The fourth design was based on the fuel bag configuration but with the bags in a close in configuration (Figure 290 , Appendix XIV) and a 10% hole area ratio in the retainer. For these configurations the changes in accumulator gas volume with system pressure were plotted; with the results shown in Figures 84 through 94 . The bag precharge pressure in each case was 15 PSIA. In the figures the accumulator compliance at a given pressure is related to the slope of the volume change-pressure curve (M) by

$$C = \rho M \tag{62}$$

where: ρ is the fluid density

a. Influence of Retainer Hole Area. The influence of retainer hole area on compliance for a given design can be observed by comparing the data of Figures 84, 85 and 86 for the fuel bag standard configuration, Figures 88, 89 and 90 for the checkout bag configuration, and Figures 91, 92 and 93 for the flex-sleeve accumulator. A comparison of the data of Figures 84 through 90 show that variations in geometry for the fuel bag, both standard and close configuration, and the checkout bag produce only minor variations in compliance. The change in geometry from these configurations to that associated with the

flex sleeve accumulator produces a substantial variation in compliance. This behavior can be observed by comparing the data of Figures 91, 92 and 93 with that of Figures 84 through 90. Recalling the relationship between slope (M) of the P-ΔV curve and compliance (Equation (62)) the flc~ sleeve accumulator exhibits more compliance at a given system pressure than do the three other designs. Considering design differences, the added compliance of the flex-sleeve configuration can probably be associated with the lower structural rigidity of the retainer sleeve coupled with the bag compliance. With these conclusions established the variation of compliance with system static pressure for the fuel bag configurations and checkout bag can be studied independent of their relative geometries. The differences between these three designs and the flex-sleeve design will couple geometry with pressure effects.

b. **Influence of Basic Geometry.** Considering Figure 84 to be typical of the P-ΔV curves of the fuel bag and checkout bag configurations it is apparent that accumulator compliance decreases with increasing system pressure. The same result applies to the flex-sleeve design (Figures 91 through 93). This effect is also shown in Figure 94 where the parameter C/ϕ is plotted as a function of system pressure. Referring to Figure 94 the behavior of the curves is not significant from the standpoint of any unique physical process. The data cannot be related to either a gas compression process or a structural deformation process. Considering the physical elements contributing in the process a combination of the two is probably responsible for the behavior indicated.

c. **Conclusions.** The conclusions drawn from this phase of testing are 1) Retainer hole area ratio does not significantly affect accumulator static compliance and 2) Accumulator geometry and system static pressure both influence compliance; however, the extent of each is probably related to the stiffness of the retainer sleeve.

5. **PHASE II RESULTS**

As was done in other phases of testing the sealed bag accumulator test data was analyzed in terms of frequency response. In all, four basic accumulator designs were examined along with three combinations of retainer sleeves. The configurations were the same as described in part 2 above. Figures 97 through 106 present plots of the experimental $P_a/\Delta V$ amplitude as a function of frequency. P_a is the amplitude of the accumulator
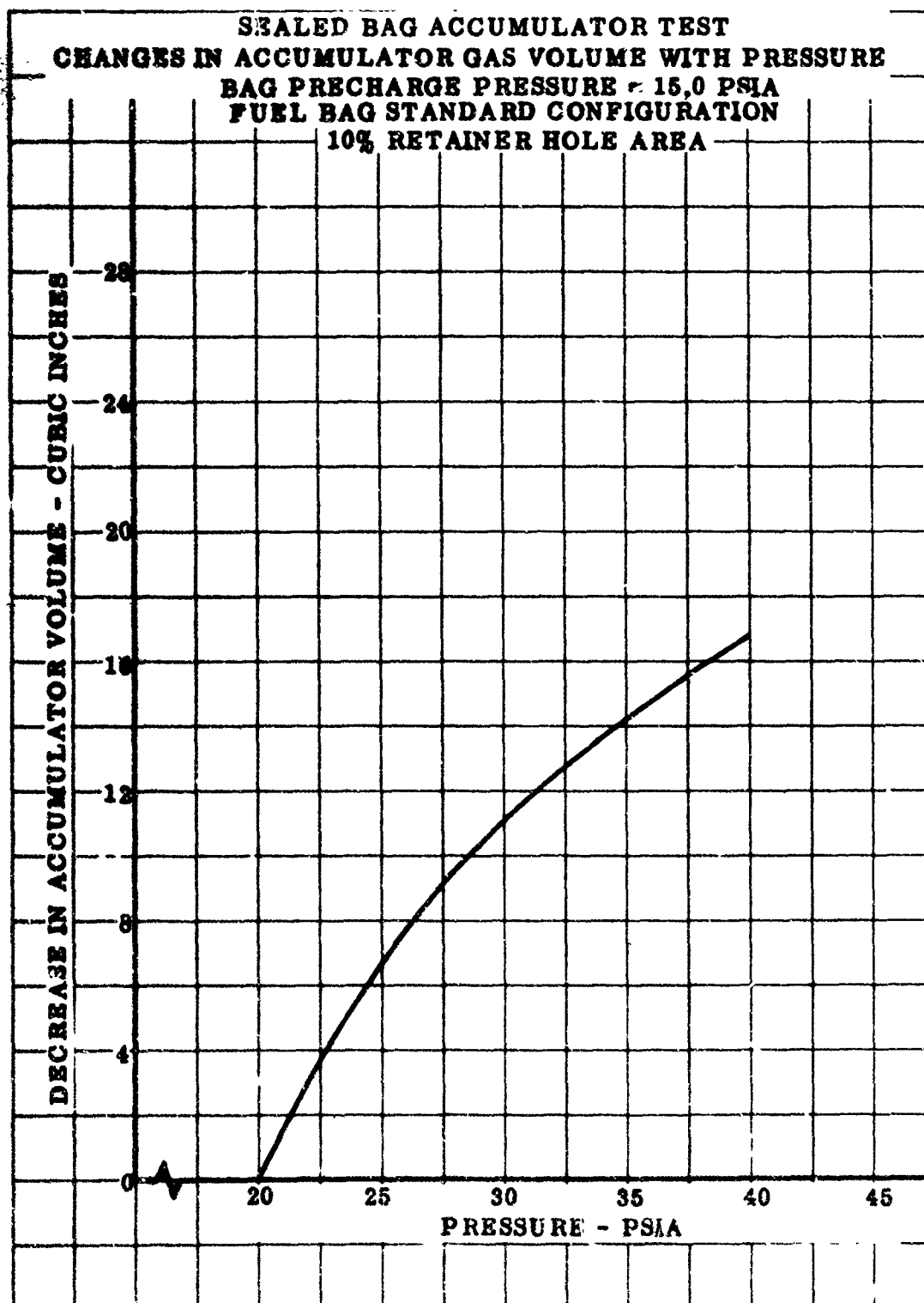
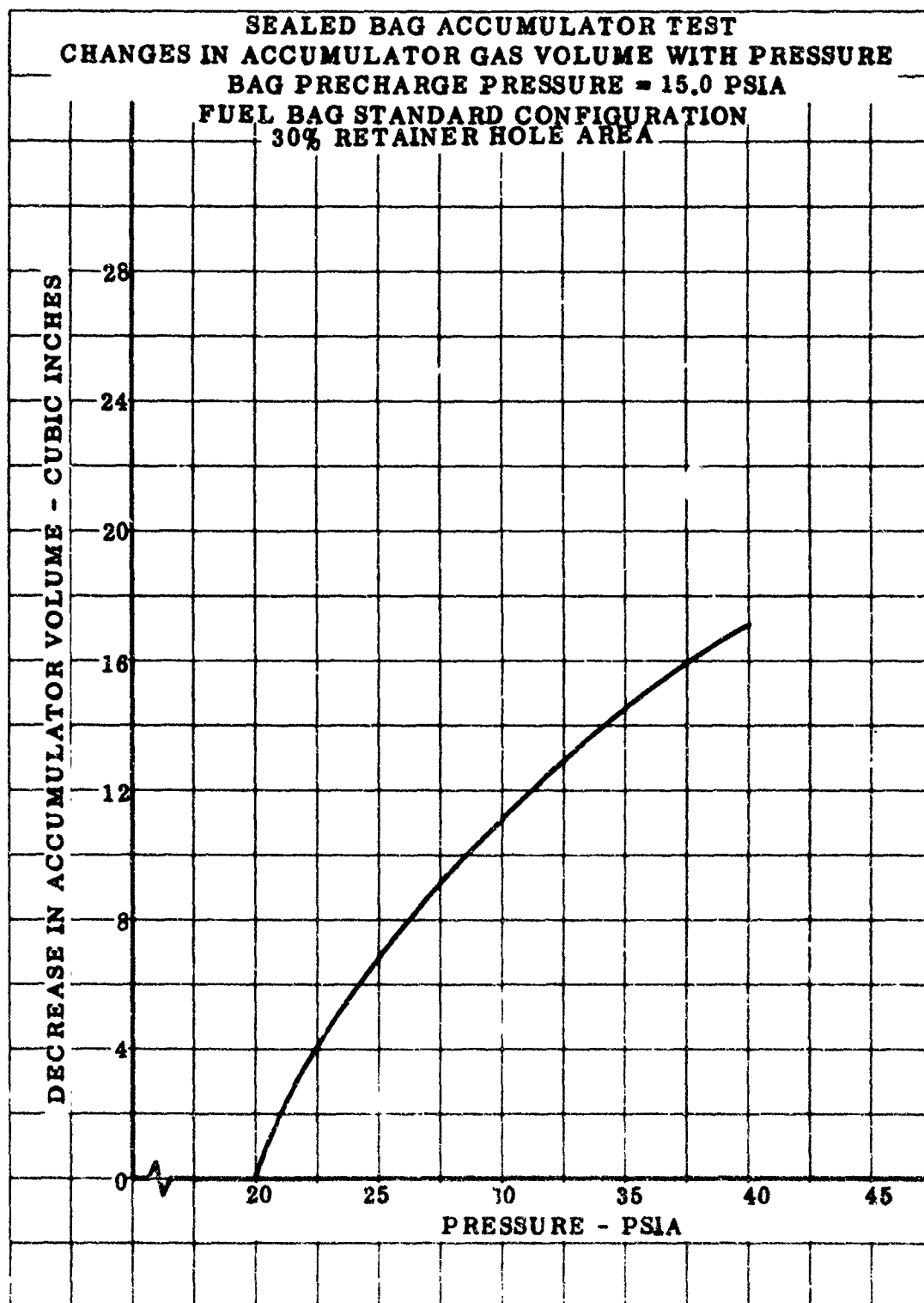Figure 84 Sealed Bag Accumulator ΔV, Pressure Relationship

146

SEALED BAG ACCUMULATOR TEST
CHANGES IN ACCUMULATOR GAS VOLUME WITH PRESSURE
BAG PRECHARGE PRESSURE = 15.0 PSIA
FUEL BAG STANDARD CONFIGURATION
30% RETAINER HOLE AREA

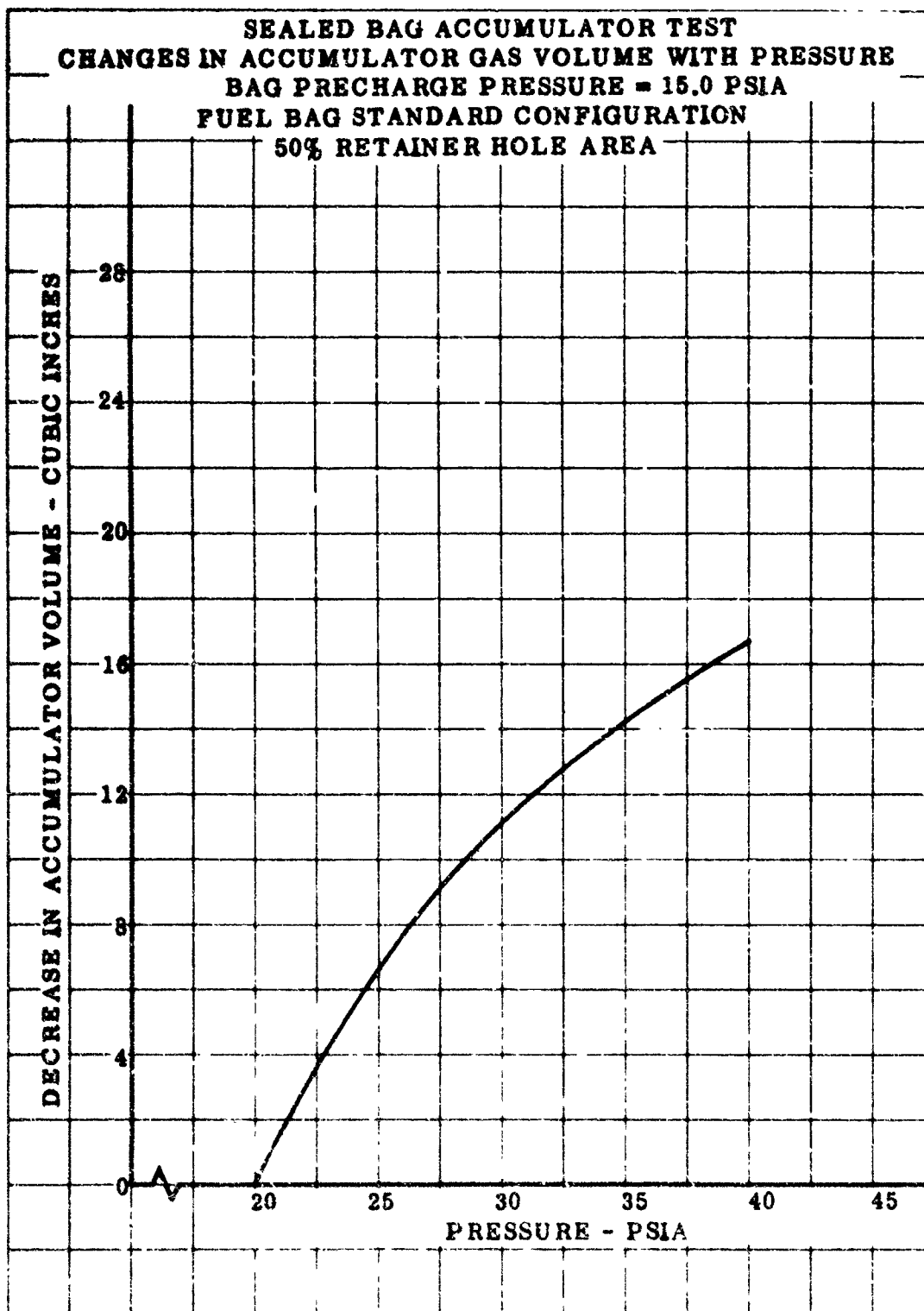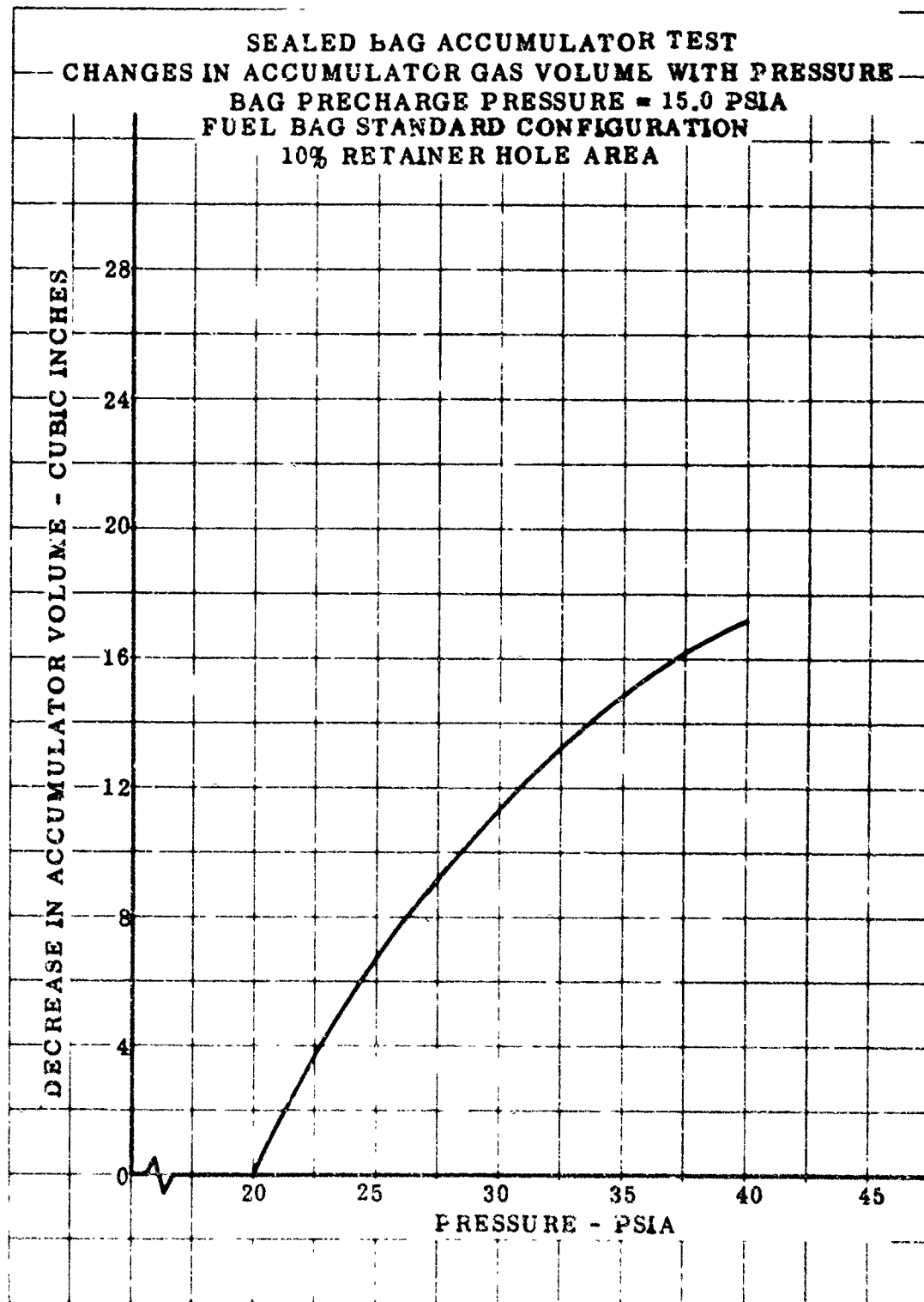Figure 85   Sealed Bag Accumulator ΔV, Pressure Relationship

147

Figure 86   Sealed Bag Accumulator ΔV, Pressure Relationship

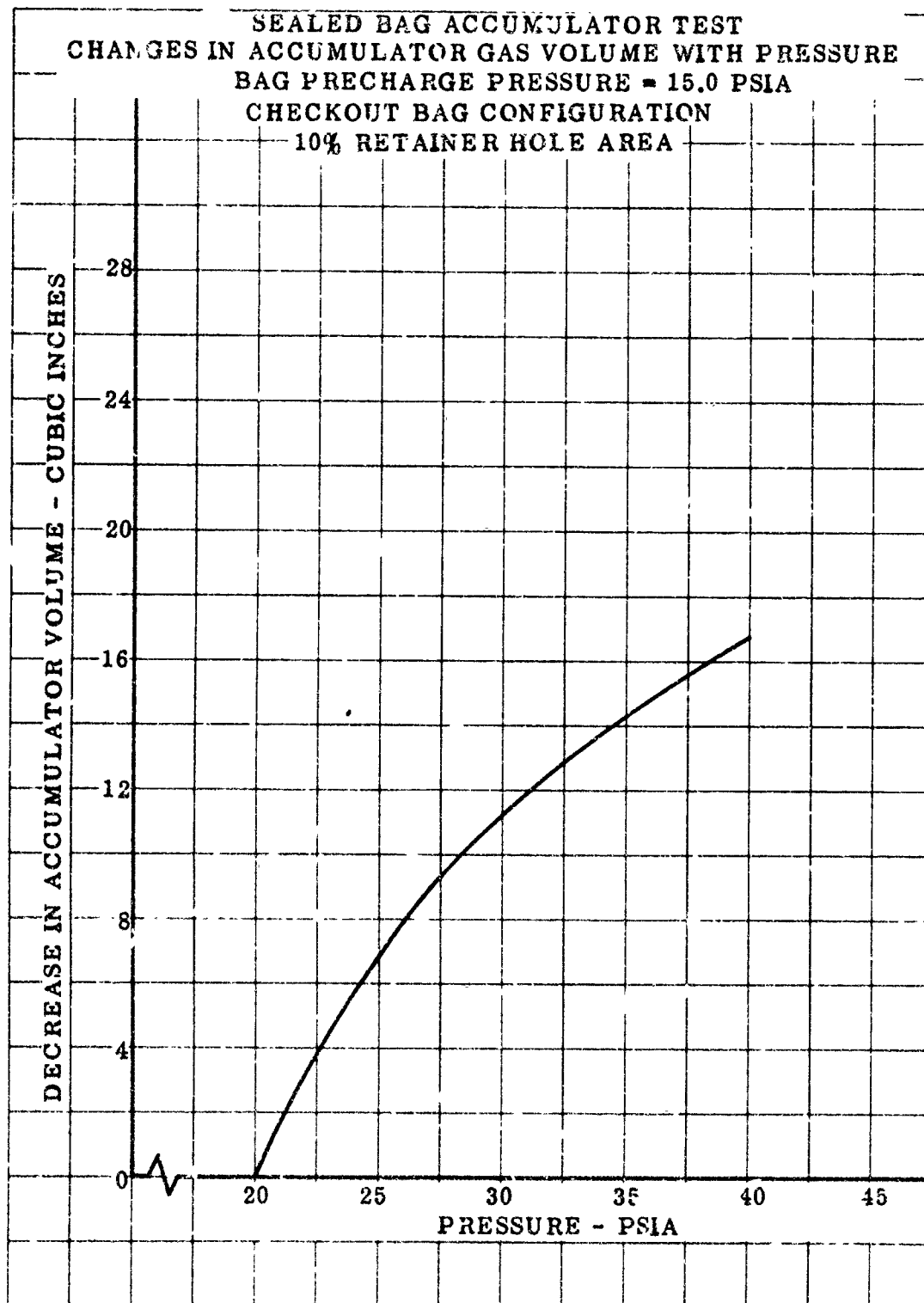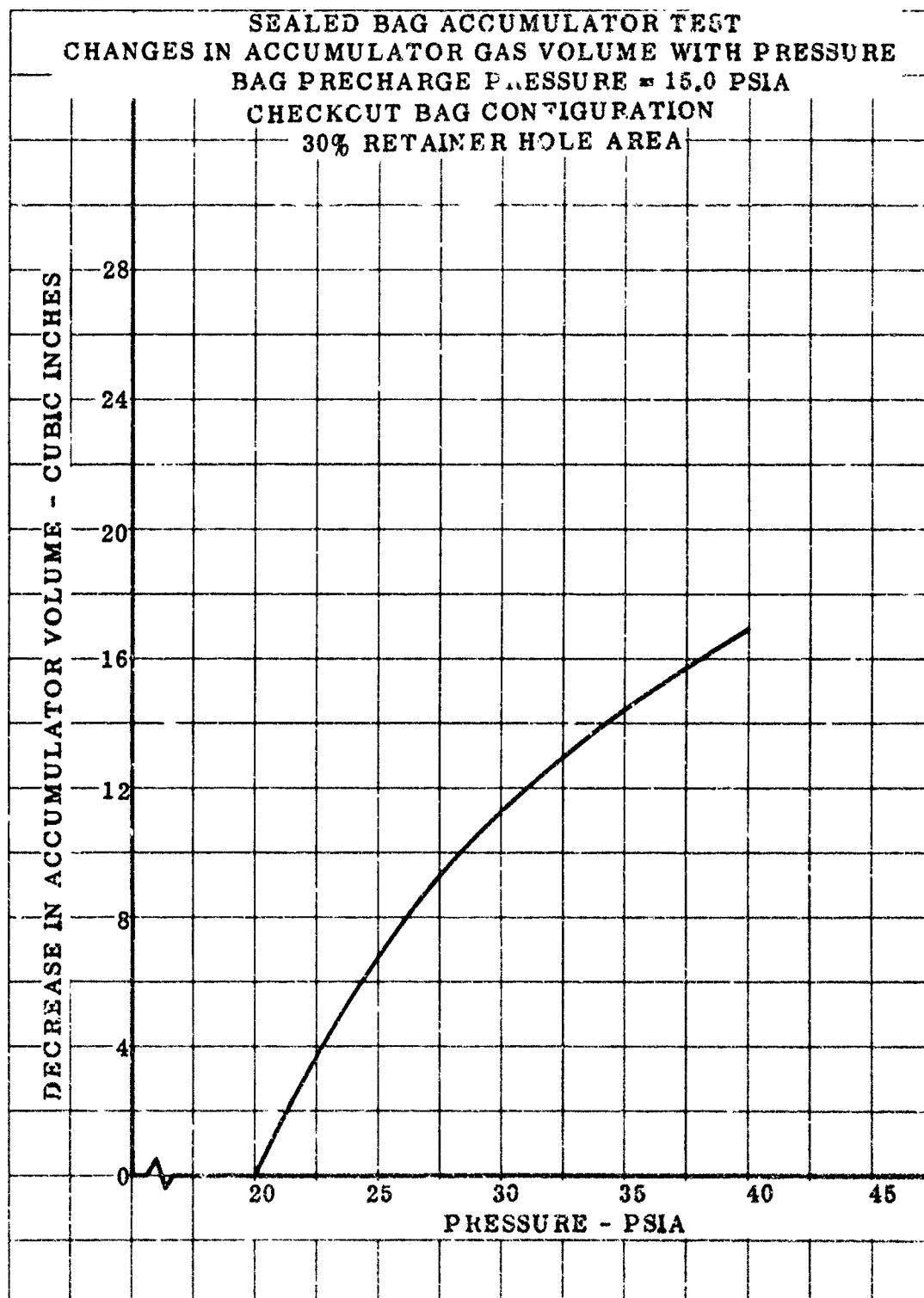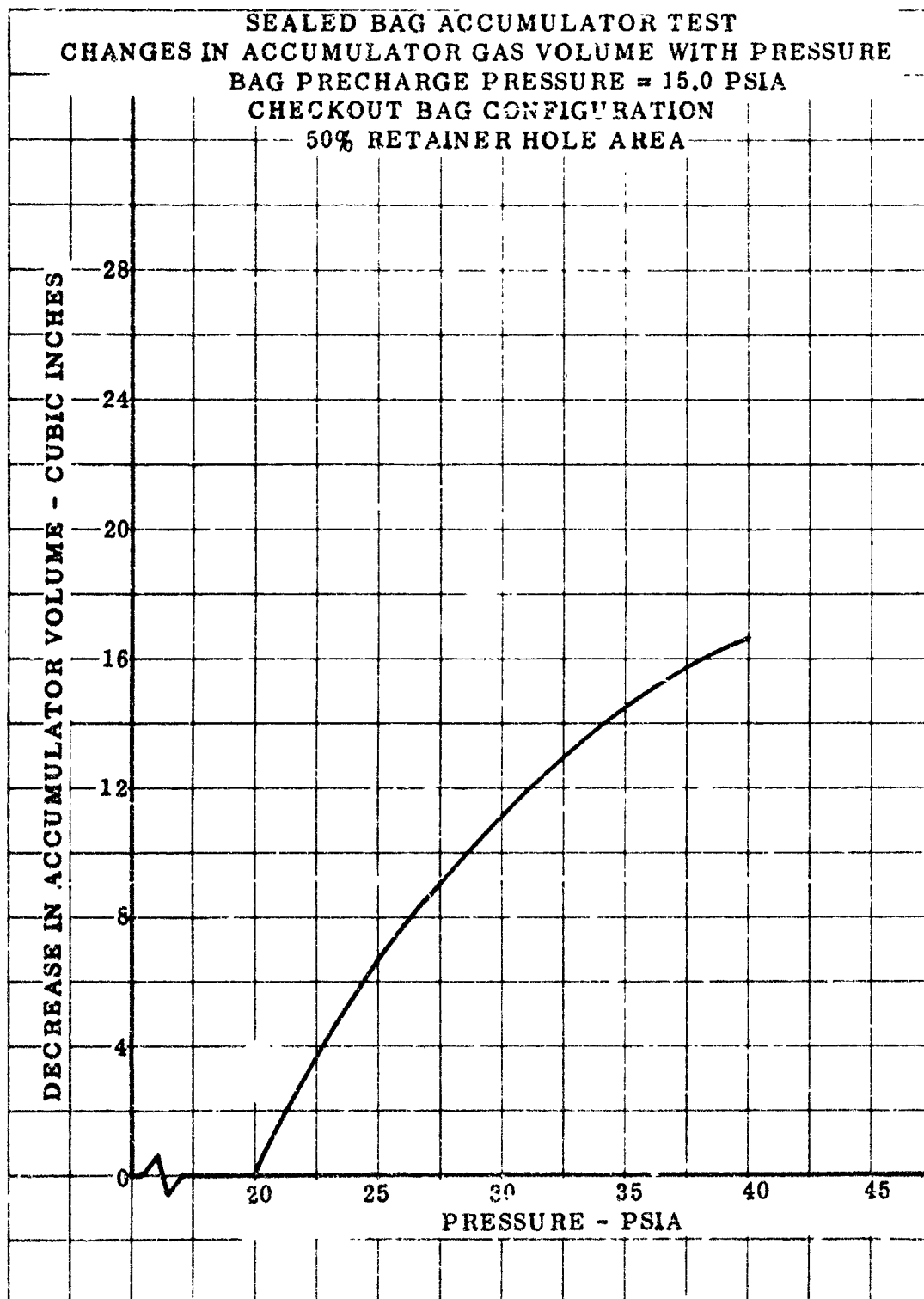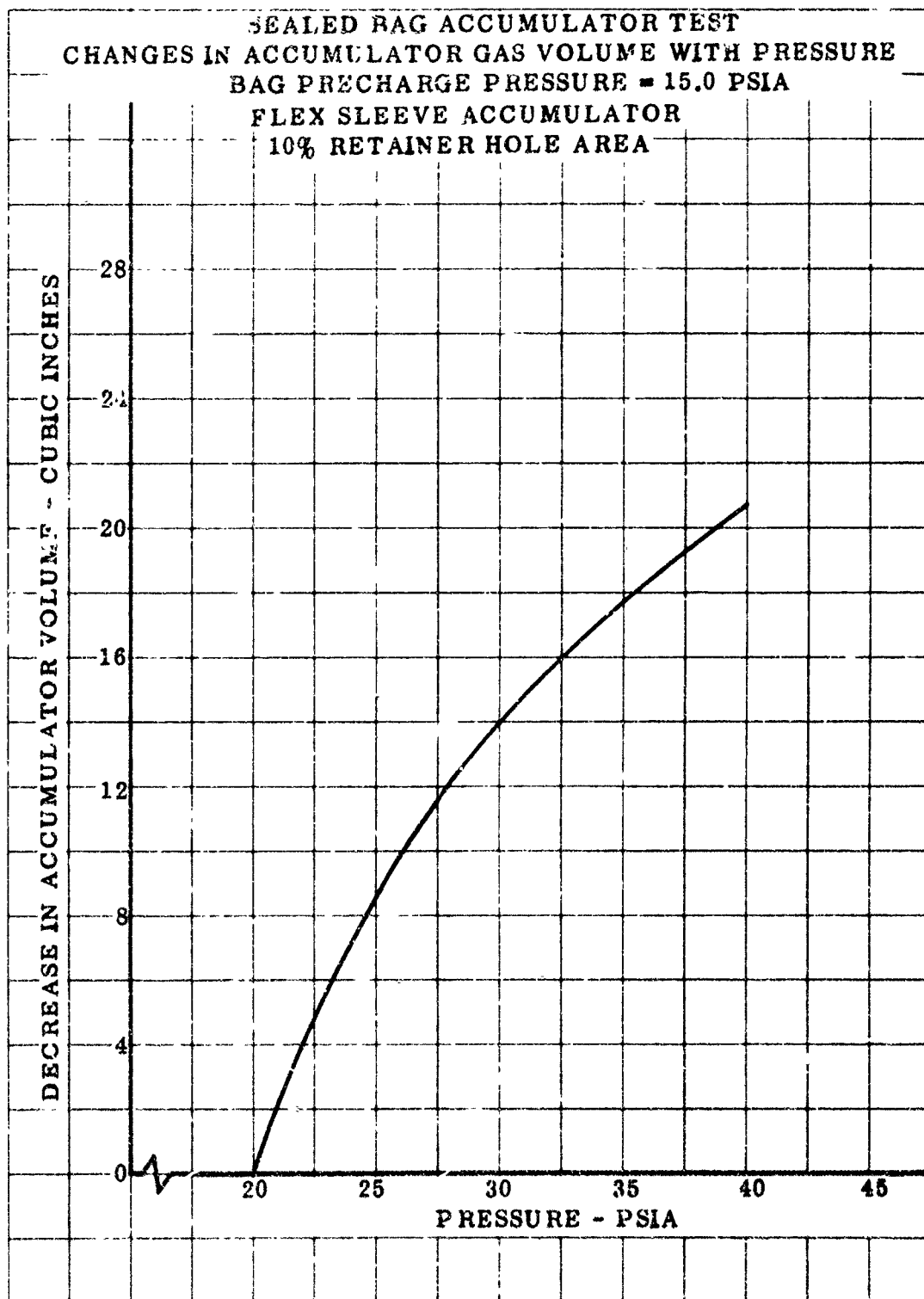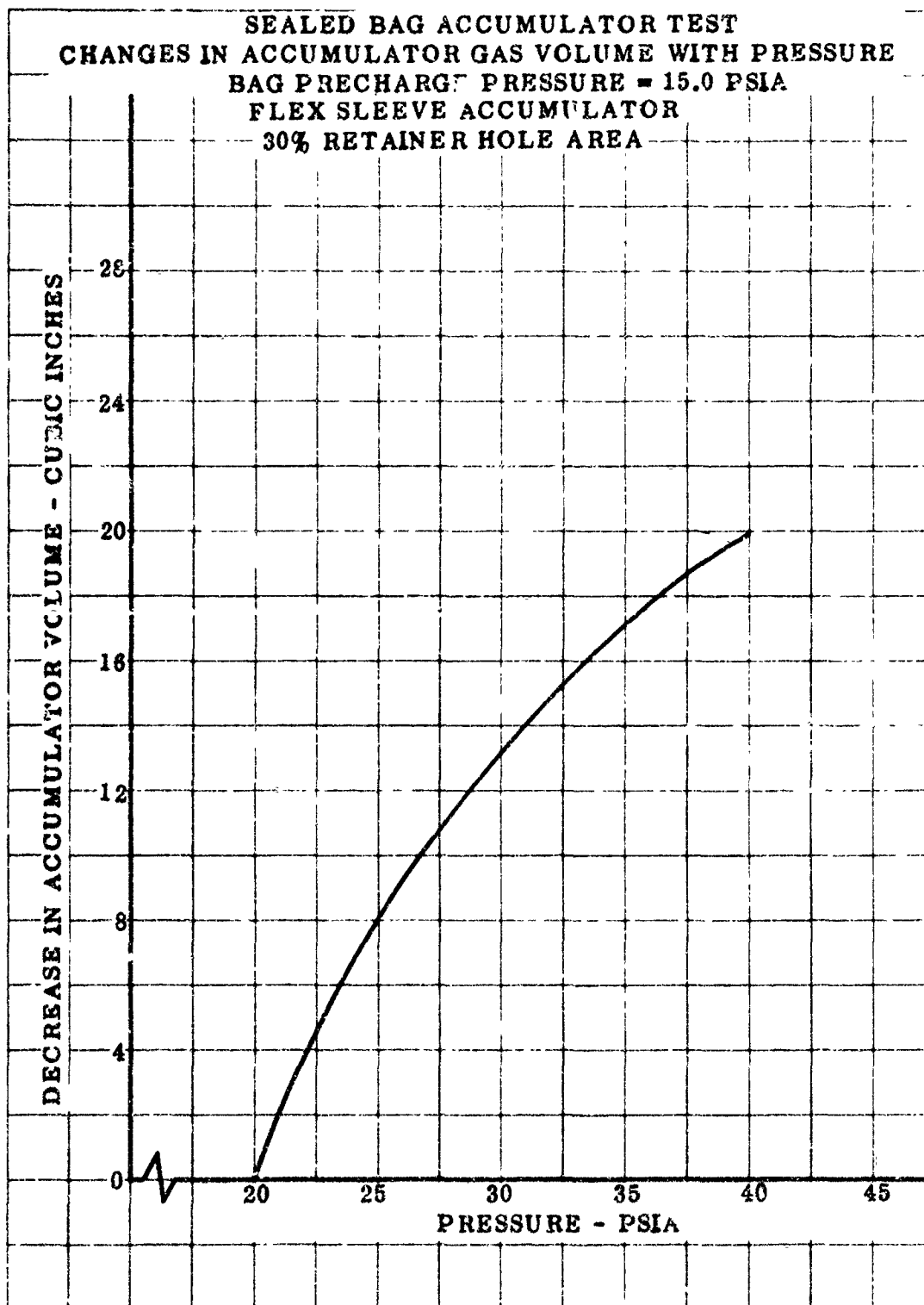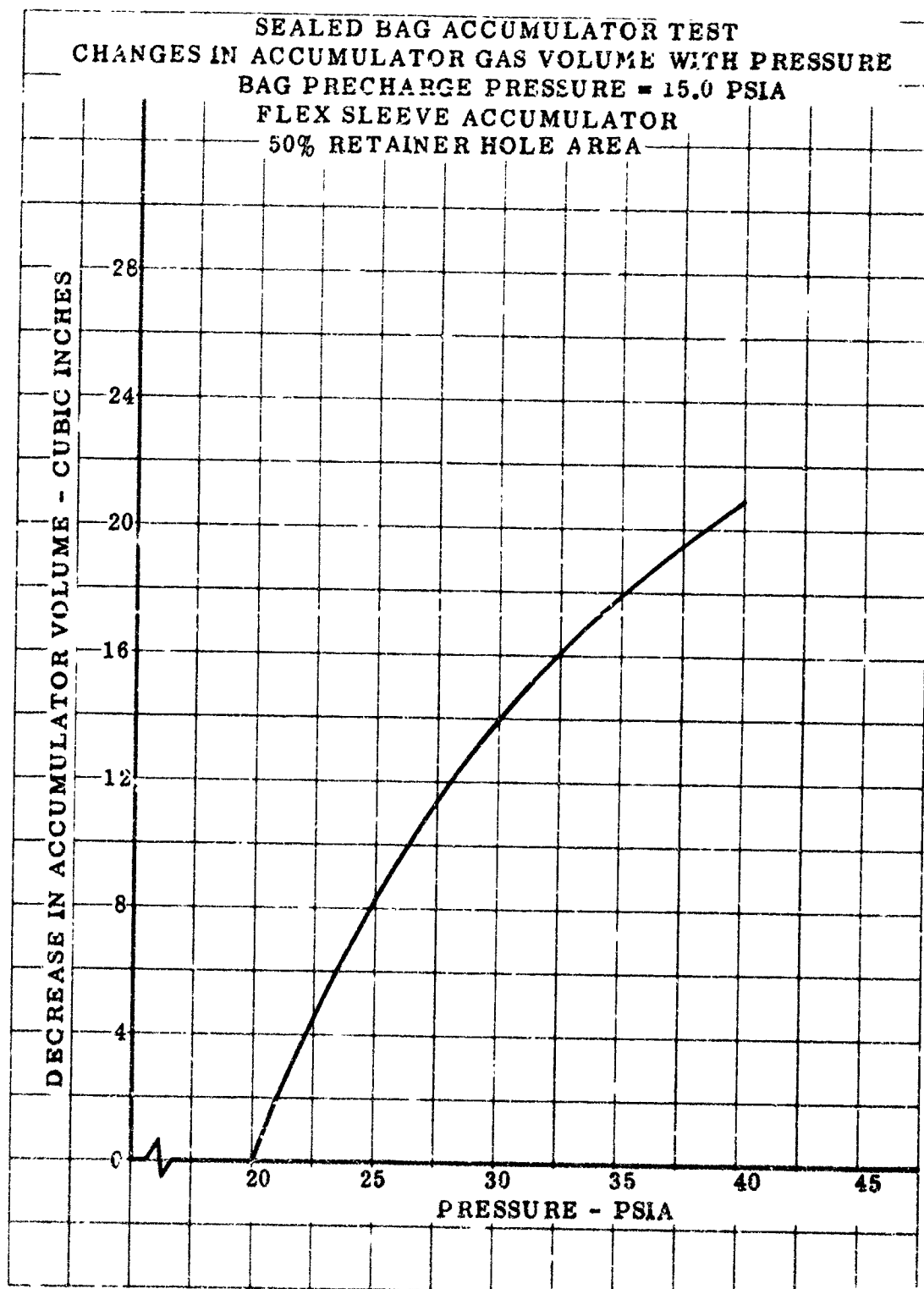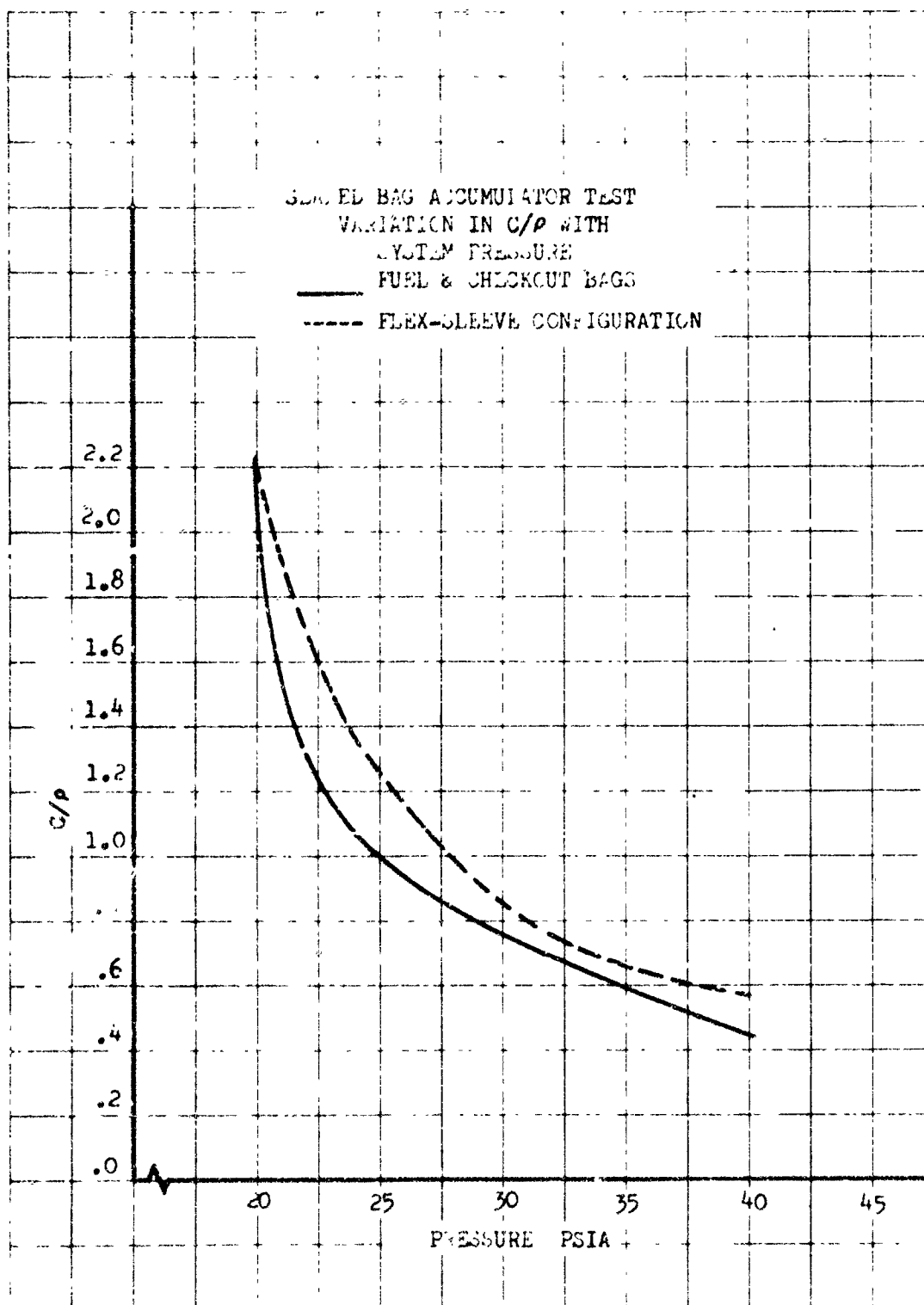Figure 87   Sealed Bag Accumulator ΔV, Pressure Relationship

Figure 88   Sealed Bag Accumulator ΔV, Pressure Relationship

150

Figure 89   Sealed Bag Accumulator ΔV, Pressure Relationship

151

Figure ∞   Sealed Bag Accumulator ΔV, Pressure Relationship

152

Figure 91 Sealed Bag Accumulator ΔV, Pressure Relationship

153

Figure 92   Sealed Bag Accumulator ΔV, Pressure Relationship

154

Figure 93 Sealed Bag Accumulator ΔV, Pressure Relationship

155

Figure 94   Sealed Bag Accumulator Observed C/ρ

156

oscillatory pressure and ΔV the amplitude of the pulsar volumetric displacement. ΔV for all sealed bag accumulator tests was 20 Cu. CM. Initial examination of the data in this form indicates that for the designs tested both the frequency corresponding to maximum response and the amplitude at maximum response increase with increasing system pressure. This behavior suggests that changes in pressure influence accumulator compliance primarily, with a lesser if any affect on inertance.

    a.   Correlation with Math Model. One purpose of the accumulator test was to determine if the observed behavior correlated with the mathematical development described in Section IX. The fact that the experimental observations do not match the theory is apparent from a comparison of the data of Figure 74 with that of Figures 97 through 106. The lack of agreement is found both in the frequency range for maximum response as well as the amplitude of maximum response. To determine if the lack of agreement was due to the values of parameters used in the analysis of error in the basic system synthesis, the test data was replotted as bode diagrams. Assuming the math model to be correct Figure 95 would be a typical bode plot of the analytical results. Recalling the general form of the $P_s/\Delta V$ transfer function (Equation 63)

$$\frac{P_s}{V} = \frac{s(s + a)}{s^2 + bs + c} \tag{63}$$

The following information would be available from the test data. In Figure 95 the asymptote from the origin to the first break point $(f = f_1)$ corresponds to the parameter $R_1\omega$. The asymptote from the first break to the second break $(f = f_2)$ yields the parameter $L_1\omega^2$ and finally the horizontal asymptote produces the parameter $1/C$. When replotted, the test data did not produce the expected behavior. Rather than approaching a horizontal asymptote with increasing frequency the data indicated a high frequency asymptote with a slope of 12 DB/octave (Reference Figure 96).

    b.   Indicated Model. This behavior indicates therefore that the basic model synthesis is in error. If the asymptotes indicated by the test data are considered in detail the experimental behavior of the system would correspond more closely the circuit analog given in Figure 107.
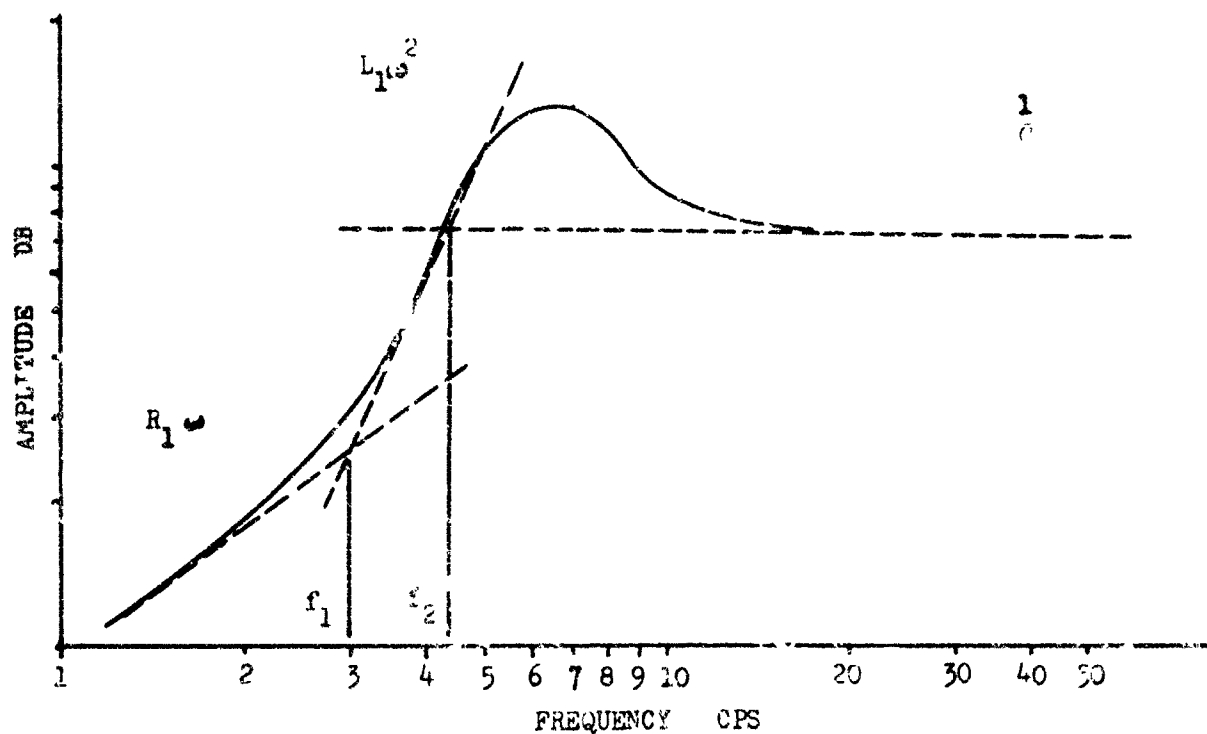
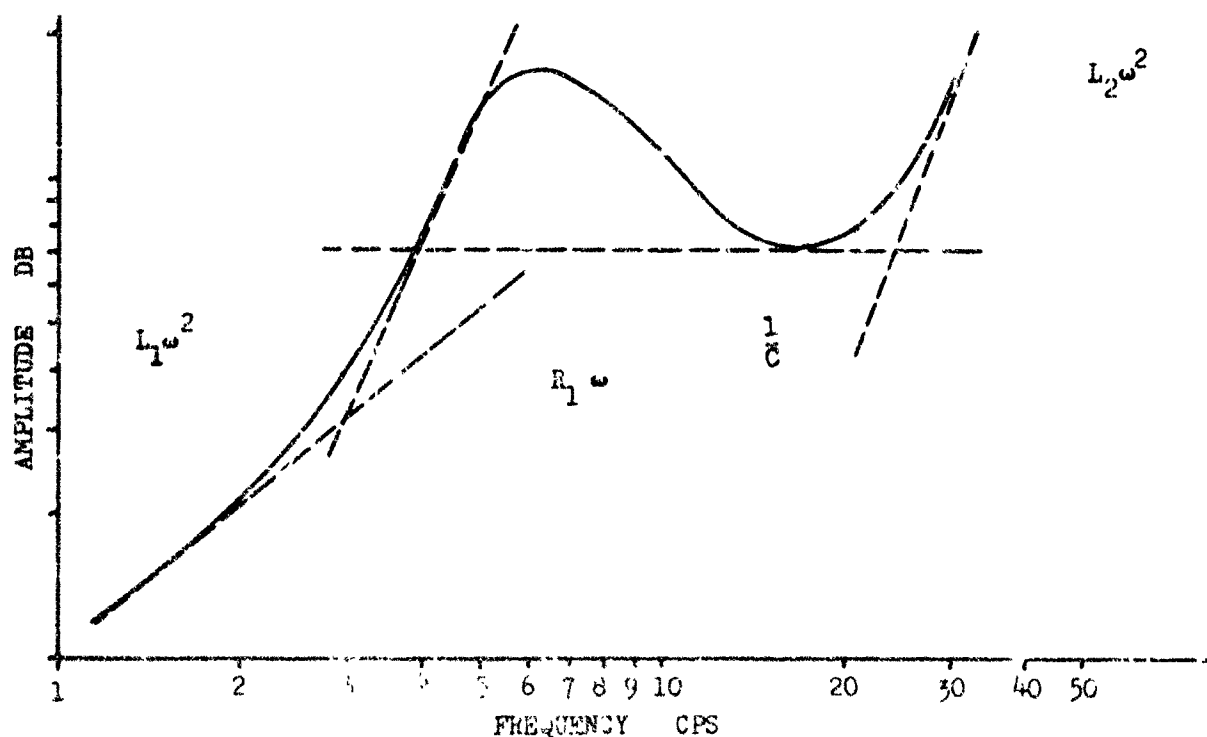**Figure 95** Sealed Bag Accumulator Predicted Response

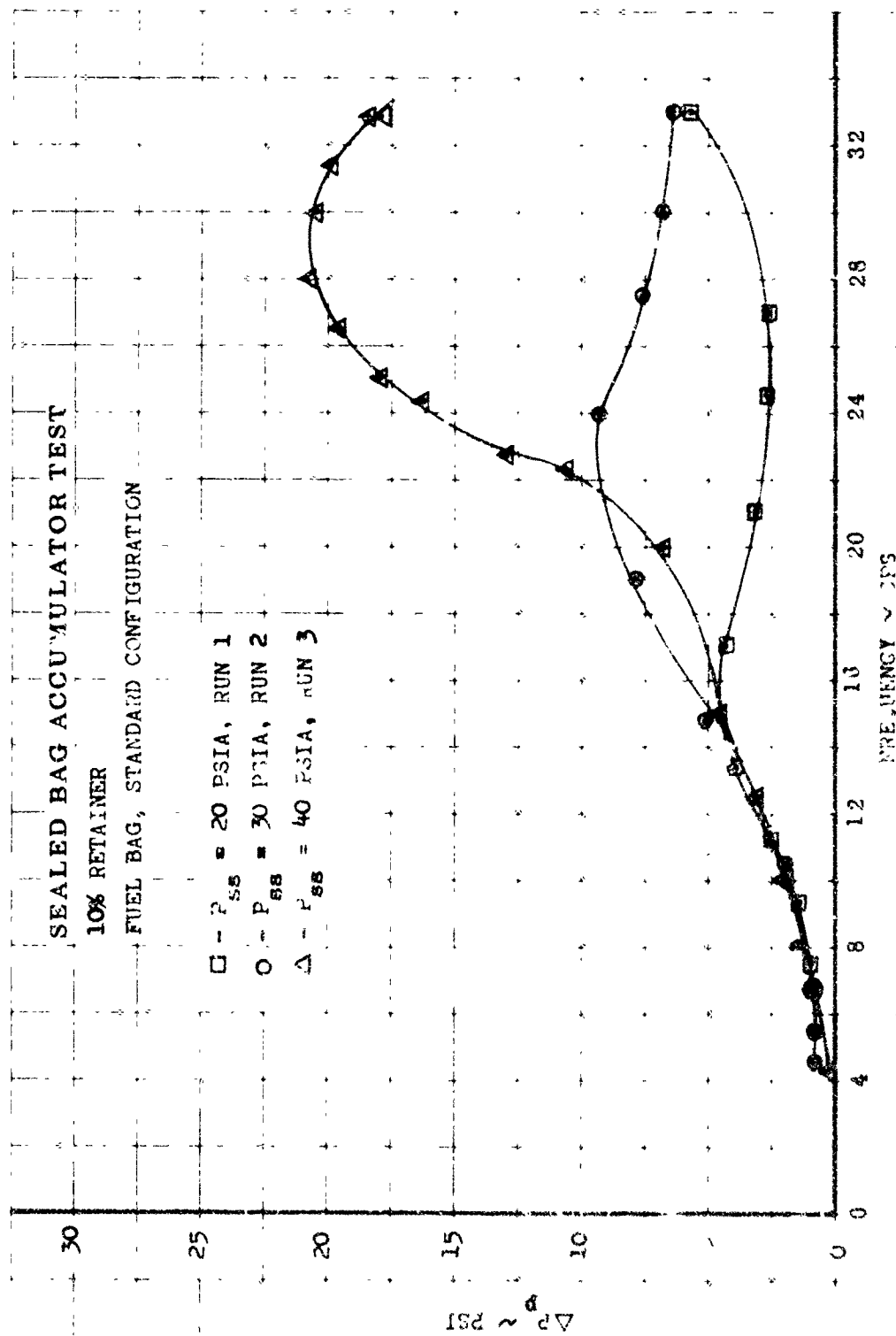Figure 96 Sealed Bag Accumulator Observed Response
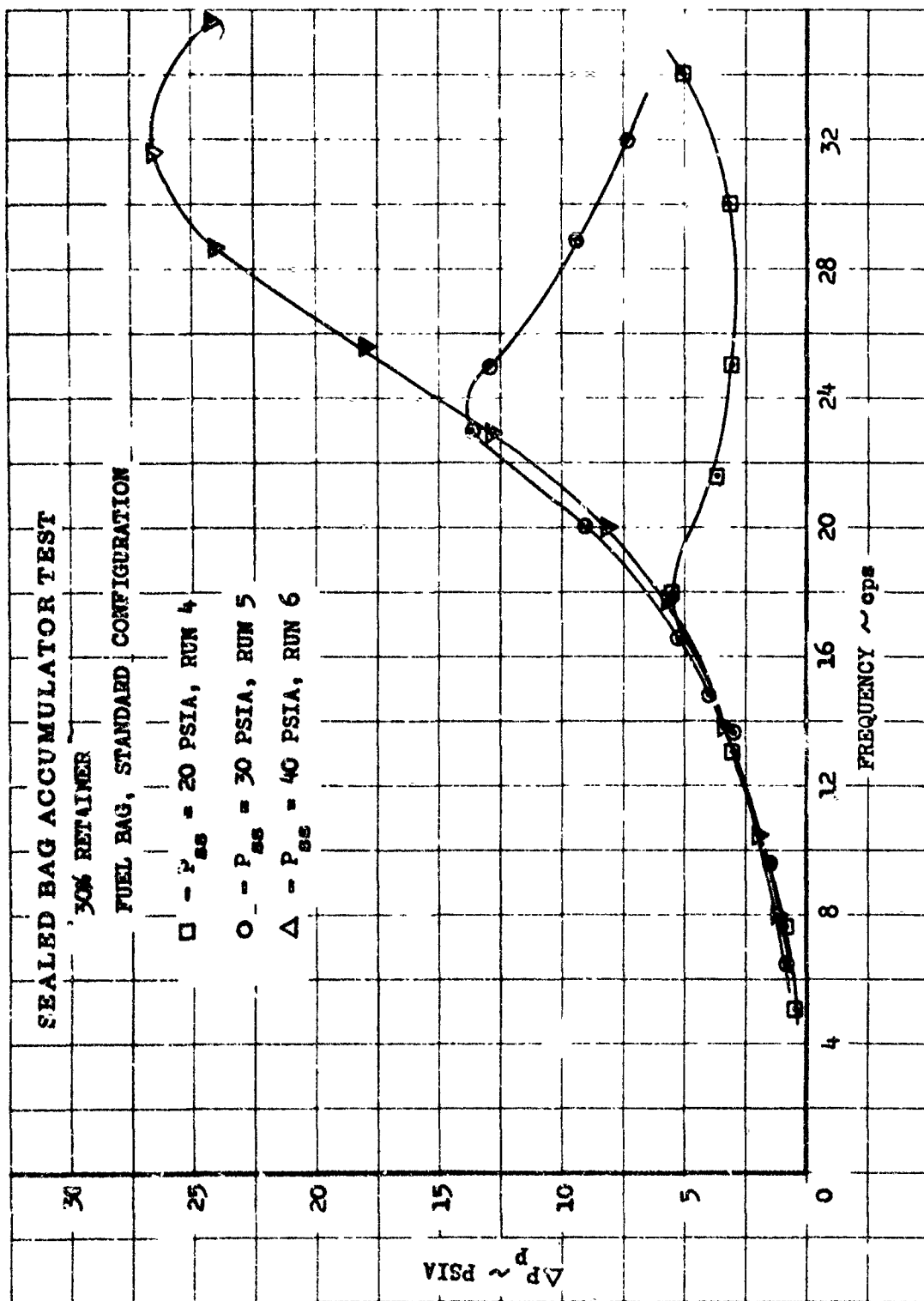
Figure 97 Sealed Bag Accumulator. Run 3

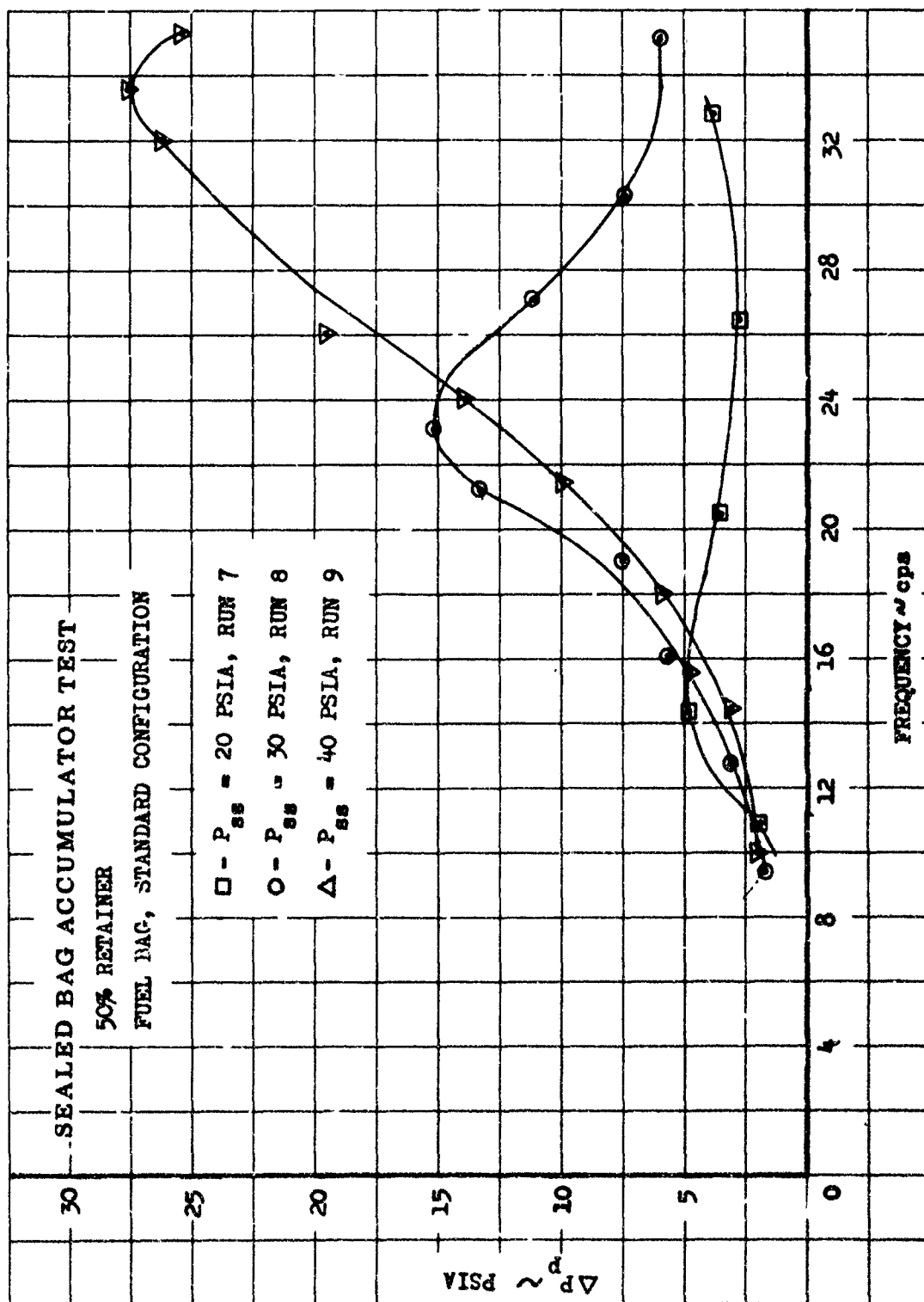Figure 98   Sealed Bag Accumulator, Runs 4, 5, 6
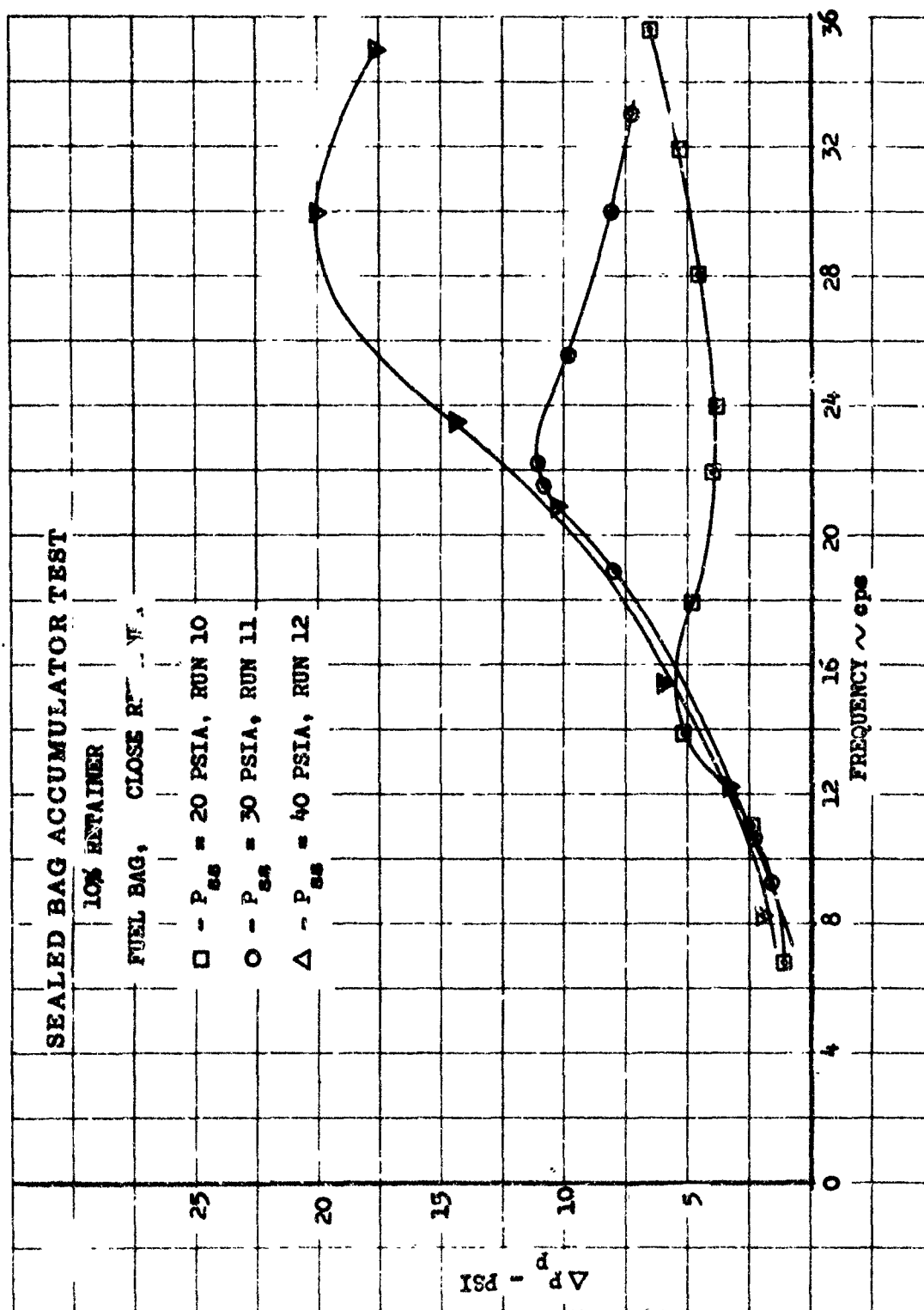
Figure 99   Sealed Bag Accumulator, Runs 7, 8, 9
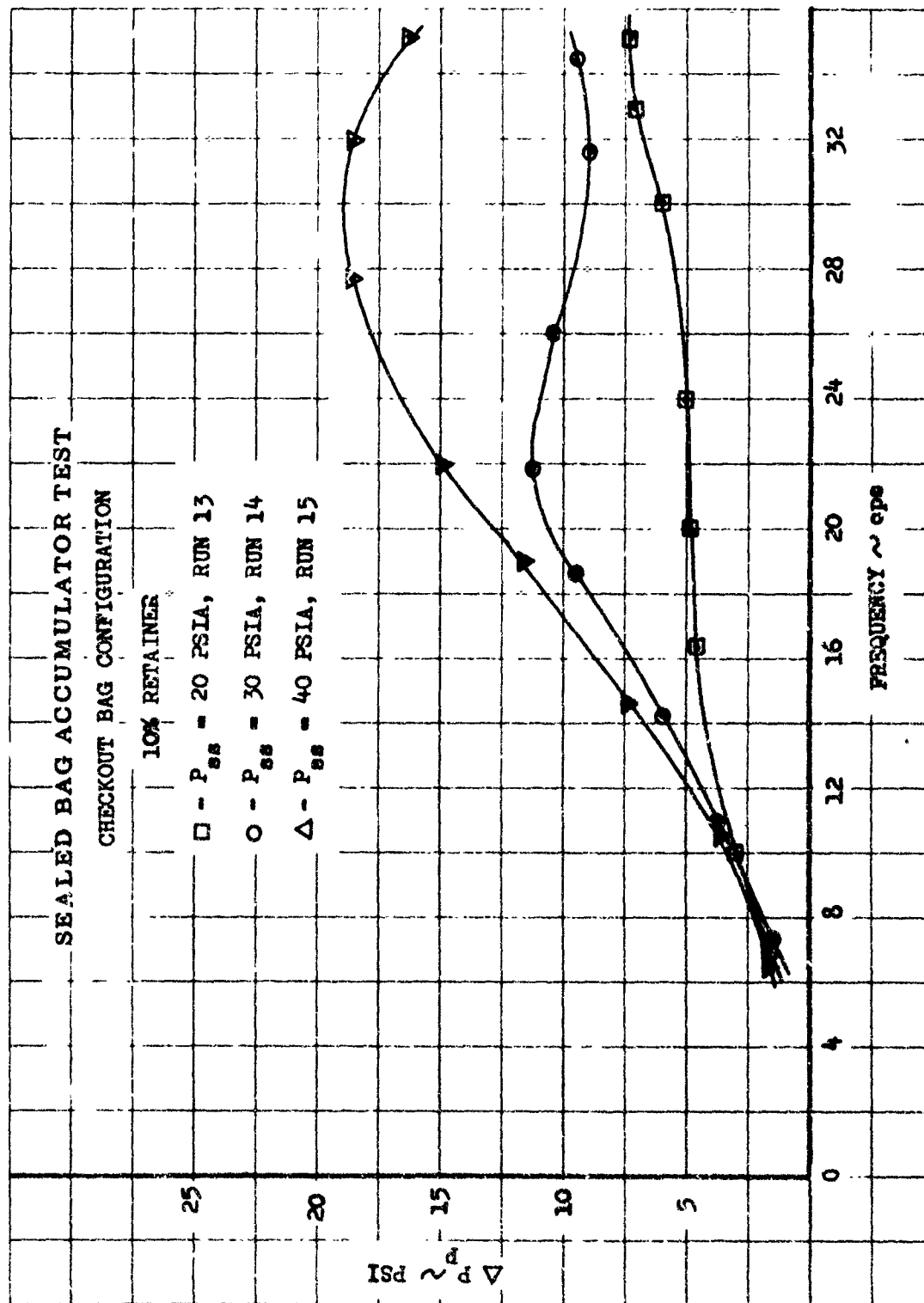
Figure 100 Sealed Bag Accumulator, Runs 10, 11, 12
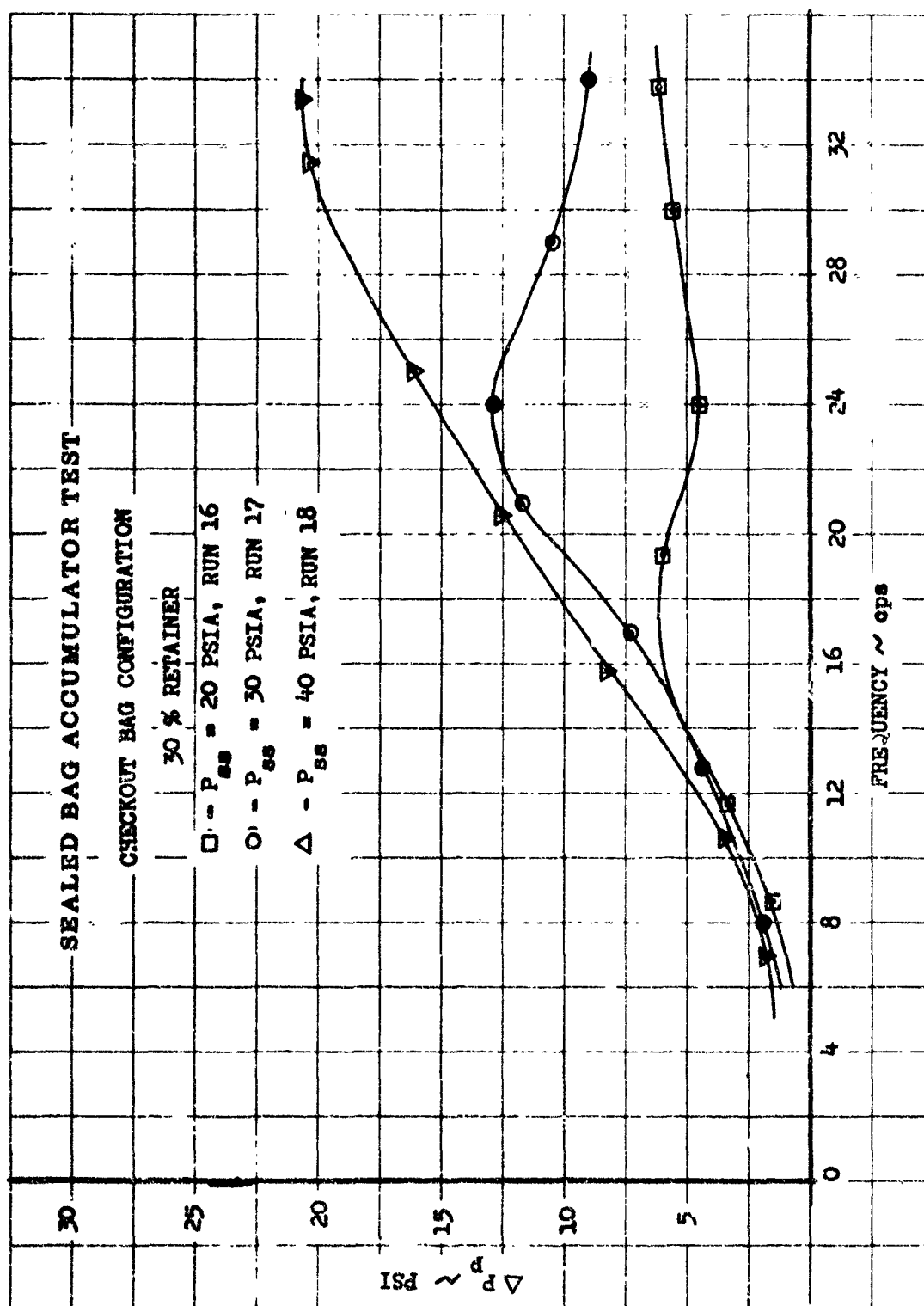
Figure 101 Sealed Bag Accumulator, Runs 13, 14, 15

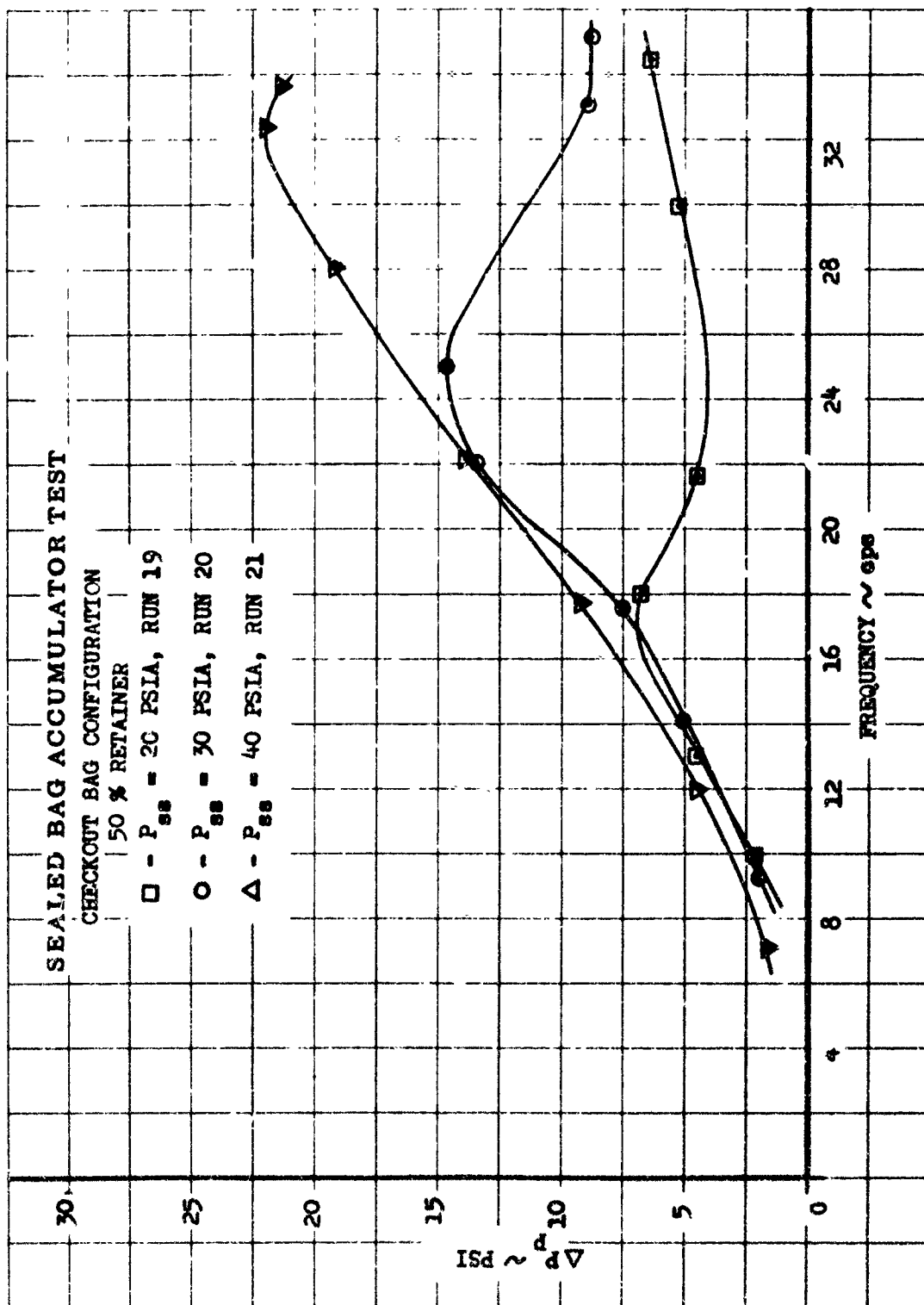Figure 102 Sealed Bag Accumulator, Runs 16, 17, 18

164

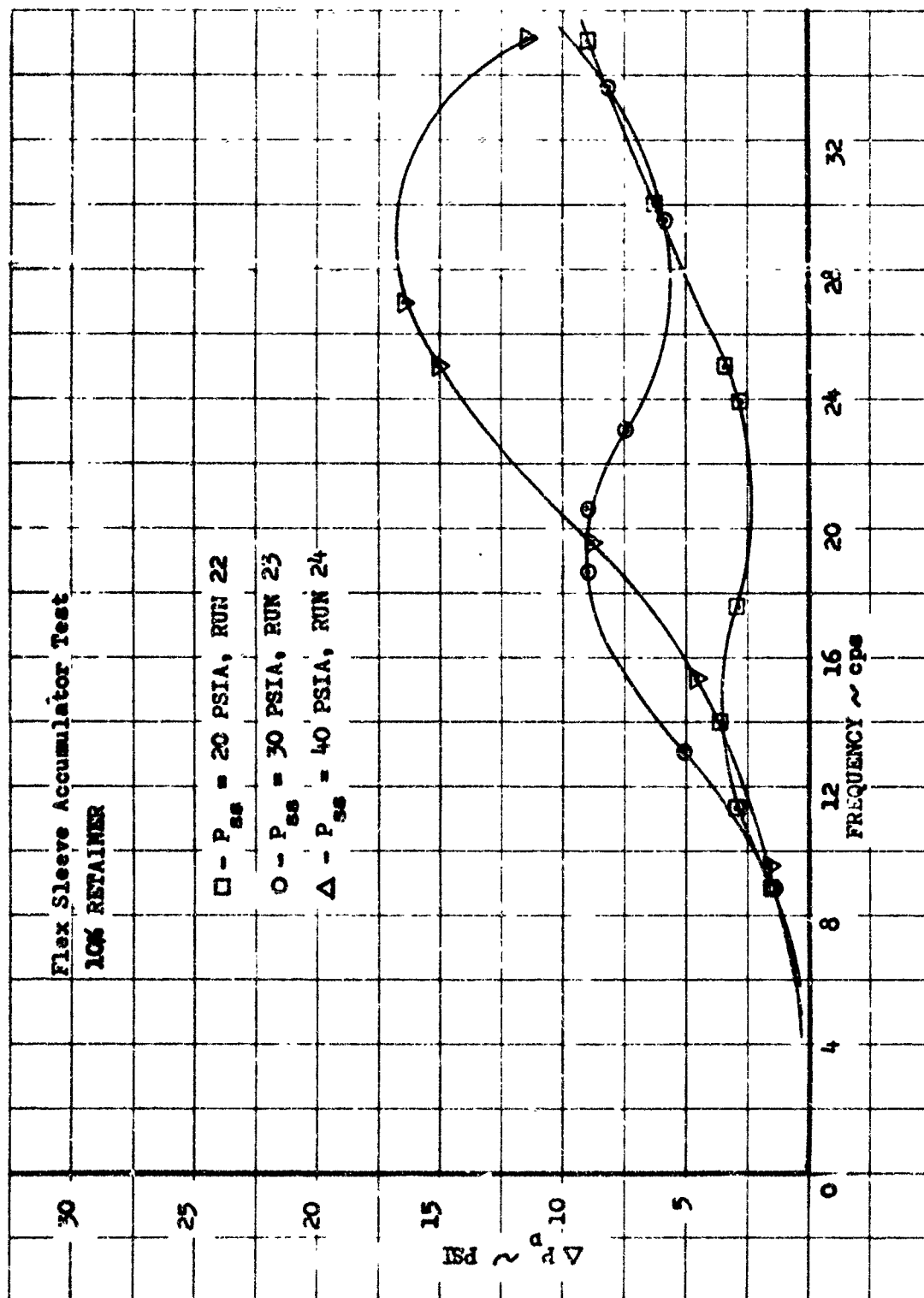Figure 103 Sealed Bag Accumulator, Runs 19, 20, 21

165

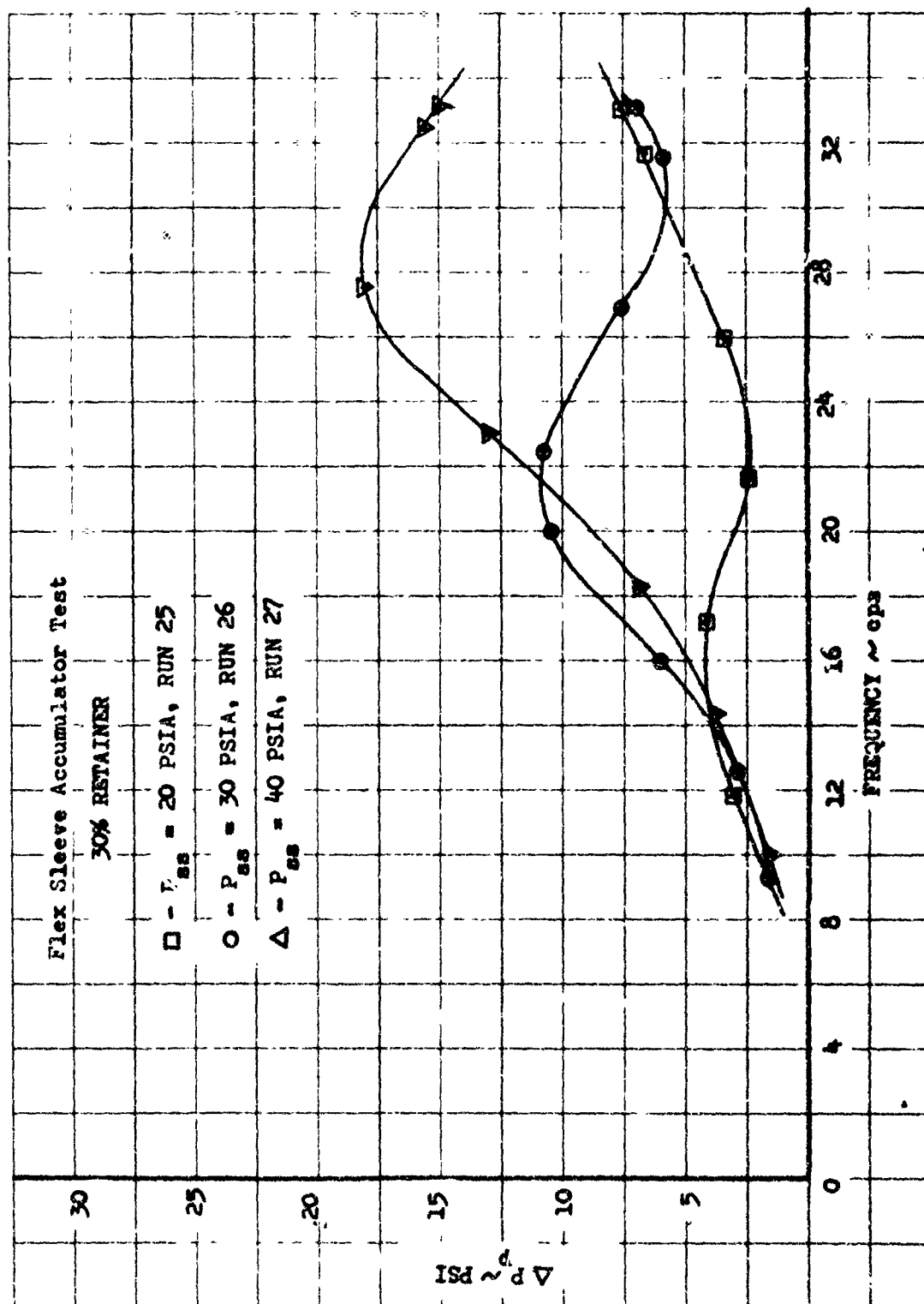Figure 104 Sealed Bag Accumulator, Runs 22, 23, 24

166

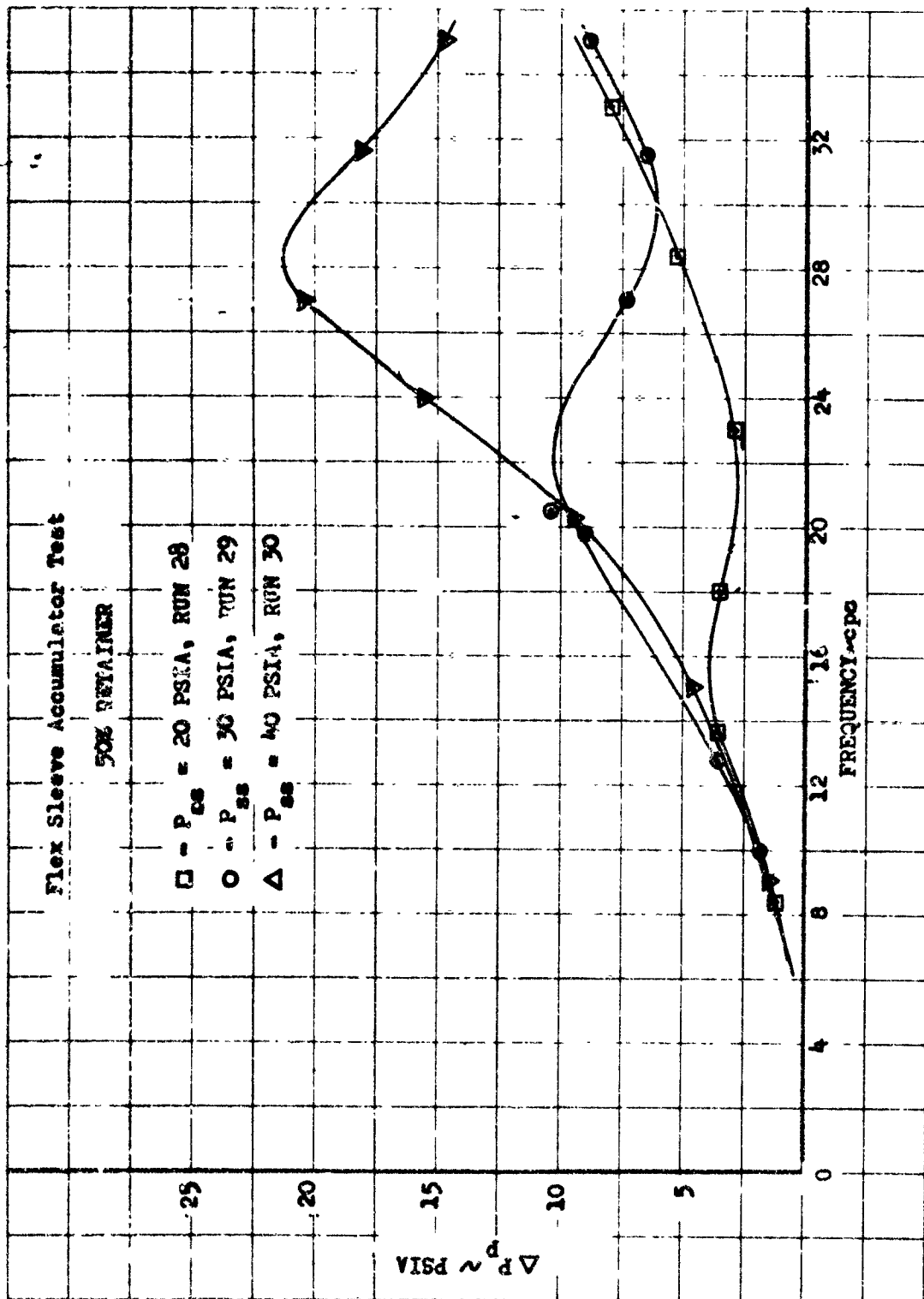Figure 105 Sealed Bag Accumulator, Runs 25, 26, 27

167

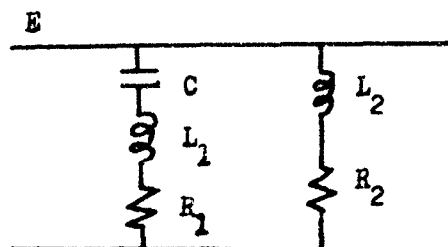Figure 106 Sealed Bag Accumulator, Runs 28, 29, 30

168

Figure 107 Sealed Bag Accumulator Circuit Analog

For this circuit the E/Q transfer function would be

$$\frac{E}{Q} = \cfrac{s}{\cfrac{1}{L_1 s + R_1 + \cfrac{1}{c_1 s}} + \cfrac{1}{L_2 s + R_2}} \qquad (64)$$

Equation (64) where E is analogeous to P_s and Q analogeous to V can be rewritten as

$$\frac{E}{Q} = \cfrac{L_1 L_2 s\ (s^2 + \frac{R_1}{L_1} s + \frac{1}{c_1 L_1})\ (s + \frac{R_2}{L_2})}{(L_1 + L_2)\ s^2 + (\frac{R_1 + R_2}{L_1 + L_2})\ s + \frac{1}{L_1 + L_2 c}} \qquad (65)$$

To evaluate the experimental parameters for this function either additional test data would be required or the value of certain parameters would have to be known. Unfortunately neither set of information was available from the analysis or experimental data. The test data therefore could be evaluated on a qualitative basis only. For this evaluation the maximum response frequency and amplitude were considered in terms of geometry system pressure, and retainer hole area.

c.   Effect of Retainer Hole Area. The first relationship examined was the effect of retainer hole area on the maximum response frequency. Figure 108 shows this effect for each of the accumulator designs with system pressure as a parameter. The data indicates that for certain geometry and pressure conditions a maximum exists in the maximum response frequency - retainer hole area relationship. Of the three basic designs the checkout bag configuration for hole area ratios greater than 30% appears to have the higher frequencies associated with it. The next relationship be examined was that between the amplitude of maximum response and hole area ratio. Figures 109 thru 111 show this effect; respectively, for the fuel bag standard configuration, checkout bag configuration and flex sleeve accumulator designs. Of the three sets of data only the fuel bag standard configuration consistently indicates a maximum in the maximum response amplitude. Furthermore, these maximums are the highest response obtained for the three designs.

d.   Effect of Pressure. The third experimental relationship examined was the influence of system pressure on maximum response frequency. Figure 112 thru 114 present plots of the experimental data demonstrating this effect. In each figure retainer hole area ratio is a parameter. A comparison of the three sets of curves show that an increase in system pressure produces an increase in maximum response frequency for all three designs throughout the range of hole area ratios tested. The final qualitative analysis performed on the data involved plotting the accumulator maximum response as a function of system pressure with retainer hole area ratio as a parameter. Figures 115 thru 117 show these results. The trends indicated by the data are that an increasing system pressure produces an increase in amplitude of the maximum response.

e.   Conclusions. The sealed bag accumulator tests produced results which could be evaluated on a qualitative basis in terms of pressure and geometry effects. The most significant test result was that the test data showed the math model of Section IX to be in error and the accumulator to be a more complicated system than was originally anticipated. In order to properly evaluate the sealed bag accumulator on a qualitative basis it will be necessary to revise the analytical model along the lines of Equation (65) and to significantly modify the methods of testing. Although the model of Figure 107 seems to best explain the experimental data a number of parameters in the model (L_a, R_a) could not be identified in this program. It is not certain whether the additional inertance and resistance

170

terms are associated with the accumulator; ar! if so where are they physically located, or with the system external to the accumulator. In order to properly understand the accumulator characteristics additional analysis and possibly experimenta- tion will be needed in the area of parameter identification.

SEALED BAG ACCUMULATOR TEST
VARIATION OF MAXIMUM RESPONSE
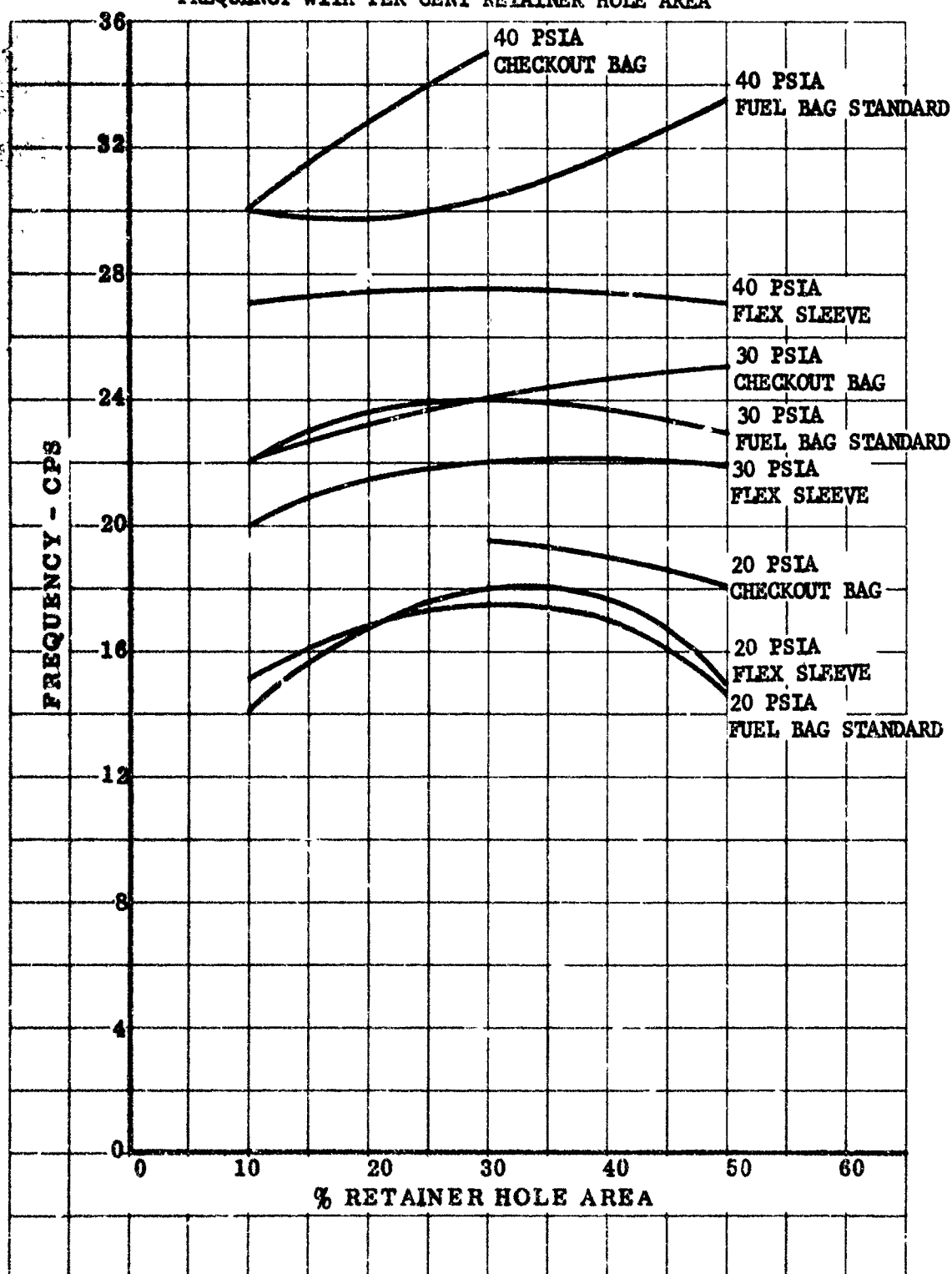FREQUENCY WITH PER CENT RETAINER HOLE AREA

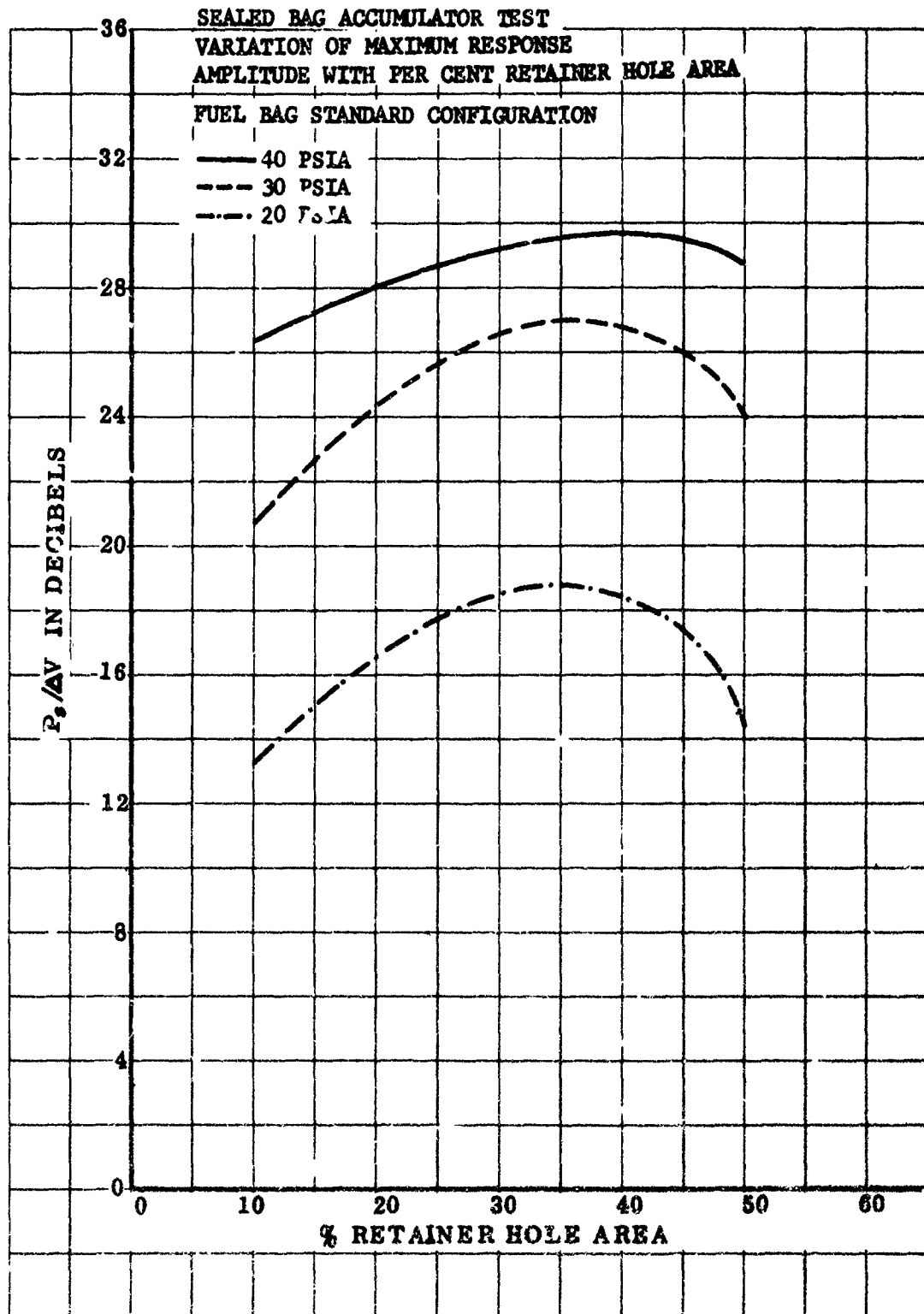Figure 108 Sealed Bag Accumulator, Maximum Frequency/Hole Area

Figure 109 Sealed Bag Accumulator, Pg/ΔV with Hole Area

SEALED BAG ACCUMULATOR TEST
VARIATION OF MAXIMUM RESPONSE
AMPLITUDE WITH PER CENT RETAINER HOLE
AREA

CHECKOUT BAG CONFIGURATION

———— 40 PSIA
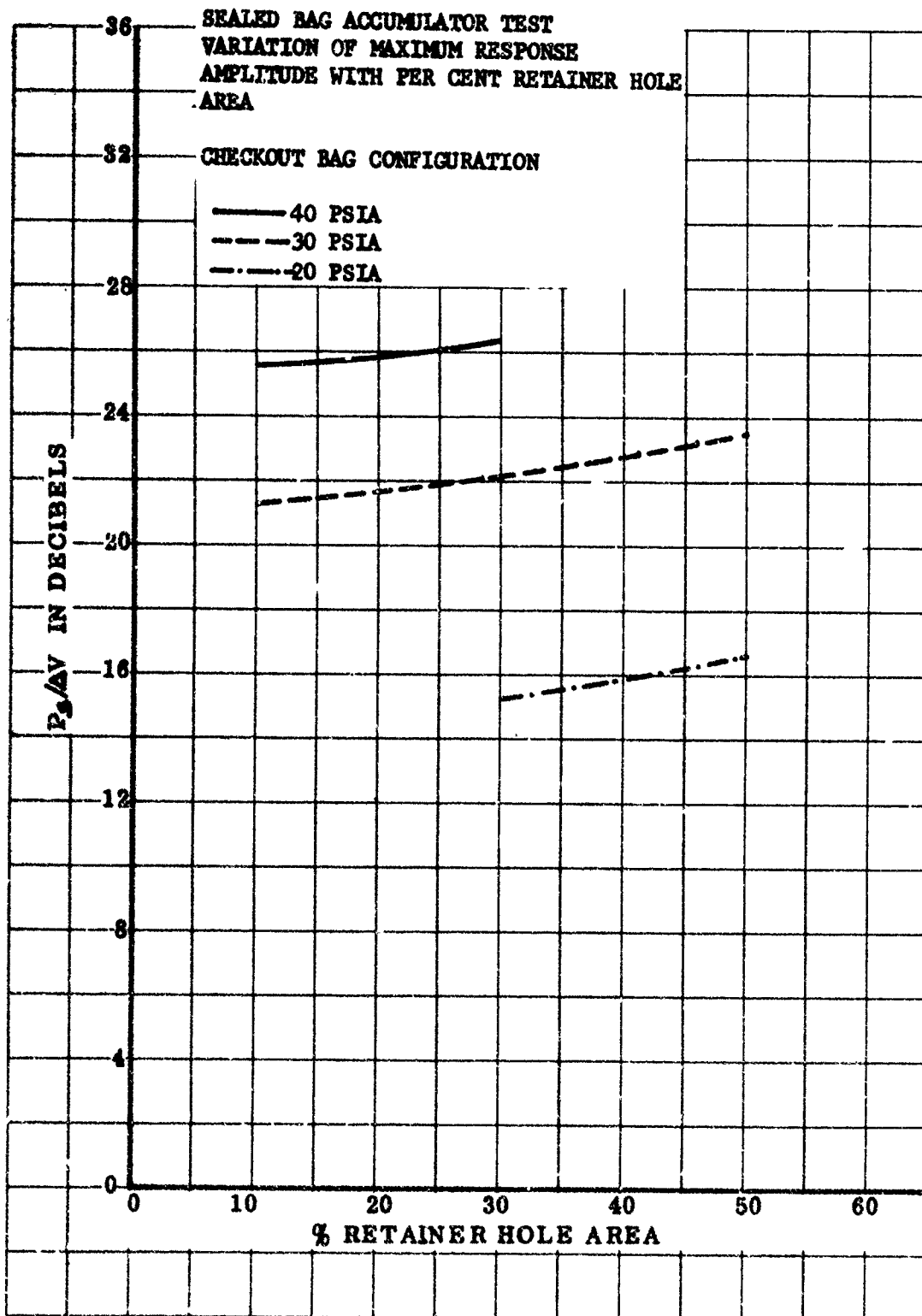— — — 30 PSIA
—·—·— 20 PSIA

Figure 110 Sealed Bag Accumulator, $P_S/\Delta V$ with Hole Area
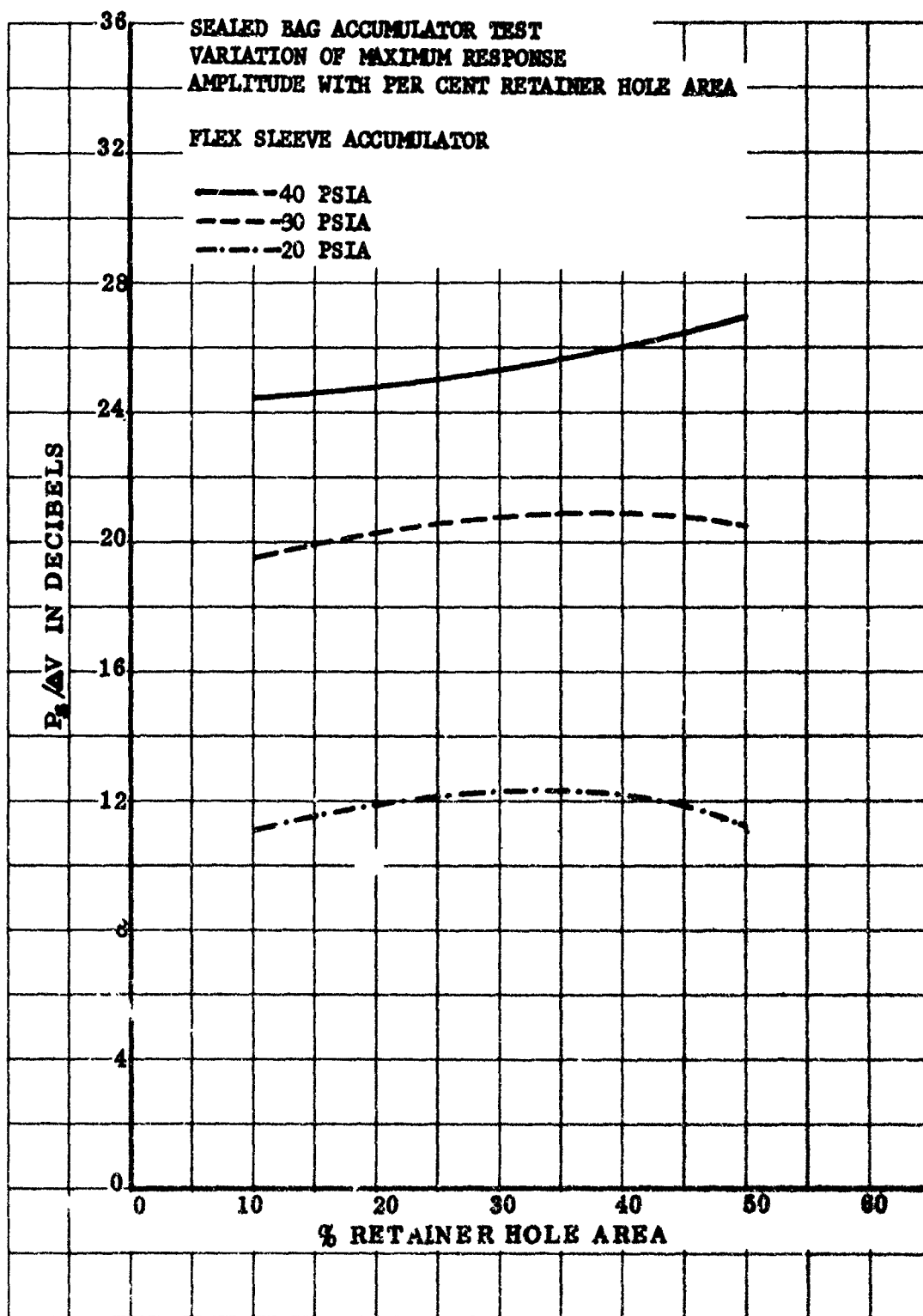
Figure 111 Sealed Bag Accumulator, $P_s/\Delta V$ with Hole Area

SEALED BAG ACCUMULATOR TEST
VARIATION OF MAXIMUM RESPONSE
FREQUENCY WITH BAG PRECHARGE PRESSURE

FUEL BAG STANDARD CONFIGURATION
————— 50% RETAINER HOLE AREA
— — — 30% RETAINER HOLE AREA
—·—··— 10% RETAINER HOLE AREA
—··—··—10% RETAINER HOLE AREA -
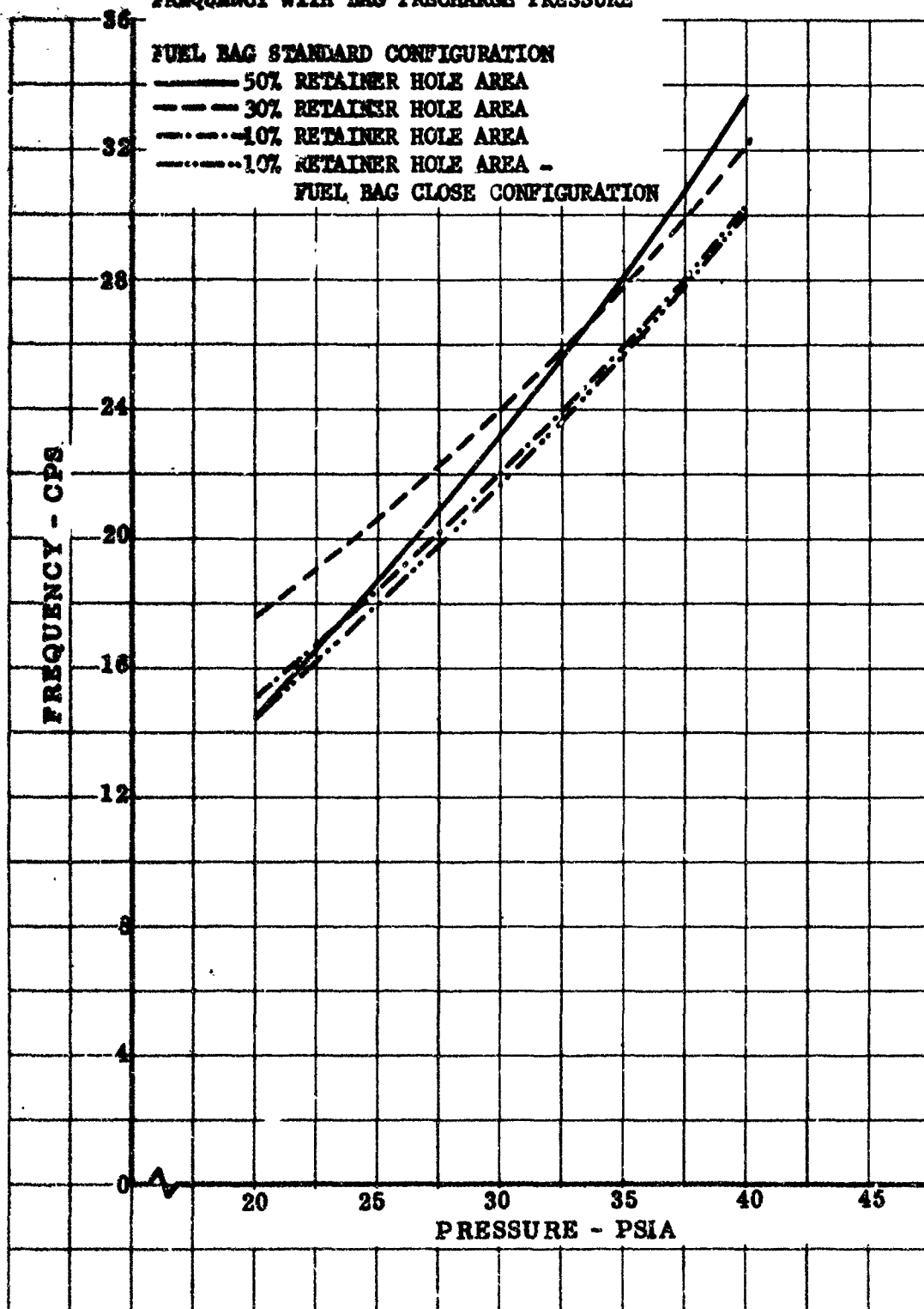   FUEL BAG CLOSE CONFIGURATION

Figure 112 Sealed Bag Accumulator, Maximum Frequency/Pressure

SEALED BAG ACCUMULATOR TEST
VARIATION OF MAXIMUM RESPONSE
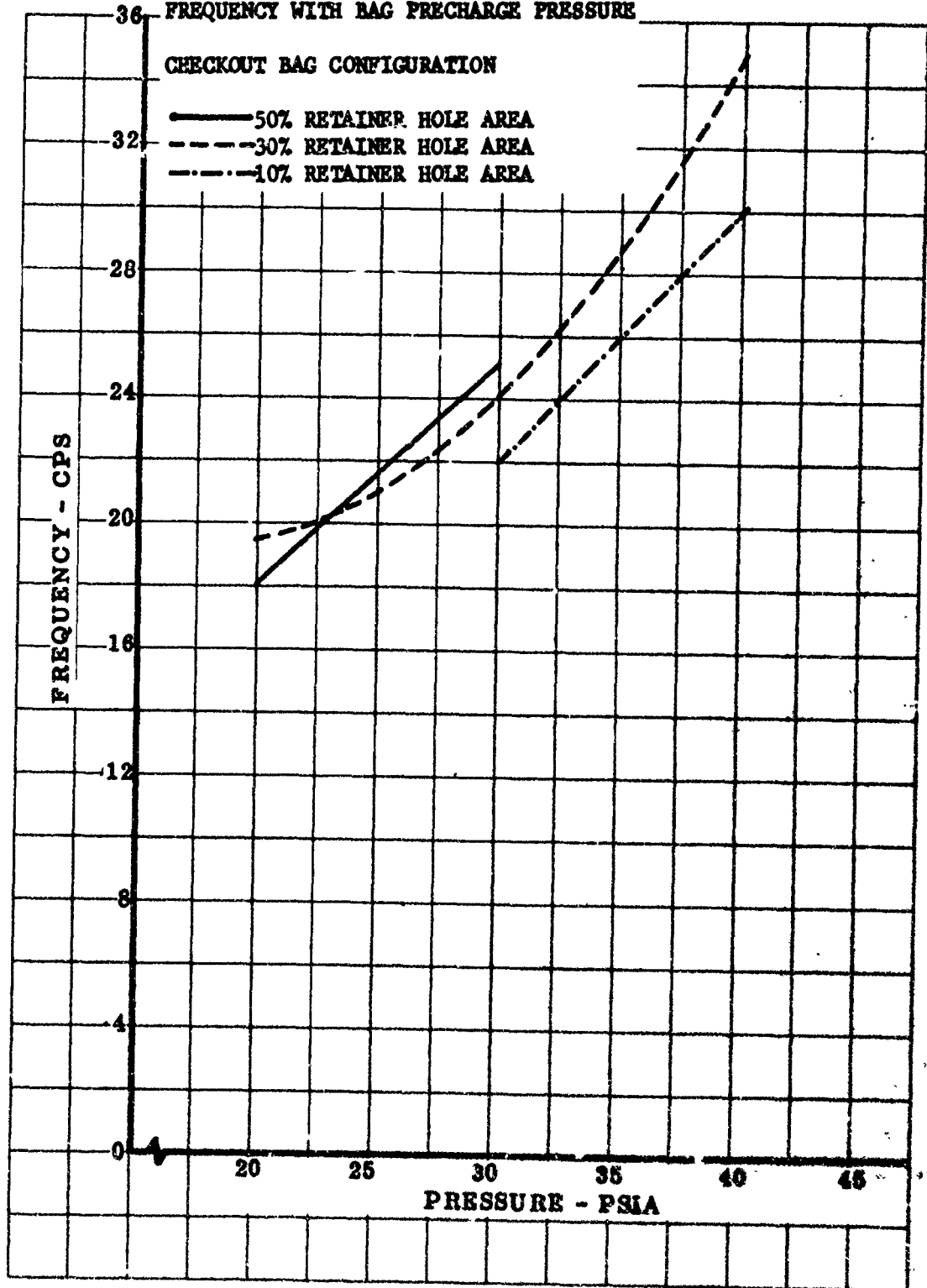FREQUENCY WITH BAG PRECHARGE PRESSURE

CHECKOUT BAG CONFIGURATION

—————50% RETAINER HOLE AREA
— — — —30% RETAINER HOLE AREA
—·—·—·10% RETAINER HOLE AREA

Figure 113 Sealed Bag Accumulator, Maximum Frequency/Pressure
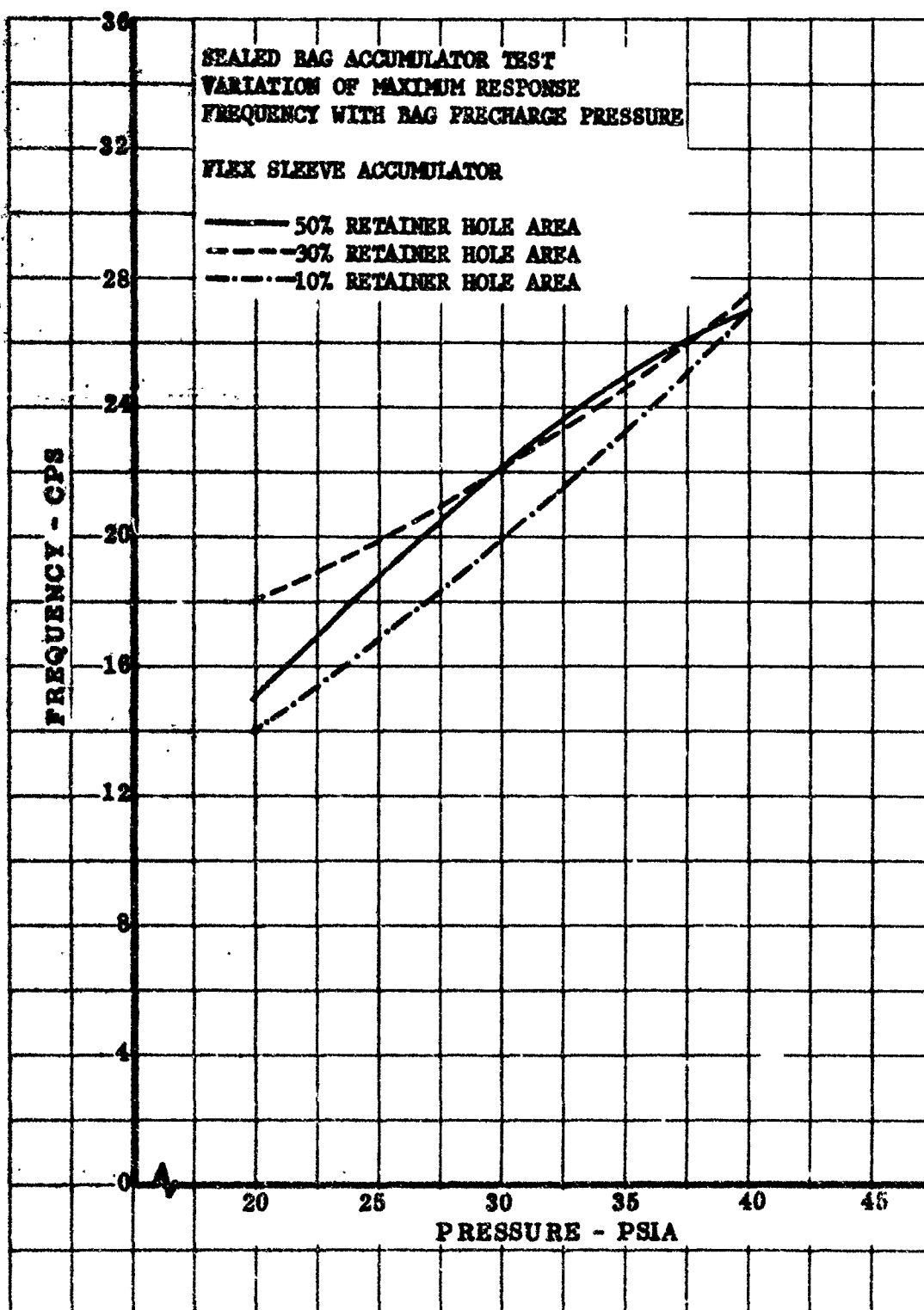
Figure 114 Sealed Bag Accumulator, Maximum Frequency/Pressure

178

SEALED BAG ACCUMULATOR TEST
VARIATION OF MAXIMUM RESPONSE
AMPLITUDE WITH BAG PRECHARGE PRESSURE

FUEL BAG STANDARD CONFIGURATION
———————50% RETAINER HOLE AREA
— — — —30% RETAINER HOLE AREA
—··—··—10% RETAINER HOLE AREA
—···—··· 10% RETAINER HOLE AREA -
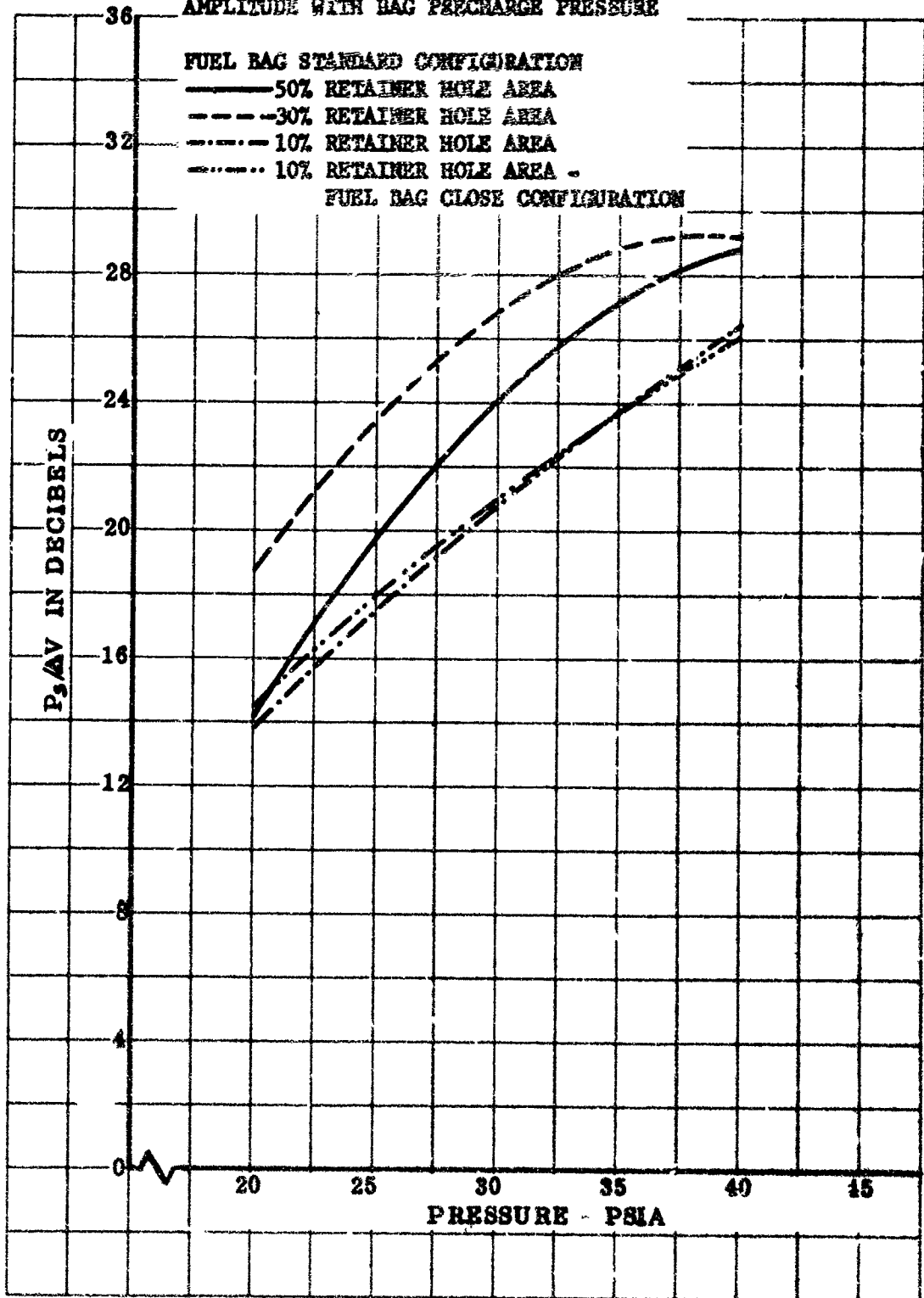FUEL BAG CLOSE CONFIGURATION

Figure 115 Sealed Bag Accumulator, $P_s/\Delta V$ with Pressure
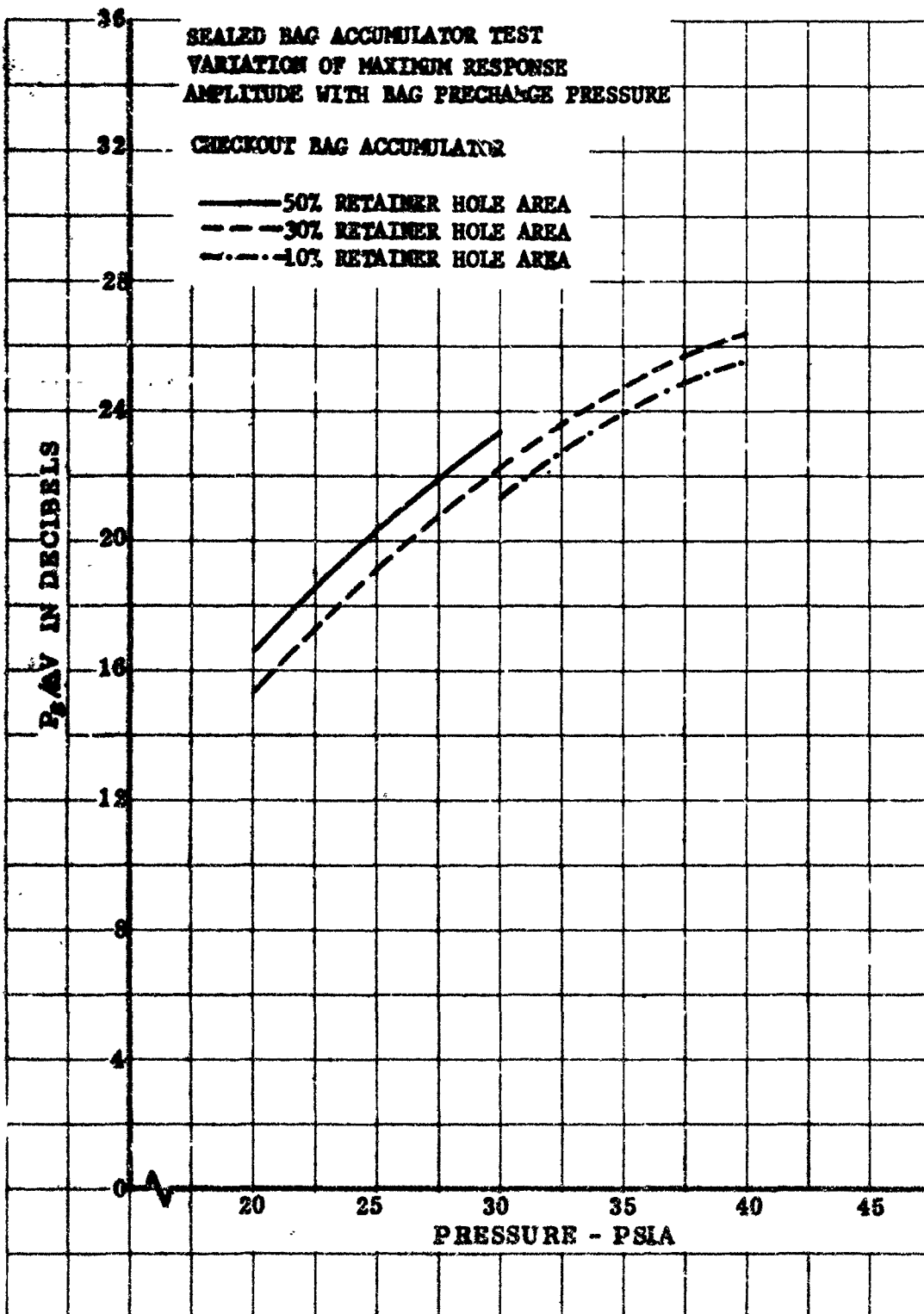
179

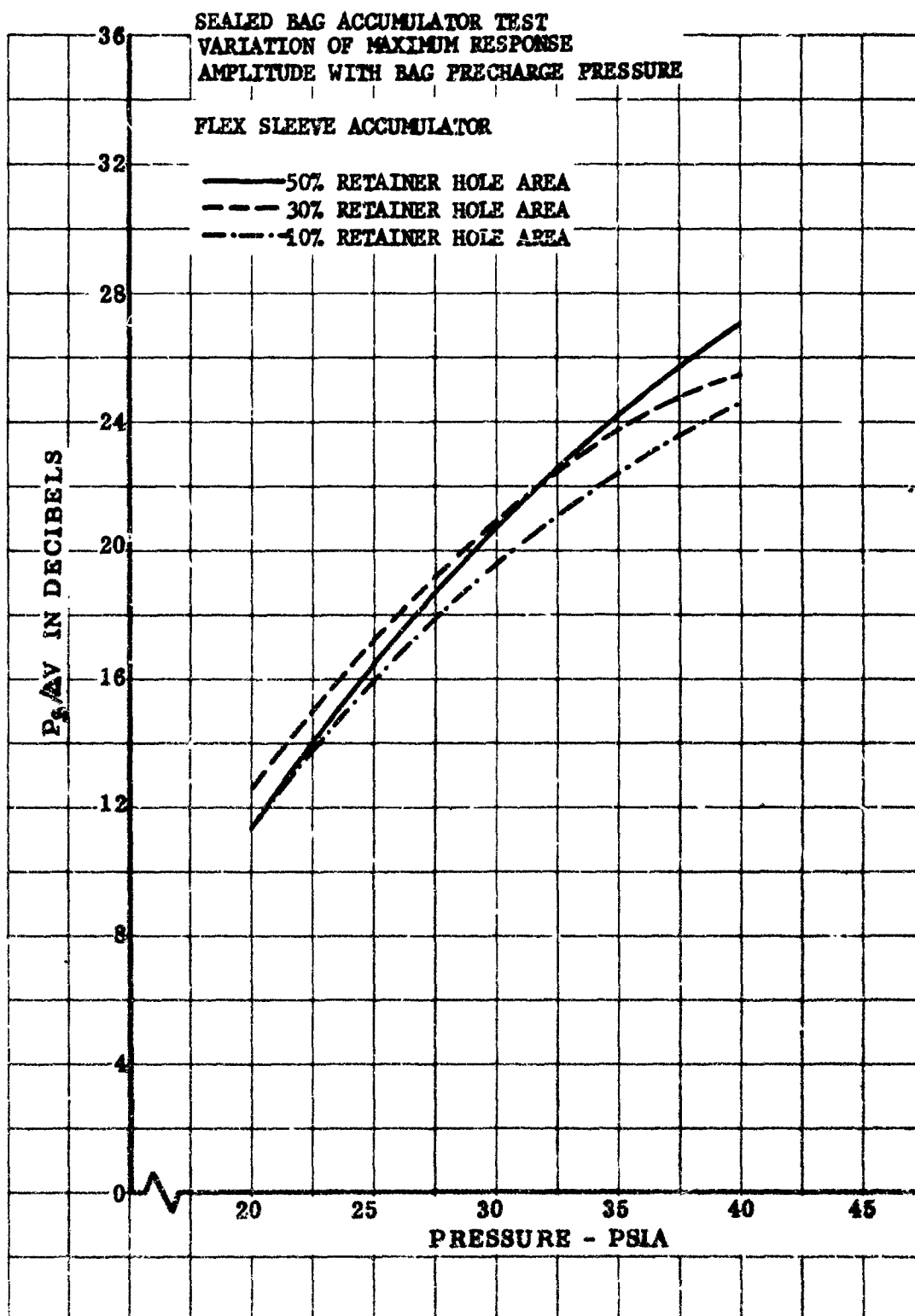Figure 116 Sealed Bag Accumulator, $P_g/\Delta V$ with Pressure

Figure 117 Sealed Bag Accumulator, $P_s/\Delta V$ with Pressure

SECTION XI

CAVITATING VENTURI ANALYSIS

1.   INTRODUCTION

During the development of POGO compensation devices for
the Titan II vehicles a cavitating venturi was considered as
a possible means of shifting suction line frequencies. The
vapor phase associated with the venturi would produce addition-
al compliance in the system and thereby lower the suction sys-
tem natural frequency. Upon examining the pressure losses
inherent in the concept, it was found that at incipient cavi-
tation the maximum pressure recovery attainable was on the
order of 85 percent. To accomplish the required frequency
shifts, the venturi would have to operate in the range of well
developed cavitation with associated pressure losses of 25 per-
cent or more. These losses were incompatible with pump per-
formance and tank pressure limitations; hence, the design was
abandoned. As a phase of the POGO amplitude limiting and control
program an alternate to the pure cavitating venturi was exam-
ined for POGO compensation. The modified concept also utilizes
a cavitating venturi; however, a low loss tube bypasses the
major portion of the suction flow. Figure 118 illustrates the
basic features of the design. Considering that most of the
suction flow goes through the low loss bypass tube, the overall
pressure recovery should be improved over that of the pure
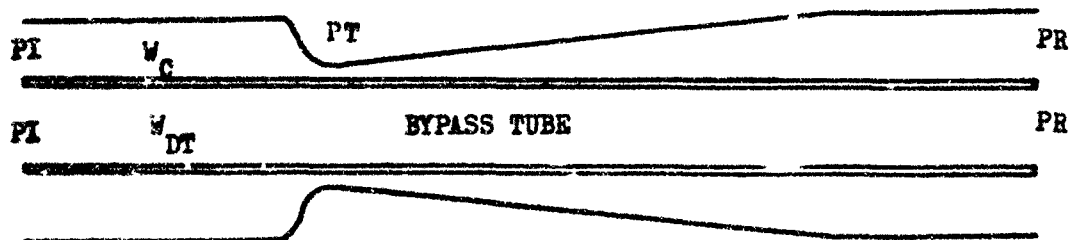cavitating venturi.

Figure 118 Cavitating Venturi

a. Analysis. To determine the degree of improvement, an analysis was conducted in which several designs were examined for various inlet conditions and cavitation to bypass flow ratios. The basic design was oriented toward flow parameters associated with the cold-flow test fixture. If analysis demonstrated the bypass venturi to be feasible, the results could be verified experimentally without additional design analysis.

The analysis was conducted for incipient cavitation conditions with the intent of extending the investigation to fully developed cavitation if, with the maximum idealized pressure recovery, the feasibility of the concept could be demonstrated.

Referring to Figure 118, the flowrate through the cavitating section W_c is related to the inlet pressure PI and throat pressure PT by

$$W_c = AT.CD \sqrt{2g_c \bullet (PI - PT)/ \left[1 - (AT/AI)^2 \right]} \qquad (66)$$

where   AT is the throat area
AI is the inlet area
$\bullet$ is the liquid density
CD is the flow coefficient for the venturi

At incipient cavitation PT is equal to the vapor pressure (PV) of the fluid.

The recovered pressure (PR), again for incipient cavitation, is given by (Reference 17)

$$PR = PV + \eta (PI - PV) \qquad (67)$$

where $\eta = .85$

With the boundary condition of incipient cavitation, the pressure drop and thereby the flowrate through the bypass section is established. A curve of $R_e\sqrt{f}$ vs R_e was first plotted for the bypass tube (Reference Figure 119). R_e is the Reynolds number and f the friction factor for the tube. The quantity $R_e\sqrt{f}$ is then calculated by

$$R_e\sqrt{f} = \frac{D \bullet}{\mu} \sqrt{\frac{(PI - PR)D}{2L_e}} \qquad (68)$$

183

where   D is the tube diameter
         L_e is the tube length
         μ is the fluid viscosity

With $R_e \sqrt{f}$ defined, the Reynolds number and flowrate can be established from Figure 119. The streams exiting the cavitating section and bypass section are at the same pressure but have different velocities. Upon mixing an additional pressure recovery will be realized. The overall pressure recovery is evaluated by considering the momentum of the two streams at the tube exit and at a station downstream after complete mixing has taken place (Reference 18, Page 221).

In addition to the pressure losses in the tube and Venturi sections, the inlet pressure must be corrected for approach losses. These losses are basically those associated with the contraction of the fluid stream (Reference 18, Page 217).

b. Results. The results of the analysis are presented in Figures 120 through 126. Figure 120 shows the variation of cavitating section throat area as a function of inlet pressure and cavitating flow rate for all diameters of bypass tubes. Figures 121, 122, and 123 display the variation of bypass flowrate as a function of inlet pressure and cavitating flowrate for bypass tube diameters of 0.5 in., 0.625 in. and 0.75 in., respectively. The pressure recovery ratio is given in Figures 124, 125, and 126.

c. Conclusions. The feasibility of the bypass venturi as a POGO compensation device is established by Figures 124 125, and 126. Since the maximum attainable recovery pressure ratio is no more than 90 percent, which is at the limit of acceptable losses, fully developed cavitation will easily increase the pressure losses to unacceptable levels. Although the analysis just described applies to a subscale system compared to the flight system, the Reynolds number and cavitation to bypass flow ratios would be comparable. The systems therefore will also be similar in terms of recovery pressure ratios. Hence, from the analysis results, it was concluded that the bypass cavitating venturi would not be a practical POGO compensation device. Considering the range of flight inlet pressures over which such a fix would have to operate, the performance would be compromised even further.

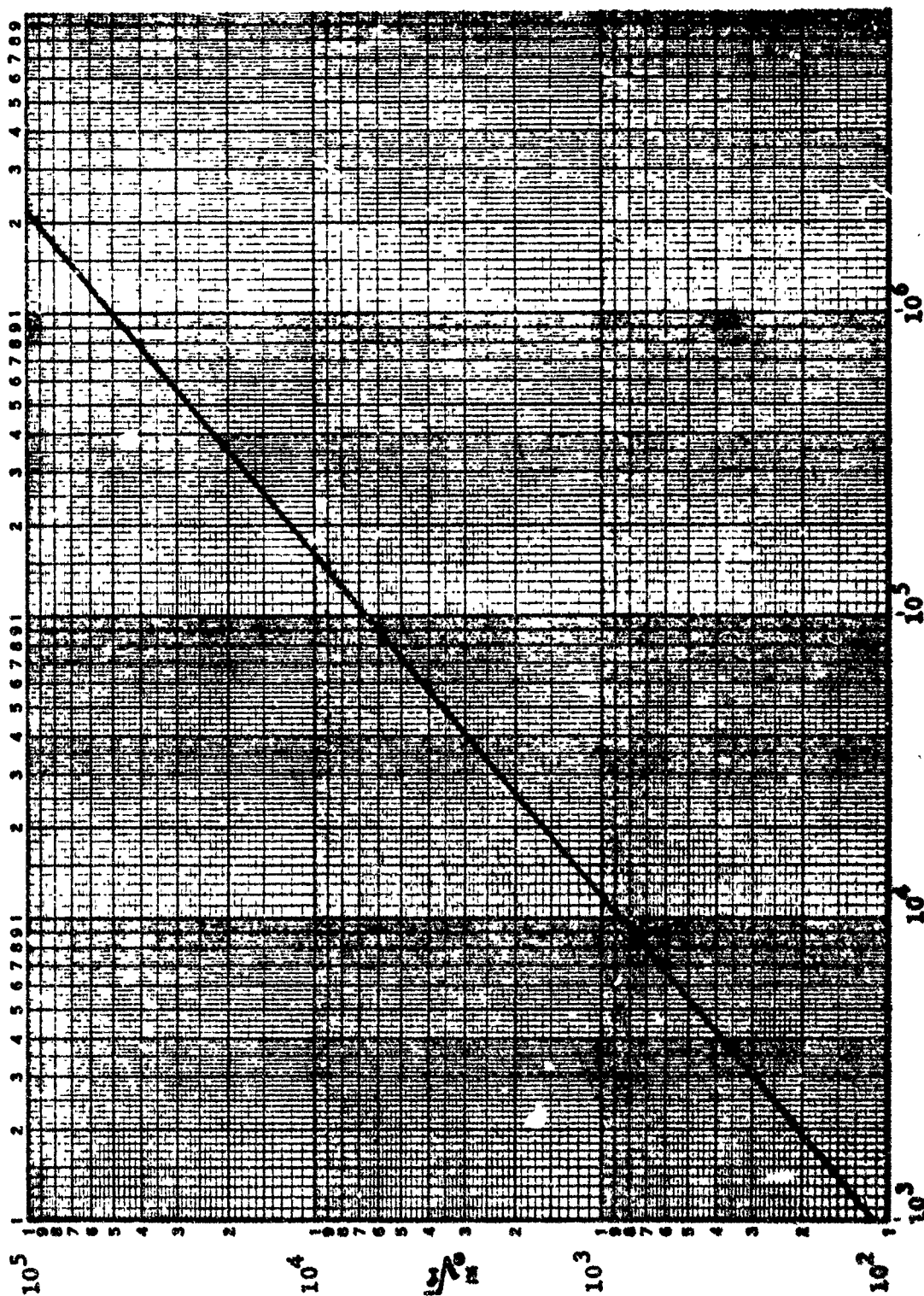BY-PASS TUBE LOSS CHARACTERISTICS

Figure 149 Reynolds Number/Friction Factor
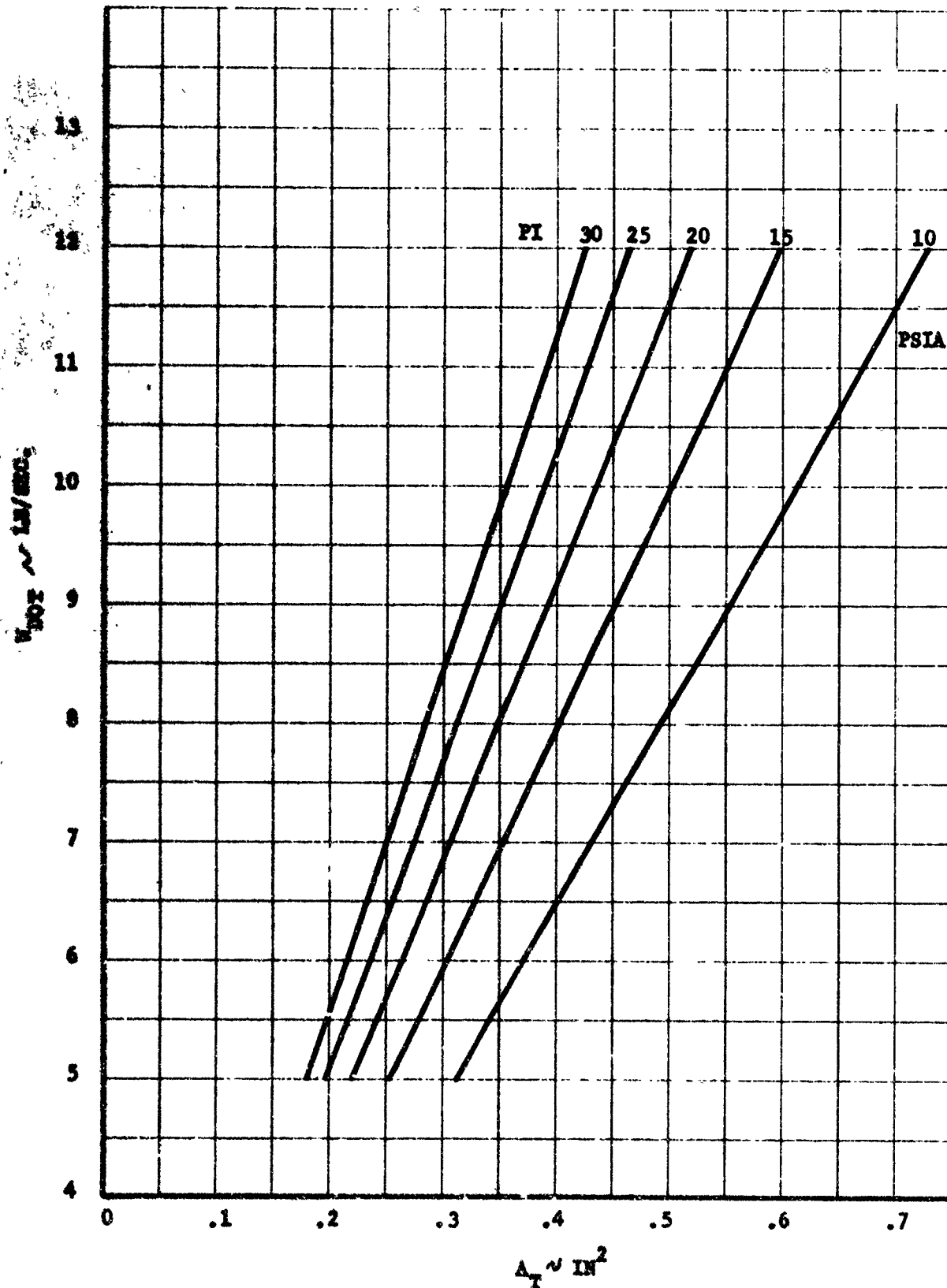
By-Pass Cavitating Venturi

Figure 120 By-Pass Cavitating Venturi, Flow Rate/Area Ratio
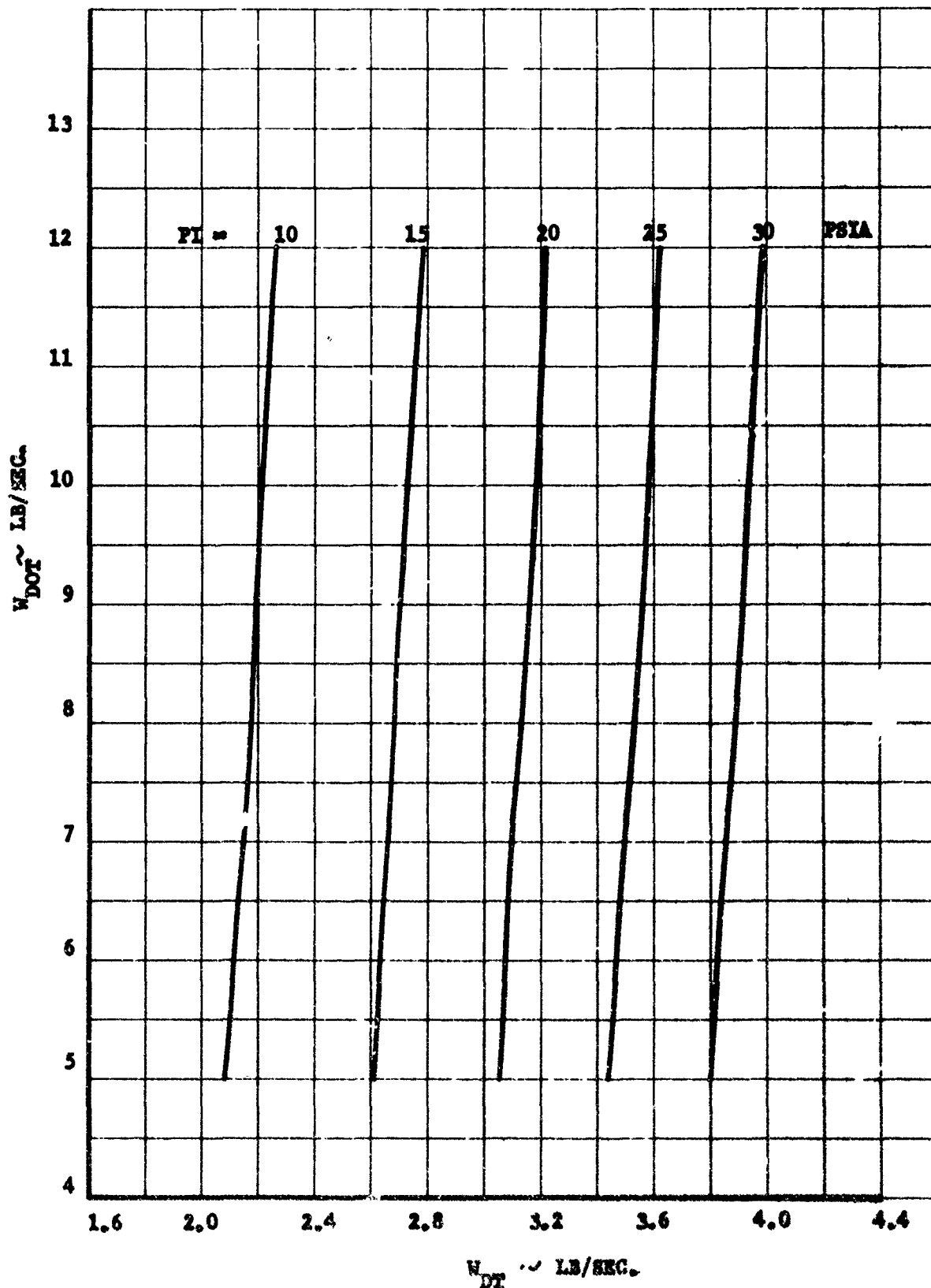
By-Pass Cavitating Venturi

DI = .5   IN

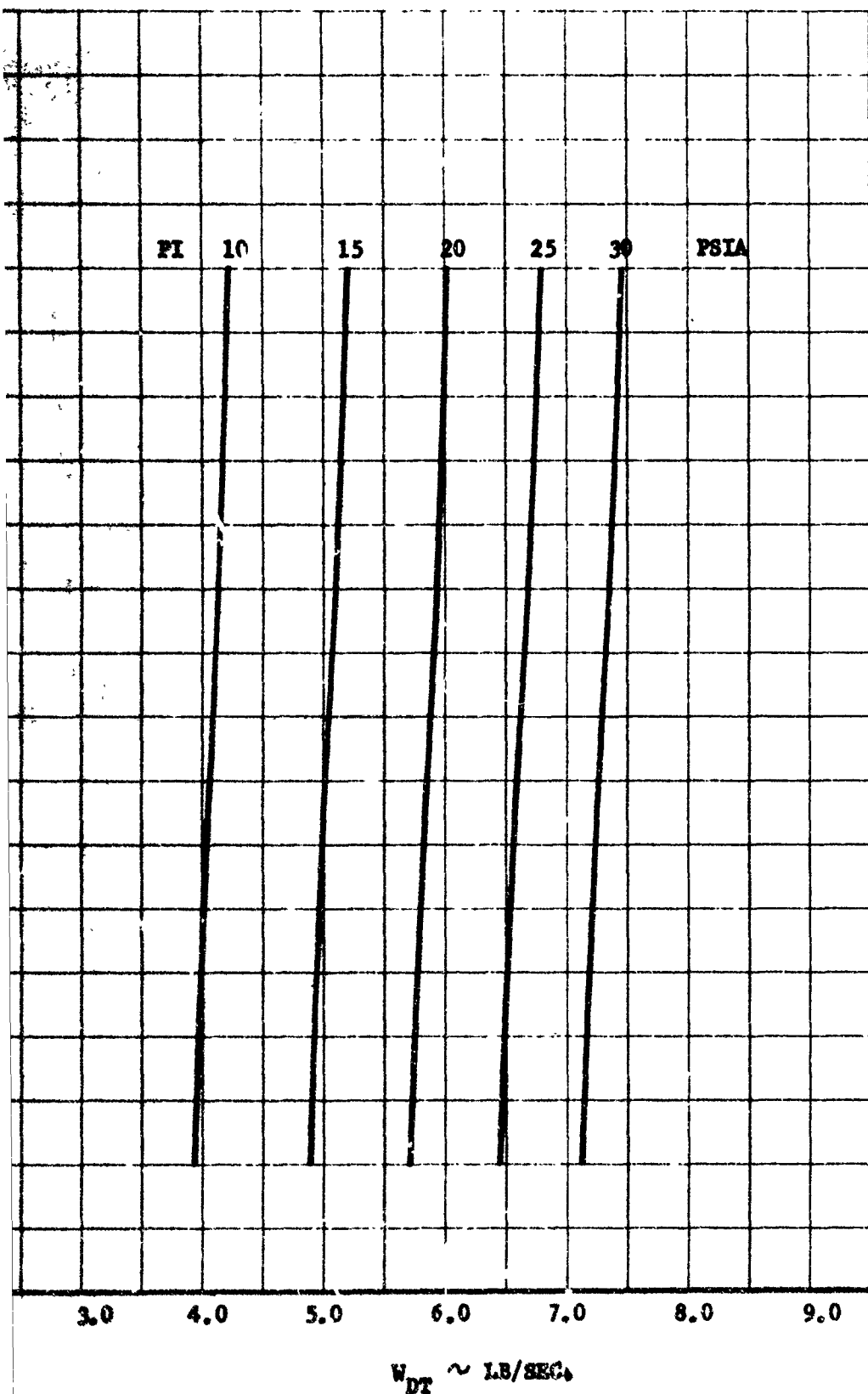Figure 121 By-Pass Cavitating Ventui, By-Pass Flow/Total Flow

By-Pass Cavitating Venturi

DI = .625   IN

Figure 122 By-Pass Cavitating Venturi, By-Pass Flow/Total Flow

188

By-Pass Cavitating Venturi

DI = .75 IN

Figure 123 By-Pass Cavitating Venturi, By-Pass Flow/Total Flow

Bypass Cavitating Venturi

DT = 0.50 in.

Figure 124 By-Pass Cavitating Venturi, Pressure Ratio/Total Flow
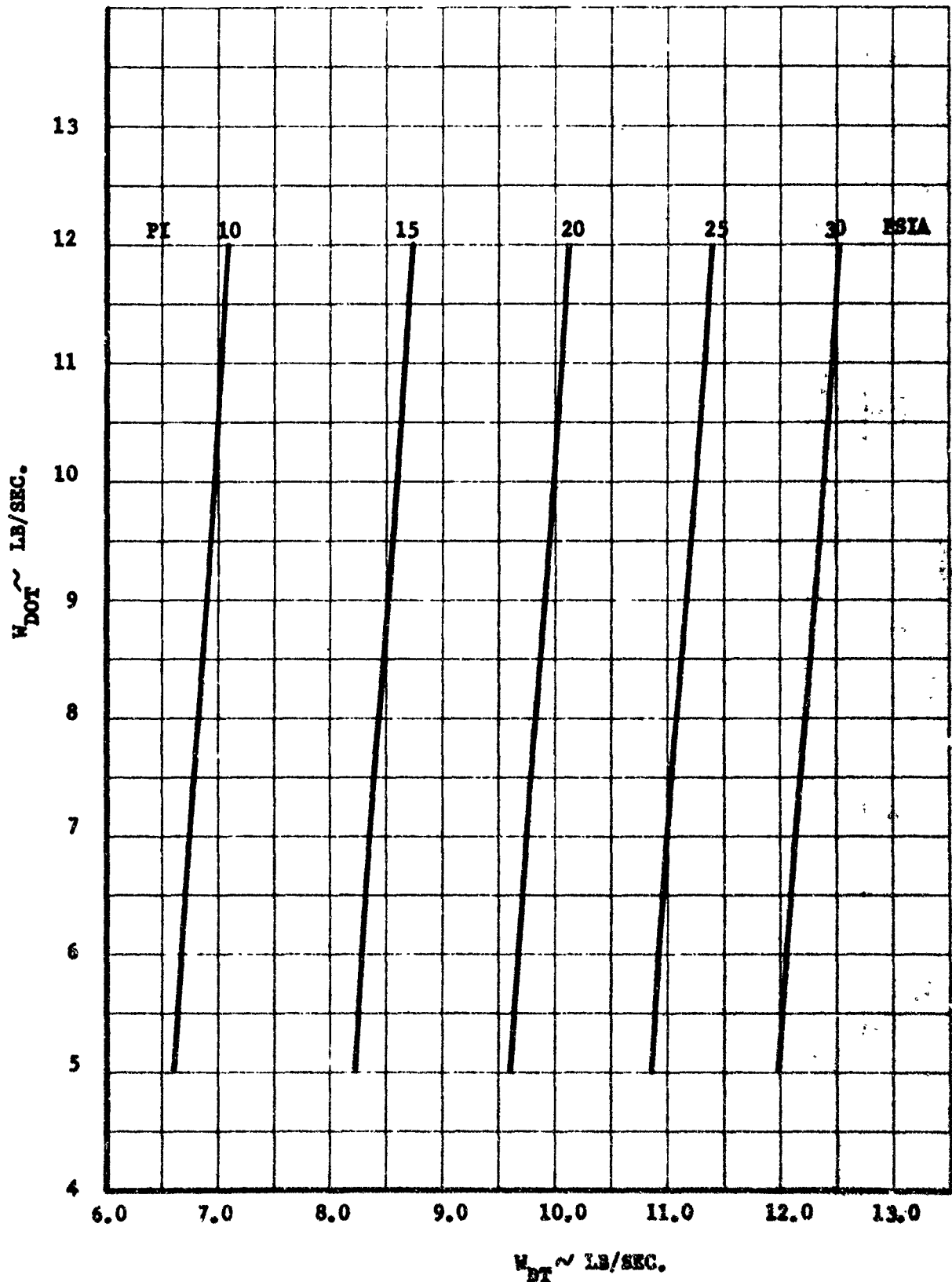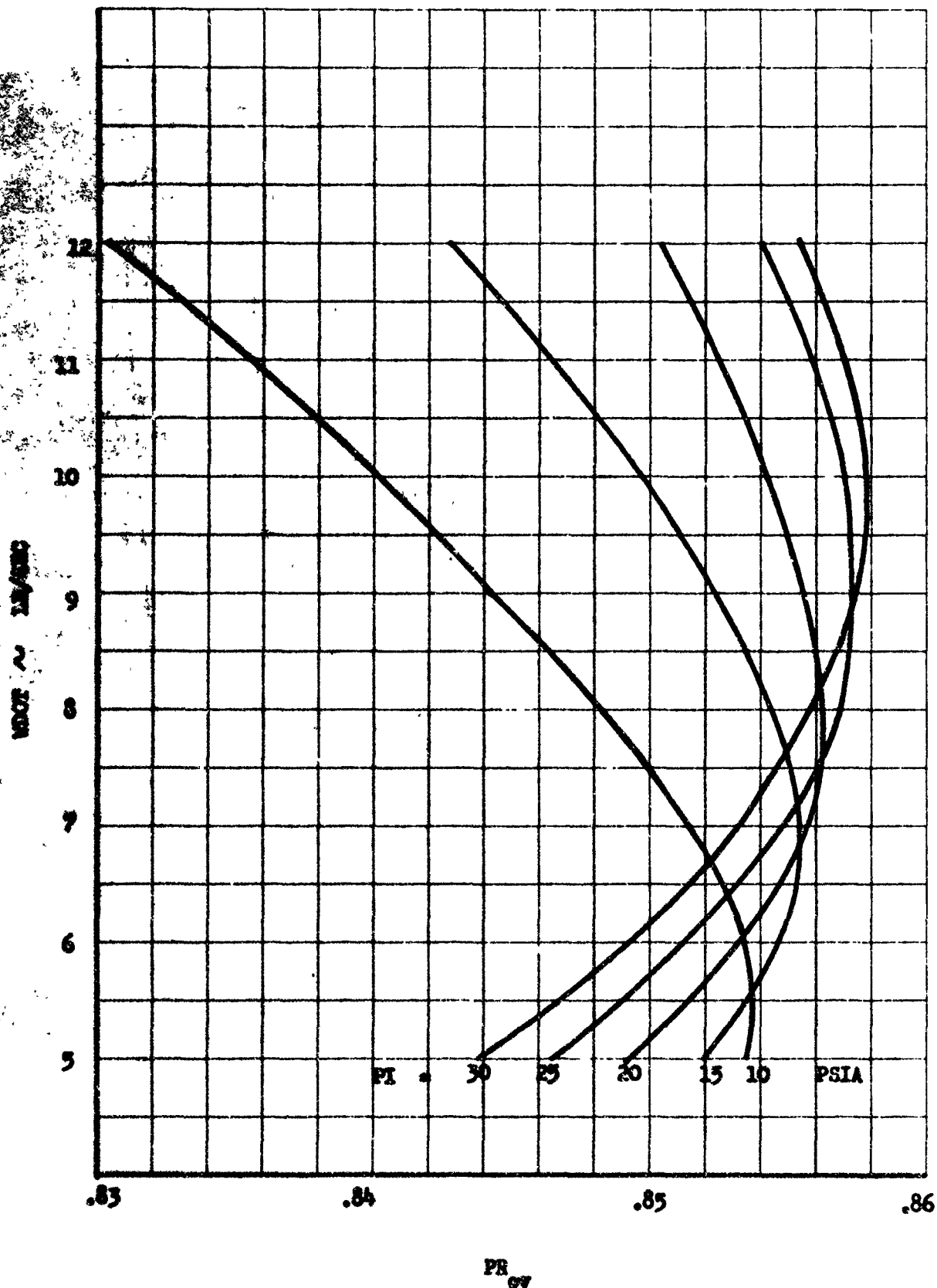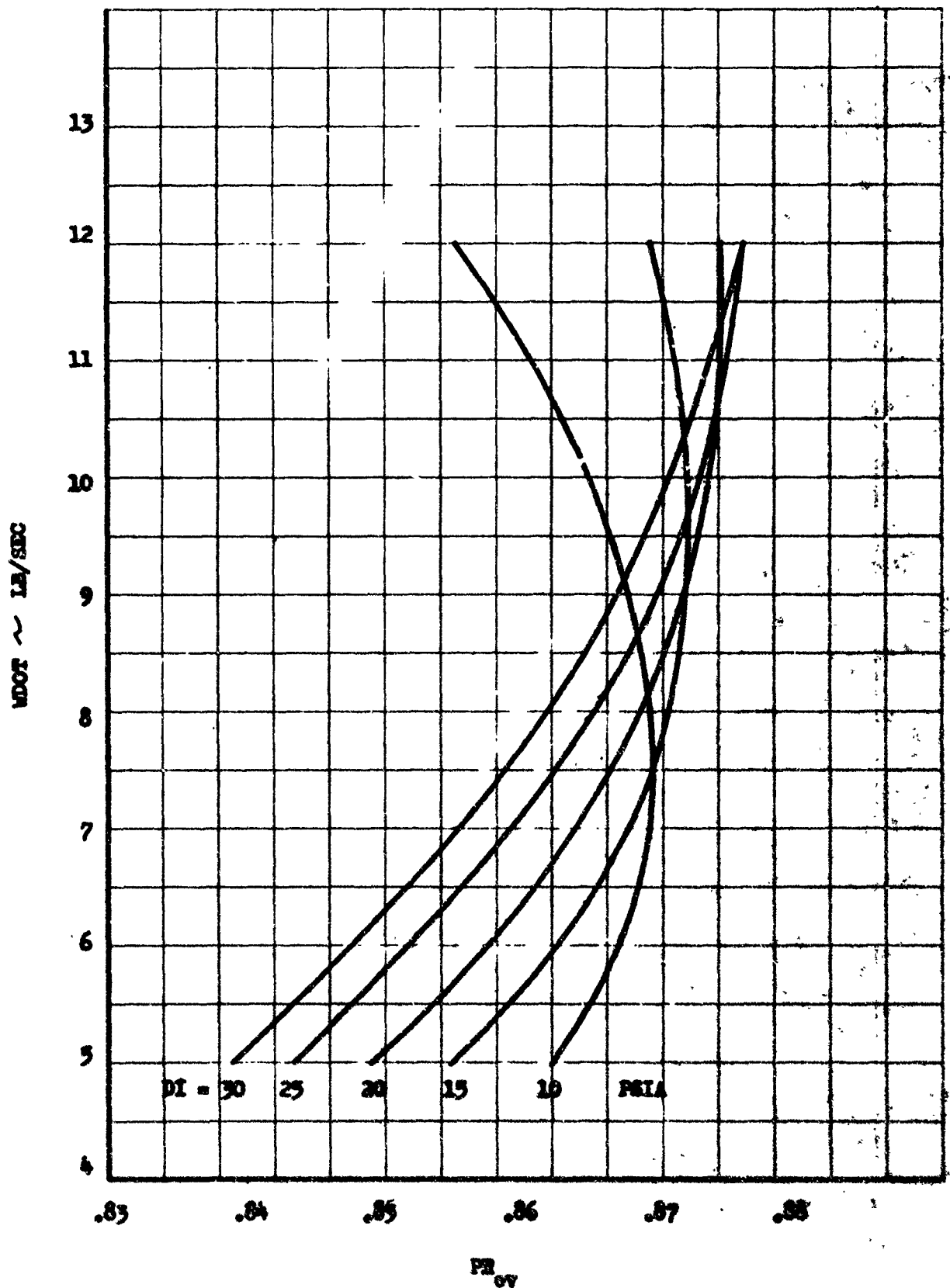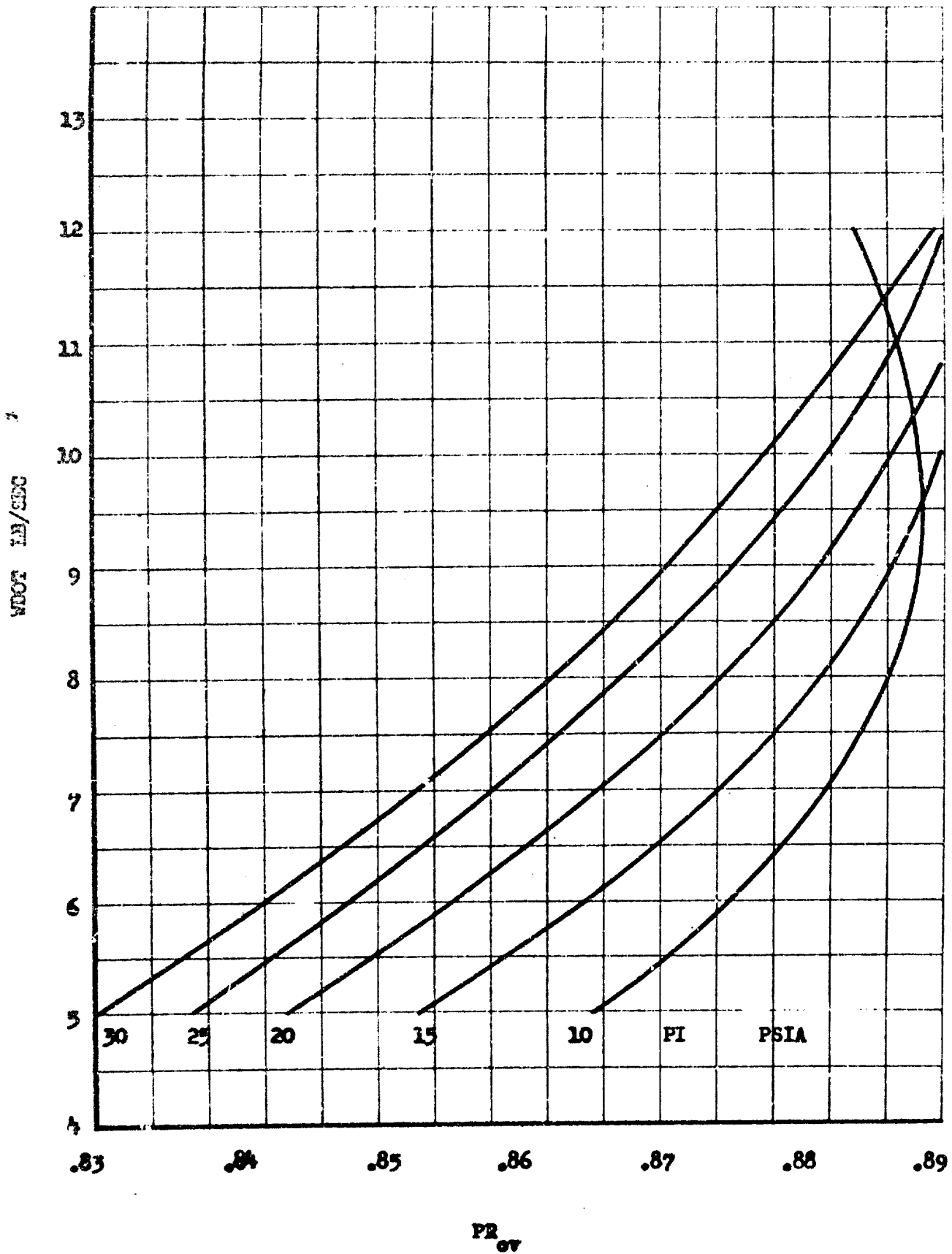
Figure 125 By-Pass Cavitating Venturi, Pressure Ratio/Total Flow

ByPass CAVITATING VENTURI

DI = 0.75 in

Figure 126 By-Pass Cavitating Venturi, Pressure Ratio/Total Flow

DOCUMENT CONTROL DATA - R&D

(Security classification of title, body of abstract and indexing annotation must be entered when the overall report is classified)

1. ORIGINATING ACTIVITY (Corporate author)	2a. REPORT SECURITY CLASSIFICATION
Martin Marietta Corporation	Unclassified
	2b. GROUP N/A

3. REPORT TITLE

System Coupled Dynamic Instability Amplitude Limiting Analysis and Evaluation

4. DESCRIPTIVE NOTES (Type of report and inclusive dates)

Final Report

5. AUTHOR(S) (Last name, first name, initial)

Bikle, Fred E.; Fidler, Larry E.; Hendricks, Tom C.

6. REPORT DATE	7a. TOTAL NO. OF PAGES	7b. NO. OF REFS
March 1968	521	18

8a. CONTRACT OR GRANT NO.	9a. ORIGINATOR'S REPORT NUMBER(S)
AF04611-67-C0031	
b. PROJECT NO.	MCR-68-20
c. 3058	9b. OTHER REPORT NO(S) (Any other numbers that may be assigned this report)
d.	AFRPL-TR-68-41

10. AVAILABILITY/LIMITATION NOTICES

This document is subject to special export controls and each transmittal to foreign governments or foreign nationals may be made only with prior approval of AFRPL (RPEI/STINFO), Edwards, California.

11. SUPPLEMENTARY NOTES	12. SPONSORING MILITARY ACTIVITY
	Air Force Rocket Propulsion Laboratory
	Air Force Flight Test Center
	Edwards Air Force Base, RPRPP

13. ABSTRACT

This report is concerned with the study of instabilities, generally referred to as POGO, resulting from coupling between liquid-fueled propulsion systems and structural dynamics. The report deals specifically with analysis of active and passive methods of stability compensation, methods of predicting POGO limit cycle amplitudes, and statistical methods of evaluating POGO stability margins. In addition, experimental studies were conducted to evaluate certain passive compensation methods. Specifically, sealed bag accumulator, gas injection, and cavitating venturi concepts were studied.

DD FORM 1473 (JAN 64)

14. KEY WORDS	LINK A		LINK B		LINK C	
	ROLE	WT	ROLE	WT	ROLE	WT
POGO Stability Transient Flow Limit Cycle Experiment						

INSTRUCTIONS

1. **ORIGINATING ACTIVITY:** Enter the name and address of the contractor, subcontractor, grantee, Department of Defense activity or other organization (corporate author) issuing the report.

2a. **REPORT SECURITY CLASSIFICATION:** Enter the overall security classification of the report. Indicate whether "Restricted Data" is included. Marking is to be in accordance with appropriate security regulations.

2b. **GROUP:** Automatic downgrading is specified in DoD Directive 5200. 10 and Armed Forces Industrial Manual. Enter the group number. Also, when applicable, show that optional markings have been used for Group 3 and Group 4 as authorized.

3. **REPORT TITLE:** Enter the complete report title in all capital letters. Titles in all cases should be unclassified. If a meaningful title cannot be selected without classification, show title classification in all capitals in parenthesis immediately following the title.

4. **DESCRIPTIVE NOTES:** If appropriate, enter the type of report, e.g., interim, progress, summary, annual, or final. Give the inclusive dates when a specific reporting period is covered.

5. **AUTHOR(S):** Enter the name(s) of author(s) as shown on or in the report. Enter last name, first name, middle initial. If military, show rank and branch of service. The name of the principal author is an absolute minimum requirement.

6. **REPORT DATE:** Enter the date of the report as day, month, year; or month, year. If more than one date appears on the report, use date of publication.

7a. **TOTAL NUMBER OF PAGES:** The total page count should follow normal pagination procedures, i.e., enter the number of pages containing information.

7b. **NUMBER OF REFERENCES:** Enter the total number of references cited in the report.

8a. **CONTRACT OR GRANT NUMBER:** If appropriate, enter the applicable number of the contract or grant under which the report was written.

8b, 8c, & 8d. **PROJECT NUMBER:** Enter the appropriate military department identification, such as project number, subproject number, system numbers, task number, etc.

9a. **ORIGINATOR'S REPORT NUMBER(S):** Enter the official report number by which the document will be identified and controlled by the originating activity. This number must be unique to this report.

9b. **OTHER REPORT NUMBER(S):** If the report has been assigned any other report numbers (either by the originator or by the sponsor), also enter this number(s).

10. **AVAILABILITY/LIMITATION NOTICES:** Enter any limitations on further dissemination of the report, other than those imposed by security classification, using standard statements such as:

(1) "Qualified requesters may obtain copies of this report from DDC."

(2) "Foreign announcement and dissemination of this report by DDC is not authorized."

(3) "U. S. Government agencies may obtain copies of this report directly from DDC. Other qualified DDC users shall request through

_____."

(4) "U. S. military agencies may obtain copies of this report directly from DDC. Other qualified users shall request through

_____."

(5) "All distribution of this report is controlled. Qualified DDC users shall request through

_____."

If the report has been furnished to the Office of Technical Services, Department of Commerce, for sale to the public, indicate this fact and enter the price, if known.

11. **SUPPLEMENTARY NOTES:** Use for additional explanatory notes.

12. **SPONSORING MILITARY ACTIVITY:** Enter the name of the departmental project office or laboratory sponsoring (paying for) the research and development. Include address.

13. **ABSTRACT:** Enter an abstract giving a brief and factual summary of the document indicative of the report, even though it may also appear elsewhere in the body of the technical report. If additional space is required, a continuation sheet shall be attached.

It is highly desirable that the abstract of classified reports be unclassified. Each paragraph of the abstract shall end with an indication of the military security classification of the information in the paragraph, represented as (TS), (S), (C), or (U).

There is no limitation on the length of the abstract. However, the suggested length is from 150 to 225 words.

14. **KEY WORDS:** Key words are technically meaningful terms or short phrases that characterize a report and may be used as index entries for cataloging the report. Key words must be selected so that no security classification is required. Identifiers, such as equipment model designation, trade name, military project code name, geographic location, may be used as key words but will be followed by an indication of technical context. The assignment of links, rules, and weights is optional.